ISBN 978-82-471-2783-4 (printed ver.)
ISBN 978-82-471-2784-1 (electronic ver.)
ISSN 1503-8181

Lene Amundsen

Doctoral Thesis

Doctoral theses at NTNU, 2011:123

Lene Amundsen

An experimental study of oil-water flow in horizontal and inclined pipes

NTNU
Norwegian University of
Science and Technology

Doctoral theses at NTNU, 2011:123

NTNU
Norwegian University of
Science and Technology
Thesis for the degree of
doctor philosophiae
Faculty Engineering Science and Technology
Department of Energy and Process Engineering

NTNU
Norwegian University of
Science and Technology

Høgskolen i Telemark

Lene Amundsen

An experimental study of oil-water flow in horizontal and inclined pipes

Thesis for the degree of doctor philosophiae

Trondheim, May 2011

Norwegian University of
Science and Technology
Faculty of Engineering Science and Technology
Department of Energy and Process Engineering

NTNU
Norwegian University of
Science and Technology

Høgskolen i Telemark

NTNU
Norwegian University of Science and Technology

Thesis for the degree of doctor philosophiae

Faculty of Engineering Science and Technology
Department of Energy and Process Engineering

ISBN 978-82-471-2783-4 (printed ver.)
ISBN 978-82-471-2784-1 (electronic ver.)
ISSN 1503-8181

Doctoral Theses at NTNU, 2011:123

Printed by Tapir Uttrykk

ABSTRACT

The large discrepancies between model predictions and experimental data reported in the literature reveal that the physics of oil-water flow is complex and not yet fully understood. The knowledge of oil-water flow behaviour is essential in both field development and in production of gas and oil. Oil and water models, which are based on knowledge about the flow characteristics, are used to predict important parameters such as flow rates and pressure drop in production pipelines. Reliable simulation tools ensure safe production and high regularity. To find the features of the oil-water flow, a flow facility was built to enable visual observations and measurements of pressure gradient, local volume fractions, velocities and turbulence in horizontal and inclined pipes. The pipe inclination is an essential parameter since both production pipelines and wells can incline from 0° to 90° angle. Due to the uneven seabed the production pipelines contains sections with different inclinations, which normally varies between -10° to +10° angle. In the present work the effect of pipe inclination (-10° to +10°) and input water cut was studied at a constant mixture velocity equal to 1 m/s. A mixture velocity of 1 m/s is representative for the velocity in wells and production pipelines. A gamma densitometer measured the vertical phase distributions at input water cut from 10 to 90% and a Laser Doppler Anemometer measured the vertical velocity and turbulence distributions in the centre line of the pipe at 25 and 50% input water cut. The experiments were conducted in a 2-in. stainless steel pipe at atmospheric conditions and the fluids used were Exxsol D60 and tap water. An oil-water model was validated against the horizontal pipe flow data from this study at a mixture velocity equal to 1 m/s and against the horizontal pipe flow data of Elseth (2001) taken at higher mixture velocities equal to 2 and 3 m/s.

The experimental results give a good foundation for model validation and development. The pressure drop experiments showed that the frictional pressure gradient in two-phase flow was higher than that of single-phase oil flow, except in upward flow at low input water cuts. A steep frictional pressure gradient increase at high input water cut was observed in horizontal, downward and upward flow. The peak was observed at approximately 80% input water cut and was in the same order of magnitude; 1.7 times larger than that of pure oil. The abrupt increase is attributed to the increase in effective viscosity of the upper dispersed layer and to a non-radial phase distribution. This study presents a classification approach to determine the flow pattern. The method uses visual observations, the measured phase distributions and a

pre-defined phase inversion point to determine whether the flow is stratified or dispersed. The identified flow regimes in the parameter range studied were three different stratified flows with different degrees of dispersion and a plug flow. The most occurring flow regime in horizontal and inclined pipe flow was stratified flow with mixing at the interface (ST & MI). An error propagation analysis of the measured phase fractions showed that the accuracy is best in the centre of the pipe and that it decreases when approaching the wall due to increased absorption in the wall compared with the liquid phase. The calculated slip ratio and LDA velocity profile measurements showed that the oil phase is the fastest moving phase in upward flow. The velocity and turbulence profiles were greatly influenced by large inclination angles (±5° and ±10°), while smaller inclinations (±1°) had less effect. The effect of pipe inclination on the velocity and turbulence profiles was larger at 50% input water cut compared to 25%. A dampening effect of the cross-moments occurred in both horizontal and downward moving flow at 25 and 50% input water cut.

The oil-water model presented is an important step in improving of existing simulations tools used in the oil and gas industry. The oil-water flow model is developed by Schulkes (2000) and compared with experimental phase fractions, pressure gradient and slip ratio in horizontal pipe flow. The model is a combined two-fluid model and dispersion model and calculates the vertical phase fraction distributions, slip ratios and pressure gradients as function of input water cut. The dispersion model is a balance between turbulent and buoyancy forces. Experimental data published by Elseth (2001) were used in the comparison at higher flow velocities (2 and 3 m/s). In horizontal flow at the highest mixture velocity equal to 3 m/s the flow pattern predictions matched the experimental data perfectly. The predictions at lower velocities showed larger deviations. Although the model was able to predict important trends as increasing degree of mixing between oil and water with increasing mixture velocity, the model predictions of the frictional pressure gradient and phase fractions became gradually worse with increasing mixture velocity. However the slip ratio deviations do not increase with increasing mixture velocity as observed for the pressure gradient and phase fractions. The frictional pressure gradient predictions agreed reasonable well at 1 m/s except at high input water cuts. Here, the model was unable to reproduce the sharp increase in the frictional pressure gradient due to dispersed layer in top of the pipe. Strong correlations between the experimental and predicted phase fractions were also seen at 1 m/s, except at 50% input water cut and water cuts larger than 80%. The frictional pressure gradient was in general over

predicted at 2 and 3 m/s. The deviations observed between predictions and experiments could be due to a wrong model assumption of a non-radial phase distribution (structured layer), inadequate closure relations or due to additional mechanisms such as flocculation, interfacial waves, surfactants or lift forces that are not included in the model. The main contribution to the deviations in frictional pressure drop at 1 m/s at high input water cuts is attributed to the increase in viscosity in the upper dispersed phase and the effect of drop entrainment and the oil-water interface on the closure relations for single-phase shear stresses. Possibly explanation for the observed differences in phase distribution with increasing velocity is the assumption of a dilute phase for calculation of the closure relations for the turbulent diffusion coefficient and buoyancy forces. The closure relations will in addition be affected by the existence of the oil-water interface. The poor correlations between pressure drop predictions and experiments at higher velocities is most likely caused by the affect of multiphase flow behaviour on the single-phase shear stress correlations.

ACKNOWLEDGEMENT

Foremost I would like to thank Professor Morten Christian Melaaen for the valuable guidance and discussions as my supervisor. His knowledge within multiphase flow and his quick response has been very helpful. Special appreciation to my industrial co-supervisor Dr. Geir Elseth at Statoil for his guidance and input to the study.

The building of the horizontal flow loop to study oil-water flow in inclined pipes was supported financially by Norsk Hydro a.s. Special thanks to the technical research support team, who helped building the facility and to Pål Midtbøen for his support on the gamma instrument.

My great appreciation to Prof. Reidar B. Schüller at the University of Life Sciences at Ås for the fruitful discussions regarding multiphase flow behaviour, for his contribution to the instrumental error analysis and for commenting on the thesis.

I would like to extend my profound gratitude to my present colleagues at Statoil for sharing their experience, knowledge and being a source for inspiration. Special thanks to Prof. Ruben Schulkes for the invaluable guidance and support to the modelling part of this study. Particularly thanks to Atle J. Gyllensten for conducting the computational fluid dynamic simulations and to my former and present managers Pål Eirik Hedne and Bjørn Meland for their support to finish my PhD study at Statoil. I would give my grateful thanks to Dr. Arne Valle and Dr. George William Johnson for helpful discussions.

Sincere gratitude to my former PhD colleagues Sondre Vestøl, Amaranath Sena Kumara, Jon Are Julshamn, Marit Kleven, Anette Mathisen and employees Brit Halvorsen, Wenche Bergland, Thorstein Fåne, Stig Nilsen, Øyvind Johansen and IT services at Telemark University College for contributing to an enjoyable working environment. Specially thanks to Sondre Vestøl for the contribution to the experimental work and to Talleiv Skredtvedt for the first-class technical support on the facility. Especially thanks for the utmost support provided by Øyvind Urkedal, Øystein Gjertsen and Jarle Teigen at the IT services and thanks to my dear beloved friend Gry Sofie Fahrendorff for her comments on my abstract in a busy schedule as a mother of a young child.

Acknowledgement

Thanks to the summer students at Telemark University College and at Statoil for contributing to both experimental and modelling work. Particular, thanks to Camilla Dyvik for the contribution to the experimental work at Telemark University College and to Marte Kristine Valle and Vibeke Bredvold Karlsen for contributing with the model comparison.

NOMENCLATURE

Roman symbols		**Unit**
A	Radius of the fluid particle (droplet)	(m)
A	Area	(m^2)
A_m	Atomic mass number	(kg/kmol)
API gravity	American Petroleum Institute gravity	(°API)
C	Speed of light in vacuum	(m/s)
c_1, c_2	Constants in mixture viscosity correlation	(-)
C_D	Particle drag coefficient	(-)
c_m	Speed of light in a substance	(m/s)
C_H	Tunable constant, Eq. (2.20)	(-)
CFD	Computational fluid dynamics	(-)
D	Inner pipe diameter	(m)
d_f	Fringe distance	(m)
D_g	Gamma beam diameter	(m)
D_H	Hydraulic diameter	(m)
D_o	Outer pipe diameter	(m)
D	Drop diameter	(m)
d_{max}	Maximum droplet diameter	(m)
$d(\varepsilon_w)$	Total measurement error in phase fraction	(-)
$d(\varepsilon_w)_I$	Measurement error due to error in transmitting gamma intensity	(-)
$d(\varepsilon_w)_{I_0}$	Measurement error due to error in incident/source gamma intensity	(-)
$d(\varepsilon_w)_{\gamma_1}$	Measurement error due to error in linear attenuation coefficient for fluid 1.	(-)
$d(\varepsilon_w)_{\gamma_2}$	Measurement error due to error in linear attenuation coefficient for fluid 2.	(-)
$d(\varepsilon_w)_H$	Measurement error due to error in liquid length	(-)
d_f	Fringe distance	(m)
$d_{\max}$	Maximum droplet size in a turbulent flow	(m)
dP	Pressure gradient	(Pa/m)
dp_f	Frictional pressure drop	(Pa)
dp_m	Measured pressure drop	(Pa)
dp_s	Static pressure drop	(Pa)
dp_T	Total pressure drop	(Pa)
$D(x)$	Instrumental accuracy	(-)
d_{step}	Uncertainty in the traversing device	(-)
Dz_0	Uncertainty in zero point	(-)
E	Gamma energy	(keV)
E_c	Convergence criteria	(-)
F	Friction factor	(-)
f_{int}	Interfacial friction factor	(-)
f_D	Doppler frequency	(1/s)
F_D	Drag forces on a spherical particle	(N)

Nomenclature

f_e	Friction factor of finely dispersed emulsion	(-)
F_g	Gravity force acting on an individual drop	(N)
f_{ow}	Interfacial friction factor	(-)
F_T	Net driving force on a drop due to turbulent fluctuation	(N)
g	Gravity constant	(m/s^2)
g_N	Normal gravity component	(m/s^2)
g_Z	Parallel gravity component	(m/s^2)
h	Interfacial height	(m)
H	Local pipe height between the inner walls	(m)
H_o	Local pipe height between the outer walls	(m)
I	Transmitting gamma intensity	(1/s)
I_0,	Incident/source gamma intensity	(1/s)
I_0	Initial gamma intensity in air	(1/s)
I_o	Transmitting gamma intensity in oil filled pipe	(1/s)
I_w	Transmitting gamma intensity in water filled pipe	(1/s)
I_{pipe}	Transmitting gamma intensity in pipe filled with air	(1/s)
J	Stability criteria parameters	(m^2/s^2)
J_s	Stability criteria parameters, sheltering effect	(m^2/s^2)
K	Concentration function constant	(-)
L	Pipe length (Axial direction)	(m)
l_k	Kolmogorov microscale	
N	Number of absorbed gamma ray photons	(-)
n_0	Initial number of gamma ray photons	(-)
n	Number of measurements	(-)
N_A	Avogadro number	(-)
n_r	Refraction of light, Snell's law	(-)
n_s	Sedimentation velocity exponent	(-)
N_{Vi}	Dimensionless viscosity group (Eq. 2.13)	(-)
N_{We}	Generelized Weber number (Eq. 2.12)	(-)
$(N_{We})_{crit}$	Critical Weber number	(-)
P	Pressure	(Pa)
R	Inner pipe radius	(m)
Ro	Outer pipe radius	(m)
Re	Reynolds number	(-)
Re_{crit}	Critical Reynolds number	(-)
Re_p	Particle Reynolds number	(-)
rms	Root mean square	(-)
Q	Input volumetric flow rate	(m^3/s)
QCV	Quick Closing Valves	
S	Perimeter of the pipe surface	(m^2)
SG	Specific gravity	(-)
S_i	Width of interface	(m^2)
S_v	Maximum velocity gradient in external flow field	(1/s)
STD	Standard deviation	(-)
S_{ow}	Holdup ratio/slip ratio between oil and water	(-)
T	Time	(s)
T_{int}	Integral fluid time scale	(s)
Tu	Turbulence intensity	(-)

Nomenclature

u	In-situ axial velocity	(m/s)
$\overline{u}$	Axial mean velocity	(m/s)
U	Average axial velocity	(m/s)
u'	Fluctuating component of velocity in the x-direction (axial direction)	(m/s)
u^*	Friction velocity	(m/s)
U^+	Non-dimensional velocity component	(-)
Z^+	Non-dimensional position	(-)
u_s	Average slip velocity	(m/s)
$\overline{u^2}$	Mean square of velocity fluctuations	(m^2/s^2)
u_{rms}	Root mean square axial velocity	(m/s)
u_s	Slip velocity	(m/s)
V	Radial velocity component	(m/s)
$\overline{v}$	Radial mean velocity	(m/s)
v'	Fluctuating component of velocity in the y-direction (radial direction)	(m/s)
v_s	Sedimentation velocity	(m/s)
v_∞	Sedimentation velocity	(m/s)
v_{rms}	Root mean square radial velocity	(m/s)
w	Width of control volume	(m)
wc	Input water cut	(%),(-)
X	Lockard Martinelli parameter	(-)
x	Distance traversed through the pipe material	(m)
x_1	Local height of fluid 1 in pipe flow	(m)
x_2	Local height of fluid 2 in pipe flow	(m)
x_3	Local height of fluid 3 in pipe flow	(m)
z	Vertical position, from top to bottom of the pipe	(m)

Greek symbols

α	Input water cut (Input phase fraction)	(-)
α_o	Input oil cut	(-)
ε	In situ/local phase fraction	(-)
ε_{inv}	Dispersed phase fraction at point of inversion	(-)
ε_{cw}	Are averaged volume fraction of the continuous water phase	(-)
ε_{co}	Are averaged volume fraction of the continuous oil phase	(-)
ε_{dw}	Are averaged volume fraction of the dispersed water phase	(-)
ε_{do}	Are averaged volume fraction of the dispersed oil phase, Eq. (7.32)	(-)
τ	Shear stress	(N/m^2)
τ_w	Mean wall shear stress for water	(N/m^2)
τ_o	Mean wall shear stress for oil	(N/m^2)
τ_{ow} , τ_i	Interfacial shear stress	(N/m^2)

Nomenclature

τ_{ow}^{w}	Interfacial shear stress included effect of waves	(N/m^2)
τ_s	Shear stress due to waves	(N/m^2)
μ	Absolute/dynamic viscosity	(Pas),(cp)
μ_{ab}	Mass absorption coefficient	(m^2/kg)
ρ	Density	kg/m^3
σ	Surface tension (interfacial tension)	(N/m)
η_i	Weighing factor	(-)
σ^2	Variance	(m^2/s^2)
σ_a	Atomic absorption cross section	(m^2/kmol)
σ_{ow}	Interfacial tension between oil and water	(N/m)
ϕ	Lockard Martinelli parameter	(-)
β	Inclination angle	(°)
β_i	Inner angle in Figure A7 and Figure A8	(°)
β_o	Outer angle in Figure A7 and Figure A8	(°)
μ_{ab}	Mass attenuation coefficient	(m^{-1})
γ_p	Constant which accounts for the particle inertia effects	(-)
γ	Linear absorption coefficient	(1/m)
γ_p	particle diffusion constant	(-)
λ	Wavelength of light	(m)
θ	Angle between two intersecting beams	(º)
Y	Kinematic viscosity, μ/ ρ	(m^2/s)
Γ	Turbulent particle diffusion coefficient	(m^2/s)
Γ_f	Turbulent fluid diffusivity	(m^2/s)
δ	Wetted angle	(º)

Subscript

0	Initial
c	Continuous phase
co	Continuous oil phase
d	Dispersed phase
f	Fluid
m	Mixture
max	Maximum
o	Oil phase
p	Particle
s	Superficial
sco	Superficial velocity of oil continuous layer
sdo	Superficial velocity of dispersed oil droplets
w	Water phase

Table of contents

1 INTRODUCTION

Crude oil is the most important energy carrier on a global scale and since all kinds of transport rely heavily on oil, the future availability of crude oil is of vital importance. The oil and gas industry processes include exploration, extraction, refining, transportation (by oil tankers and pipelines) and marketing of petroleum products. The production, distribution, refining and retailing of petroleum represent the world's largest industry in terms of dollar value, in which fuel oil and gasoline is the largest volume products of the industry. Petroleum is in addition vital to many other industries such as pharmaceutical, solvents, fertilizer, plastics, chemical, nuclear and geothermal.

Zittel and Schindler (2008) and Aleklett et al. (2010) report that the world's oil production has peaked and that the production will decline at a rate of several percent per year. The world's oil production forecast from currently producing fields, fields yet to be developed, fields yet to be found, additional EOR, non-conventional and natural gas liquids is shown in Figure 1.1. By 2020-2030 global oil supply will be dramatically lower. This will create a supply gap which cannot be closed by growing contributions from other fossil, nuclear or alternative energy sources in this time frame provided that current technology will be the same. Since the accessible gas and oil reserves are depleting it is increasingly more important to develop marginal fields that were once considered uneconomic and to increase the exploration of new fields. Since the demand of energy is accelerating and most of the remaining energy sources exist in harsh, deep, shallow and cold environment there is a need to develop technology to manage producing oil and gas from these challenging regions. Production of non-conventional oil and gas as oil sands, viscous oil and shale gas are many oil companies's strategy to grow. With the exploration activity and production decline in the Norwegian Continental shelf (NCS) Statoil want to explore the opportunities in the north in the Barents Sea and Arctic Ocean, where the environment is harsh and cold and the ecosystem is vulnerable. Enabling production from such fields require long distance transport of oil and gas from the well to an on-shore facility due to the large risks of having an off-shore facility.

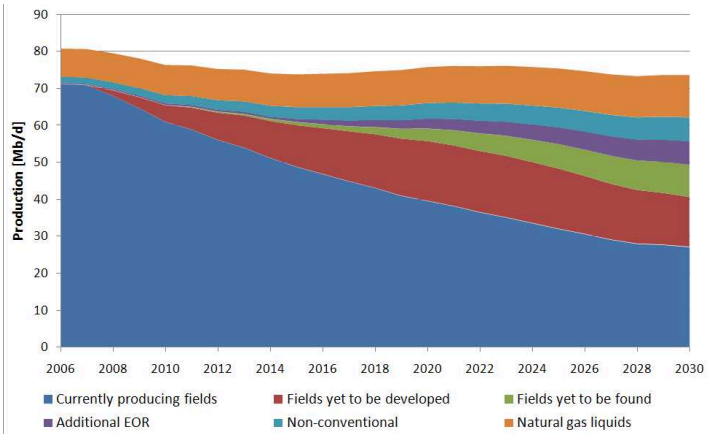

Figure 1.1 Predictions of the world's total oil production from currently producing fields, fields yet to be developed, fields yet to be found, additional EOR, non-conventional and natural gas liquids [Aleklett et al. (2010)].

1.1 Multiphase flow

Multiphase flow occurs in the whole process from the reservoir to the final product. Figure 1.2 illustrates the process from the reservoir to an offshore processing facility. From the offshore processing facility the fluids are transported by either oil tankers or pipelines for refining. Multiphase flow occurs frequently since layers of gas, oil and water often are present in the reservoir. The fluids flow through the reservoir and into the oil wells as illustrated in Figure 1.2 and then to an off-shore or on-shore installation for processing. To ensure reliable and optimum gas and oil production, actions need to be taken in the whole oil and gas value chain. Reservoir drainage, well design, multiphase flow and topside separation have a large impact on the recovery and optimization of oil and gas production. Horizontal wells are often utilized to improve oil and gas recovery efficiency and total well productivity. The dynamic and stationary characteristics of multiphase flow are important in many aspects of the field development and in operation such as design of wells, control, production-logging instruments, process optimization and topside equipment. Computer codes are used to estimate essential parameters in field development projects and in operation. The parameters could be production rate, flow regime, pressure drop, temperature drop, liquid hold-up, hydrodynamic slugging, slugging in risers, hydrate formation, inhibition requirements, wax formation, emulsion, scaling, corrosion and erosion. One of the world's longest unprocessed multiphase flow pipeline is the gas pipe at Snøhvit. The pipeline is 143 km long and is located

in cold Arctic regions. The transport of unprocessed multiphase flow, through such long seabed pipelines, requires that the multiphase computer codes are reliable. The development and verification of multiphase models in present study is contributing to achieve this.

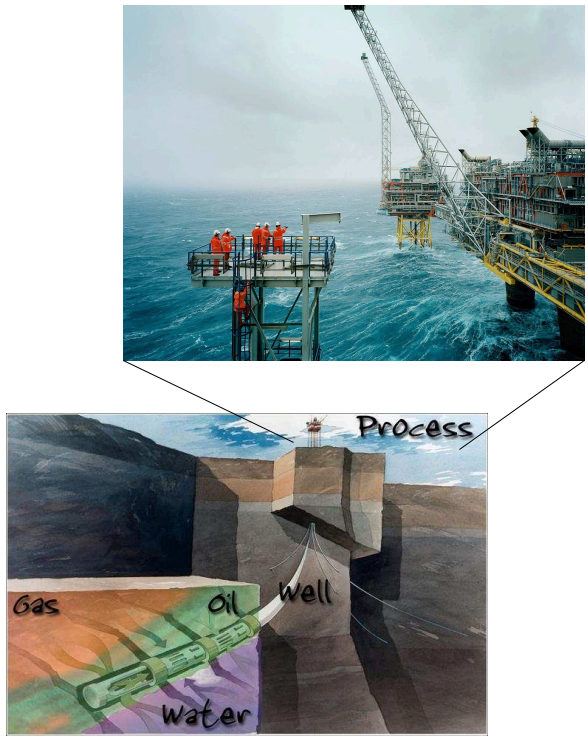

Figure 1.2 Multiphase flow production of gas, oil and water (Picture bottom; Jan Ulriksen and top; Manfred Jarisch/Statoil).

The multiphase flow can appear as gas-liquid (e.g. gas-condensate), liquid-liquid (e.g. oil-water) and gas-liquid-liquid (e.g. gas-oil-water). The geometrical arrangement of the fluids is termed flow pattern and have large influence on the flow parameters. To understand the physics of multiphase pipe flow, experiments are usually conducted to study parameters like pressure drop and phase distributions. Data produced from experimental campaigns are used to either validate existing models or to develop physical models or empirical correlations. Most of the reported multiphase flow studies concern gas-liquid flow. Gas-liquid flows have been studied extensively since 1950's and most of the reported studies use air and water at

atmospheric conditions [e.g. Johnson (2005)]. In contrast to two-phase gas-liquid flow, the literature on three-phase gas-oil-water and two-phase oil-water is relatively limited. Literature review's on three-phase experiments and modelling given by Khor (1998), Valle (2000) and Bannwart et al. (2009) report that the existing three-phase models are often incapable of predicting the behaviour of the flow and Spedding et al. (2005) specifically confirmed that the flow structure of water and oil in a three phase system can have dramatic effect on important flow parameters. The fluids used in most experimental studies are inert gas (air and nitrogen), model oils (Exxsol D60, Exxsol D80, kerosene) and freshwater at atmospheric conditions. The advantage of using this system is the possibility of visual observations, visual based instrumentation (Laser Doppler Anemometry) and low operational costs. Experiments that use real crude oil, natural gas and reservoir water at real life conditions (e.g. high pressure and temperature) are rather limited, but some data have been reported by e.g. Kvandal et al. (1998), Utvik et al. (1998), Solbakken and Schüller (2001) and Elseth et al. (2005).

The flow characteristics of oil-water flow are generally different from gas-liquid systems in the respect of smaller buoyancy forces (low density difference between the two phases), lower viscosity ratio and more complex interfacial chemistry. The complexity in oil-water flow makes it harder to find the deciding physical phenomena that determine the flow characteristics such as flow pattern, pressure gradient and slip ratio. This is reflected in large deviations between model predictions and experimental data.

1.2 Objectives

Since the physical mechanisms in oil-water flow is not yet understood and since flow of water and oil is a common occurrence in the petroleum industry, the present study will focus on the behaviour of oil-water flow. The flow of oil and water has in addition a remarkable influence on three-phase flow. The first objective in the present study is to find some general trends in oil-water flow as function of inclination angle and input water cut. The wells and the production pipelines can vary from approximately +10º to -10º inclination angle due to an uneven ocean bed. The effect of inclined pipes could be tremendous on the flow parameters and is not well documented. For this purpose the flow parameters; flow pattern, pressure gradient, in-situ phase fraction distribution, slip ratio, in-situ velocity and turbulence distribution were measured in an experimental facility. The flow was mainly stratified with different degree of mixing, fully developed and at steady state conditions. The objective was

also to establish theories about the main physical mechanisms that are dominating the flow parameters and to compare a mechanistic model with experimental data. For this reason, a oil-water model was presented and compared with experimental data for verification of the dominating mechanisms.

1.3 Structure of this thesis

The thesis is divided into six main parts. Chapter **2** presents a review of the work that has been done on two-phase oil-water steady state flow with particular attention to experimental findings. Chapter **3** presents the new experimental facility that was built to study inclined pipe flow together with experiments, analysis and model comparison for verification of the instrumentation and flow conditions. Chapter **4** outlines the gamma densitometer measurement method applied to current set-up and analysis of the measurement accuracy of the measured vertical phase fraction distributions. In addition, the chapter introduces a new flow pattern classification approach together with the measured flow patterns, phase fractions and calculated slip ratios as function of inclination and input water cut. Chapter **5** presents the total and frictional experimental pressure gradient in horizontal and inclined pipes at different input water cuts. Chapter **6** describes the current Laser Doppler Anemometer set-up and data validation together with the effect of inclination angle and input water cut on measured axial mean velocity, axial rms-velocity, vertical rms-velocity and cross-moments. Chapter **7** introduces a mechanistic oil-water model and compares the model predictions with experimental observations. The phase fraction, slip ratios and pressure gradient are used for model comparison. The main findings are summarised at the end of each chapter and Chapter **8** provides conclusions and recommendations for further work.

2 LITERATURE REVIEW ON OIL-WATER FLOW

A summary of various aspects in two-phase oil-water flow in horizontal and inclined pipes is given, with special attention on experimental findings. Due to the large differences between two-phase oil-water and oil-gas flow the lessons learned regarding oil-gas flow cannot be directly applied to oil-water flow. Important characteristics of oil-water flow are pressure drop, flow pattern, holdup, slip velocities, phase fraction, droplet size and distribution, velocity and turbulence profiles and phase inversion. Present review discusses the behavior of these flow parameters in horizontal and inclined oil-water pipe flow and Table A 1 in Appendix 1 presents a list of experimental work on oil-water flow in horizontal and small pipe inclinations (0˚ - 30˚). Most of the oil used is classified as light to medium oil and the flow is assumed to be fully developed and at steady state conditions. In particular vertical flow, slug flow, core annular flow, equal density flows (heavy oil) are not discussed in detail. A brief review on the modeling work is also presented.

2.1 Oil-water flow pattern

Classification of different flow patterns is vital in the study of multiphase flow since each regime has great influence on important parameters such as pressure drop and phase separation. Since approximately 1990's the advancement and development of instrumentation and methods used in the classification have improved the accuracy and resolution [Xu (2007)]. More details about the flow structure often leads to a re-classification of flow regimes already established in a defined system. The classification of flow regime is done subjectively and often differently by each researcher, which must be taken into account when comparing with other researchers. The classification is approached in many different ways in the literature. The researchers use different definitions, techniques and names when determining the flow patterns. The flow pattern transition boundaries between the different flow regimes are also dependent on the liquids and facility used. Oil-water flow classification can be divided into four main flow regimes and below is the most used definitions. The definitions of flow regimes are widely used [Lovick (2004)], and they are often divided further into sub regimes with more detailed descriptions of the flow structures.

Stratified flow is when two immiscible liquids flow simultaneously in separate layers according to their different densities. A common criterion to determine whether the flow is stratified is that the flow has two continuous phases. The continuous phases can be partly or

fully dispersed. Some researchers use different definitions of stratified flow, which is introduced later in this section.

Dispersed flow is when there exists only one continuous phase with the other phase dispersed in it in the form of droplets. The dispersed flow could be homogenous, with the droplets distributed uniformly in the whole pipe cross section area or there can be a concentration gradient where the droplets are concentrated in the upper or lower part of the pipe. A stable dispersion of two immiscible fluids where one is polar and the other non-polar is often called an emulsion. Stable dispersion is usually "tight" and is hard to separate. Many investigators refer the oil in water (o/w) and water in oil (w/o) dispersions as emulsions. The emulsion is homogenous only at sufficient high mixture velocities. When the emulsion goes from oil to water continuous the flow goes through a phase inversion process.

Annular flow is when one of the fluids forms an annular film on the pipe wall and the other flows in the centre of the pipe. The flow regime occurs especially when two liquids have equal densities (water and heavy oil) or when one of the liquid phases has large viscosities.

Plug/bubble flow is when bubbles or plugs of oil flows one after the other in the top of the pipe.

2.1.1 Horizontal pipe flow

The investigation of oil-water flow started during the 1950's. Since then, a large number of researchers have studied oil-water flow patterns. Table A 2 in Appendix 2 presents several of the flow patterns classified by different researchers and demonstrates the variety. The researchers use both different definitions and different names in the classification of flow patterns. One of the first to classify oil-water flow pattern was Russel et al. (1959). He studied oil-water flow patterns in horizontal pipe flow and identified visually three flow regimes by varying the input volume ratio of oil and water. The three flow regimes are mixed flow, stratified flow and bubble flow. The bubble flow was characterized by oil bubbles flowing in top of the pipe. In 1995 Trallero proposed a flow pattern classification which incorporated most of the flow configurations observed in published experimental studies and acquired data [Russel et al. (1959), Guzhov et al. (1973), Malinowsky (1975), Laflin and Oglesby (1976), Oglesby (1979), Cox (1985), Scott (1985), Stapelberg and Mewes (1990), Nädler and Mewes (1995), Valle and Kvandal (1995)]. Trallero (1995) was the first to combine several different measurement techniques in the classification of flow patterns. Trallero (1995) used camera, differential pressure transducers and conductance probes to measure the local phase

continuity. Trallero (1995) distinguished six flow regimes and classified them into two major categories, segregated flow and dispersed flow. The re-classification of established flow regimes were based on original data and careful analysis of the measured flow pattern descriptions, pictures/drawings, pressure drops and/or holdups measurements. Trallero's (1995) flow regime classification is presented in Figure 2.1. In the segregated flow regimes, the flow can either be stratified flow (ST) or stratified flow with mixing at the interface (ST & MI). The interface in the stratified flow regime (ST) is smooth and the two phases are completely segregated. Long interfacial waves compared to the pipe diameter were measured in the stratified flow regime. In the stratified flow with mixing at the interface flow regime (ST & MI) water droplets exist in the oil layer and oil droplets in the water layer and the droplets remain close to the interface. Increasing the velocity increased the formation and spreading of droplets. The reported mechanisms acting simultaneous on the droplets are dynamic and buoyant forces. In the dispersed flow one phase can be either fully or partially dispersed in the other. The dispersions are represented by dispersion of oil in water and water (Do/w & w), oil in water emulsion (o/w), water in oil emulsion (w/o) and dispersion of water in oil and oil in water (Dw/o & Do/w). In the dispersion of oil in water and water (Do/w & w) flow regime, the oil is dispersed as a dense layer in the top of the pipe with one continuous phase and occurred at sufficient large velocities and large input water cut. The oil in water emulsion (o/w) and water in oil emulsion (w/o) are characterized with one continuous phase, where water is continuous in the (o/w) flow regime and oil in the (w/o) flow regime. The (o/w) and (w/o) emulsions can be homogenous or have a radial gradient concentration. Homogenous emulsion was only observed at sufficiently high mixture velocities. The dispersion of water in oil and oil in water (Dw/o & Do/w) has two continuous layers where the (o/w) and (w/o) coexist. Trallero (1995) classifies this flow regime as dispersed flow. According to the definitions presented above, this flow regime classifies as stratified flow due to the existence of two continuous phases.

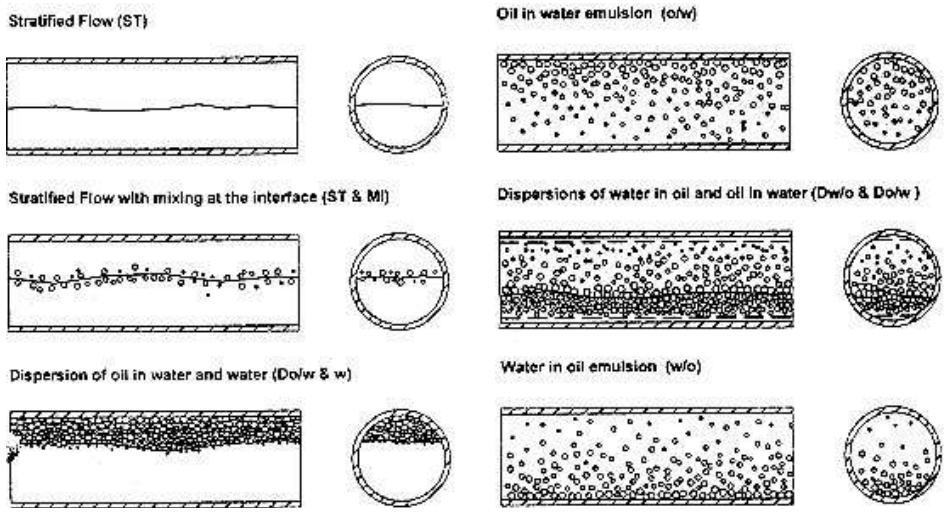

Figure 2.1 Horizontal oil-water flow patterns [Trallero et al. (1997)].

Angeli (1996) and Soleimani (1999) classified a flow regime containing one continuous phase with a dispersed fraction of oil or water droplets in the top or bottom of the pipe as stratified flow as shown in Figure 2.2. The oil continuous flow with dispersed water droplets in the bottom of the pipe was classified as stratified mixed with an oil continuous layer (SM/oil layer) by Angeli and as stratified mixed/oil layer (1) by Soleimani. Trallero (1995) did not classify the oil continuous flow regime with dispersed water droplets in the bottom of the pipe.

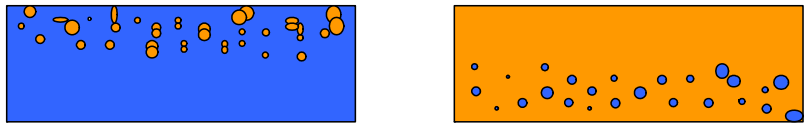

Figure 2.2 Classification of Angeli (1996) and Soleimani (1999), stratified flow with mixing of oil droplets (to the left) and mixing of water droplets (to the right).

Angeli (1996) observed six different flow regimes, five stratified and one mixed flow regime. In contrast to Trallero (1995), the dispersion of water in oil and oil in water (Dw/o and Do/w) regime were classified as stratified flow. Angeli (1996) measured a stratified mixed flow with water continuous layer (SM/water layer), which is in accordance with Trallero's Do/w & w flow regime. Angeli (1996) described a three layer flow regime (3L), where a water continuous phase exists in the bottom of the pipe, a mixed layer in the centre and a continuous

oil phase in the top of the pipe. This flow regime has a larger degree of dispersion than the corresponding ST & MI of Trallero (1995). Soleimani (1999) measured a variety of flow patterns in a stainless steel section by observing the flow with a high speed camera together with interpretation of local volume fractions measured by conductivity and densitometer. Soleimani (1999) identified two new flow regimes, which are shown in Figure 2.3. The flow patterns had two continuous phases and were named stratified mixed/water layer 2 (on the left hand side) and stratified mixed/oil layer 2 layer (on the right hand side). The first regime had an oil layer completely mixed with water droplets and a water layer mixed with oil droplets close to the interface. The second regime had a water layer completely mixed with oil droplets and an oil layer with mixing of water droplets close to the interface. The conductivity probes and gamma densitometer (tomography and vertical distribution) made it possible to distinguish whether the flow contained two or one continuous phase as shown in Figure 2.2 and Figure 2.3.

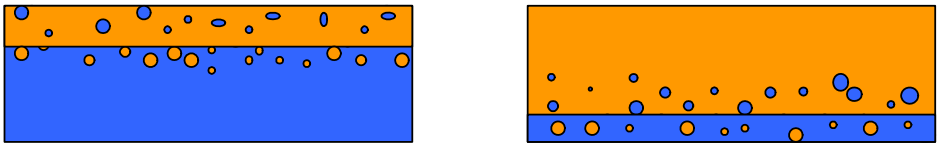

Figure 2.3 Stratified mixed/water layer (2) and stratified mixed/oil layer (2).

Several researchers use the same classification as that of Trallero (1995), but often additional flow regimes are defined. Alkaya (2000) used the same nomenclature as Trallero (1995), but with an additional flow pattern measured in inclined flows called dispersion of water-in-oil and oil (Dw/o and o). This flow regime is in accordance to Soleimani's (1999) stratified mixed/oil layer flow regime.

Kvandal et al. (2000) presented four different flow regimes, which were classified by using measured phase fraction profiles as shown in Figure 2.4. The four different flow regimes were classified as stratified dispersed flow (SD), dispersed flow with an inhomogeneous bulk mixture (DIH-B), dispersed flow with an inhomogenous wall mixture (DIH-W) and dispersed homogenous flow (DH).

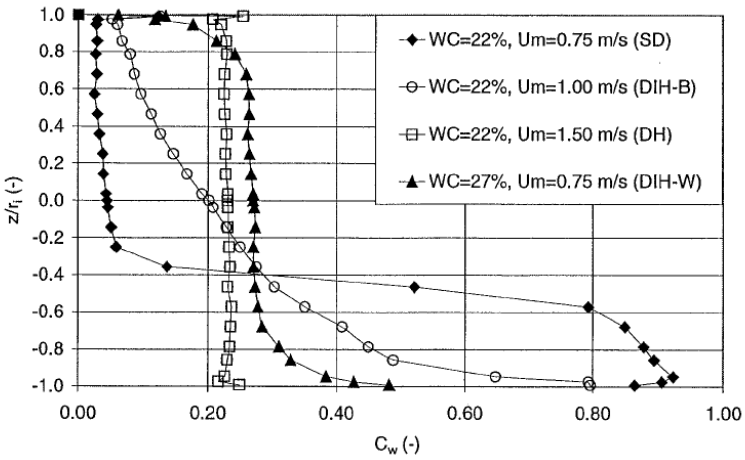

Figure 2.4 Phase fraction measurements and flow pattern classification [Kvandal et al. (2000)].

Elseth (2001) subjectively classified nine different flow regimes by use of visual observations and gamma densitometer measurements. The facility that was used to generate the data was the same as the one used in present study. Three of the flow regimes were classified as stratified and six were classified as dispersed flow. The three stratified flow were described as stratified smooth (SS), stratified wavy (SW) and stratified mixed (SM). The six dispersed flow regimes were oil continuous dispersions with dense packed layer of water droplets (Do-DP), water continuous dispersions with dense packed layer of oil droplets (Dw-DP), oil continuous dispersion inhomogeneous and homogenous (Do-I, Do-H) and water continuous dispersion inhomogeneous and homogenous (Dw-I, Dw-H). The water continuous dispersions with dense packed layer of oil droplets is in accordance with Trallero's (1995) Do/w and w flow regime and the oil continuous dispersions with dense packed layer of water droplets is the same as the stratified mixed/oil layer (1) measured by Soleimani (1999).

Some publications report slug, bubble or plug flow in oil-water flow. A plug/slug was described in both horizontal and inclined pipe flow in the literature. The descriptions of the flow structure are very similar, but they are named differently. Angeli (1994), Beretta et al. (1997), Valle (2000), Liu et al. (2003), Abduvayt et al. (2006) and Mandal et al. (2007) measured a flow pattern characterized by oil bubbles/plugs flowing in the top of the pipe. Angeli (1994) measured bubble flow, which was characterized by elongated oil "bubbles"

that flowed one after the other on top of the water layer. The drop layer between the oil and water layers bridged the pipe from time to time. Beretta et al. (1997) measured plug flow with large elongated bubbles in small pipe diameter equal to 3 mm.

Real crude oil system

Figure 2.5 shows a schematic description of how crude oil can be classified. Physical properties that can distinguish heavy crudes from conventional ones are viscosity and specific gravity and the composition of heavier molecules (asphaltenes and resins). The specific gravity is a measure of the relative density of oil and water. The conventional crude oil is also termed light oil, which means that the low viscosity of the oil makes it easy to produce, transport and refine. Heavy oil is often referred to as non-conventional oil and is more difficult and costly to produce and refine and have a larger environmental impact relative to conventional oil production. The viscosity of the light crude oil can range from 1 to 10 cP, while the extra heavy crudes can have viscosities up to 10 000cP. As the viscosity increases the specific gravity decreases, which means that the density of the oil is getting close to that of water. American Petroleum Institute gravity, API gravity is a measure of how heavy a petroleum liquid is compared to water as shown in Eqs. (2.1) and (2.2).

$$API\ \ gravity = \frac{141.5}{SG} - 131.5 \qquad (2.1)$$

Where SG is the specific gravity at standard conditions.

$$SG_{1bar,15^0C} = \frac{\rho_o}{\rho_w} \qquad (2.2)$$

For light oil the API is larger than 20 and less than 20 for heavy oils. For extra heavy oil the API is less than 10. The main difference between heavy crude oil and extra heavy oil is that the extra heavy oil generally does not flow at all. Heavy and extra heavy oil make up about 70% of the worlds total oil resources of 9 to 13 trillion barrels [Alboudwarej et al. (2006)]. Countries with largest amounts of heavy oil are Kuwait, Iraq, Canada and Venezuela and the largest exports of fossil fuels are Saudi Arabia, while the United States are the largest consumers.

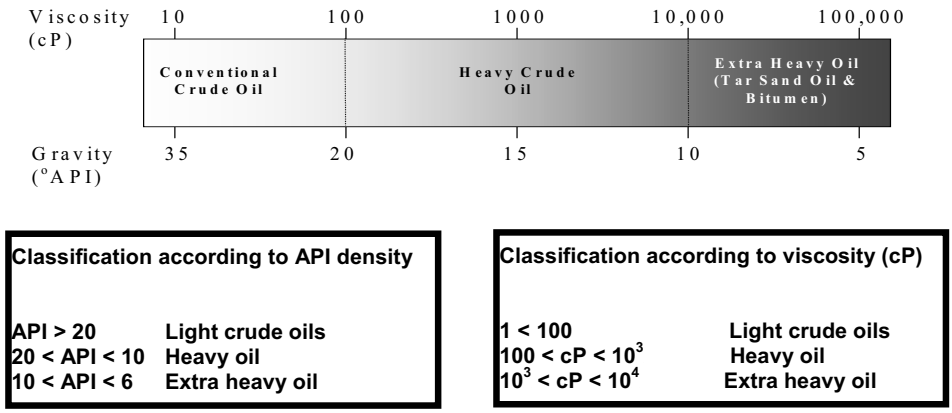

Figure 2.5 Fluid characterization of light to extra heavy crude oils.

Studies with use of real crude oils at real life conditions are very scarce. One of the first to publish data with use of a recombined crude oil-water system was Valle and Utvik (1997). They observed an oil continuous flow with dispersed water droplets at water cuts below 45% and stratified flow above 45% at three different flow rates, which indicated that the mixture velocity did not influence the transition boundaries between dispersed to stratified flow. Valle (2000) observed that the mixture velocity did not influence the transition boundaries in some cases, but in the majority of the experiments the mixture velocity did influence the transition from dispersed to stratified flow. Valle (2000) used four different classification terms in oil-water experiments using model oil and a recombined reservoir system: separated, dispersed oil continuous, dispersed water continuous and slug. A two-wire capacitance probe was used in the classification of flow patterns. The probe was capable to distinguish between the fluids of the continuous phase. In the Exxsol D60 model oil system the flow was stratified at low water cuts, even for high flow rates. The dispersed oil continuous flow regime was observed only at one experimental condition at 2.4 m/s and 20% water cut. A slug flow regime was identified at 2.4 m/s and 30 % input water cut. Decreasing the density difference between oil and water and increasing the viscosity difference, generally increased the occurrence of dispersed oil continuous flow regime, when using a real crude oil system. Both Valle (2000) and Utvik et al. (2001) investigated the difference between a recombined hydrocarbon-water fluid and a model fluid system. The results showed a significant deviation in flow patterns for both two and three phase flow. They compared a model oil system with a crude oil system with approximately identical fluid density, viscosities and interfacial tensions. The flow

pattern map for crude oils displayed an opposite trend compared to the model oil flow map. The crude oil-water flow pattern map generally showed oil continuous dispersed flow at low water cut, even at low velocities. When the water cut exceeded 50% the flow was either separated or water continuous dispersions. In contrast, the model oil-water system showed separated flow pattern at lower water cuts, even at high velocities. The different behaviour of the two systems was probably due to different coalescence efficiencies. The water drops in oil seemed to be able to coalesce more easily for the model oil system, creating a separated flow at low water cuts and high velocity. And the oil drops coalesced more slowly for the model oil system leading to a dispersed water continuous flow. Fairuzov et al. (2000) executed oil-water experiments in a horizontal pipe with use of a real crude oil in a full scale pipe diameter equal to 40.6 cm. They showed that in stratified crude oil-water flow, complete phase separation could not be achieved. A small amount of water was at all times dispersed uniformly in the oil layer. Increasing the water cut generally increased stratification of the flow.

Influence of viscosity and density

Larger degree of mixing is seen for the light oils compared with the heavier oils in horizontal and inclined pipes. The observed flow patterns conducted by Charles et al. (1961) were similar for each oil and were found to be largely independent of the oil viscosity, except for the most viscous oil with a viscosity equal to 65 cp. Nädler and Mewes (1997) also showed that the effect of viscosity ratio required for emulsification was not significant in the viscosity range studied (22 - 35 cp). Vedapuri et al. (1997) measured that different flow configurations appeared when two different oil viscosities equal to 2 and 90 cp were used by measuring the in situ water distribution with an isokinetic sampling probe. High viscosity oil gave less mixing and less amount of water penetrating the oil. Charles et al. (1961) did not measure stratified flow when equal densities were used and observed only dispersed and annular flow regimes. Hapanowicz et al. (1997) studied two oils with equal viscosity and a large difference in density equal to 285 kg/m^3. The different oils produced different flow regimes. Flows of drops and plugs occurred only for the low density oil, while flow of foam occurred for the high density oil. Yao and Gong (2004) executed experiments with use of heavy oil (high viscosity and high density) and compared the flow patterns with light oil flow patterns and found large differences. Sotgia et al. (2008) showed that the appearance of annular flow is the

dominating flow pattern with use of heavy mineral oil. When viscous oil and water are mixed through a mixing device e.g. a pump or valve the separation/sedimentation takes longer time.

Influence of material properties – wall wetting and roughness

The degree of wetting of the wall is dependent on the wall material, the history and dynamics of the liquid motion close to the pipe surface and the properties of the liquid. Angeli (1994) measured the transition from stratified to fully mixed flow regime to start in the steel pipe at lower mixture velocities (1.3 m/s) than in the transpalite pipe (1.7 m/s), which were most likely due to the difference in pipe wall roughness. Angeli (1996) and Angeli and Hewitt (1998) reported a difference in flow configuration between the transpalite/acrylic pipe and the steel pipe. Angeli and Hewitt (1998) observed that the acrylic pipe was preferentially wetted by oil despite the history of the sample. A larger area of stratified/mixed flow with oil layer was measured in the acrylic pipe, which meant that the oil in the acrylic pipe tended to remain continuous over a larger range of conditions than in the steel pipe. Experiments conducted by Liu et al. (2003) however pointed out that the flow pattern and their transitions have similar trends in plexiglas and stainless steel pipes, but their quantities are shifted. The study of Hasson and Mann (1970) indicated that one of the major parameters governing the stability of annular flow is related to the wall-wetting properties. By using a hydrophilic treatment of the pipe surface the annular flow pattern was stabilized.

Influence of inlet design, pipe diameter and surfactants

The way oil and water are introduced into the test section influences the flow regime greatly and the inlet design of the mixers used in the literature varies to a great extent. In a real production system, oil and water are also being mixed in different ways by e.g. pumps and valves. Kocianova et al. (1995) studied the inlet design in horizontal pipe flow of two immiscible liquids and found that the flow patterns were depended on the arrangement and geometry of the inlet. Without using a nozzle at the inlet it was impossible to make any kind of dispersion in the tested range of flow rates. Mandal et al. (2007) tested three different designs of a mixer and showed that the flow pattern downstream could change severely.

An important scale-up parameter is the pipe diameter, since most of the reported experiments are conducted in small scale pipe diameters. Since the diameter of the production pipeline are in most cases much larger than the experimental one, the experimental Re numbers and shear stresses cannot both be matched with the ones in production. To match the Re number in the

production pipeline the experimental flow rate needs to be high, leading to a much larger experimental shear stress than the one in production. The shear stress matches when the flow rates are low, but then experimental Re number will be to low. Coleman and Garimella (1999) reported that the size of the pipe does not influence the flow pattern boundaries for diameters greater than 0.010 m. On the contrary Mandal et al. (2007) showed that the diameter of the pipe had a remarkable influence on the flow regime when the pipe diameter increased from 0.012 to 0.025 m. Three-layer appeared to be very common in large diameter pipe, but it did not occur in the narrow pipe and some of the flow patterns observed in the narrower pipe did not occur in the larger pipe. A possible explanation was attributed to the increased effect of surface tension and equilibrium contact angle in the narrow pipe. Decreasing the pipe diameter makes it easier for the interfacial tension forces to overcome the gravitational forces.

Kokal (2005) reports that chemical composition (asphaltenes, resins and waxes), solids (clays, scales and corrosion products) can influence the flow regime significantly. In subsea pipelines the fluids are cooled down from the well head to the platform. Cooling of waxy crude oils leads to precipitation of wax particles, which can lead to more stable emulsions. Asphaltenes and wax particles tend to accumulate at the oil-water interface, around the droplets, leading to suppression of sedimentation and coalescence rate. Shi et al. (2000, 2001) showed from the measured phase distributions that surfactants enhanced mixing of oil and water at low water cuts. When increasing the concentration of surfactants the water layer disappeared, oil and water mixed at a lower mixture velocity, and the homogenous flow pattern occurred at a lower input mixture velocity. Valle (2000) observed that surfactants (precipitated wax crystals) from waxy crude oil below its cloud point, created stable dispersions, which could not be separated in the gravity separator.

2.1.2 Interfacial structure and radial distribution in horizontal flow

A way to measure the level of the interface is to use an impedance probe, which measure both the resistive and capacitive components of materials. Kurban et al. (1995b) measured the level of the interface with a high frequency impedance probe. Since the interface in many cases was wavy and contained different degree of dispersion, an average interfacial value was measured by scanning the probe through the interfacial zone. A curved interface was measured in horizontal pipe flow by several researchers like e.g Soleimani (1999), Lovick and Angeli (2004a), Lum et al. (2004), Abduvayt et al. (2006). Soleimani (1999) measured a radial

distribution by use of both tomography gamma and conductivity probes. Soleimani (1999) found that the interface was not behaving like a structured layer, but had a strongly curved interfacial region at low velocity (1.25 m/s). A curved water continuous dispersion close to the wall, encapsulated the oil phase in the centre of the pipe. The phenomenon was dependent on both the velocity and the input water cut. Lovick and Angeli (2004a) and Lum et al. (2004) measured an upward curved interface in the dual continuous flow regime at 50% input water cut and 1.5 m/s. Lum et al. (2004) measured in addition an upward curved interface at a velocity equal to 2 m/s and 50% input water cut. Valle and Kvandal (1995) also measured a high fraction of water around the edge of the pipe wall. In the dispersed water continuous flow regime the oil droplets were concentrated in the centre of the pipe. Aslina (2006) and Hussain et al. (2008) measured cross sectional distributions by a traversing gamma densitometer and measured that the distribution of oil and water varied strongly with radial and axial position. The measurements reflect the many competing processes in liquid-liquid flow (turbulence, gravitational separation, droplet break-up and coalescence). Munaweera et al. (2002) reported from visual observation a highly dynamic interface for stratified flow. In the stratified flow with dual dispersion, the oil-water interface together with the dispersed phase moved in a wavy motion.

2.1.3 Large pipe inclination (15 - 90° from horizontal)

Cox (1985) reported a flow pattern map for downward (-15º, -30º) oil-water flow and observed that the stratified flow pattern in inclined oil-water flow were characterised by the presence of waves or mixing at the interface. An increased amount of waves and mixing at the interface was also observed by Scott (1985) in upward (+15°, +30°) pipe flow. Scott (1985) also observed a new flow pattern with large waves that at times touched either the bottom or top of the pipe in horizontal and inclined pipes, like a type of slug flow. At +15° angle Scott (1985) measured a back flow of water near the bottom of the pipe due to the axial gravity component. Back flow of water was also measured by Flores et al. (1997) in the transitional (stratified with mixing) and in the water dominated flow patterns. Oddie et al. (2003) were able to measure stratified flow with mixing at the interface only at low oil and water flow rates and low inclination (-2°, +2°, +20° angle). They measured only fully dispersed and homogenous flow at inclination angle between 45° and 90° from horizontal, which indicated that oil and water mixed relatively easy at large inclinations. Flores et al. (1997) showed that the transition to dispersed flow took place at lower flow rates for inclined pipes compared

with horizontal pipe flow. They analysed the flow pattern both visually and by use of electrical conductance probes in large pipe inclination ranging from +45º to +90° from horizontal. The conductance probes proved to be a key element in the objective determination of oil-water flow pattern. The inclined upward moving flow differed a lot from both vertical and horizontal pipe flow with respect to flow pattern.

2.1.4 Small pipe inclinations (0 - 10° from horizontal)

Even fewer researchers have studied flow pattern in slightly inclined oil-water pipe flow compared to horizontal and vertical pipe flow. Table A 3 in Appendix 3 summarizes the flow pattern classification studied in inclined flow. Vedapuri et al. (1997) measured that semi-segregated and semi-mixed flows were the most occurring flow pattern in slightly inclined pipes (±2°), which were characterized by having two continuous phases with different degree of mixing (see Figure 2.6).

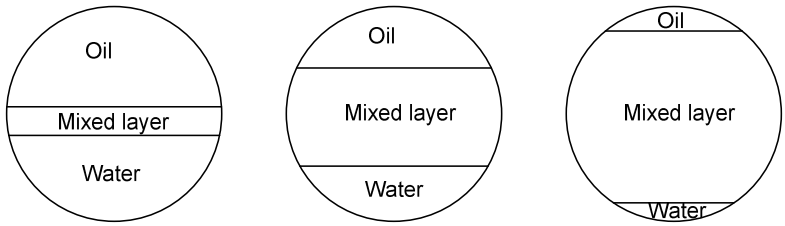

Figure 2.6 Flow patterns measured by Vedapuri et al. (1997) in inclined flow.

Alkaya et al. (2000) investigated flow pattern at inclinations angles equal to ±0.5°, ±1°, ±2° and ±5°. Alkaya et al. (2000) used the same classification as Trallero (1995), except from one additional flow regime called dispersion of water in oil and oil (Dw/o & o). This flow regime was also measured by Angeli (1996) and Soleimani (1999), but the difference was that Angeli (1996) and Soleimani (1999) observed this flow regime in horizontal pipe flow, while Alkaya et al. (2000) observed the dispersed water in oil and oil (Dw/o & o) only in inclined flow. Oddie et al. (2003) measured segregated, semi-segregated, semi-mixed, mixed, dispersed, and homogenous flow pattern at inclination angle from 0° to ±2° in a large diameter pipe. They classified the flow pattern according to the definitions of Oglesby (1979). In the downward moving flow most of the flow regimes were stratified, with only one dispersed flow at high oil and water rates. In upward moving flow four dispersed flow

regimes occurred, which indicated that upward inclinations gave larger degree of mixing between oil and water. Lum et al. (2006) identified the following flow regimes in inclined flow; stratified wavy (SW), plug flow (PG), dual continuous (DC), dispersed oil in water (Do/w) and dispersed water in oil (Dw/o). The flow regimes were was also measured in horizontal flow but with different boundary conditions. Abduvayt et al. (2006) classified 12 different flow patterns in large diameter pipe, which were grouped into three basic categories: segregated, semi segregated, and semi dispersed flow for horizontal and hilly terrain (±0.5°, ±3°), with some of them occurring only in inclined pipe flow. The segregated flow had no mixing at the interface. In the semi segregated flow some droplets occurred at the interface and in the semi dispersed flow the dispersion volume was less than half of the total pipe volume. None of the measured flow patterns were fully dispersed. In accordance to Trallero's (1995) classification, Rodriguez and Oliemans (2006) observed seven different flow regime in horizontal and inclined pipes (-1.5°, +1°, ±2°, ±5°) except for one additional flow regime called stratified wavy (SW). Stratified wavy (SW) had a wavy interface with no mixing on the interface and was only observed in inclined flow. Rodriguez and Oliemans (2006) observed stratified smooth (ST), stratified wavy (SW), stratified flow with mixing at the interface (ST & MI), dispersion of oil in water and water (Do/w & w), oil in water homogenous dispersion (o/w), water in oil homogenous dispersion (w/o) and dispersions of water in oil and oil in water (Dw/o and Do/w). Abduvayt et al. (2006) also measured stratified wavy (SW) flow only in inclined flow.

Alkaya et al. (2000) described an intermittent flow regime during the transition from stratified flow with mixing at the interface (ST & MI) to dispersion of oil-in-water and water (Do/w & w) in inclined pipe flow, but did not give this flow regime a name. In the intermittent flow regime the dispersion of oil in water layer was not continuous, and sometimes the pipe was filled with only single-phase water. This intermittent flow regime is similar to the plug/slug flow regimes measured by Angeli (1994), Beretta et al. (1997), Valle (2000), Liu et al. (2003), Abduvayt et al. (2006) and Mandal et al. (2007) in horizontal flow. Abduvayt et al. (2006) described a flow regime named thin oil line at the top of pipe and fine dispersion of oil in water (ThO/TP and FDO/W) in large pipe diameter experiments. This flow regime was classified as semi dispersed flow. The oil flowed with a snake like shape at the top of the pipe at high water flow rates and relatively low oil flow. The flow pattern was observed in both horizontal and hilly terrain (±0.5° and ±3°). Lum et al. (2006) reported a new flow regime

characterized by a thick plug of oil flowing at the top of the pipe for several pipe diameters. The plug became gradually thinner until it was replaced with oil droplets or water. This flow pattern appeared only at +5° and +10° inclination angle and the plug were much clearer at +10° than at +5° angle.

Transition boundaries

Pipe inclination has a significant effect on the stratified flow region. The stratified region decreases due to transition from stratified to stratified flow with mixing at the interface (ST and MI) flow pattern. The interface is generally more wavy and dispersed in inclined pipes, except for the more smooth interface measured by Alkaya et al. (2000) in upward flow and the stratified smooth flow measured by Kumara et al. (2009a) in downward inclination (-1°).

Vedapuri et al. (1997), Alkaya (2000), Lum et al. (2004) and Lum et al. (2006) showed that the shift of the boundary between stratified (ST) and stratified with mixing at the interface (ST & MI) took place at a lower superficial oil velocity for upward inclinations (+5° and +10°) compared with horizontal flow. Rodriguez and Oliemans (2006) measured that the stratified (ST) region tends to disappear and substituted by the stratified wavy (SW) flow regime in both downward and upward inclinations. Lum et al. (2006) measured the transition boundary between dual continuous (DC) and dispersed oil in water (Do/w) to be greatly affected by inclination, while the boundary between dual continuous flow (DC) and dispersed water in oil (Dw/o) were not affected. The dispersed oil in water (Do/w) appeared at a lower mixture velocity in inclined pipes compared to horizontal pipe flow. This does not agree with Alkaya's (2000) findings, where the transition boundary between DC and dispersed flow was not affected by pipe inclination.

The stratified region shrinked in terms of both superficial oil and water velocities when downward inclinations (-1º, -2º, -5°) were compared with the horizontal flow pattern map. At -5° angle a new flow pattern, dispersed water in oil and oil (Dw/o & o) were observed [Alkaya (2000)]. Lum et al. (2006) observed that the transition from dual continuous (DC) to dispersed oil in water flow (Do/w) took place at a much lower velocity compared to horizontal and upward flow. One possible reason for this was that the higher velocity of the water phase increased the amount of dispersed oil in water. The dispersed water in oil boundary (Dw/o) did not change significantly and only dual continuous and dispersed flows appeared at -5° angle, while stratified and wavy flow were not observed.

2.1.5 Interfacial structure and radial distribution in inclined flow

The interface could be either flat, convex or concave and is generally more curved in inclined flow compared to horizontal flow. The interface is usually measured to be wavier and more dispersed in inclined flow, with a few exceptions. Alkaya et al. (2000) measured different interfacial wave structures by use of isokinetic sampling probes in uphill and downhill (±0.5°, ±1°, ±2° and ±5°) stratified flow. In the stratified flow regime they observed a smoother interface in upward inclinations, whereas in downhill inclination the interface was covered with large amplitude waves. According to Abduvayt et al. (2006) the stratified smooth pattern observed in horizontal pipe disappeared at -3° angle and was replaced by stratified wavy flow. Lum et al. (2006) observed a wavier stratified flow in inclined upward flow compared to horizontal pipes and measured a larger degree of dispersion at +10° compared to +5° angle in the dual continuous dispersed flow regime. In downward inclination the stratified wavy flow pattern disappeared and was replaced with a dual continuous pattern (DC). They observed an enhanced mixing of the two phases in the dual continuous flow regime (DC) in both upward and downward flow together with a more wavier and irregular interface. The degree of mixing was most pronounced in downward flow. They measured more droplets at -5° than at +5° angle for the same flow rates, which were due to a more disturbed interface in downward flow. Kumara et al. (2009a) measured also an enhanced mixing between oil and water at -5° compared to +5°. Abduvayt et al. (2006) measured that the smooth interface observed in horizontal flow was completely replaced by large amplitude waves with no mixing at the interface at +3° angle. Rodriguez and Oliemans (2006) observed stratified wavy flow pattern in downward (-1.5°, -2°, -5°) and upward (+1°, +2°, +5°) flow. The wavy structure was also observed in horizontal flow, but then it was always traces of mixing at the interface. Kumara et al. (2009a) also observed a stratified smooth flow in downward inclination (-1°), while a stratified flow with mixing was observed at upward inclination (+1°). Decreasing the pipe from -1° to -5° angle led to significant mixing at the interface. A new wavy flow, caterpillar waves, at low water and mid oil superficial velocities was observed. They seemed to appear due to water backflow and water recirculation near the interface.

Lum et al. (2004, 2006) measured the in situ phase fractions in a pipe cross section by impedance probes at different inclination angle and showed that the nature of the interface was curved and did not have a structured layer. Lum et al. (2006) measured large

concentration gradients of oil droplets in the dispersed oil in water (Do/w) regime. Both an upward and downward curved interface was measured in the dual continuous (DC) flow regime in +5° upward moving flow. The upward curved interface was seen at 50% input oil fraction and velocity equal to 1.5 m/s and downward curved interface was seen at 80% input oil fraction at 2.0 m/s. The interface was much more curved in inclined pipe flow than in horizontal flow. In stratified-roll-wave (SR) at +3° angle Abduvayt et al. (2006) observed an interface that was characterized by a downward curvature. Atmaca et al. (2008) indicated that the measured convex and concave interfacial structure by use of conductivity probes in their study was due to interpolation between the data and were not an actual physical phenomenon.

2.2 Pressure drop

The pressure drop in production pipelines has large impact on the design of a new field and on the operational costs. The pressure drop limits the maximum flow and is thus a critical parameter, both in terms of cost evaluations and production optimization. The pressure gradient in Eq. (2.42) is a function of the friction factor, density, diameter, velocity and inclination.

2.2.1 Experimental procedure

Valle (2000) observed large difference in the pressure drop dependent on the experimental procedure. Difference in pressure drop was seen depending whether the experiments went from 100 to 0% water cut or 0 to 100% water cut (see Figure 2.7). Angeli (1996) showed that pre-wetting of the steel and acrylic pipe with oil gave lower pressure gradients than if the pipe was pre-wetted with water. For the lower mixture velocities in the acrylic pipe the pre-wetting of the pipe did not affect the pressure gradient.

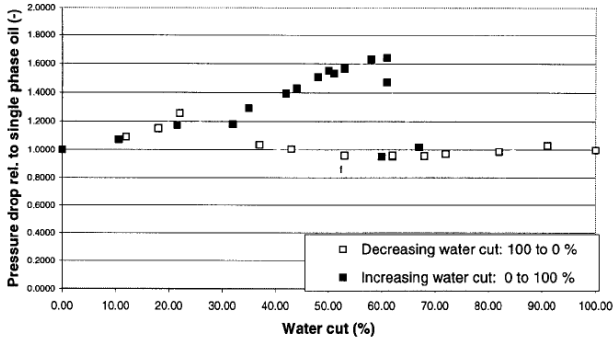

Figure 2.7 Pressure drop relative to single phase oil flow [Valle (2000)].

2.2.2 Horizontal pipe flow

Influence of flow regime

Most studies show that the flow pattern has a great influence on the measured pressure gradient. Trallero (1995) observed a small decline in the pressure gradient in the transition from stratified flow to dispersed water continuous flow. The pressure drop fell since the oil continuous phase was replaced with a water continuous phase, which reduced the wall friction. Valle and Kvandal (1995) measured a small decrease in pressure gradient, when the flow changed from stratified smooth (SS) to stratified wavy (SW). Valle (2000) observed that for stratified flow the pressure gradient were similar to that of single-phase flow and Lovick and Angeli (2004a) measured the pressure gradient in two-phase flow to be less than that of single-phase oil flow at the input oil fractions studied (10 to 95%). Lovick and Angeli (2004a) observed only small variations in pressure gradient as function of oil fraction at the lowest velocity (0.8 m/s). Increasing the mixture velocity up to 1 m/s led to an initial decrease in pressure gradient up to minimum when water was added to single-phase oil flow. Further increase in input water cut led to an increase up to the single phase water value. Valle (2000) measured also an initial decrease in pressure gradient in the stratified flow regime (1.17 m/s) followed by a slight increase with increasing input water cut, except for an abrupt increase in the pressure gradient that were observed at approximately 80% input water cut. The abrupt change in pressure gradient occurred during flow transition from separated to dispersed water continuous flow. Several other investigators have also observed this phenomenon by use of Exxsol D60. Elseth (2001) and Wahumpurage et al. (2008) observed a sharp increase in pressure gradient by use of the same facility and Exxsol D60 at low mixture velocities. The

peak in pressure gradient was observed at approximately 80 % input water fraction at 1 m/s and the flow changed from stratified mixed to dispersed oil in water and water (Do/w & w). Elseth (2001) observed the peak in pressure gradient at velocities ranging from 0.67 to 1.67 m/s with the peak appearing at a decreasing input water cut as the velocity increased. Angeli and Hewitt (1998) observed a sharp increase in pressure gradient with Exxsol D80 in the stratified flow regime, but the peak was observed at lower input water cut at approximately 40% compared to that of Elseth (2001) and Wahumpurage (2008). However, the peak in pressure gradient in the stratified flow regime was not seen in the study of Soleimani (1999), even though Soleimani (1999) used the same facility and fluids as Angeli and Hewitt (1998). A possible reason could be due to different experimental setup and procedure. Kvandal et al. (2000) measured a sharp peak in pressure gradient when the flow shifted from stratified to dispersed flow with an in-homogenous wall mixture (DIH-W). The peak in pressure gradient was recorded at 28% input water fraction at 0.75 m/s. Kvandal et al. (2000) measured a large gradient in the phase distribution in the upper wall region, when the increase in pressure gradient was observed. During stratified flow Munaweera et al. (2002) measured an increasing trend in the pressure gradient with increasing water cut, which were explained by formation of dense packed layers of droplets and due to flocculation. Vielma et al. (2007) observed that increasing the superficial water velocity at constant superficial oil velocity resulted in a large increase in the pressure gradient due to increasing degree of mixing at the interface as was also supported by Valle and Kvandal (1995). This trend was only observed for low superficial oil velocities.

The addition of water to single-phase oil can lead to a significant decrease in pressure drop, as observed by Pal (1993), Angeli (1996), Soleimani et al. (1997), Angeli and Hewitt (1998), Soleimani (1999), Elseth (2001) and Lovick and Angeli (2004a) in the dispersed flow regime. Pal (1993) observed a drag reduction in both water in oil and oil in water emulsions. The drag reduction increased with increasing concentration of the dispersed phase. Pal (1993) suggested that the coalescence and breakup of water droplets modified the turbulence of the continuous phase. Pal (1993) also confirmed that presence of surfactants prevented interactions between droplets and thus no drag reduction were observed at this experimental condition. Soleimani (1999) claimed that the large drops could suppress the turbulence and thus decreasing the pressure gradient. Lovick and Angeli (2004a) measured a decrease in pressure gradient at medium to large velocities ranging from 1 to 3 m/s and water cut ranging

from 0 to 20%. The effect was seen in both dual continuous and fully dispersed oil continuous flow.

Valle and Utvik (1997), Valle (2000), Kvandal et al. (2000) observed an increase in the frictional pressure gradient with increasing input water cut in the oil continuous flow regime, instead of a decrease as shown above. Valle and Utvik (1997) showed that the pressure gradient increased monotonically when the input water cut increased up to the point where the flow transformed from being dispersed oil continuous to stratified flow by use of real crudes. At approximately 45% input water cut where the transition in flow regime took place, an abrupt decrease in pressure drop down to single phase oil values were observed. Munaweera et al. (2002) measured that addition of small amounts of water to single-phase oil had minor effect on the pressure gradient by use of a light crude oil provided the flow was fully dispersed.

Influence of oil viscosity

Arirachakaran et al. (1989) executed experiments with six different oils with viscosities ranging from 4.7 to 2116 cp. They observed that when the oil viscosity were much larger than that of water and when the oil was dispersed in water the observed pressure drop was in the same order of magnitude as single-phase water pressure drops. For a water-in-oil dispersion the pressure drop was highly affected by temperature and thus also the oil viscosity.

Influence of pipe material and inlet design

Oil pipelines are made from carbon steel or plastics. Carbon steel pipes are in some cases coated on the inside for pipeline protection (e.g. erosion and corrosion) or to prevent deposition (e.g. wax). Angeli (1994, 1996) and Angeli and Hewitt (1998) showed that the pressure gradient was higher in stainless steel than in the transpalite pipe. The difference observed, increased with increasing mixture velocity and was most likely due to the difference in pipe roughness and not difference in flow regime. The rougher steel pipe produced higher pressure gradients than the smoother transpalite pipe. Experiments conducted by Angeli and Hewitt (1998) showed that at low mixture velocities (up to about 1 m/s) the pressure gradients were relatively unaffected by the water volume fraction in the acrylic pipe, while a large influence were seen in the steel pipe. In addition to the pipe roughness, the pipes have different wetting characteristics which can be a reason for the observed deviations in pressure gradient between the two pipes. Valle and Kvandal (1995) experienced formation of

water continuous films on the pipe wall for all observed flow patterns and formation of an annular film surrounding a dispersed oil flow in the stratified-dispersed flow regime. They started all their experiments with use of single-phase water and the pipe was made of glass.

Soleimani et al. (1997) reported that inline mixers at the tube inlet had a great influence on flow behaviour and pressure gradient. The inline mixers sharpened the pressure gradient peak in dispersed flow and a secondary pressure gradient peak occurred over a range of conditions. This confirms the importance of entrance conditions in oil-water flow behaviour.

Real crude oil system

Utvik et al. (1999), Valle (2000), Solbakken and Schüller (2001) and Utvik et al. (2001) investigated the difference between a recombined hydrocarbon-water and a model fluid system. The results showed significant deviations with respect to pressure drop. Real fluids from multiphase reservoir contained surfactants that influenced the formation of droplets and bubbles, which affected the pressure gradient. Solbakken and Schüller (2001) investigated the difference between a model and re-combined reservoir fluid system in a multiphase flow loop. They found a large difference between horizontal condensate/distilled water flow and Exxsol D60/Formation water flow at large velocities, even though the fluid properties were approximately the same. The relative pressure drop was 100% higher for Exxsol D60 compared with condensate/water flow. At low mixture velocity, equal to 1.17 m/s, large differences were seen at 80% input water cut, where the relative pressure gradient for the Exxsol D60 system were 80% larger than that for the condensate system. The difference in flow pattern and pressure gradient between a model and a real crude oil system indicated that the fluid properties, density, viscosity and interfacial tension, were not sufficient to describe the behaviour of the flow.

2.2.3 Upward inclination

Lum et al. (2004, 2006) found that the frictional pressure gradient in upward inclined flow (+5°, +10°) was below the single-phase oil values and in general lower than that of horizontal flow. This was attributed to a higher measured in situ water fraction in upward inclined flow and to the increase of dispersion that lead to drag reduction. In most cases the pressure gradient decreased to a minimum, when oil was added, before it increased to single-phase water value. A decrease in pressure gradient was observed in both water in oil dispersion

(w/o) and dual continuous flow (DC) and the phenomena where attributed to drag reduction and/or interfacial shape. Drag reduction in dispersed oil continuous flow regime at +10° was measured by Lum et al. (2006). The change in pressure gradient slope was associated with the boundaries of the dispersed water in oil (w/o) flow regime and dual continuous (DC) flow. The frictional pressure gradient at +5° and +10° were generally very similar, both in terms of trends and of absolute values. Abduvayt et al. (2006) measured that the total pressure drop appeared to be very similar between ±0.5° and between ±3° inclination angles.

2.2.4 Downward inclination

Lum et al. (2006) observed similar trends as was seen for upward inclined flow. The frictional pressure gradient was at all input oil fractions lower than in single-phase oil flow. A reduction in frictional pressure gradient was seen when adding water to single-phase oil flow, followed by an abrupt increase. The increase in frictional pressure gradient observed between 60 and 72% input oil fraction was found to be due to a downward curved interface measured by conductivity probes. A downward curved interface lead to an increase in the oil wall contact area, thus creating a frictional pressure gradient peak. The frictional pressure gradient was very similar or even slightly lower at -5° angle compared with the pressure gradient at 0° and +5° angle. This was the opposite of what was expected. In downward flow it was presumed that the oil would accumulate in the pipe and thus cause a larger pressure gradient. One possible explanation given for the low frictional pressure gradient at -5° angle was due to increased mixing of oil into the water leading to a velocity ratio close to one.

2.3 Oil-water holdup and slip ratio

2.3.1 Definitions

Holdup is the in situ volume fractions of the phases flowing in a pipe as shown in Eq. (2.7). The in situ volume fractions can be different from the input volume fractions and holdup is a measure of this. Holdup ratio (slip ratio) is defined as the ratio of the in situ oil velocity to the in situ water velocity as shown in Eq. (2.12). The accurate determination of holdup is important to determine pressure drop and volumetric flow rates. The input water cut can be calculated from Eq. (2.3), where Q_w and Q_o is the volume flow rates of water and oil and U_{sw} and U_{so} is superficial water and oil velocity.

$$\alpha_w = \frac{Q_w}{Q_w + Q_o} = \frac{U_{sw}}{U_{sw} + U_{so}} \quad (2.3)$$

The sum of input water cut and oil cut equals 1, as shown in Eq. (2.4).

$$\alpha_w + \alpha_o = 1 \quad (2.4)$$

The input mixture density as function of the input water fraction is shown in Eq. (2.5), where ρ_m is the input density of the mixture and ρ_w and ρ_o are the densities of water and oil.

$$\rho_m = \alpha_w \rho_w + \alpha_o \rho_o \quad (2.5)$$

Combining Eqs. (2.4) and (2.5) give the expression for input water cut as function of input mixture density and the densities of oil and water as shown in Eq. (2.6).

$$\alpha_w = \frac{\rho_m - \rho_o}{\rho_w - \rho_o} \quad (2.6)$$

The in situ phase fraction or holdup of water is expressed in Eq. (2.7), where A is the cross sectional pipe area and A_w is the cross sectional area occupied by water.

$$\varepsilon_w = \frac{A_w}{A} \quad (2.7)$$

The superficial velocities and flow rates of oil and water are defined in Eqs. (2.8) and (2.9) where u_o and u_w is the in situ velocities of oil and water.

$$U_{so} = \frac{Q_o}{A}, \; U_{sw} = \frac{Q_w}{A} \quad (2.8)$$

$$Q_o = A_o u_o, \; A_w u_w \quad (2.9)$$

Combining Eqs. (2.7), (2.8) and (2.9) gives the in situ fraction of water as function of the superficial and in situ water velocity as shown in Eq. (2.10).

$$\varepsilon_w = \frac{U_{sw}}{u_w} \quad (2.10)$$

The in situ water fraction can also be expressed as function of in situ mixture density and the densities of oil and water as shown in Eq. (2.11).

$$\varepsilon_w = \frac{\rho_m - \rho_o}{\rho_w - \rho_o} \tag{2.11}$$

The holdup ratio (slip ratio) is defined in Eq. (2.12). The oil is the fastest moving phase when the holdup ratio is above one and conversely below one when the velocity of water is dominant.

$$S_{ow} = \frac{u_o}{u_w} \tag{2.12}$$

The average slip velocity u_s between the phases at a given cross section is shown in Eq. (2.13).

$$u_s = u_o - u_w \tag{2.13}$$

2.3.2 Horizontal pipe flow

Soleimani (1999), Lovick and Angeli (2004a), Lum et al. (2006) and Vielma et al. (2007) showed that the slip ratio between oil and water was in general close to unity in horizontal pipe flow at large velocities, where a dispersed flow usually occurred. Valle and Utvik (1997) and Valle (2000) observed that the holdup ratio between oil and water was below one (0.6) for high flow rates in the dispersed oil continuous flow, which indicated that the dispersed water droplets moved much faster than the continuous oil phase. Valle (2000) showed that the phenomenon was most severe for the lightest crude oils. Valle (2000) also measured similar holdup ratio trend for water continuous flows, where the dispersed oil droplets moved faster than the water continuous flow. However the slip ratio was closer to unity for water continuous flow compared to oil continuous flow. Angeli (1996) and Lovick and Angeli (2004a) observed similar tendency at high flow rates using light oils. Angeli (1996) observed that the water droplet concentration increased towards the centre of the pipe where the velocity is largest. Lift forces was one explanation given to the increased concentration of droplets in the centre of the pipe.

At low to medium mixture velocities Valle (2000), Lovick and Angeli (2004a) and Lum et al. (2006) measured a large slip ratio (above 1) at low water cuts with a decreasing trend with increasing water cut. With other words, the oil velocity was the fastest moving phase at low

water cuts and approached the water velocity as the amount of water increased and became less than the water velocity at large water cuts. At large water cuts Lovick and Angeli (2004a) and Lum et al. (2006) measured that the oil formed a thin continuous layer at the top of the pipe which lead to a large wall contact area compared to its volume. The oil therefore experienced large frictional forces, which reduced its velocity compared to that of water and resulted in a holdup ratio less than 1. Valle (2000) measured an especially low oil-water slip ratio (down to 0.5) compared to that of Lum et al. (2006). The reason to the low slip ratio measured by Valle (2000) was probably due to the formation of a dense viscous dispersion in the upper part of the tube, which led to an increase in the effective viscosity and thus retarding the oil phase. The reason for the different behaviour could be due to the difference in viscosity (see Table A1 in Appendix 1). In the dual continuous (DC) flow regime Lovick and Angeli (2004a) measured that the interface curved upwards at 50% input water cut which caused the water to have a higher wall contact than the oil, leading to a slip ratio above one. The oil and water were measured to have equal velocities below 40% input water cut due to the curved interface, while Valle (2000) measured the slip ratio to be equal to one at 50% input water cut.

Angeli (1996) observed that the slip ratio was in general lower than unity in the transpalite pipe and closer to unity in the steel pipe. The preferential wetting of oil in the transpalite pipe was one possible explanation. The oil which were in contact with the wall had a tendency to accumulate in the pipe. Xu et al. (2008) measured the slip to increase with decreasing diameter.

2.3.3 Large pipe inclination (15 – 90° from horizontal)

Mukhopadhyay (1977), Mukherjee et al (1981), Cox (1985), Vigneaux et al. (1988), Flores et al. (1998) showed that the oil water holdup were dependent on the inclination angle. Since the density was different between oil and water the expectations were that bouncy forces would cause an increasing holdup at larger pipe inclinations. This was not the case. The water holdup was most severe at the smallest inclination angle studied (-30°, -15°, +25°). This trend was probably due to stratification of the flow at lower inclinations.

2.3.4 Small pipe inclination (0 - 10° from horizontal)

Alkaya (2000), Lum et al. (2004), Abduvayt et al. (2006), Lum et al. (2006), Kumara et al. (2009a) measured that even a slight inclination (within ±10°) had a significant effect on the holdup distribution in the pipe. They generally found a large holdup of water in the upward pipe flow and a low holdup in downward flow at low mixture velocities. Kumara et al. (2009a) measured that the holdup was most pronounced in upward flow compared to downward flow. Lum et al. (2006) observed that the slip ratio trend at high velocities was opposite of the trend observed at low velocity. At high velocity the slip ratio increased with increasing water cut and at low velocity the slip ratio decreased.

Upward flow

Kumara et al. (2009a) measured the largest effect on holdup when the pipe was inclined from 0° to +1° compared with inclining the pipe from +1° to +5°, which were attributed to increased level of mixing at higher inclinations. Alkaya (2000), Lum et al. (2004), Abduvayt et al. (2006), Rodriguez and Oliemans (2006), Atmaca et al. (2008) showed that low upward inclination (+0.5° to +5°), generally resulted in higher water holdup ratio than in horizontal flow. Lum et al. (2004), Abduvayt et al. (2006) and Lum et al. (2006) measured the hold up ratio at most compositions and mixture velocities to be above one. This was attributed to a more dense water phase being retarded by gravity forces in the direction opposite to the flow direction. Increasing the velocity the hold up ratio approached one and the slippage decreased as the degree of mixing increased, as was also observed in horizontal flow. At low mixture velocities Lum et al. (2006) measured the hold up ratio to increase with increasing oil fraction. At low input oil fractions the holdup ratio was measured to be below 1. At these low input oil fractions the dispersed oil accumulated in the top of the pipe. At approximately 30% input oil fraction the hold up was measured to be above 1 for all inclinations as a result of both gravitational forces and due to the interfacial shape. An upward curved interface was measured both in horizontal and inclined pipe. Due to the convex interfacial curve the water phase had relatively large contact area with the pipe wall, which combined with the gravity forces, lead to a decreased water velocity. A significant increase in velocity ratio was seen in the plug flow regime at +10° angle and 30% water cut.

Downward flow

Lum et al. (2006), Abduvayt et al. (2006), Rodriguez and Oliemans (2006) and Atmaca et al (2008) showed that low downward inclination generally resulted in lower water holdup and a

larger water velocity compared with horizontal flow, especially at lower mixture velocities. In contrast to upward flow Lum et al. (2006) measured the hold up ratio to decrease with increasing oil fraction. They observed a higher degree of mixing which resulted in slip ratios close to one in many cases. At high velocity the slip ratio remained above one up to 70% input oil fraction as was seen in the upward moving flow, indicating that oil were travelling faster than water even the pipe was inclined downwards.

2.4 Velocity and velocity fluctuations

2.4.1 Horizontal pipe flow

Kvandal et al. (2000) were the first to measure the local velocities and velocity fluctuations in dispersed flows by use of a Laser Doppler Velocimetry (LDV). They showed that the data seemed to follow the conventional theory for single-phase turbulent pipe flow. The data followed the law of the wall and the theory presented by Hinze (1959) for Reynolds stresses, except for one data set, which were most likely due to local phase inversion or undeveloped flow pattern transitions. Shi et al. (2000, 2001) measured the in situ velocity distribution in large diameter pipe (100 mm) by use of pitot tube. The velocity profile was affected by input water cut, mixture velocity and surfactants. The oil velocity was higher than that of water, for input water cut equal to 20% and for larger water cuts the mixed layer was the fastest moving phase. The velocity profile at input water cut equal to 5% and low velocity were similar to that of single phase oil profiles. They also showed that adding an increasing amount of surfactants to the system influenced the velocity profiles.

Vedapuri et al. (1997) measured the in situ phase fraction distribution with a pitot tube and calculated the in situ density profiles, which were used to generate the velocity profiles in +2° upward moving flow. The integrated in situ velocities of the mixed layer were approximately 1.2 times the input mixture velocity for the low viscosity oil (2 cp) at velocities ranging from 0.6 to 1.4 m/s. The velocity of the water layer was lowest and the oil velocity was close to the input mixture velocity. Increase of the oil viscosity up 96 cp lead to a decrease in the average in situ oil velocity and an increase in the average in situ water velocity. The oil was slower due to the increase of oil hold up and due to the larger in situ cross section of the pipe the oil occupied. The in situ mixed layer at large viscosity travelled at velocities close to the input mixture velocity. Elseth (2001) measured vertical centre velocity profiles by use of Laser Doppler Anemometry in stratified flow and showed that the velocity profiles were highly

asymmetrical. The oil flow was measured to flow faster than the water phase at 50% input water cut, even the oil had a slightly higher viscosity. The reason was attributed to the larger wall shear in the water phase compared with the oil phase. Wahumpurage et al. (2008), Kumara et al. (2009a, 2009b) measured also a higher oil phase velocity at 50% input water cut by use of Particle Image Velocimetry (PIV) at 0.5 m/s and 1 m/s. The PIV measurements failed near the interface due to optical disturbances caused by interfacial waves and droplets.

Elseth (2001), Kumara et al. (2009a, 2009b) measured that the interface seemed to dampen the turbulence in the flow, which were seen in the calculated cross moments and Reynolds stresses. The interface seemed to act like an oscillating wall, preventing turbulent diffusion across it. The dampening effect was found to be wider than the interfacial zone. Kumara et al. (2009a) measured the dampening effect in smooth stratified flow by use of PIV. Elseth (2001) measured the effect at mixture velocities ranging from 0.41 to 1.71 m/s using LDA. The interface had different degree of mixing. Elseth (2001) and Wahumpurage et al. (2008), Kumara et al. (2009a, 2009b) presented the fluctuating axial velocity (u-rms) and showed that the value was largest close to the wall and had a decreasing trend towards the interface. At the interface a slight increase was observed, which were attributed to the large velocity gradients at the interface. There was good agreement between LDA and PIV measurements in terms of velocity and u-rms.

2.4.2 Small pipe inclination (0 – 10° from horizontal)

Kumara et al. (2009a) measured the maximum axial velocity to be in the oil phase for horizontal pipes and in upwardly inclined flows, whereas it was located in the water phase for downwardly inclinations. The velocity was equal to 0.25 m/s and input water cut was equal to 25%. Kumara et al. (2009a) measured the Reynolds stresses to be much larger around the large amplitude waves at +5° compared to the observation made at +1° angle, in horizontal flow and in downward moving flow (-1° and -5°), where the waves was less pronounced. The rolling motion of the interface waves increased the velocity fluctuations in the interfacial region. The pictures of the flow also show that the degree of mixing was most pronounced at -5° compared to +5°.

2.5 Phase inversion

Phase inversion is by definition when the continuous phase becomes the dispersed phase and the dispersed phase becomes the continuous phase. In oil-water flow the phase inversion is the region where conversion from oil to water continuous or water to oil continuous flow occurs. A review of phase inversion experiments and models can be found in Yeo et al. (2000), Xu (2007) and Piela et al. (2008). The process is very complex and is dependent on the properties of the fluids, surface active agents, flow pattern, pipe material, droplet-droplet mechanisms, flow rates, inlet conditions and experimental procedure. There exist many publications on phase inversion in stirred tanks but less has been published from pipe flow. The point of phase inversion can occur from 10 to 90% input water cut, but usually the inversion point is measured to be in the region of 20–50%. The inversion fraction of 90% can occur if oil droplets are polyhedral in shape and separated by thin interfacial aqueous films. Studies of e.g. Pal et al. (1986), Pilehvari et al. (1988) and Plegue et al. (1989) measured the maximum volume fraction of the dispersed phase to be up to 90%. In the studies of Pilehvari et al. (1988) emulsions where stabilized with emulsifiers and the experiments where carried out in a rheometer. Pilehvari et al. (1988) and Plegue et al. (1989) used viscous oil in their experiments.

2.5.1 Phase inversion in pipe flow

Phase inversion in a pipe has been measured by use of several different methods. Many investigators measured the phase inversion at the point where a peak in the frictional pressure gradient occurred, which were substantially larger than single-phase oil value. Malinowsky (1975), Laflin and Oglesby (1976), Martinez et al. (1988), Arirachakaran et al. (1989), Pal (1993), Nädler and Mewes (1995) observed a narrow pressure drop peak, which indicated that a phase inversion process had taken place. Nädler and Mewes (1997) distinguished between phase inversion in emulsions containing one continuous phase with dispersed oil or water droplets and local phase inversion which took place in the dispersed flow region in the stratified flow regime. Angeli (1996) measured the phase inversion to be around 37 - 40% in both the stainless steel pipe and transpalite pipe. The phase inversion was measured by observing a peak in pressure gradient and by measuring the fluid of the continuous phase with a conductivity needle probe. Ioannou et al. (2005) measured that the change in mixture conductivity close to phase inversion (50–60% input oil fraction) was reflected to change in the pressure gradient. Ioannou et al. (2005) also measured that dispersion initialization (from

oil to water continuous or from water to oil continuous) in the large pipes did affect the phase inversion point significantly and reported how velocity and pipe material affected the point of inversion. The phase inversion was not instantaneous but lasted for some time. During this time the pressure gradient and impedance of the mixture fluctuated significantly. Piela et al. (2008) measured the point of inversion by use of two different experimental set-ups, continuous and direct measurements. In the continuous measurements there was a constant injection of the dispersed phase and in the direct measurement oil and water were introduced by a T-mixer at the pipe inlet at a predefined concentration. Although the point of phase inversion did not happen at the same concentration in the two set-ups the change in morphological structures were the same. Far away from the inversion point the dispersed droplets were spherical and close to the point of inversion they observed larger morphological structures in the form of pockets (multiple drops) and regions of the originally dispersed phase. The pockets and regions started to coalesce until the continuous phases inversed. In the direct experimental set-up, the flow became unstable between 50 and 60% input oil fraction. The instabilities in differential pressure transducers and conductivity probes indicated that the oil continuous and water continuous phases co-existed, which is often referred to as the ambivalent range. The interactions between the water and oil continuous regions lead to a high effective viscosity and hence a large friction factor. In 2006 Piela et al. observed multiple drops consisting of oil droplets in water drops, while multiple drops consisting of water droplets in oil droplets were never found.

There have been some attempts to try to model the phase inversion phenomenon in two-phase pipe flow [Brauner and Ullmann (2002), Poesi and Beretta (2008), Ngan et al. (2009)]. The most important mechanisms in modeling phase inversion are the instability between droplet coalescence and break up, minimization of the total free energy content (gravitational potential energy and interfacial energy) and effects of dynamic forces.

Pipe material and viscosity

The phase inversion was observed at higher mixture velocities in acrylic pipe than in steel pipe, since the dispersed flow pattern was established at higher mixture velocities in acrylic pipes [Angeli and Hewitt (1998)]. Ioannnou et al. (2005) also observed the phase inversion point to differ between steel and acrylic pipe. In the acrylic pipe the point of inversion

occurred at higher oil fraction than in the steel pipe. The pressure gradient increase in the acrylic pipe was also measured to be much higher and sharper than in steel pipe.

Inclination angle and inlet conditions

Mukherjee et al. (1981) measured the phase inversion point by observation of a peak in the frictional pressure gradient. They observed that the phase inversion was dependent on the inclination angle. The phase inversion was found to be between input water cut equal to 40 and 50% at all inclinations studied (±30° to ±90° from horizontal), except at -30° angle. At -30° angle the phase inversion point was measured between 70 and 80% input water cut.

Soleimani et al. (1997) observed that the point of inversion shifted to higher water cuts at higher mixture velocities when inline mixer was used. Ioannnou et al. (2005) measured no effect of initial conditions on the inversion point for the small acrylic pipe.

2.6 Droplet mechanisms

The basic droplet mechanism described in the literature is droplet formation, coalescence, break-up, flocculation and escape. Droplet escape was described by Piela et al. (2008) and occurred when the entrapped droplet or pocket film broke. Valle (2000) described flocculation of droplets as a non-Newtonian dispersion which was composed of chemically bounded drops (flocs) surrounded by a continuous phase. The flocs were acting as a crystalline compound, making the system stiffer and thus increasing the effective viscosity. Forces acting on a droplet in a turbulent flow that needs to be considered are gravity, turbulent diffusion, drag, inertia, lift, virtual mass, basset forces and surface forces.

2.6.1 Droplet coalescence

Droplet coalescence occurs when to droplets collides and remains in contact with each other for sufficient period of time to allow them to merge. The surface area will be reduced when the droplets emerge, which leads to an energetically favorable state. The coalescence will therefore occur readily if the dispersed phase concentration is large. Former studies e.g. Chester (1991) and Yeo et al (2000) described the coalescence process to first start with deformation of the droplets. Then a film of the continuous phase is trapped between the deformed droplets. Gravity, inertia, interfacial forces causes drainage of the film until the film eventually reaches a critical thickness at which it ruptures and coalescence proceeds. Piela et

al. (2008) took pictures of the coalescence process in pipe flow demonstrating the interactions between drops, pockets and regions. Howarth (1964) presented an equation for the frequency of coalescence of uniformly sized drops in a homogenous isotropic turbulent suspension.

2.6.2 Drop size

Most of the experimental data on average drop size are done in stirred vessels [Zhou and Kresta (1998)] and only a few data have been reported during pipe flow. A significant share of the droplet determination is in fully dispersed dilute systems. Only a few high concentration systems have been reported, and most of them used surfactant stabilized emulsions. The limited data on average droplet size and distribution are partially due to the difficulty in performing such measurements [Vielma et al. (2007)]. A wide variety of measurement techniques have been employed and can be found in Simmons and Azzopardi (2001) publication. The drop size and distribution is dependent on the fluid properties, superficial velocities, pipeline configuration and pipe length.

Drop breakup

The two main mechanisms which is steering the droplet size is droplet breakup and coalescence. Taylor's (1934) theory showed that deformation and breakup of a droplet were predominantly determined by the generalized Weber group as shown in Eq. (2.14).

$$N_{We} = \frac{\mu_c S_v d}{\sigma} = \frac{Visous\ force}{Surface\ force} \tag{2.14}$$

Where μ_c is the absolute viscosity of the continuous phase, S_v is the maximum velocity gradient in the flow field, d is the drop diameter and σ is the surface tension. When surface forces overcome the inertial forces (deformation of droplets) the drop will break up. Both Kolmogorov (1949) and Hinze (1955) concluded independently that the force from the continuous phase deformed the droplet, while the interfacial and viscosity of the dispersed phase stabilized it. They proposed two dimensionless groups, the generalized Weber number in Eq. (2.14) and a viscosity group in Eq. (2.15) as the parameters determining the droplet size, where μ_d and ρ_d are the dispersed phase absolute viscosity and density.

$$N_{Vi} = \frac{\mu_d}{\sqrt{\rho_d \sigma d}} \tag{2.15}$$

According to Hinze (1955) the viscosity group can be ignored when the dispersed phase viscosities are low (N_{Vi} <<1), therefore drops will break up when the Weber number exceeds a critical number. Hinze (1955) also claimed that the turbulent fluctuations breaking the droplets are too short to allow any significant viscosity effect within the droplet. The critical Weber number derived in Eq. (2.16) gives the maximum drop size, $d_{\max}$, that could resist break-up in a turbulent flow field, where ρ_c is the density of the continuous phase, $\overline{u^2}$ is the mean square of velocity fluctuations over a distance equal to $d_{\max}$.

$$(N_{We})_{crit} = \frac{d_{\max}\rho_c \overline{u^2}}{\sigma} \tag{2.16}$$

The proposed model for predicting the maximum diameter of bubbles or droplets in a turbulent flow field is a balance between the turbulent kinetic energy and the drop surface energy as shown in Eq. (2.17).

$$\frac{\rho_c \overline{u^2}}{2} = \frac{4\sigma}{d_{\max}} \tag{2.17}$$

Kolmogorov (1949) and Hinze (1955) derived a model as shown in Eq. (2.18) for the maximum droplet diameter. The factor equal to 0.725 was found by using experimental drop size data obtained from Clay (1940), ρ_c is the density of the continuous phase, σ is the surface tension, f_c is the friction factor, U_c is the average axial velocity of the continuous phase and D is the pipe diameter.

$$d_{\max} = 0.725\left(\frac{\sigma}{\rho_c}\right)^{3/5}\left(\frac{2 f_c U_c^{\,3}}{D}\right)^{-2/5} \tag{2.18}$$

The model assumes that maximum droplet diameter must be much large than the Kolmogorov micro scale and less than the length of the energy containing eddies in a pipe of diameter D [Eq. (2.19)].

$$l_k = \left(\frac{\mu_c^{\,3}}{\rho_c^3 \varepsilon}\right)^{1/4} << d_{\max} < 0.1D \tag{2.19}$$

where μ_c is the absolute continuous phase viscosity, l_k is the Kolomogorov micro scale and $0.1D$ is the length scale of energy containing eddies in a pipe of diameter D. The flow is

assumed to be isotropic and homogenous. Since the model of Hinze (1955) is not valid for drops larger than 0.1*D*, Kubie and Gardner (1977) derived a new expression for determination of larger diameter droplets as shown in Eq. (2.20).

$$d_{\max} = 5.53 \frac{\sigma}{f_c \rho_c U_c^{\ 2}} \tag{2.20}$$

Karabelas (1978) concluded that the Hinze (1955) model satisfactory predicted the maximum droplet size in dilute pipe flow dispersions. Sleicher (1962) modified the Hinze (1955) model based on the occurrence of droplet break up close to the wall, where the turbulence is least isotropic and suggested a different viscosity group as shown in Eq. (2.21).

$$\left(\frac{d_{\max}\rho_c U_c^2}{\sigma}\right)\left(\frac{\mu_c U_c}{\sigma}\right)^{0.5} = 38\left(1+0.7\left(\frac{\mu_d U_c}{\sigma}\right)^{0.7}\right) \tag{2.21}$$

Tsouris and Tavlarides (1994) and Brauner and Ullmann (2002) developed the Hinze (1955) model for dense dispersions. Eqs. (2.22) and (2.23) show the model developed by Brauner and Ullmann (2002).

$$d_{\max} = 2.22 C_H \left(\frac{\rho_c U_c^2 D}{\sigma}\right)^{-0.6} \left(\frac{\rho_m}{\rho_c(1-\varepsilon_d)} f\right)^{-0.4} \left(\frac{\varepsilon_d}{1-\varepsilon_d}\right)^{0.6} \tag{2.22}$$

where ρ_m is the mixture density, C_H is a tuneable constant, f is the wall friction factor and ε_d is given by Eq. (2.23). U_{sd} and U_{sc} is the superficial velocity of the dispersed and continuous phase.

$$\varepsilon_d = \frac{U_{sd}}{U_{sd} + U_{sc}} \tag{2.23}$$

Angeli and Hewitt (2000) correlated the maximum droplet diameter with the continuous phase velocity and friction factor as shown in Eq. (2.24).

$$d_{\max} U_c^{1.8} = 4.2 \times 10^{-2} f_c^{-3.13} \tag{2.24}$$

Kouba (2003) developed two models, one for determination of the smallest droplet and one for the largest droplet, as shown in Eqs. (2.25) and (2.26), where g_c is the gravity constant.

$$d_{\min} = \frac{8\sigma g_c}{\rho_c U_c^{\,2}} \tag{2.25}$$

$$d_{\max} = \frac{20\sigma g_c}{\rho_c U_c^{\,2}} \tag{2.26}$$

2.6.3 Droplet size in stratified and dispersed pipe flow

The flow behaviour of dispersions depends on the volume fraction and the droplet size distribution of the dispersed phase [Pilehvari et al. (1988)]. The influences of flow regime, velocity, material and turbulent suppression on the droplet size in pipe flow have been studied experimentally by several researchers.

Influence of flow regime

Trallero (1995) claimed that water droplets in the dispersed water in oil and dispersed oil in water flow regime (Dw/o and Do/w) were larger than the oil droplets due to larger turbulent forces in the water phase which causes droplet breakup. However, Lovick and Angeli (2004c) did only observe small difference in size between oil drops in the lower water continuous layer and water drops in the upper oil layer. In contrast to Trallero (1995), Vielma et al. (2007) measured that the oil droplets were in general larger than the water droplets in the dual dispersions of o/w and w/o flow regime. Increasing the superficial water velocity led to a decrease in the oil droplet size due to an increase in turbulence energy. Al-Wahaibi and Angeli (2008) measured that the oil droplets were larger than the water droplets in the dual continuous flow regime. Al-Wahaibi and Angeli (2008) explanation to the larger oil droplets compared with the water droplets is that the oil droplets coalesce easier which leads to larger droplets.

Influence of velocity

Angeli and Hewitt (2000), Lovick and Angeli (2004c) and Vielma et al. (2007) observed that the droplets were influenced by the nature and the velocity of the continuous phase. The droplet size generally decreased with increasing continuous phase velocity. Lovick and Angeli (2004c) observed that higher velocities tended to decrease the drop size, but the affect was not that severe. In full dispersion of o/w and w/o Vielma et al. (2007) measured the SMD (Sauter mean diameter) to increase as the internal phase velocity increased at the same

continuous phase velocity (level of turbulence), since the droplets got closer, thus increasing the coalescence tendency. Larger droplets were also observed when the percentage of the dispersed phase increased at the same level of turbulence, which was also attributed to a increase in coalescence rate. Su and Hanzevack (1988) showed from experimental results that the maximum droplet size depended more strongly on velocity and pipeline diameter than on viscosity. Lovick and Angeli (2004c), Al-Wahaibi and Angeli (2008) measured the number of large drops to decrease with increasing water superficial velocity, while no clear effect was observed of oil superficial velocities on drop size.

Influence of material and turbulent suppression

Angeli and Hewitt (2000) showed that the channel wall had also an effect on the drop size with smaller drops formed in steel than in the acrylic test section under the same flow conditions. Water drops were in general faster than the velocity of their respective oil layer while oil drops could be either faster or slower. Angeli (1996) observed that turbulent suppression may occur in dispersed flows when the size of the dispersed particles is smaller than 0.1 times the diameter of the pipe.

Modelling

Kurban et al. (1995b) showed that the Hinze (1955) and Levich (1962) models always under-predicted the maximum measured droplet size. The most likely reason for the deviations observed was due to a high concentration of the dispersed phase in the experiments and due to the fact that the largest measured drops were larger than the length scale of the energy containing eddies ($d_{max}>0.1D$). Angeli and Hewitt (2000), Lovick and Angeli (2004c), Vielma et al. (2007) showed that the often used Hinze (1955) equation under-predicted the experimental results in both concentrated flows and dual continuous flows. Angeli and Hewitt (2000) also tested the Kubie and Gardner (1977) and the Sleicher (1962) model. The models were able to reproduce the droplet size close to the experimental values, but were unable to predict the influence of the pipe material and the velocity of the continuous phase. Vielma et al. (2007) tested the experimental droplet size data with the models of Hinze (1955), Kubie and Gardner (1977), Angeli and Hewitt (2000) and Kouba (2003). The models assume dilute dispersions. The Hinze (1955) model predicted the maximum diameter in o/w and w/o dispersions best with average percentage relative errors of -25% and -42 %, respectively. The model by Kubie and Gardner (1977) gave the poorest predictions for both o/w and w/o

dispersions. Al-Wahaibi and Angeli (2008) found that the models of Brauner and Ullmann (2002), Tsouris and Tavlarides (1994) and Sleicher (1962) under-predicted the maximum drop size and that the model of Hinze (1955) gave the poorest results. Simmons et al. (2000) measured the droplet size with two different optical techniques and found a good match with the theory of Hinze (1955) for dilute dispersions (up to 3%), but not for concentrated ones.

2.6.4 Droplet distribution

A comprehensive study of drop size distributions in turbulent pipe flow of unstable dispersions mainly in fully dispersed dilute systems can be found in Lovick and Angeli (2004b). Karabelas (1978), Su and Hanzevack (1988), Angeli (1996), Angeli and Hewitt (2000) results showed good agreement between Rosin Rammler distribution and experimental data in fully dispersed systems and Lovick and Angeli (2004c) and Al-Wahaibi and Angeli (2008) reported reasonable predictions in dual continuous flow regime. Vielma et al. (2007) found on the other hand that the Log-normal distribution was the best fit in full dispersion of oil in water (o/w) and water in oil (w/o) and in dual dispersions (Do/w and Dw/o). Some deviations were seen in the dual dispersions, which were attributed to the fact that most of the oil droplets were of the same size as the water layer, producing secondary breakage due to shear at the interface. The secondary breakage was observed as a secondary peak in the experimental distribution (bi-normal distribution). Simmons et al. (1998) showed that an upper limit Log-normal distribution fitted the normalised data well. The droplet size data where conducted with a laser. Karabelas (1978) used both Rosin-Rammler and upper limit log-probability equation to predict the distribution with small deviations. The size distribution measurement technique, encapsulation technique, appeared to be more accurate than the photographic method. Su and Hanzevack (1988) showed that the Rosin-Rammler distribution represented the measured water droplet size distribution in an oil continuous flow well, but the measurements showed a much larger degree of small sized drops. The deviation was explained by the ability to obtain more information on smaller sized drops than previous investigators. They used a pulsed laser combined with digital imaging. Angeli (1996) also measured a greater population of smaller water drops in the oil continuous flow compared to the dispersed water continuous flow and showed that a Rosin-Rammler distribution law adequately represented the experimental data.

By measuring the chord lengths with use of dual impedance probe Lovick and Angeli (2004c) and Al-Wahaibi and Angeli (2008) found that the drop size decreased with increasing distance from the interface in the dual continuous flow regime. Close to the interface the local dispersed volume fraction were high leading to a higher coalescence ratio, thus larger droplets were observed close to the interface. In all the cases studied the water droplets had a larger velocity.

2.7 Modelling of oil-water flow

Experimental correlations indicate relationships between variables and are widely used to predict flow parameters. These experimental correlations are often termed as empirical models. Mechanistic modelling is modelling of the most important processes and neglecting other less important effects that can complicate the problem. Mechanistic modelling is often combined with empirical models as shown in the two-fluid models. Computational Fluid Dynamics (CFD) uses numerical methods and algorithms to solve and analyze systems involving e.g. fluid flow and heat transfer. The governing equations of fluid flow are conservation of mass, momentum (Navier-Stokes equations) and energy.

2.7.1 Empirical models

Flow pattern predictions

Testing of generalized flow regime maps developed for gas-liquid flow with liquid-liquid experiments has been found inadequate by many researchers e.g. Cox (1985) and Scott (1985). Scott (1985) showed that dimensional flow regime maps were dependent on the flow conditions and were therefore not applicable to other flow cases. Cox (1995) and Scott (1985) compared measured flow pattern in both horizontal and inclined pipes with gas-liquid model prediction methods such as Taitel and Dukler (1976) and Barnea (1987) and showed that the models were inadequate.

Pressure drop predictions

Lockard and Martinelli's (1949) similarity method as shown in Eqs. (2.27) and (2.28) have been used by many investigators [Charles and Lilleleht (1966), Stapelberg and Mewes (1990), Angeli (1994)]. The relationship between x and ϕ are based on empirical correlations and curve fitting, where $\left(dP/dx\right)_{so}$ and $\left(dP/dx\right)_{sw}$ are the pressure gradients for the oil and water phases flowing alone in the pipe, and $\left(dP/dx\right)_{TP}$ is the two phase pressure gradient.

$$X^2 = \frac{\left(dP/dx\right)_{so}}{\left(dP/dx\right)_{sw}} \tag{2.27}$$

$$\phi^2 = \frac{\left(dP/dx\right)_{TP}}{\left(dP/dx\right)_{so}} \tag{2.28}$$

Charles and Lilleleht (1966) showed that pressure gradients could be predicted within an error of 25% by using the Lockard and Martinelli (1949) correlations in a laminar-turbulent flow regime. But the method acquired a precise prediction of the various flow regimes. Angeli (1994) and Angeli and Hewitt (1998) compared dispersed experimental data with Theissing's (1980) model and showed very good agreement, especially for the transpalite pipe. Theissing (1980) matched the Lockard and Martinelli (1949) data for gas-liquid flow and oil-water flow by including the density ratio between the two phases. The model is not restricted to a specific flow pattern and does not include parameters, such as pipe diameter or the interfacial tension between the liquids. Alkaya (2000) compared experimental data [Angeli and Hewitt (2000), Angeli and Hewitt (1998), Oglesby (1979), Trallero (1995)] with empirical model of Theissing (1980). The model predicted the pressure gradient quite well in horizontal flow for dispersed flow for almost all data sets, except for Oglesby's (1979) data with the large viscosity oil. In inclined pipes (±1° and ±5°) the model predictions gave large discrepancies from the experimental data. The best match was found at large measured frictional pressure drops, where the degree of dispersion was largest.

2.7.2 Two-fluid models

A mechanistic stratified one-dimensional flow model, the so called two-fluid model, is presented in Eqs. (2.29) and (2.30), where A is the area occupied by the fluid, $\frac{dP}{dx}$ is the pressure gradient, τ_w is the water shear stress, τ_o is the oil shear stress, τ_i is the interfacial shear stress, S is the circumference occupied by the fluid, ε_w is the water fraction, ρ is the density of the fluid, g is the gravitational constant, β is the inclination angle. The equation yields for horizontal and inclined pipes and the flow is assumed to be isothermal ($\frac{\partial T}{\partial t} \approx 0$),

incompressible ($\frac{\partial \rho}{\partial t} \approx 0$), at steady state condition ($\frac{\partial (U)}{\partial t} \approx 0$) and fully developed ($\frac{\partial U}{\partial x} \approx 0$). The model also assumes that the radial velocity is equal to zero ($\bar{v}_r \approx 0$), that there is no change in momentum due to mass transfer between oil and water (fully immiscible liquids) and that the hydrostatic pressure distribution in the y-direction is equal to one ($\frac{\partial P}{\partial y} \approx 0$). The two-fluid model is a balance between the pressure gradient and the wall and interfacial shear forces. The closure parameters are the wall and interfacial shear stresses. The interfacial shear stresses are often defined differently [Taitel and Dukler (1976), Barnea and Taitel (1992), Brauner and Maron (1993)]. The pressure gradient can be eliminated and reduced to a one non-algebraic equation, where all the parameters are known except for the in situ phase fraction and the height of the water liquid phase. The equation has to be solved iteratively with respect to the in situ water fraction.

$$-\varepsilon_w\left(\frac{dP}{dx}\right) - \tau_w \frac{S_w}{A} \pm \tau_i \frac{S_i}{A} + \varepsilon_w \rho_w g \sin\beta = 0 \tag{2.29}$$

$$-(1-\varepsilon_w)\left(\frac{dP}{dx}\right) - \tau_o \frac{S_o}{A} \pm \tau_i \frac{S_i}{A} + (1-\varepsilon_w)\rho_o g \sin\beta = 0 \tag{2.30}$$

The wall shear stress for oil and water and interfacial shear stress are conventionally expressed in terms of the corresponding friction factors as shown in Eqs. (2.31) to (2.33).

$$\tau_o = \frac{1}{8} f_o \rho_o U_o^2 \tag{2.31}$$

$$\tau_w = \frac{1}{8} f_w \rho_w U_w^2 \tag{2.32}$$

$$\tau_{ow} = \frac{1}{8} f_{ow} \rho_o (u_o - u_w)|u_o - u_w| \tag{2.33}$$

The oil and water friction factors can be found by using single phase flow relationships as Haaland's friction factor (1983) and the hydraulic diameter must be used when calculating the friction factors. Many of the reported interfacial friction factors have used the friction factor of a smooth pipe single-phase oil flow due to the difficulties in measuring the interfacial shear

stress. Valle (2000) used the maximum of a smooth pipe friction factor and a constant friction factor given by Taitel et al. (1995) as shown in Eq. (2.34).

$$f_{ow} = Max(f_{ow}(\mathrm{Re}_{o,\varepsilon=0}), 0.014) \tag{2.34}$$

Most of the two-fluid models assume a plane interface between the stratified layers, but Brauner et al. (1998) and Lovick (2004) proposed a two-fluid model for stratified flows with curved interfaces. In liquid-liquid systems with small density differences compared to gas-liquid flow, surface phenomena may dominate, which leads to a curved interface. Flow parameters like e.g. pressure gradient will be largely influenced when the interface is curved since curvature determines the fluids contact area with the pipe wall. Lovick (2004) assumed that the interface was curved which was also seen in the experiments. The interfacial curve was also assumed to be circular [Brauner et al. (1998) and Ng et al. (2001)]. In most of Lovick's (2004) experiments the radius of the curvature was approximately twice the pipe radius apart from the high and low oil fractions where it was approximately equal to the pipe radius.

Trallero (1995) included the effect of waves into the interfacial shear stress as shown in Eq. (2.35), where τ_s accounts for the effect of waves.

$$\tau_{ow}^{w} = \tau_{ow} + \tau_s \tag{2.35}$$

Lovick and Angeli (2004b) modified the two-fluid model by accounting for the turbulence damping by implementing a friction factor for the dispersed flow (f_d). The dispersed phase friction factor was suggested by Rosentsvaig (1982) as shown in Eq. (2.36), were f_e is the friction factor of a finely dispersed emulsion with the same dispersed phase concentration, and k is the concentration function constant (0.5 to 1.125). The friction factor f_e was calculated by use of the model of Brinkman (1952).

$$f_d = \frac{f_e}{1 + k\varepsilon} \tag{2.36}$$

Vedapuri et al. (1997) developed a model which treated the system as three phase flow, with clear water layer, a mixed layer and clear oil layer as shown in Figure 2.6. The model predicts

the holdup and pressure drop and is similar to the two-fluid model, only here three momentum equations, one for each layer is modelled. The shear stresses are found by use of Taitel and Dukler (1976) correlation and the friction factors were similar to the approach of Brauner and Maron (1989). The model required the water fraction and the in-situ velocity of the emulsion layer as input.

Jayawardena et al. (2000) developed a two-fluid model to predict the holdup and pressure gradient for the dispersed oil in water and water (Do/w & w) flow regime. The model combines the two-fluid model used for stratified flows with the homogenous model. Calculation of the interfacial wall and shear stresses was done by using the model presented by Taitel and Dukler (1976). The model of Brinkman (1952) predicted the mixture viscosity as shown in Eq. (2.37).

$$\mu_{mix} = \mu_c (1-\varepsilon_d)^{-2.5} \tag{2.37}$$

Flow pattern predictions

The mechanism of droplet formation is a complex process and several attempts have been made to model the transition from stratified to dispersed flow. Trallero (1995) published the first complete model for oil-water flow pattern transitions for light oil. The interface was assumed to be flat in the cross section and wavy in the axial direction. Different kinds of stability analysis where used to predict the flow transitions in the stratified flow regime. The stability analysis linearises the two-fluid model equations (continuity and momentum equations) by implementing harmonic perturbations into the equations, which reduce the equations to algebraic equations [Wallis (1969), Barnea and Taitel (1993)]. Trallero (1995) developed stability criteria for stratified flow as shown in Eq. (2.38), where J_μ is the viscous term, J_u is the velocity term, J_g is the gravity term, J_σ is the surface tension term and J_s is the sheltering effect. The viscous term includes the effect of shear and is a function of the wave velocity and the critical wave velocity.

$$J_\mu + J_u - J_g - J_\sigma + J_s < 0 \tag{2.38}$$

The velocity, gravity and surface terms comprise the stability criterion for the inviscid analysis, which is the well-known Kelvin-Helmholtz (KH) instability criterion. In the viscous KH theory the viscous term is included. The viscous Kelvin-Helmholtz (VKH) predicted the stratified flow regime and the inviscid Kelvin-Helmholtz (IKH) predicted the ST & MI

pattern. In the dispersed flow regime the flow pattern were predicted by use of a force balance between the gravity and turbulence. The gravity and turbulent forces is shown in Eqs. (2.39) and (2.40), where $\overline{u'^2}$ is the fluctuating component of the radial velocity. The fluctuating radial velocity is estimated by Levich (1962) as shown in Eq. (2.41). The droplets will be suspended if the turbulence forces are larger than the gravitational forces. Trallero (1995) accounted for the effect of high concentration of the dispersed phase on the droplet size by implementing an empirical correlation for the coalescence phenomena. Trallero (1995) adjusted the empirical coalescence factors to match the experimental flow pattern transition.

$$F_g = \frac{4}{3}\pi\left(\frac{d}{2}\right)^3(\rho_c - \rho_d) \tag{2.39}$$

$$F_T = \frac{1}{2}\rho_c \overline{u'^2}\frac{\pi}{4}d^2 \tag{2.40}$$

$$\overline{u'^2} \cong u_c\sqrt{\frac{1}{2}f} \tag{2.41}$$

The performance of the model was remarkable good in horizontal pipe flow considering the diversity of conditions found in the literature. Moreover, the model gave reasonable predictions for pipeline inclination angles ranging from -15º to +10°. Alkaya (2000) tested Trallero's (1995) flow pattern prediction model for 0°, +1°, +5° and -5° pipe flow. In general the model failed to predict the boundary between stratified (ST) and stratified with mixing at the interface (ST & MI) flow patterns for all inclinations. Some good predictions at low superficial oil velocities and small inclinations (0° and ±1°) were seen. The model also predicted very few stratified (ST) flow patterns at +5° angle and no stratified flow patterns at -5°, which did not match with the experiments. Good predictions for transition between stratified with mixing at the interface (ST & MI) and dispersion of oil in water and water (Do/w & w) flow regimes were seen for superficial velocities higher than 0.1 m/s for all inclinations. The model agreed well for dispersed flow pattern boundaries, except for the boundary between dispersion of water-in-oil (w/o) and dual dispersion (Dw/o & Do/w). The model predicted the boundary at a lower superficial water velocity for all inclinations. Atmaca et al. (2008) also observed that the model was not able to predict the transition from ST to ST & MI flow regime, but most of the other data point were located within the predicted boundaries.

Fairuzov et al. (2000) used the model presented by Brauner and Maron (1992), which is to some degree complementary to the model of Trallero (1995). The models deviate because Trallero (1995) used low viscosity oils, while Brauner and Maron (1992) used high viscosity oils in the model development [Valle (2000)]. Fairuzov et al. (2000) found that the stratified/non stratified transition in large scale diameter, using a real crude oil, can be predicted with reasonable accuracy based on the Kelvin-Helmholtz analysis.

Valle (2000) predicted four flow regimes by use of a one-dimensional two-fluid momentum balance. The model discriminates between stratified smooth flow, stratified wavy flow, stratified flow of water and oil continuous dispersions and dispersed flow. The two-fluid model was compared with experimental data using model oil and real crude oil. Different sets of mobility factors, which accounted for the different coalescence of oil and water droplets, had to be used to be able to predict the flow patterns. One set of mobility factors was able to predict the crude oil flow patterns, while another mobility factor had to be used for the Exxsol-salt water system. A third set was used to describe the Exxsol-fresh water experiments by Soleimani (1999). For the lightest crude oils the model over-predicted the area of the stratified flow with dispersed drops (STD). For viscous and medium viscous crude oils (>2 cp) the model predicted the flow pattern at low water cuts well. Comparison of the model with the data presented by Soleimani (1999) gave good transitional predictions.

Al-Wahaibi and Angeli (2007) studied droplet formation due to unstable waves. They developed a criteria for the transition between stratified stable and unstable liquid-liquid flows based on Kelvin-Helmholtz instability and finite wavelength that related the critical amplitude and wavelength to the onset of instability. They found that the onset of droplet formation coincided with the appearance of unstable waves. However, even if the model was able to predict the transition from stable to unstable waves, it was not able to predict the conditions for drop formation using light oils. The required amplitude and lengths of the waves for drop formation needed to be above the point where the wave became unstable. To be able to predict the region of unstable wave amplitude and lengths that lead to drop formation Al-Wahaibi et al. (2007) implemented a drop entrainment equation and used this together with the wave stability equation. The wave deformation was attributed to the drag force balance that originates from the relative movement between two phases, exceeding the stabilising

surface tension. The model agreed well with experimental data provided that a new correlation for the drag coefficient suitable for liquid-liquid flow on the waves was used.

Pressure drop predictions

Valle and Utvik (1997) compared a two-fluid model against experimental data and showed that the pressure gradient was predicted quite well, but the predicted slip ratios were over-predicted in the stratified flow regime. They defined the interfacial friction factor to be equal to the smooth wall oil friction factor. Alkaya (2000) compared three different models, empirical [Theissing (1980)], homogenous and two-fluid model, with a new data set and with three published data sets. Alkaya (2000) showed that the pressure drop model for an oil-water flow should be selected based on the observed flow pattern. The model comparison was best for low viscosity oil and much worse for high viscosity experiments. The two-fluid model gave much better prediction of the pressure gradient than the homogenous model in the dual dispersion (Dw/o and Do/w) flow regime. Alkaya (2000) addressed the two fluid model by following the theoretical analysis of Taitel and Dukler (1976) and Brauner and Maron (1989). The two-fluid model for stratified flow performed within 20% error for all the acrylic data sets in both horizontal and inclined pipes, when compared with the measured pressure gradient of Angeli and Hewitt (1998). The data sets included stratified flow patterns in horizontal, upward and downward inclinations (±1° and ±5°). Larger disagreements were seen in the dispersed flow regimes, especially in oil-in-water (o/w) dispersions. The stratified model performed poorer on Angeli and Hewitt's (1998) steel pipe experiments. Large deviations were seen between Oglesby's (1979) experiments and model predictions, which were probably due the viscous oil used. Angeli and Hewitt (1998) under-predicted the pressure gradient in steel pipe and over-predicted the pressure gradient in the acrylic pipe by use of a two-fluid model [Taitel and Dukler (1976)] in the separated flow regime. The under-prediction in the steel pipe was explained by increased interfacial mixing in the experiments which lead to a larger interfacial friction factors than the calculated one. The deviations between predictions and experiments could also be due to wetting phenomena and drag reduction effects. Jayawardena et al. (2000) developed a new mechanistic model for dispersed oil in water and water (Do/w and w) flow regime and showed that the results agreed well with experimental data. Lovick and Angeli (2004a) were not able to predict the pressure gradient and hold up during dual continuous flow by use of a standard two-fluid model. The experimental data were over-predicted at input oil fraction from 20 to 90% and under-predicted below 20%. Lovick and Angeli (2004b) improved the predictions by taking into

account entrainment of oil in water and water in oil by using the measured phase distributions and turbulence damping. Atmaca et al. (2008) compared the model of Zhang and Sarica (2005), (2006) with pressure gradient data for horizontal and inclined pipes (+1°,-2°). Zhang and Sarica (2005) developed a unified model of gas, oil and water pipe flow. The correlation developed by Churchill (1977) was used to estimate the friction factor in the oil and water phases and the interfacial friction factor between oil and water was set equal to 0.0142. The model predicted almost all the pressure gradient data within ±20% error band width for horizontal and +1° inclination angle. In general, the model over-predicted the pressure gradient. The model predictions were reasonable well for low superficial velocities, while they got gradually worse as the superficial velocities increased.

Parametric study

Hadziabdic and Oliemans (2007) performed parametric studies of the two-fluid model in order to determine the wall and interfacial shear stresses in the ST & MI flow regime. The parametric studies are done by imposing the measured pressure drop and hold-up in the two-fluid model and considering the effect of interfacial waves and drop entrainment. It was found that the wall shear stresses was most affected for the flow conditions characterized by a thin layer oil or water at the top or bottom of the pipe, where the phase-Reynolds number was smaller than 4000. This supports that the shear stresses are greatly influenced by multiphase flow phenomena like the oil-water interface and its position. The parametric study of the influence of interfacial waves shows that only high amplitude waves have a significant effect on the wall-shear stresses. The main conclusion from the entrainment study suggests that drop entrainment is not the main reason for the high prediction errors when the water forms a thin layer at the bottom of the pipe. However, the predictions of the thin oil phase velocity are improved in the entrainment parametric study.

2.7.3 Homogenous model

The homogenous model is used for dispersed flow and its main assumption is the non-slip condition between the phases. The average in situ volume fraction of each phase will therefore be equal to the inlet volume fractions of the mixture. The pressure gradient can be expressed as a single phase analogy as shown in Eq. (2.42).

$$\left(\frac{dP}{dx}\right) = \frac{f\rho_m U_m{}^2}{2D} - \rho_m g \sin\beta \tag{2.42}$$

Where f is the Moody friction factor, ρ_m is the mixture density, U_m is the mixture velocity, D is the inner pipe diameter and β is the pipe angle.

Many different viscosity models have been proposed in the literature for oil-water dispersions. Pal and Rhodes (1989) extended the empirical correlation of Pal and Rhodes (1985) by including additional data. The viscosity of Pal and Rhodes (1989) is shown in Eq. (2.43), where ε is the no-slip mean concentration of the dispersed droplets. For oil continuous flow ε is equal to the no-slip water fraction.

$$\mu_m = \mu_o \left[1.0 + \frac{\varepsilon / 0.765}{1.19 - \varepsilon / 0.765}\right]^{2.5} \tag{2.43}$$

Brinkman (1952) developed the correlation shown in Eq. (2.44) from Einstein's relationship for the viscosity of suspensions.

$$\mu_m = \mu_c (1-\varepsilon)^{-2.5} \tag{2.44}$$

Pressure drop predictions

Initial pressure drop models had a focus on homogenous flow [Russel et al. (1959), Malinowsky (1975), Laflin and Oglesby (1976), Oglesby (1979), Segev (1984), Arirachakaran et al.(1989), Angeli (1994)]. Valle and Utvik (1997) showed that the homogenous model combined with Pal and Rhodes (1989) viscosity model [see, Eq. (2.43)] worked best at high mixture, despite the fact that large slip between oil and water was measured. At the lowest flow rate the model under-predicted the pressure drop. Alkaya (2000) showed that the homogenous model was inadequate for predictions of pressure gradients in the stratified flow regime and that better predictions were seen for dispersed flow. Alkaya (2000) used the viscosity correlation of Brinkman (1952).

2.7.4 Computational fluid dynamics (CFD)

Computational fluid dynamics as a tool for multiphase pipe flow predictions are not widely used, since the computational effort is too large to be used in real production pipelines.

Instead CFD is usually used to understand the basic mechanisms in flow behavior in small scale pipes.

Dispersed flow

Soleimani (1999) compared CFD simulations of spatial phase fraction distributions with experimental phase fractions measured with gamma densitometer in dispersed flow and found good agreement. The model included particle drag, lift force, virtual mass force and turbulent dispersion force. Soleimani (1999) found that the lift force and the turbulent dispersion influenced the oil drop distribution a great deal. The simulations were not able to predict the higher concentration of oil drops in the centre of the pipe seen in the experiments. Walvekar et al. (2009) used CFD (Fluent 6.2) for predictions of phase fraction profiles and compared them with measurement of Soleimani (1999). Good agreement was seen at large mixture velocities (3.0 m/s), where slip is negligible, but decreasing the velocity to 2.12 m/s led to deviations in the vertical phase distributions. Walvekar et al. (2009) used the Eulerian-Eulerian approach to predict flow behaviour in dispersed system. Forces such as drag, lift and turbulent dispersion were included.

Stratified flow

Soleimani (1999) developed a mathematical model for prediction of the curve of the interface between oil and water. The results showed that three different curves can exist; convex, concave or flat configuration. Soleimani (1999) also showed that at high viscosity ratio, the velocity profile was different for each interface shape. Elseth et al. (2000) used the Fluent CFD code and selected the VOF (Volume of Fluid) model to predict the vertical velocity profiles. Large deviations between the model and LDA experiments were disclosed. The flow patterns observed was mainly in the stratified mixed flow regime. Gao et al. (2003) applied a modified VOF model together with a continuum surface force (CSF) to include the effect of surface tension to predict the vertical velocity distributions. They compared the experimental velocity, phase distributions, pressure gradient and slip ratio of Elseth et al. (2000) at 1.05 m/s with the CFD model and showed relatively good agreement. Good agreement in the pressure gradient was observed up to 80% input water fraction, while the model under-predicted the experimental data at higher input water fraction by approximately 16%. Largest deviations in the phase fraction and velocity profiles were seen at low and high input water fraction (25 and 75%). Kumara et al. (2008) used the commercial CFD code Fluent 6.3 and used the same models (a modified VOF model together with a continuum surface force) as Gao et al. (2003)

did. The predictions were compared with Elseth et al. (2000) data. The same conclusion were drawn, large deviation were observed in the pressure gradient at input water cuts above 80% and accurate results were observed at intermediate input water cuts (25-75%) for both the velocity profiles, pressure gradients, interface heights and slip ratios. The model slightly over-predicted the slip ratio at intermediate water cuts.

3 FLOW FACILITY

This chapter describes the multiphase flow facility at Telemark University College built to study oil-water flow in horizontal and inclined pipes. Preliminary experimental analysis are presented to verify the instrumental set-up and to confirm if the flow is fully developed and at steady state condition. Experimental studies of oil-water flow in the multiphase flow loop has also been published by Elseth et al. (2000), Elseth (2001), Wahumpurage et al. (2008), Kumara et al. (2009a) and Kumara et al. (2009b).

3.1 Flow facility modifications

In the start of this PhD study the flow facility was built to run flow experiments in inclined pipes. The new elements in the flow facility are:

- Inclinable pipe (Figure 3.1)
- Pre-separator (Figure 3.8)
- Water centrifugal pump
- New mixing unit

A more detailed description of the modifications on the multiphase flow facility is described in Appendix 4.

3.2 Flow facility specifications

This chapter presents the flow facility and fluid specifications, flow sheet and a description of the main components. The test facility and fluid specification are shown in Table 3.1 and Figure 3.1. Tande (2008) measured the viscosity of Exxsol D60 and tap water using a rheometer. The results are presented in Appendix 5, Figure A 5. The density of Exxsol D60 was measured using Anton Paar [Orr (2009)] and the density of water was found in East R. C. et al. (1984-1985). The density data is presented in Appendix 6, Figure A6. Orr (1995) measured the interfacial tension by a pendant drop technique at a temperature equal to 25°C.

Table 3.1 Flow facility parameters and fluid properties.

Temperature	15-27 °C
Pressure	1 bar
Volume rates water	30 m3/h
Volume rates model oil	30 m3/h
Test pipe length (from inlet to outlet)	13.2 m
Inner Steel pipe diameter:	0.0563 m
Inner Plexiglas diameter:	0.0555 m
Pipe roughness:	$1x10^{-5}$ m
Length PDT-120:	10.22 m
Length PDT-121:	5.38 m
Fluids	Model oil (Exxsol D60), tap water and air
Density Exxsol D-60:	785 kg/m^3 @ 25^{o}C
Viscosity Exxsol D-60:	0.00164 Pa s @ 15^{o}C
Density water:	997 kg/m^3 @ 25^{o}C
Viscosity water:	0.00102 Pa s @ 20^{o}C
Interfacial tension (o/w):	$43x10^{-3}$ N/m @ 25^{o}C

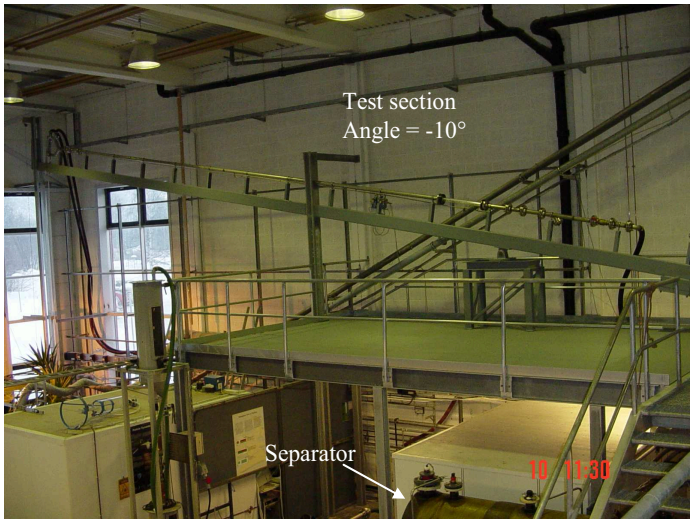

Figure 3.1 Multiphase flow facility and the inclined test section.

3.2.1 Flow sheet

A technical drawing of the multiphase flow loop is shown in Figure 3.2 and a tag list of the main components is shown in Table 3.2. The flow facility can handle model oils, tap water and inert gas environment. Two separated pumps circulate the oil and water phases and the individual flow rates are measured down stream of the pumps by two turbine transducers. Two pressure controllers measure the static pressure down stream of the turbine transducers. The oil and water phases are then mixed in the mixing unit before entering the test section. The test section is a 15 m long pipe, which can be inclined from - 10° to + 10° angle. The flow is moving upwards when the inclination angle is positive (equal to +10°). Differential pressure, velocity profiles, turbulence profiles and in-situ oil-water fractions are measured in the test section. The oil and water flows into a pre-separator tank down stream the test section. The pre-separator tank increases separation time and reduces oil-water emulsions in the main separator. The oil and water flow then into the main separator and back into the storage tanks.

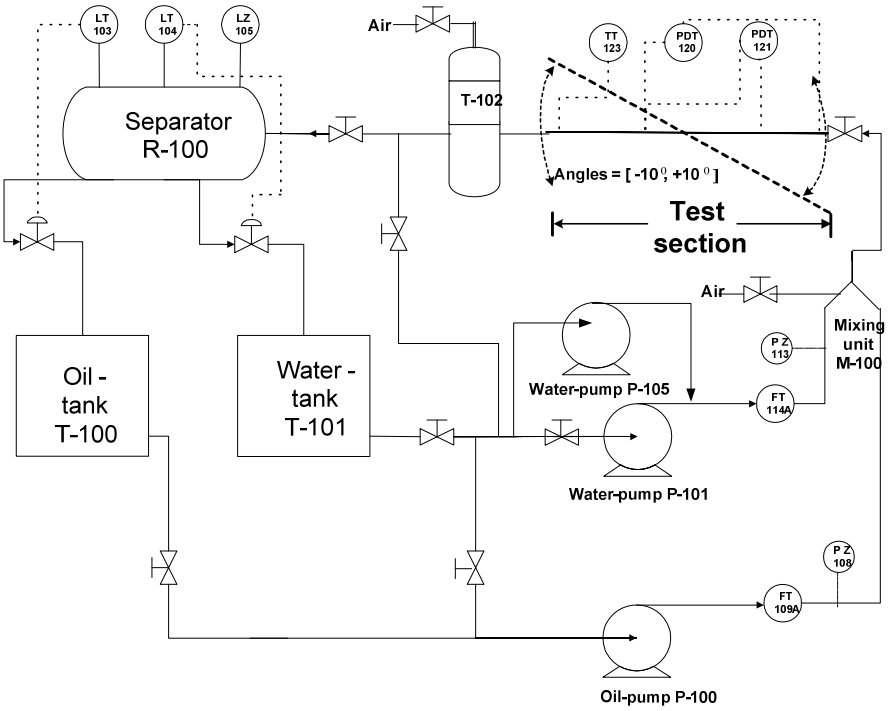

Figure 3.2 Flow sheet of the multiphase flow facility.

Table 3.2 Multiphase flow facility tag list.

Components	**Tag nr.**
Main oil-water separator	R-100
Intermediate storage tanks for oil and water	T-100, T-101
Mono eccentric water pump	P-101
Centrifugal water pump	P-105
Positive displacement oil pump	P-100
Flow transducers	FT-109A, FT-114A
Pressure controllers for oil and water	PZ-108, PZ-113
Oil-water mixing unit	M-100
Pre-separator tank	T-102
Level controller for the water phase	LT-104
Level controller for the oil phase	LT-103
Level switch	LZ-105
Temperature transmitter	TT-123
Pressure differential transducers	PDT-121, PDT-120

3.2.2 Oil-water separator, storage tanks and pumps

The oil-water main separator shown in Figure 3.3 separates oil and water. The separator is made out of glass fiber with a transparent viewing section and has an inner diameter of 0.8 m and a length of 2 m. The total volume of oil and water must be less than the total volume of the separator (0.9 m^3), because of safety regulations. The separator includes a flow straightening section and a partition wall. The straightening section is a bundle of tubes inside the separator, which improves the separation. The level controllers for the water phase and the oil phase are installed to prevent the water from rising above the partition wall and make sure that the oil flows into the oil storage tank before the separator is full. In addition, there is a level switch, which shuts down the oil and water pumps if the separator is overfilled. After the separation, the oil and water flows back to the oil and water storage tanks, which are shown in Figure 3.4. The outlet pipes, from the separator to the storage tanks are connected to ball valves, which are controlled either by the level controllers or manually. The storage tanks have approximate dimensions of 1×1×1 meter and are made of polypropylene covered with a steel shielding. There is a rubber float indicating the liquid level in the storage tank and to prevent flooding there is a 2” tube about 30 cm from the top connecting the two tanks. The piping material from the storage tanks to the pumps is stainless steel. The stainless steel material in the rig is 316 Schmelze 443645 DIN 17457 K1 W-1 CCY.

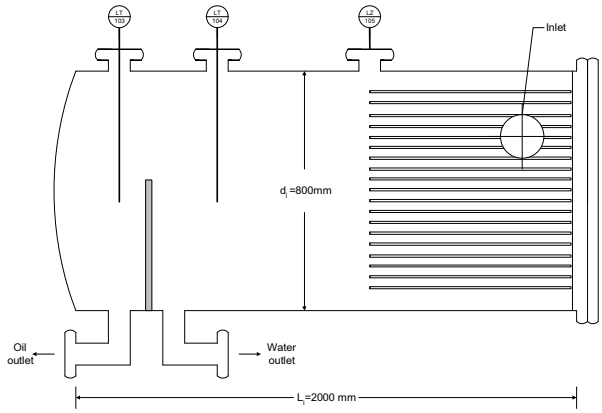

Figure 3.3 The oil-water separator [Elseth (2001)].

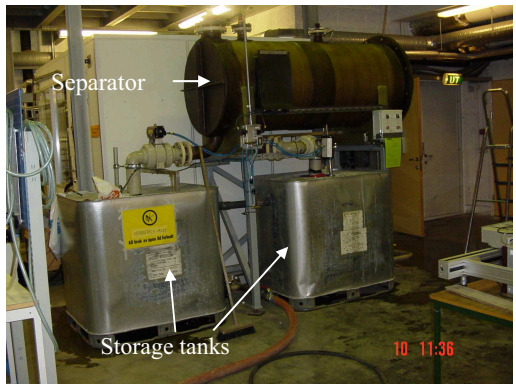

Figure 3.4 Separator and storage tanks.

The mono eccentric water pump and the positive displacement oil pump provide low shear and low noise level. It is desirable to avoid pressure fluctuations caused by the pumps, since the measured pressure drops can be as low as a few mbar. Since initial experiments with the mono eccentric water pump revealed pressure pulses in the low flow region, a centrifugal water pump was installed. The centrifugal water pump gives less pressure pulses, but the shear forces exerted is higher in this pump. Low shear is important to prevent further mixing of oil and water. The water pumps were used one at a time in the experiments.

The oil pump is a positive displacement pump. The pump model is Waukesha U-130 and delivers a constant volume flow with delivery per revolution equal to 0.946 l/rev independent

of the pressure difference between the inlet and outlet. The minimum and maximum capacity is 4.8 and 26 m^3/h. The maximum differential pressure is 6 bars from inlet to outlet. The pump medium is used as lubricant. The mono eccentric screw water pump is also a constant volume pump with a stainless steel screw eccentrically rotating in a rubber stator. The pump model is Allweiler SEBP 550.1 and delivers a total volume of 1.285 l/rev. It has a minimum and maximum capacity of 4.8 and 33 m^3/h. The centrifugal pump is a KSB Etanorm 50-200 with a minimum and maximum capacity of 2.4 and 15 m^3/h.

The positive displacement oil pump and the mono eccentric screw water pump are connected to a shutdown circuit that cuts the power to their drives if there is blockage in the pipe (high pressure) or overflow in the separator. To regulate the volumetric flow through the pumps, frequency control modules are installed for the oil pump and the mono eccentric screw water pump. When using the centrifugal pump, a valve on the pump regulates the volumetric flow.

3.2.3 Mixing unit

Armoured rubber hoses are connected between the pumps and the unit where oil and water are mixed before entering the test section. Bends are mounted at the oil and water inlet to avoid bending of the hoses when the test section is inclined. The mixing unit is made of stainless steel and is designed to initiate fully developed flow in the stratified flow regimes before the measuring section. The mixing unit is presented in Figure 3.5. The oil is introduced at the top and water at the bottom of the unit. A 0.3 m long plate inside the mixing unit separates both phases. A rubber hose connects the air-inlet to the compressed air system and a valve regulates the airflow. The air is used during cleaning. The mixing unit can also be used to drain the test pipe.

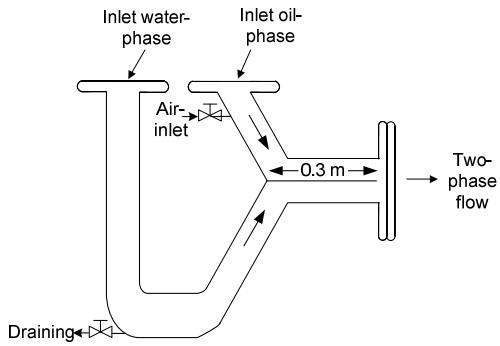

Figure 3.5 The mixing unit.

3.2.4 Test pipe and measurement sections

The entry length, exit length and the design of the mixing unit are important parameters in achieving fully developed single-phase and two-phase flow in the flow measurement section. Once the flow is fully developed the flow field does not vary in the flow direction. The test pipe shown in

Figure 3.6 can be inclined from -10^{o} to $+10^{o}$ and is made of stainless steel except for a 0.8 m transparent plexiglas section for measurements of local velocities by LDA and for visualization of the flow and a 0.4 m polypropylene section for measurements of local volume fractions by a gamma densitometer. The steel pipe has an inner diameter of 56.3 mm and an outer diameter of 60.3 mm. The distance from the mixing unit to the first differential pressure (PDT-120) measurement point is 0.85 m (L/D=15) and to the second (PDT-121) is 5.69 m (L/D=86). The differential pressures are measured over two distances equal to 10.22 m and 5.38 m. The LDA section is located approximately 9.2 m (L/D= 163) and the gamma section is located 10.3 m (L/D= 183) down stream of the mixing unit. Table 3.3 summarizes both the entry and exit lengths of the differential pressure, LDA and gamma measurements.

Table 3.3 Entry and exit lengths for pressure, LDA and gamma measurements.

Intrument	**Entry length, L [m]**	**Entry length, L/D [-]**	**Exit length, L [m]**	**Exit length, L/D [-]**
PDT-120	0.85	15	2.13	38
PDT-121	5.69	101	2.13	38
LDA	9.2	163	3.2	57
Gamma	10.3	183	2.5	44

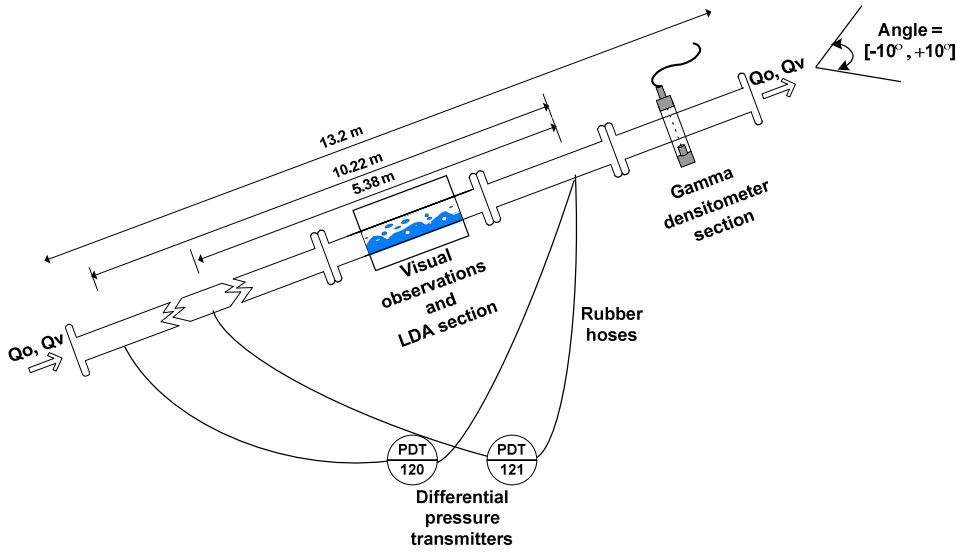

Figure 3.6 Test section.

3.2.5 Pre-separator tank

The pre-separator tank in Figure 3.7 is installed down stream of the gamma densitometer section and helps to avoid oil-water emulsions to be formed. The dimensions of the tank are shown in Figure 3.8. The tank is made of stainless steel. It is 1.5 m high and has a diameter of 0.5 m. The design of the bearer system prevents the tank to vibrate and fall. A 1.5 m long rubber hose connects the test section and the pre-separator tank. The small pipe at the top of the tank is 0.7 m long and is connected to a hose, which is always placed above the highest point in the facility and works as a vent. Placing the hose above the highest point creates a backpressure at the end of the test pipe. At the end of the hose, a ball valve enables atmospheric air to come into the pre-separator tank. The air-supply creates atmospheric pressure in the test section. This is necessary because a sub atmospheric pressure causes air-bubbles in the flow. The air can come into the test section because of the sub atmospheric conditions in the test section or because air is solved in the oil or water tank at 1 atmosphere and can be dissolved when the pressure is below 1 atmosphere in the rig. Since the test section was thoroughly checked for air leakage, the air bubbles must appear due to dissolved air in the water and oil. The hose at the top of the small pipe goes down to the oil tank to avoid

spilling. When the ball valve is fully open, the pressure is 1 atm and no air-bubbles are seen in the test section. The flow enters the tank tangentially to the wall with low shear to prevent oil-water emulsion. The oil-water outlet is at the bottom of the tank. The oil and water flow in a rubber hose from the pre-separator tank and approximately 1 m down to a 3-in. stainless steel pipe and then to the separator. The 3-in. stainless steel pipe also helps separating the fluids before entering the oil-water separator due to a larger diameter giving lower fluid velocity.

Figure 3.7 Pre-separator tank.

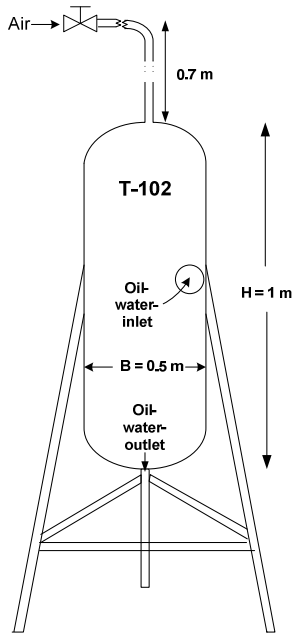

Figure 3.8 Pre-separator tank dimensions.

3.2.6 Control and safety instrumentation

Two different turbine meters measure the liquid flow rates down streams of the pumps as indicated on the flow chart in Figure 3.2. The measurement range for the flow meters is 53 - 533 l/min (3.2 - 32 m^3/h) and has an accuracy of +/- 0.3% of the output signal. Both flow meters are from the same manufacturer: Euromatic Machine & Oil Co. Ltd and the model is EMO LFL-1.5 -120. A computer logs the flow rates every third second. The turbine flow meters were calibrated with Coriolis flow meters (see Appendix 7 and 8).

The water and oil pressure controllers measure the static pressure in the system down stream

of the water and oil turbine meters. The system is designed for a pressure up to 3.5 bars, and it is not allowed to exceed this limit because of the transparent plexiglas test pipe.

Two equal pressure transmitters mounted 2 meters below the horizontal test pipe, measure the differential pressure over two distances. Rubber hoses connect the transmitters to the test pipe. The rubber hoses are always filled with water. The transmitter PDT-120 measures the differential pressure over a length of 10.22 m, while transmitter PDT-121 measures over 5.38 m. The model of the pressure transducer is Rosemount 3051CD. Further analysis of the experiments presented later in this thesis uses the short-range transmitter (PDT-121). A computer logs the pressure drop every third second.

A thermocouple instrument logs the temperature, which is located in the 3-in. stainless steel-pipe down streams of the test pipe. There is no regulation of the temperature, but only small variations in the temperature are measured during the experiments at a specified water cut. The temperature can vary between different water cuts with approximately 6 °C in the temperature range of 15-27°C. The temperature variations depend on the ambient temperature and the time between water replacement and experimental start. Since a temperature increase from 15 to 27°C in turbulent single-phase oil flow at 1 m/s lowers the pressure gradient only by 1% the temperature changes is assumed to be negligible in two-phase flow.

3.3 Accuracy of turbine meters and dp cells

Table 3.4 indicates the instrumental accuracy of the turbine meters and dP cells. The accuracy is depended on both the transmitter and the logging (I/O signal convertor). The total accuracy can be derived from Eq. (3.1), where the absolute error in the transmitter and logger are added. The error in logging is equal to ±0.06%.

$$d(x) = \left|dx_{transmiter}\right| + \left|dx_{\log ging}\right| \ [\%] \qquad (3.1)$$

As an example (see Table 3.4), the total accuracy for flow meter FT-109A, is equal to ± 0.36% of the span (533 l/min), which equals ± 1.9 l/min. The turbine meters were calibrated by a Coriolis mass flow meter, which is shown in Appendix 7 and 8. For the dP cell, PDT-120, the total accuracy is equal to ± 0.16% of the span (100 mbar), which equals ±0.16 mbar. These deviations are valid within the instrumental range, so if the instruments operate outside

the instrumental range the deviations are larger and unknown.

Table 3.4 Total instrumental deviations.

Parameter	**Instrument tag number**	**Range**	**Transmitter accuracy [%]**	**Logging [%]**	**Total**
Volume flow	FT-109A FT-114A	53-533 l/min	± 0.3	± 0.06	± 0.36% of 533 l/min = **± 1.9 l/min**
Long diff. pressure	PDT-120	0-100 mbar	± 0.1	±0.06	± 0.16% of 100 mbar = ± **0.16 mbar**
Short diff. Pressure	PDT-121	0-50 mbar	± 0.1	±0.06	± 0.16% of 50 mbar = **± 0.08 mbar**
Temp.	TT-123	0-1300°C	±0.75 (of 333°C)	±0.01 (of 1300°C)	0.75% of 333°C + 0.01% of 1300°C = **± 2.6°C**

3.4 Verification experiments and analysis

Preliminary single-phase experiments were performed as a part of the verification of the flow facility and instrumentation. Experiments with single-phase water and oil in horizontal and inclined flow were conducted to verify the pump, differential pressure transmitters, and volumetric flow instrumentation and laser Doppler Anemometer specifications. All the parameters used in the verification experiments are listed in Table 3.1.

3.4.1 Pump speed vs. volumetric flow rate

To verify the pump specifications from the suppliers, single water and oil phase experiments were done to check that the volume flow rates were linear with respect to the pump speed for the positive displacement oil pump and water eccentric screw pump. The frequency transformers measure the pump speed (rpm) and the turbine flow meters FT-114A and FT-109A measure the volume flow rates. A high degree of linearity in the operating range of the pumps will also serve as verification of the flow meters. From Figure 3.9 it is shown that the experiments follow a linear path as expected for the volumetric oil and water pumps. The results are in accordance with the given data from the suppliers.

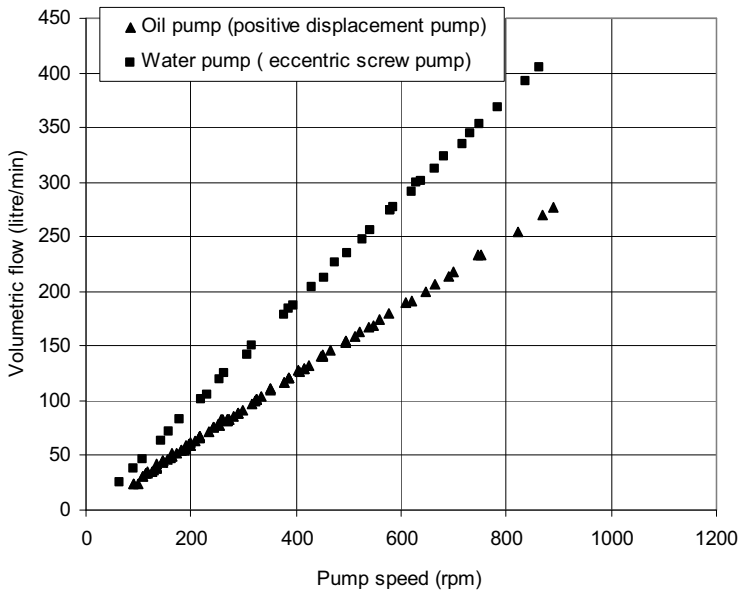

Figure 3.9 Volumetric flows vs. pump speed.

3.4.2 Experimentally obtained friction factor vs. models

In the verification of the differential pressure transmitters (PDT-120, PDT-121) and the turbine meters (FT-114A and FT-109A) the pressure drop and volume flow in single-phase oil and single-phase water flow are measured. The experimental friction coefficient can be calculated from the measured pressure drop, $\frac{dp}{dx}$, and fluid velocity, U, as shown in Eq. (3.2). In Eq. (3.2) U is the bulk velocity of the flow calculated from the measured volumetric flow rate divided by the cross section flow area. The friction factor f is the Darcy friction factor. The experimental friction factor is compared with three different friction factor in a friction factor vs. Re number plot.

$$f = \frac{D}{\frac{1}{2}\rho U^2}\frac{dp}{dx} \tag{3.2}$$

The friction factor correlations used are Blasius [Kays and Crawford (1993)], Haaland (1983) and a correlation that closely fits the Kármán-Nikuradse equation [Kays and Crawford (1993)]. The three friction correlations are given by Eqs. (3.3), (3.4) and (3.5) and they presume fully developed turbulent flow. The first friction factor is the classical Blasius

friction factor given by

$$f = 0.312\,\mathrm{Re}^{-0.25} \tag{3.3}$$

The correlation of Blasius is known to fit experimental data well for Re between 10000 and 50000 and when the wall roughness is equal to that of smooth pipes. The next correlation is the Haaland (1983) friction factor given by

$$\frac{1}{\sqrt{f}} = -1.8\log\left(\frac{6.9}{\mathrm{Re}} + \left(\frac{e}{3.7D}\right)^{1.1}\right) \tag{3.4}$$

The coefficient of Haaland is valid for Re between 4000 and 10^8. The roughness parameter, e, used for the present experiments, is 10 μm.

Eq. (3.5) is a correlation that closely fits the Kármán-Nikuradse equation (i.e. it is a correlation that is more convenient to use than the Kármán-Nikuradse equation, which requires an iterative solution procedure) and is valid for Re between 30000 and 1000000 [Kays and Crawford (1993)].

$$f = 0.184\,\mathrm{Re}^{-0.20} \tag{3.5}$$

The experimental data for horizontal and inclined single-phase water and oil flows are compared with the three friction factors correlations and are presented in Figure 3.10 to Figure 3.12. The comparison in Figure 3.10 shows that the experiments in horizontal single-phase water flow fit the Blasius, Haaland and Kármán-Nikuradse correlations well. The Re number varies between 19800 and 79000, corresponding to a water flow between 53 l/min and 216 l/min. The experimental data deviates from 0.1 to 1.9% from the Kármán-Nikuradse correlation in the validated Re range (85 to 216 l/min). The Blasius correlation can be used to validate the experiments at low flow rates, since the correlation is valid for lower Re numbers. The comparison between experimental friction factor and Blasius correlation shows that the deviations are equal to 4.8 and 2.5% at flow rates equal to 53 and 55 l/min. The larger deviations at lower flow rates are probably because the flow rate and pressure drop is close to the lower limit of the instrumental range.

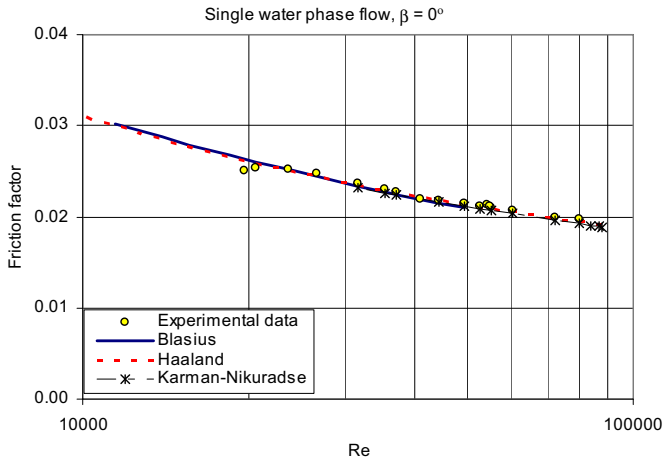

Figure 3.10 Single-phase horizontal flow of water (PDT-121).

Figure 3.11 shows that the experimental friction factor fits the Blasius, Haaland and Kármán-Nikuradse correlations well for oil flow with Re between 10400-36100, which corresponds to a flow between 57 l/min and 200 l/min. The Haaland correlation matches the experimental data best, with a deviation between 0.8 to 2.8% to from the experimental data.

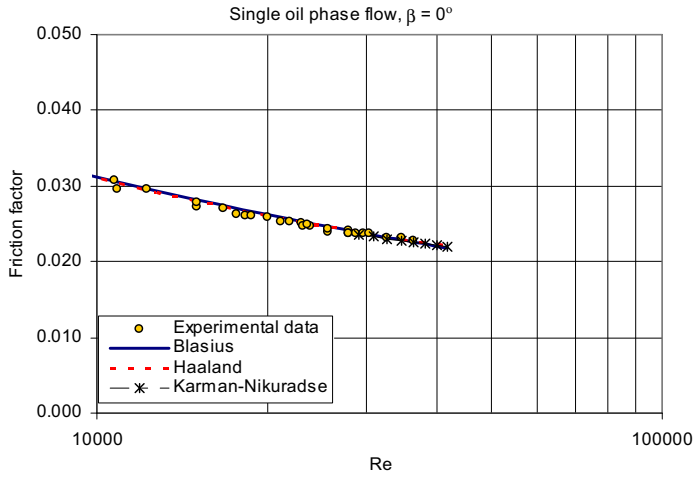

Figure 3.11 Single-phase horizontal flow of oil (PDT-121).

When running single-phase oil and two-phase experiments the impulse hoses have to be filled with water at all times. There is no membrane to keep the phases in the test pipe and in the impulse lines separate. To verify the differential pressure set up for inclined flow, single-phase oil experiments at -1° are compared with correlations. The measurements are adjusted with the gravitational forces to give only the frictional pressure loss. The equations used are shown in Chapter 5. Figure 3.12 shows only minor deviations between the experiments and correlations in inclined pipe flow. Deviations from Haaland correlation range from 0.3 to 3%.

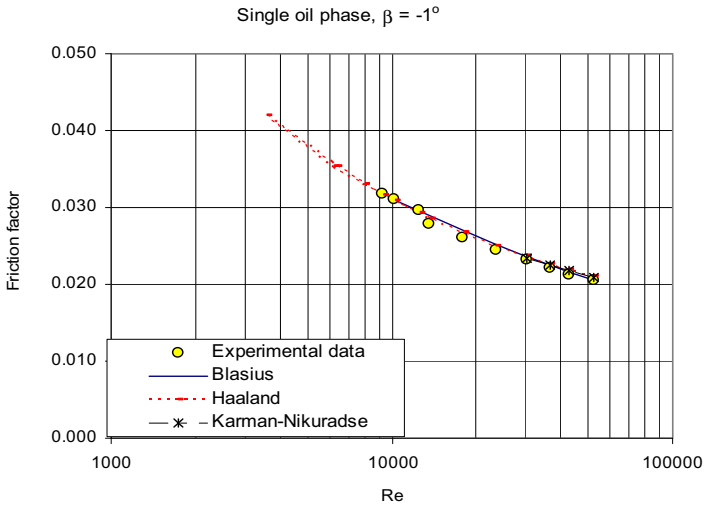

Figure 3.12 Single-phase flow of oil at -1° angle (PDT-121).

The overall conclusion from the pressure drop measurements in single-phase flow in horizontal and inclined pipes is that the experiments show good agreement with friction factor correlations. This means that the pressure drop and flow rate measurements are satisfactory.

3.4.3 Nature of the flow - Laminar or turbulent

Reynold (1883) states that the transition from laminar to turbulent flow takes place at a critical number equal to approximately 2300 as shown in Eq. (3.6). Where U is the bulk velocity, D is the inner diameter and μ is the dynamic viscosity.

$$\mathrm{Re}_{crit} = \left(\frac{\rho U D}{\mu} \right)_{crit} \approx 2300 \tag{3.6}$$

The onset of turbulence, at the critical Reynolds number, depends particular on the conditions of the pipe entrance and in the approach to it. The Re_{crit} has been measured up to 40 000 by Ekman (1910) when the entrance was free from disturbances. Different experiments also reveal a lower Re_{crit} limit of about 2000. Below this Reynolds number, the flow remains laminar regardless of the size of the disturbances [Shlichting and Gersten (2000)]. Incropera and DeWitt (2002) claim that the critical Reynolds number normally lies between 2300 and 10 000. The range in Reynolds number where the transition from laminar to turbulent flow occurs is often called the intermittent region. The transition from laminar to turbulent flow is not a sudden process, but composed of a number of developing steps, where the flow is occasionally laminar and occasionally turbulent.

Since the lowest Reynolds number in present study in single-phase water and oil is equal to 19 800 and 10 700 an additional analysis has been executed. A possible method to find out whether the flow is turbulent or laminar is to compare the experimentally obtained friction factors with turbulent frictional correlations, as was done in section 3.4.2. The good agreement in previous section indicates that the flow is turbulent. The mixing unit in present study prior to the test section will introduce disturbances in the flow and hence according to Reynold (1883) the Re_{crit} will decrease. The turbulence level can also be found by comparing the measured velocity profiles with laminar and turbulent correlations. Figure 3.13 shows the difference between a turbulent and laminar flow by comparing the measured velocity profile in present study at 1.03 m/s with a parabolic profile and the power law. The measured velocity profile does not follow a parabolic trend, which is characteristic for laminar flow. The parabolic equation describing the local laminar velocities (u) is shown in Eq. (3.7), where U is the mean velocity, R is the inner radius of the pipe and z is the vertical position. The turbulent velocity profile can be calculated from the one seventh power law which where originally estimated from pipe flow data [Shlichting (1979)]. The $1/7^{th}$ power law is expressed in Eq. (3.8). The maximum velocity is the centre velocity in the LDA measurements and equal to 1.23 m/s. The measured velocity profile fits the power law well, which confirms that the flow is turbulent at 1.03 m/s.

$$u = 2 \cdot U\left(1 - \left(\frac{z}{R}\right)^2\right) \tag{3.7}$$

$$u = u_{\max}\left(1 - \frac{z}{R}\right)^{1/7} \tag{3.8}$$

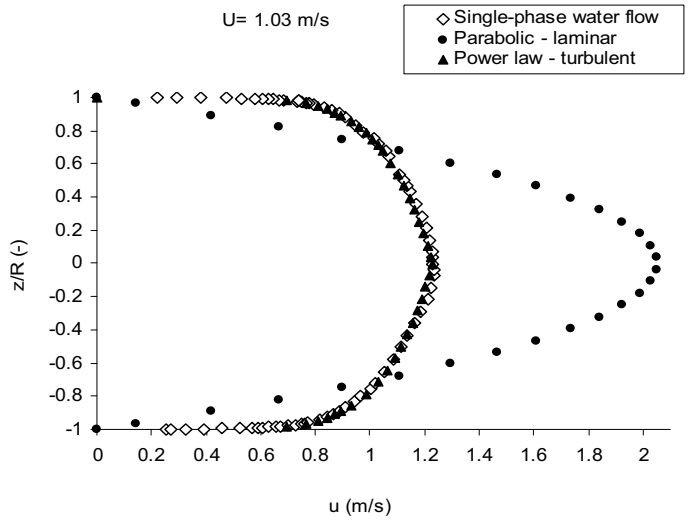

Figure 3.13 Water velocity profiles obtained from experiments and from parabolic and power law equations at a bulk velocity of 1.03 m/s.

3.4.4 Entry length - Single-phase flow

The flow is fully developed when all mean flow quantities (i.e. pressure gradient and velocity profile) and turbulence quantities (i.e. velocity fluctuations and cross-moments) are no longer changing with the pipe length. The distance from the entrance at which this condition is achieved is termed the entry length. Figure 3.14 illustrates the entry length in laminar flow. The flow is fully developed when the velocity profile is constant with the pipe length and the velocity profile has a parabolic profile. A boundary layer starts to grow at the pipe entrance and the flow is fully developed when the boundary layer height equals the pipe radius.

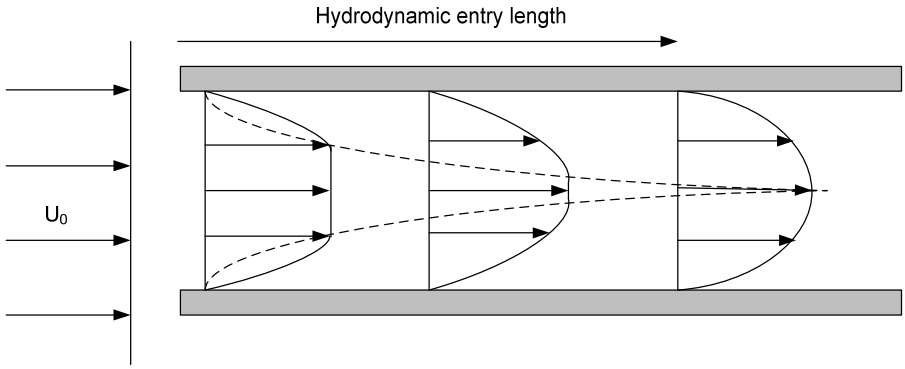

Figure 3.14 Development of velocity profile in laminar flow.

The most precise way to determine if the flow is fully developed is by conducting a series of measurements along the pipe length. When the measurements are constant along the length of the pipe, the flow is fully developed. Other ways to determine the development of the flow is by model comparison. The models are commonly developed from boundary layer theory, integral method using an assumed velocity profile and empirical correlations [Persen (1972), Langhaar (1942), Sparrow et al. (1964), Shlicting (1934), Shiller (1922) Latzko and Angew (1921)]. Another possibility is to use numerical calculations (CFD). The entry length depends on whether the flow is laminar or turbulent. In general the entry length is much shorter for turbulent flow compared to laminar flow [Kays et al. (2005)].

3.4.5 Model comparison: Turbulent flow

The models of Persen (1972) and Latzko and Angew (1921) can be used to determine the entry length in turbulent flow. Latzko and Angew's (1921) model is used in e.g Kays et al. (2005) and the solution is shown in Eq. (3.9).

$$\left(\frac{L}{D}\right)_{turbulent} = 0.623 \cdot \mathrm{Re}^{0.25} \tag{3.9}$$

Where L is the necessary distance from the mixing unit to the point in the test pipe to achieve fully developed flow, D is the inner diameter of the pipe and Re is the Reynolds number. Both the entry lengths of Latzko and Angew (1921) and Persen (1972) are shown in Figure 3.15. The Reynolds number in present study varies from approximately 10^4 to 10^5. According to Latzko and Angew's (1921) model the entry length necessary to achieve fully developed flow

in present study is 11D and according to Persen's (1972) model the length is 38D at Re number equal to 10^5.

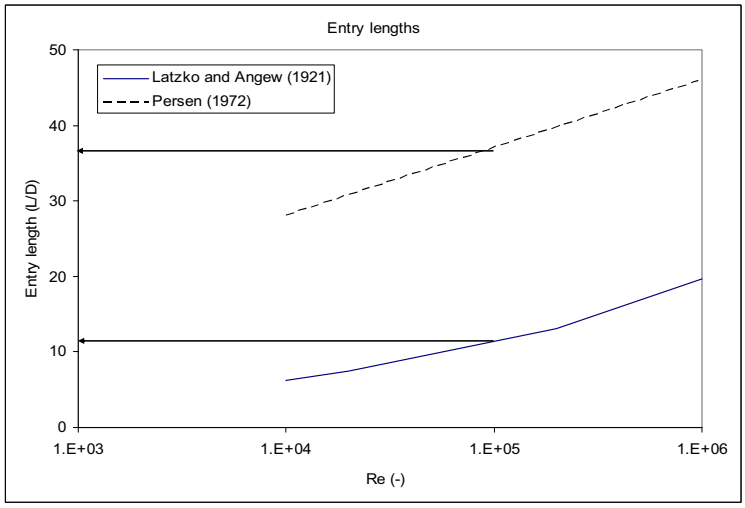

Figure 3.15 Entry lengths.

Doherty et al. (2007) studied the development of turbulent flow and found that the entry length is depending on the criteria chosen for achieving fully developed flow. Doherty et al. (2007) found that the mean velocity profile required approximately 50D to become invariant and that the higher order statistics needed an entrance length of 80D. Looking at large scale features of turbulence the entry length was even further increased. The large scale eddies are often termed hairpins. The models of Latzko and Angew (1921) and Persen (1972) predict a lower entry length compared to that of Doherty et al. (2007). Latzko and Angew (1921) model predicts an entry length equal to 11D and Persen (1972) model predicts an entry length of 38D (see Figure 3.15). The entry lengths were found at Re $\approx 10^5$. Table 3.5 gives an overview of the predictions by Latzko and Angew (1921) and Persen (1972) and measurements by Doherty et al. (2007) at Re $\approx 10^5$, together with the entry lengths in present study. As Table 3.5 shows, the concluding remark from the Latzko and Angew (1921) predictions is that all instrumentation in the test section is located in the fully developed region. According to Persen (1972) and Doherty et al. (2007) the pressure transducer (PDT-120) with the shortest entry length (15 D) is not in the fully developed region, while the PDT-121 and the LDA sections are.

Table 3.5 Entry lengths by Latzko and Angew (1921), Persen (1972), Doherty et al. (2007) and present study.

	Entry length [-] Pressure drop, velocity	**Entry length [-] Higher order statistics**	**Entry length [-] Large eddy structure**
Latzko and Angew (1921)	11		
Persen (1972)	38		
Doherty et al. (2007)	50	80	>80
Present rig, PDT-120	15		
Present rig, PDT-121	101		
Present rig, LDA	163	163	163

The pressure gradient in single-phase oil flow in the test pipe is predicted by use of computational fluid dynamics[†]. The input parameters used in the simulations are shown in Table 3.6. The mean velocity of oil is equal to 1 m/s, which equals a Reynolds number of 10^5. Course and fine grid gave equal results.

Table 3.6 Parameters used in CFD simulations.

Turbulence model	**Grid**	**Inlet velocity**
Realizable turbulent kinetic energy and dissipation model (rke), wall functions	Course[1], fine[2]	1 m/s

[1] 1000 cells, 10 cells across pipe diameter (equally spaced)

[2] 64000 cells, 64 cells across pipe diameter (growing with a factor of 10 across the radius)

Figure 3.16 shows that the local pressure gradient is constant in the flow direction after approximately 50D with only minor variations after 20D. However, during the boundary layer development, the pressure gradient has a region with a lower value than the asymptotic. Scaling the y-axis to a smaller pressure gradient range as shown in Figure 3.17 the under shoot in pressure gradient is clearly seen. Reichert and Azad (1976) and Klein (1981) measured that the development of the mean velocity field for a turbulent flow in the entrance of an axis symmetric pipe in non-asymptotic. Regions with undershoot and overshoot were observed in the developing region. Wang (1999) predicted an overshoot in the axial mean velocity by using three different models.

[†] Computational fluid dynamics software (CFD): Fluent 6.3

Since the experimental pressure gradient entry length (101 D, Table 3.5) is larger than shown by the CFD calculations, the flow is most likely fully developed in pressure transducer PDT-121 measurements. The good comparison between empirical friction factors and experimental data in Figure 3.10 and Figure 3.11 also strongly implies a fully developed in the shortest test section (PDT-121).

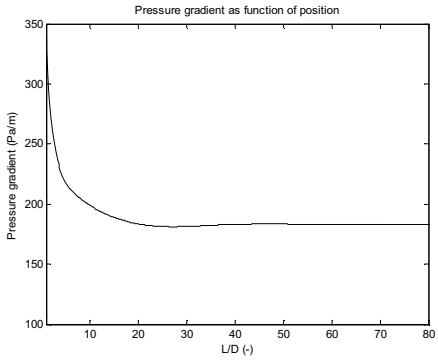

Figure 3.16 Pressure gradient vs. entry length (L/D) from CFD calculations.

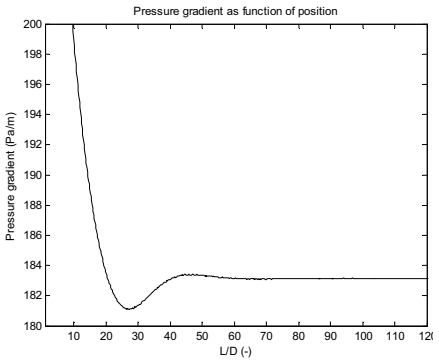

Figure 3.17 Pressure gradient vs. entry length (L/D) from CFD calculations.

Figure 3.18 shows that the pressure gradients obtained in the two sections is comparable. The pressure gradient with the longest entry length (PDT-120) is 3.3 % lower than the one with the shortest entry length (PDT-121) at the highest flow rates. The deviation decreases with decreasing flow rates. This could be explained by the region with the lower pressure as shown in Figure 3.17. Another possible reason to the difference in measured pressure gradients (PDT-120 and PDT-121) could be due to differences in the experimental set-up. Small differences in the entrance to the impulse lines as the diameter or angle of the pressure tapping holes could cause the deviations observed.

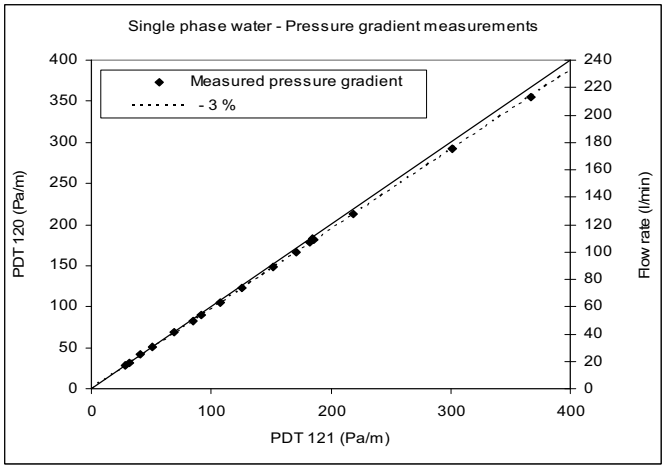

Figure 3.18 Pressure gradients as function of flow rate for single-phase water flow.

3.4.6 Entry length - Two-phase flow

Determining the entry length for two-phase flow is far more complex than for single-phase flow. In two-phase flow one must take the interfacial effects into consideration when determining the entry length. This can only be done by studying the flow development by conducting measurements along the pipe length, e.g. pressure measurements and phase distributions. Hussain et al. (2008) measured the phase fraction distribution with the beam traversed in three directions (0°, 45° and 90°) at three different positions (1.0 m, 5.85m and 7.72 m) along the pipe. They showed that the flow developed from a stratified flow in the beginning to a uniformed dispersed flow at the end of the pipe (7.72 m) at a mixture velocity of 2.76 m/s. Initially the flow was stratified due to the introduction of the oil at the top and water at the bottom of the pipe. The experiments were conducted in a horizontal 25.4 mm stainless steel pipe using Exxsol-D80.

3.4.7 Steady state conditions in single-phase flow

A system is at steady state when the flow properties are unchanged in time. One possible way to determine if the flow has reached steady state condition is to calculate the standard deviations of measured flow properties. If the standard deviations are small and close to the accuracy of the instruments, the flow is most likely at steady state condition. The standard deviations to the measured flow rates and pressure drops are calculated by using Eq. (3.10), where N is the number of measurements and x is the measured parameter.

$$STD = \sqrt{\frac{1}{N}\sum_{i=1}^{N}(x_i - \bar{x})^2}, \quad \bar{x} = \frac{1}{N}\sum_{i=1}^{N} x_i = \frac{1}{n}(x_1 + \cdots + x_n) \tag{3.10}$$

The standard deviations in the pressure drop, flow rate and temperature are calculated in Table 3.7. The standard pressure drop deviations using the water centrifugal pump and positive displacement oil pump are calculated for flow rates from 56 to 200 l/min. The pressure drop was logged every fourth second for four minutes. Since the standard deviations in volume flow, pressure drop and temperature are smaller than the accuracy of the instruments, the flow is most likely at steady state condition.

Table 3.7 Standard deviations for single-phase flow.

Measurement	**Pump**	**Standard deviations**	**Instrument accuracy**
Volume flow (FT-114A)	Water, centrifugal	0.3 – 1.2 l/min 0.2 –1.2 %	± 1.9 l/min
Volume flow (FT-109A)	Oil, (P-100)	0.3 – 0.7 l/min 0.3 – 0.7 %	± 1.9 l/min
Short diff. pressure (PDT-121)	Water, centrifugal	0.03 – 0.08 mbar 0.6 – 2%	± 0.16 mbar
Short diff. pressure (PDT-121)	Oil, (P-100)	0.03 – 0.08 mbar 0.4 – 5 %	± 0.08 mbar
Temperature (TT123)	-	0.01 – 0.02 °C 0.05 – 0.1%	±0.25°C

3.4.8 Steady state conditions in two-phase flow

The standard deviations in pressure drop, volume rates and temperature for two-phase horizontal flow are shown in Table 3.8. The standard deviations in volume flow are lower than the instrumental accuracy, but the deviations in pressure drop are slightly higher than the instrumental accuracy. However, since the standard deviation in measured pressure drop is close to the accuracy of the instrument, the flow is assumed to be at steady state condition.

Table 3.8 Standard deviations for two-phase flow.

Measurement	**Pump**	**Standard deviations**	**Specific Instrument accuracy**
Volume flow (FT-114A)	Water, centrifugal	0.4 – 0.9 l/min 0.4 – 3.9 %	± 1.9 l/min
Volume flow (FT-109A)	Oil, (P-100)	0.4 – 0.8 l/min 0.45 – 4.6 %	± 1.9 l/min
Short diff. pressure (PDT-121)	Oil, (P-100) & Water, centrifugal	0.04 – 0.28 mbar 0.6 – 1.9 %	± 0.08 mbar
Temperature (TT123)	-	0.013 – 0.019 °C 0.06 – 0.1%	0.25°C

3.4.9 Comparison of LDA velocity profile and turbine meter measurements

Figure 3.19 presents the LDA measurements of the axial velocity in single-phase water and single-phase oil flows. The velocity profiles presented are measured in horizontal pipe flow at a volume flow of 149 l/min, corresponding to a bulk velocity of 1.03 m/s inside the plexiglas.

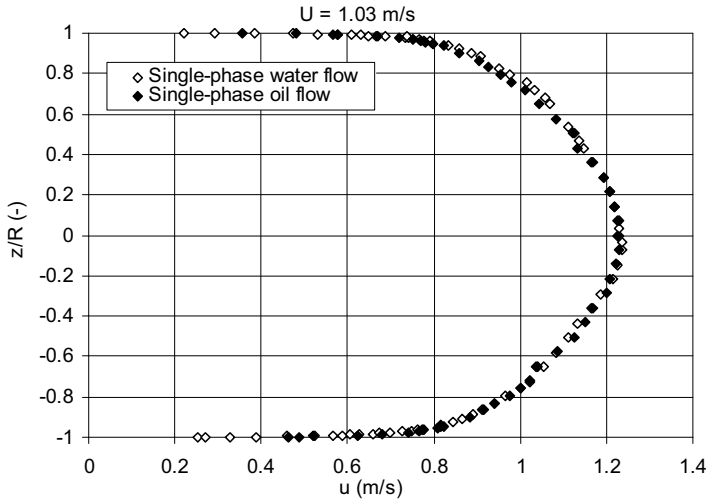

Figure 3.19 Axial velocity profiles for single-phase flows of water and oil at a bulk velocity of 1.03 m/s.

The velocity profiles for single-phase water and single-phase oil flow are integrated over the entire cross section of the pipe, from the centre to the inner radius of the pipe. This is based on the upper and lower part of the pipe. The total flow rate is then an average of the flow rate from upper and lower part of the pipe. The integration of the velocity profile is shown in Eq. (3.11).

$$Q = \int_{r=0}^{R} u(R) 2\pi \, R dR = 2\pi \sum_{i=1}^{i=N} u_i R_i \Delta R_i \tag{3.11}$$

Where u is the measured time average velocity and R is the inner pipe radius. The resulting volume flows from the LDA measurements are then compared with the flow rate measured by the turbine meters and the deviations are calculated by

$$\Delta Q = \frac{(Qreadings - Q\,\mathrm{int}\,egrated)*100\%}{Q\,\mathrm{int}\,egrated} \tag{3.12}$$

The results from the comparison of the flow meter reading and LDA measurements are presented in Table 3.9. For single-phase water flow the flow rate measured by the turbine meters is 0.5 % lower than the flow rate obtained from the integrated velocity profile and for the single-phase oil flow the flow rate measured by the turbine meters is 0.1 % higher than the flow rate obtained from the integrated velocity profile. The difference between the flow rate measured by the turbine meters and the flow rate obtained from the integrated velocity profile is small and well within the accuracy of the turbine meters.

Table 3.9 Comparison of flow meter reading and LDA measurement.

	Water flow rate	**Oil flow rate**
Flow meter reading (l/min):	145.1± 1.9 (1.3%)	146.3 ± 1.9 (1.3%)
Integrated velocity profile (l/min):	145.8	146.2
Deviation (l/min):	-0.7	0.1
Deviation, ΔQ (%):	-0.5	0.1

3.5 Summary

A horizontal flow facility for oil and water flow was re-built to study the differential pressure drops, local velocities and local volume fractions in inclined pipes. Experimental analysis of both single-phase and two-phase experiments is conducted to verify the basic instrumentation in the facility and to indicate whether the flow is fully developed and at steady state condition.

- A new two-phase inclinable flow facility was successfully built and accurate measurements were achieved.
- The high degree of linearity of volume flow vs. pump speed for the positive displacement water pump and eccentric screw oil pump verifies the pump specifications (Figure 3.9).
- The pressure drop and volume flow measurements are presented in a friction coefficient versus Reynolds number diagram. The results show that the measurements follow the models and serve as a verification of the turbine meters and differential pressure transducers in horizontal and inclined pipes (Figure 3.10, Figure 3.11 and Figure 3.12).
- Doherty et al. (2007) experimental work together with the models of Latzko and Angew (1921) and Persen (1972) and CFD model imply that the flow is fully developed before the flow enters pressure section PDT-121.
- Experiments conducted by Doherty et al. (2007) indicate that the LDA measurement section, where the velocity and turbulence profiles are measured, are in the fully developed flow region.
- Good agreement between correlations like e.g Blasius and Haaland and experimental data indicates good measurement accuracy and that the flow is fully developed flow.
- The low standard deviations in pressure drop, flow rate and temperature in Table 3.7 and Table 3.8 indicate that the single-phase and two-phase flow is at steady state condition.
- The integration of the velocity profile from the LDA measurements shows good agreement with the turbine meters measurements (Table 3.9).

4 GAMMA DENSITOMETRY

The gamma ray technique is widely used in both multiphase flow experiments [Froystein et al. (2005), Elseth (2001), Soleimani (1999) and Johnson (2005)] and in offshore pipelines and enables measurements of the local oil and water fractions.

4.1 Theory of single gamma ray attenuation technique

In the range of energies in the electromagnetic spectrum, gamma radiation is at the high-energy, short-wavelength end of this spectrum. The gamma particles can penetrate paper, aluminium, and lead. Since the gamma particles can penetrate through all three solids makes it very useful in measurement of multiphase pipe flow. The difference between X-ray and gamma rays is that the gamma rays usually have a shorter wavelength and that the X-ray is emitted by electrons outside the nucleus, while gamma rays are emitted by the nucleus.

The principle in the single gamma ray attenuation technique is that a homogenous material will absorb a monochromatic beam of constant intensity and short wavelength radiation. The gamma beam consists of gamma ray-photons and the gamma energy is the energy of these photons. Eq. (4.1) shows the law of attenuation. The number of photons (n) that are absorbed by a material are proportionally to the thickness of the material (x) and the number of incident photons (n_0). The proportionally constant is the linear attenuation coefficient (γ). The attenuation coefficient depends on the density and elemental composition (Atomic number A_m) of the material. Bouguer (1929) discovered the attenuation of light, but the law of attenuation is commonly known as the Lambert-Beers law.

$$n = n_0 \exp(-\gamma x) \tag{4.1}$$

In pipe flow measurements, the radiation is collimated to produce a beam. The beam is attenuated through the pipe walls and the fluids inside the pipe and goes through the detector collimator before it reaches the detector. The detector system counts the number of photons in a certain interval of time and refers to the counting rate of the system, I = Number of counts (n) /Measurement time (T). Dividing Eq. (4.1) with time gives Eq. (4.2), where I (1/s) is the transmitting intensity of the gamma ray beam and I_0 (1/s) is the source intensity. μ_{ab} (m^2/kg) is the mass absorption coefficient of the material, which is a function of the material and the energy of the gamma photons. ρ (kg/m^3) is the density of the material, $\gamma = \mu_{ab}\rho$ (1/m) is the

linear attenuation coefficient, and x (m) is the distance traversed through the material. For a two-phase system, only one gamma energy is needed, but for three-phase flow, a two-energy gamma must be used to be able to distinguish between gas, oil and water.

$$I = I_0 \exp(-\mu_{ab} \rho x) = I_0 \exp(-\gamma x) \tag{4.2}$$

In the experiments, the beam passes through three materials, the pipe wall, the oil phase, and the water phase. The absorption of the gamma ray beam in air is neglected in present study, since the absorption in air is very small compared with the three other materials. The gamma ray intensity is a measure of the number of photons per unit time, and gamma ray energy is the total energy of each photon in the gamma ray beam. The expression for the transmitting intensity for the three materials wall, fluid 1 and fluid 2 is shown in Eq. (4.3), where I_0' is the initial intensity in air. The mass absorption coefficient (μ_{ab}) and the attenuation coefficient (γ), can be found from published data sources like Grodstein (1957), Pan (1996) or XCOM: Photon Cross Sections Database (Berger et al. (2007)). Another way to determine the attenuation coefficients is by calibration, which is shown in section 4.3.

$$\begin{aligned} I &= I_0' \exp(-\mu_{ab,wall} \rho_{wall} x_{wall} - \mu_{ab,1} \rho_1 x_1 - \mu_{ab,2} \rho_2 x_2) \\ &= I_0' \exp(-\gamma_{wall} x_{wall} - \gamma_1 x_1 - \gamma_2 x_2) \end{aligned} \tag{4.3}$$

The attenuation coefficient γ depends upon the composition of the absorber and is a function of the photon energy. It is related to the total atomic absorption cross section as shown in Eq. (4.4), where N_A ($6.022 \cdot 10^{23}$) is the Avogadro number, A_m ([kg/kmol) is the atomic mass number, ρ (kg/m^3) is the absorber density and σ_a (m^2/kmol) is the atomic absorption cross section.

$$\gamma = \mu\rho = \frac{N_A \rho}{A_m} \sigma_a \tag{4.4}$$

The effect of the wall can be calculated from Eq. (4.5). The initial transmitted intensity, I_0', is reduced due to absorption in the wall, when the pipe is filled with air.

$$I_{pipe} = I_0^{'} \exp(-\gamma_{wall} x_{wall}) \tag{4.5}$$

The measured transmitted intensity (I) when the pipe wall, fluid 1 and fluid 2 has absorbed the beam can then be calculated by using the initial transmitted intensity (I_{pipe}) in Eq. (4.5). The calculation of the transmitted intensity (I) is shown in Eq. (4.6).

$$I = I_{pipe} \exp(-\gamma_1 x_1 - \gamma_2 x_2) \tag{4.6}$$

Since there are two unknowns (x_1 and x_2) in Eq. (4.6) an expression of the fraction of fluid 1 and 2 has to be implemented. Figure 4.1 shows that the length of the two phases can be expressed as in Eq. (4.7), when neglecting the beam thickness. H is the local pipe height between the walls at the measurement positions. In present study the beam is assumed infinitely thin.

$$x_1 + x_2 = H \tag{4.7}$$

The volume fraction of water is a function of the measured density (ρ_m) and the density of oil (ρ_o) and water (ρ_w) as shown in Eq. (4.8).

$$\varepsilon = \frac{\rho_m - \rho_o}{\rho_w - \rho_o} \tag{4.8}$$

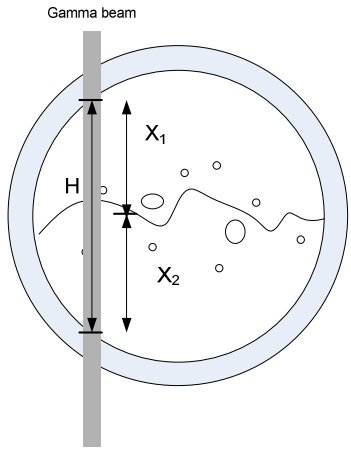

Figure 4.1 Gamma theory.

The phase fractions can then be expressed as in Eq. (4.9) by combining Eqs. (4.6) and (4.7)

$$\varepsilon_1 = \frac{x_1}{H} = \frac{\ln\left(\frac{I_0}{I}\right)/H - \gamma_2}{(\gamma_1 - \gamma_2)} \qquad (4.9)$$

$$\varepsilon_2 = 1 - \varepsilon_1$$

where ε_1 and ε_2 are the local phase fractions of fluid 1 and 2. The mass absorption coefficient for air, oil, water, aluminium and iron has been curve-fitted by Pan (1996) to obtain a relationship between the coefficients and the energy of the source. The mass absorption coefficient for oil and water are presented in Eqs. (4.10) and (4.11), where E (keV) is the gamma energy.

$$\mu_{ab,oil} = 0.1\exp(-14.794762 + 89.049017\ln\ln E - 164.299552(\ln\ln E)^2 + 131.5987(\ln\ln E)^3 - 48.73664(\ln\ln E)^4 + 6.813107(\ln\ln E)^5) \qquad (4.10)$$

$$\mu_{ab,water} = 0.1\exp(-60.439566 + 261.844766\ln\ln E - 408.63705(\ln\ln E)^2 + 296.81687(\ln\ln E)^3 - 102.856866(\ln\ln E)^4 + 13.736626(\ln\ln E)^5) \qquad (4.11)$$

The mass absorption coefficients are calculated for the present study and are presented in Table 4.1 together with the source energy and densities used as input to Eqs. (4.10) and (4.11). The calculations are comparable with the values from the XCOM's database.

Table 4.1 Input parameters.

Parameter	**Value**
E	59.5 keV
Density water	1000 kg/m^3
Density oil	790 kg/m^3
Density wall (PP-crystalline)	946 kg/m^3
Water mass absorption coefficient ($\mu_{ab,\ water}$). Calculated by use of Eq. (4.11)	0.0203 m^2/kg
Oil mass absorption coefficient ($\mu_{ab,\ oil}$). Calculated by use of Eq. (4.10)	0.0194 m^2/kg
Wall mass absorption coefficient (μ_{wall}). Berger et al (2007)	0.0188 m^2/kg

4.2 Advantages and disadvantages

The advantages and disadvantages with use of gamma ray to measure phase distributions are listed below:

Advantages:

- Non-intrusive
- Accurate
- Good repeatability
- Not time consuming (compared to QCV (quick closing valves))
- Can be applied directly in production systems
- Can measure phase profiles in gas, oil and water
- Easy available
- Large capability of achieving wide range of penetration depths

Disadvantages:

- Harmful radiation
- Time consuming in certain cases (tomography)
- Needs calibration
- Usually affected more by high atomic number solids in the beam path, than by relatively low atomic number fluid (water-steam mixtures). This can lead to poor sensitivity in applications like two-phase flow through bundles of pipes.

4.3 Calibration

When calibrating with oil and water no information about the mass absorption coefficient (μ_{ab}) and the initial energy (I_{pipe}) is needed to calculate the water holdup. Calibrating a system with oil and water flowing inside a pipe means to experimentally obtain the linear attenuation coefficient (γ) for fluid 1 and 2. This is usually done when the attenuation coefficient for the wall is unknown. The linear attenuation coefficients are required as input when designing a new gamma system and when executing error calculation. The first step is to fill the pipe with fluid 1. The transmitted intensity (I_1) is measured when the pipe is filled with fluid 1 and the initial transmitted intensity (I_{pipe}) is measured with pipe filled with air. Eq. (4.12) is used to calculate the linear attenuation coefficient (γ_1)

$$\gamma_1 = \frac{\ln\left(\frac{I_{pipe}}{I_1}\right)}{x_1} \tag{4.12}$$

The second step is to fill the pipe with fluid 2, which gives the attenuation coefficient γ_2 as expressed in Eq. (4.13).

$$\gamma_2 = \frac{\ln\left(\frac{I_{pipe}}{I_2}\right)}{x_2} \tag{4.13}$$

The third step is to find the attenuation coefficient for the wall (γ_w). This can be derived by measure the initial energy in air ($I_0^{'}$) and the transmitted energy through the pipe filled with air (I_{pipe}) from Eq. (4.5).

$$\gamma_{wall} = \frac{\ln\left(\frac{I_0^{'}}{I_{pipe}}\right)}{x_3} \tag{4.14}$$

By substituting Eqs. (4.12) and (4.13) into Eq. (4.9) the water fraction can be calculated as shown in Eq. (4.15), without any knowledge of the wall, fluid 1 and 2 attenuation coefficients. The calculation assumes a thin collimated beam with a un-directional photon flux normal to the test section.

$$\varepsilon_w = \frac{\ln\left(I/I_o\right)}{\ln\left(I_w/I_o\right)} \tag{4.15}$$

I is the measured transmitted intensity in the oil-water flow, I_o is the calibrated intensity for oil and I_w is the calibrated intensity for water. Pan (1996) describes the uncertainty and gives a systematic analysis of the techniques for a single-energy vertically stationary gamma densitometry and two-energy gamma. Elseth (2001) describes the signal processing of the gamma densitometry measurements. For oil and water systems with oil density equal to 865 kg/m^3 and viscosity equal to 0.00164 Pas at 25°C, Pan (1996) shows that it takes 30 seconds to achieve measurement accuracy of 1% using the gamma energy of 59.5 keV. The experimental set-up of Pan (1996) differs from present study in terms of source activity, pipe

diameter, wall thickness and pipe material and the gamma densitometry used in present study includes a traversing device. Since the experimental set-up between Pan (1996) and present study differ, the accuracy of Pan (1996) are not directly applicable to present set-up.

4.4 Measurement accuracy

Accuracy is defined as the closeness of the agreement between the measured value and the true value. The error of measurement is defined as the result of the measurement minus a true value of the measuring.

The evaluation of uncertainty could be done by statistical analysis of a series of measurements or based on scientific judgement using all available information. Available information could be previous measurements, experience, general knowledge of the behaviour and properties of relevant materials and instruments, manufacturer's specifications, data provided in calibration and other certificates or uncertainties assigned to reference data from handbooks [Johansen and Jackson (2004)].

Parameters that influence the uncertainties in gamma measurements are listed below and the system used in present study will be further discussed in the sections below:

- Pulse counting, n [Eq. (4.16)]. Small values of pulse counts will cause large measurement error
- Measurement time (T), calibration and experimental time
- Geometrical arrangements, section 4.4.2
- Liquid length, H (Dependent on inner pipe diameter, beam diameter, beam position and shape of beam). Either a very small or a very large value of H will cause large measurement error [Pan (1996)].
- Wall thickness (x)
- Positioning of the beam (Traversing and zero positioning)
- Shape of beam. This depends on the collimation system, diameter of beam and distance from source to detector.
- Measured phase fractions (ε).
- Fluid properties such as density (ρ) and mass absorption coefficient (μ_{ab}).
- Dynamic effects

Pan (1996) showed that the measurement error increases steeply when the gamma energy approaches zero, because the beam becomes too weak. There exists an optimum energy level dependent on the rig conditions where the error is smallest. Increasing above the optimum value gives only rice to a small increase in measurement error. The upper limit is normally restricted by safety regulations. If the energy is too high, the difference between the transmitted photons and the incident photons becomes too low and hence the measurement error increases. The measurement error is relatively insensitive to the variations in fluid densities, but the smaller the density difference between the fluids are the larger the measurement error is [Pan (1996)].

4.4.1 Pulse counting

All radioisotope intensity measurements are subject to statistical fluctuations in the number of counts due to the random nature of photon or particle emission. The random emission of radiation follows the Poisson and Gaussian distribution when the counting time is short compared to the half-life of the source isotope and when the number of counts are large (n >100). For radioisotope pulse counting (n) the relative standard deviation is inversely proportional to the square root of the number of detected photons (n) as Eq. (4.16) shows [Johansen and Jackson (2004)].

$$\frac{dn}{n} = \pm\frac{1}{\sqrt{n}} = \pm\frac{1}{\sqrt{I \cdot T}} \tag{4.16}$$

Figure 4.2 shows the calculated relative error in pulse counting as function of measurement time in present study. The intensity (I) used is measured to be equal to 12700 counts/s for single-phase oil in the centre line of the pipe. Since the measurement time (T) in the single-phase oil experiments is equal to 30 s, the relative error (Eq. (4.16)) introduced due to pulse counting in the experiments is equal to ±0.0016. Figure 4.2 shows that the largest increase in accuracy is during the first 30 seconds of counter time. Increasing the counter time further gives smaller decrease in error. The counter time will be a balance between accuracy and the time available to execute the experiments.

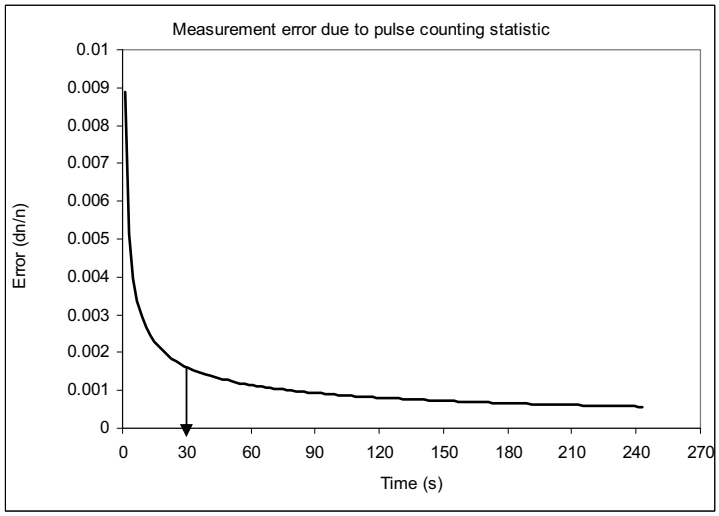

Figure 4.2 Effect of counter time on error.

4.4.2 Geometrical arrangements and dynamic effects

The measurement accuracy will depend on the position of the beam as illustrated in Figure 4.3. The beam position will influence both the liquid length and the thickness of the wall that the beam is attenuated through. In beam position 1 close to the wall, the beam goes through a thicker wall (x_{wall}) and less amount of liquid (H_{liq}) compared to beam position 2. The measurement accuracy is lowest for beam position 1, since $H_{liq1}<H_{liq2}$ and $x_{wall1}>x_{wall2}$.

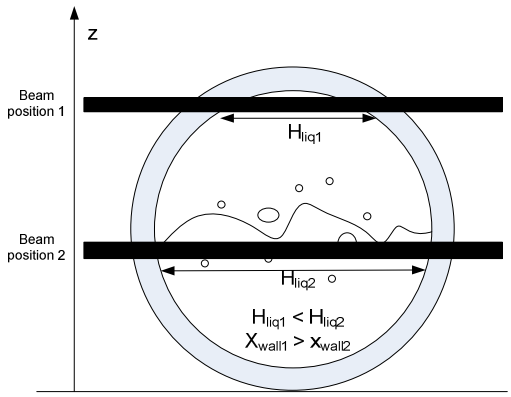

Figure 4.3 Beam positions.

As shown in Figure 4.4, the source collimator is a 3 mm circular slot and the detector collimator is a rectangular slot of 3 mm height and 12 mm width. The beam is coned in axial plane (x,y) and not in radial plane (z,y), since the height of the detector collimator is equal to the height of the source collimator. If the oil and water is not distributed evenly in the x-y plane, e.g. if the water is distributed in the location of the largest measurement volume, the gamma instrument will measure a larger density than the actual density. Uncertainties due to the shape of the beam are considered to be small in present study.

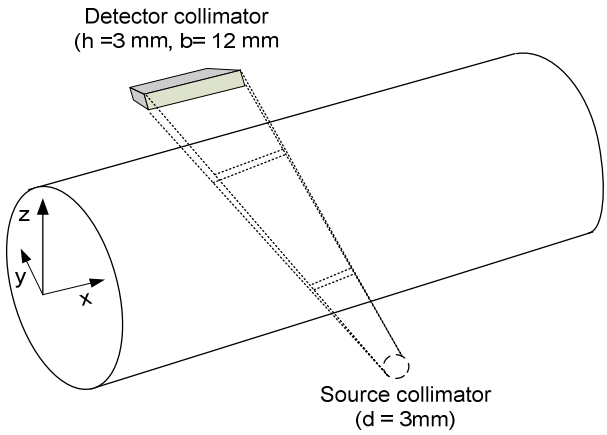

Figure 4.4 Source and detector collimator.

To be able to measure the feature of dynamic flow phenomenon like slugging and waves require a short counting time. A short counting time leads to larger uncertainties in the measurement. The accuracy can improve by increasing the strength of the source beam.

4.5 Error propagation

To find the measurement error in measured phase fractions $d(\varepsilon_w)$ one must find the error in all the variables in Eq. (4.9), which is the errors in I, I_0, γ_1, γ_2 and H. The error contribution due to the shape of the beam in present study is neglected. The error in measured phase fraction can be calculated as shown in Eq. (4.17) and (4.18). Eq. (4.17) shows the total error as the sum of absolute errors in I, I_0, γ_1, γ_2 and H. The errors can also be added according to Pythagorean theorem, as shown in Eq. (4.18), which slightly lower the measurement error.

$$d(\varepsilon_w) = \left|d(\varepsilon_w)_I\right| + \left|d(\varepsilon_w)_{I0}\right| + \left|d(\varepsilon_w)_{\gamma 1}\right| + \left|d(\varepsilon_w)_{\gamma 2}\right| + \left|d(\varepsilon_w)_H\right| \tag{4.17}$$

$$d(\varepsilon_w) = \sqrt{d(\varepsilon_w)_I{}^2 + d(\varepsilon_w)_{I_0}{}^2 + d(\varepsilon_w)_{\gamma_1}{}^2 + d(\varepsilon_w)_{\gamma_2}{}^2 + d(\varepsilon_w)_H{}^2} \tag{4.18}$$

Eq. (4.9) is differentiated with respect to I, I_0, γ_1, γ_2 and H (Appendix 9*).* Johansen and Jackson (2004) do similar approach, where the measurement error in density in a stationary system is calculated.

$$d(\varepsilon_w) = \sqrt{\left(\frac{\partial \varepsilon_w}{\partial I}\right)^2 d(I)^2 + \left(\frac{\partial \varepsilon_w}{\partial I_0}\right)^2 d(I_0)^2 + \left(\frac{\partial \varepsilon_w}{\partial \gamma_1}\right)^2 d(\gamma_1)^2 + \left(\frac{\partial \varepsilon_w}{\partial \gamma_2}\right)^2 d(\gamma_2)^2 + \left(\frac{\partial \varepsilon_w}{\partial H}\right)^2 d(H)^2} \tag{4.19}$$

4.6 Error calculations for present experimental setup

Total measurement error in phase fractions is calculated for single-phase oil and water and two-phase flow at 50 and 90% input water cut with mixture velocity equal to 1 m/s at 0° inclination angle. The equations derived in Appendix 9 and 10 are used together with the parameters listed in Table 4.2.

Table 4.2 Input parameters.

Inner diameter (D)	0.0563
Outer diameter (D_o)	0.0643
Wall thickness in centre of the pipe (x_{wall})	0.004 m
E	59.5 keV
Oil attenuation coefficient (γ_1). Calculated by use of Eq, (4.12)	14.2 1/m
Water attenuation coefficient (γ_2). Calculated by use of Eq. (4.13)	18.9 1/m
Wall attenuation coefficient (γ_{wall}). Calculated by use of eq. (4.14)	11.5 1/m
Calibration time for oil (T_1), water (T_2)and air (T_0)	60, 60,120 s
Measurement time (T)	30 s
$d(z)$ (Accuracy in positioning)	0.1 mm

Since the beam thickness is small compared to the geometry of the pipe, the beam is expressed as a thin line. The error in attenuation coefficient $d(\gamma)$ due to error in liquid length $d(H)$ is neglected in present calculations [Eq. (4.20)]. The calculation of the attenuation coefficient is executed only in the centre of the pipe by use of Eqs. (4.12) and (4.13).

$$\left(\frac{\partial \gamma_1}{\partial H}\right) d(H) \approx 0, \left(\frac{\partial \gamma_2}{\partial H}\right) d(H) \approx 0 \tag{4.20}$$

Figure 4.5 shows the calculated fluid and wall length as function of position. The thickness of the wall increases and the liquid length decreases when the beam moves towards the bottom and top of the pipe.

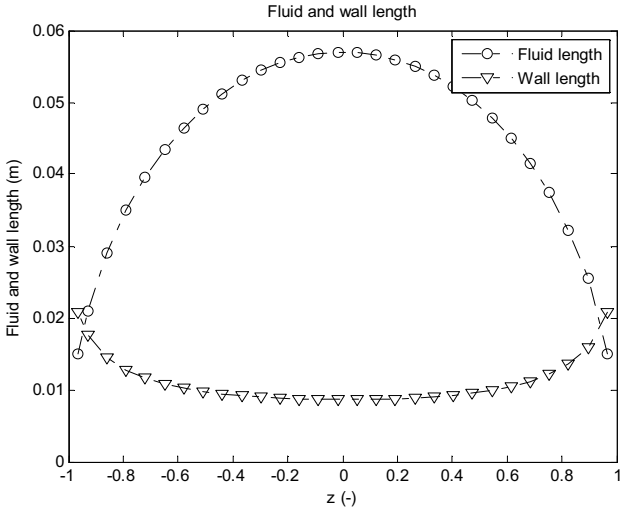

Figure 4.5 Fluid and wall length, z = -1 is bottom of the inner pipe.

4.6.1 Single-phase oil and water

Figure 4.6 presents the total error in single-phase oil and water flow and Figure 4.7 presents the different contributions of errors in water flow. The total measurement error is calculated by substituting the errors in Appendix 9 into Eq (4.19), where $I = I_1 = I_o$ and $I_2 = I_w$.

Figure 4.6 shows that the total measurement error is slightly larger in single-phase water flow compared to single-phase oil flow. The curves show that the total error in phase fraction measurements is largest in the upper and lower part of the pipe and lowest in the centre of the pipe. The small error in the centre of the pipe is because the beam is absorbed mainly in the liquid phase. The decreasing liquid length and increasing wall length when approaching the top and bottom of the pipe lead to increasing error. The error in single-phase water ranges from ±0.77% in the centre of the pipe to ±18% near the wall. This means that the consentration of oil in water must be above 0.8% in the centre and above 18% near the wall. This agrees with Hussain et al. (2008) reports of an error of around ±1% in phase holdup at the central cord position. The measurement time was set to 38.36 s.

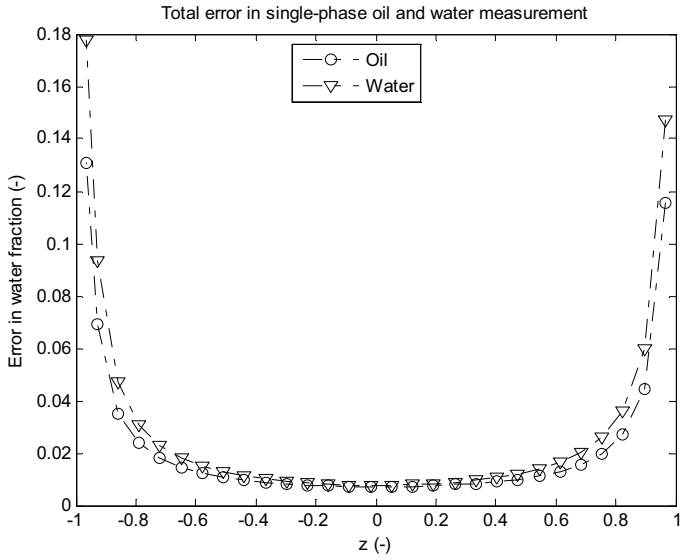

Figure 4.6 Total error in measured phase fraction using Pythagoras's theorem, *d(z)* is equal to 0.1 mm, z = -1 is bottom of the pipe.

Figure 4.7 presents the contribution of error in I, I_0, γ_1, γ_2 and H in single-phase water flow. The different contributions to the total error are smallest in the centre of the pipe and increases towards the wall. The error in attenuation coefficient (γ_2) is equal to the error in transmitted intensity (I). In error calculations executed by e.g. [Pan (1996) and Johansen and Jackson (2004)] the error in attenuation coefficients is neglected due to the assumption of long calibration time. Increasing the calibration time from 1 to 10 minutes decreases the total error in the centre of the pipe with 30% and decreases the error in attenuation coefficient with 68%. Increasing the calibration time from 10 to 30 minutes results in a slightly decrease in total error in the centre of the pipe of approximately 2%. In the upper and lower part of the pipe the error in liquid length (H) is dominating. This means that the error in the positioning of the beam [see Appenix 9 Eq. (A17)] has great influence on the total error, especially in the position where the liquid length is low.

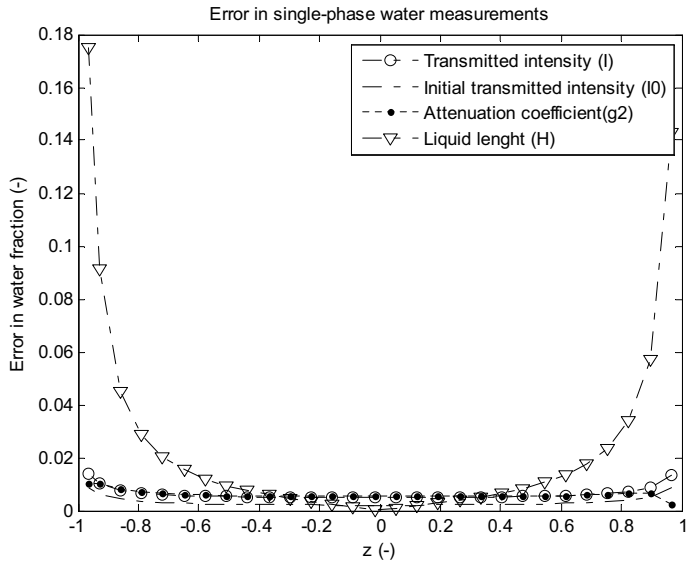

Figure 4.7 Measurement error for I, I_0, γ_1, γ_2 and H in single-phase water at 0° angle and *d(z)* equal to 0.10 mm, z = -1 is bottom of the pipe.

4.6.2 Two-phase oil and water flow at 50 and 90% input water cut

Figure 4.8 presents the experimental phase fractions at 50% input water cut and velocity equal to 1 m /s. As Figure 4.8 shows, the measured phase fractions in the top and in the lower part of the pipe is measured to be both lower than 0 and larger than 1. The phase fractions varies between -0.04 and 0.03 (±0.035) in the top of the pipe and from 0.83 to 1.04 (±0.1) in the bottom of the pipe. Since the variations in phase fractions are within the accuracy of the measurements, which is shown in the calculations below, the presented phase fraction measurement below 0 and above 1 is therefore set equal to 0 and 1. The picture in Figure 4.8 shows water droplets above the interface from position 0.2 to 0.6, but the superimposed water fractions measure only single-phase oil. Since the water droplets are not measured, the concentration must be lower than the measurement accuracy. The concentration of water droplets in the experiments are therefore to low to be "caught" by the gamma instrument.

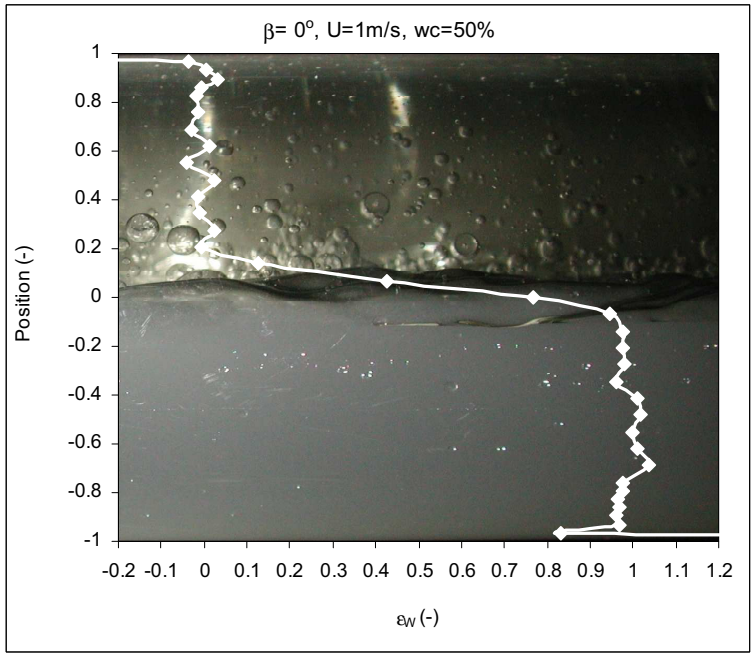

Figure 4.8 Phase fraction measurements at 50% input water cut and 0° angle.

Figure 4.9 shows the total error in phase fraction measurements calculated by summing Eqs. (A4), (A7), (A21), (A22) and (A24) in Appendix 9 in accordance to absolute and Pythagoras's sum. As expected, the sum of errors according to Pythagoras theorem is smaller than the sum of the absolute errors, but the error is in the same order of magnitude. The total phase fraction error ranges from ±0.037 in the centre of the pipe to ±0.18 near the wall when using Eq. (4.19).

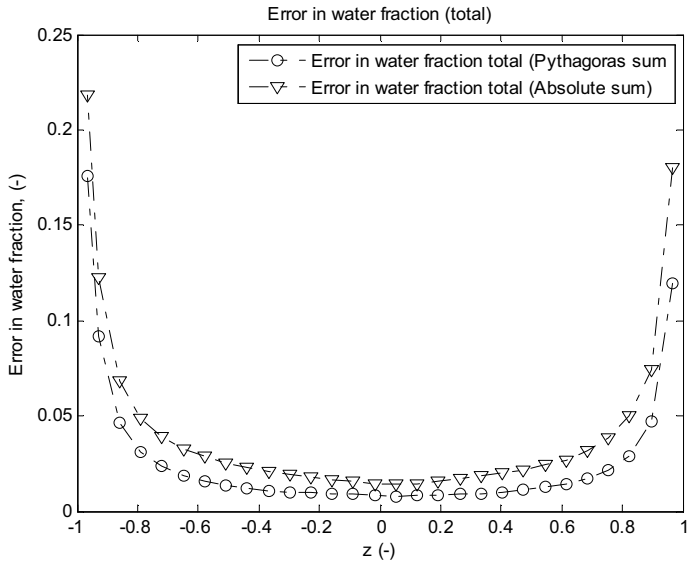

Figure 4.9 Total error in measured phase fraction using Pythagoras's and absolute sum, 50% input water cut, *d(z)* equal to 0.1 mm, z = -1 is bottom of the pipe.

Figure 4.10 presents the contribution of error in I, I_0, γ_1, γ_2 and H at 50% input water cut and velocity equal to 1 m/s. As was seen in single-phase error calculations, the error is largest in the lower and upper part of the pipe and decreases towards the centre. The largest contribution to the error in phase fraction measurements in the lower and upper part of the pipe is the error in liquid length *H. T*he largest error in the centre of the pipe is due to error in transmitted intensity *I*. Figure 4.11 shows the trend of the curves in centre of the pipe in a log-plot. The error in attenuation decreases steeply in the interfacial region. The error in attenuation coefficient for water (γ_2) can be neglected in the oil phase and the error in attenuation coefficient for oil (γ_1) can be neglected in the water phase.

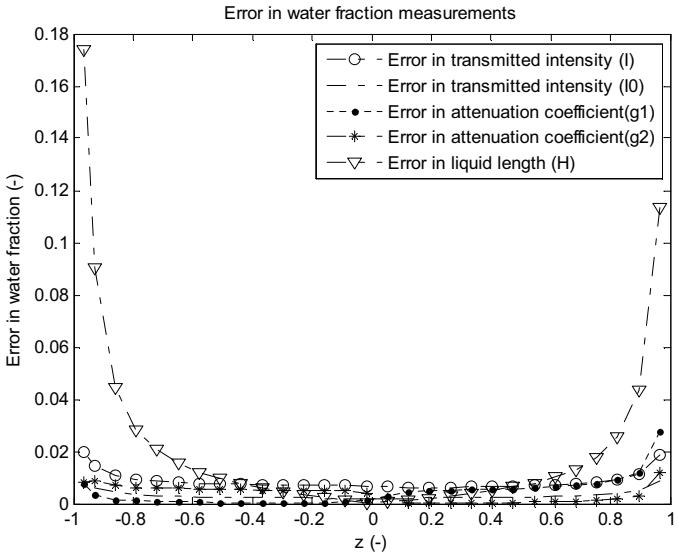

Figure 4.10 Measurement error for I, I_0, γ_1, γ_2 and H at 0° angle, 50% input water cut and $d(z)$ equal to 0.1 mm, z = -1 is bottom of the pipe.

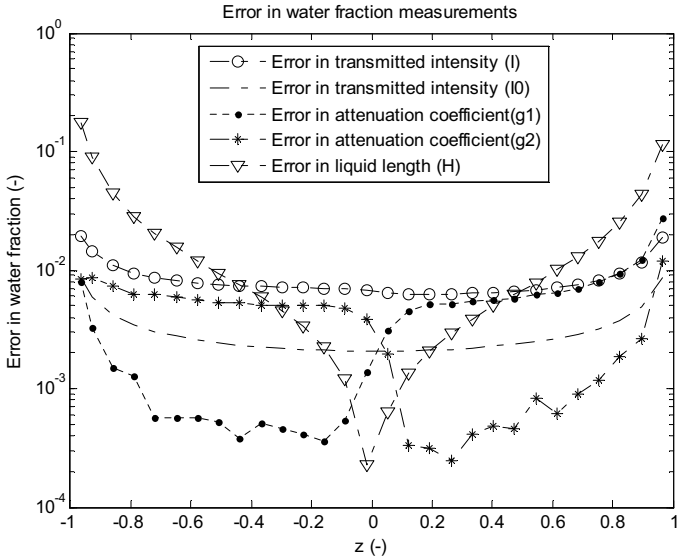

Figure 4.11 Measurement error for I, I_0, γ_1, γ_2 and H at 0° angle, 50% input water cut, and $d(z)$ equal to 0.1 mm, z = -1 is bottom of the pipe.

Figure 4.12 shows the error in measured water fraction at 50% input water cut and 0° angle. The measurement error is the sum of error due to error in I, I_0, γ_1, γ_2 and H as described above. The measurements of dispersion of oil and water in the centre of the pipe are very accurate. Moving towards the top and bottom of the pipe the error in water fraction measurements increase, since the wall thickness increases and liquid length decreases. The measurement error above position 0.8 and below -0.8 increases steeply.

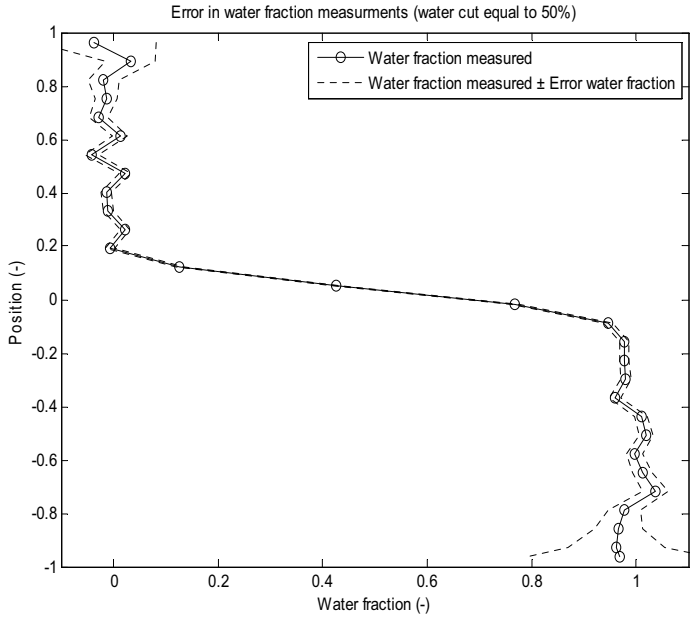

Figure 4.12 Measurement error at 0° angle and 50% input water cut, *d(z)* equal to 0.1 mm, position -1 is bottom of the pipe.

More oil droplets are dispersed in the water phase and water droplets in the oil phase when the input water cut increases to 90%, as can be seen in Figure 4.13. Since the accuracy depends on the measured phase fraction the error in phase fraction increases in top of the pipe as the degree of dispersion increases.

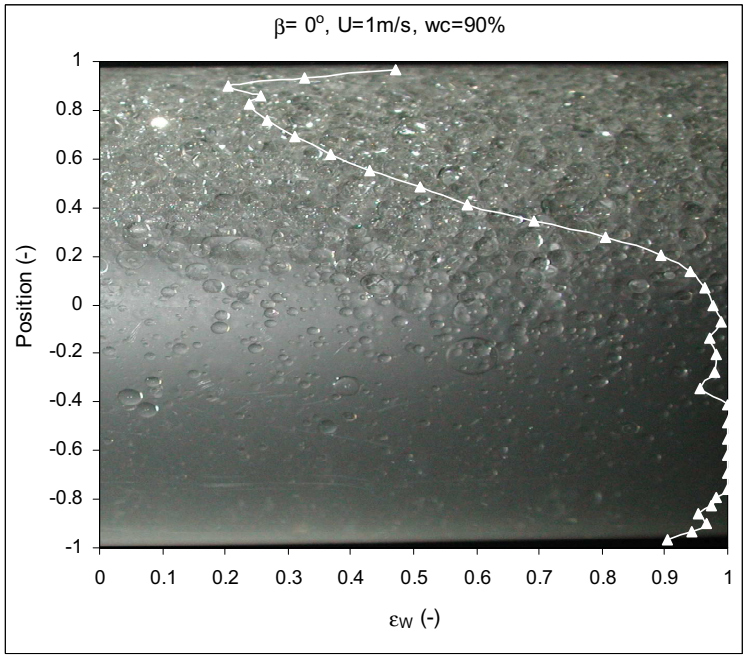

Figure 4.13 Phase fraction measurements at 90% input water cut and 0° angle.

Calculations of the error in measured phase fraction in Figure 4.14, shows that the error increases when the beam approaches the upper and lower walls. The measurement accuracy is slightly worse in the upper part of the pipe at 90% input water cut compared to 50%. In position equal to 0.96 the error in phase fraction is 9.5% larger than the error at 50% input water cut.

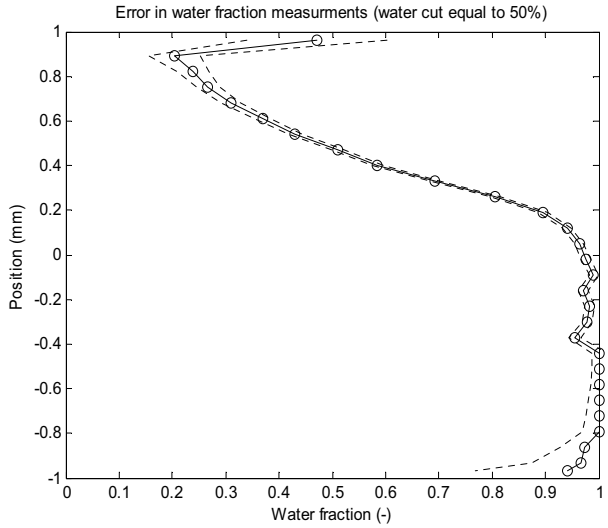

Figure 4.14 Measurement error at 0° angle and 90% input water cut, *d(z)* equal to $1 \cdot 10^{-4}$ m, position -1 is bottom of the pipe.

4.6.3 Effect of traversing accuracy

The largest contribution to the measurement error in phase fraction is due to error in liquid length *d(H)*, which is a function of the accuracy in positioning. The sensitivity of error in positioning is calculated by setting the error equal to 0.1 mm and 0 mm at 50% input water cut at a constant mixture velocity equal to 1 m/s. If the error in positioning is set equal to 0 mm (see Figure 4.15), the total error in the upper and lower part of the pipe will dramatically decrease compared to an error in positioning *d(z)* equal to 0.1 mm (see Figure 4.9). The error in water fraction in top of the pipe increases from 0.037 to 0.16 when the error in positioning increases from 0 to 0.1 mm. The accuracy in positioning can be improved by measuring the exact position of the beam with e.g. a laser.

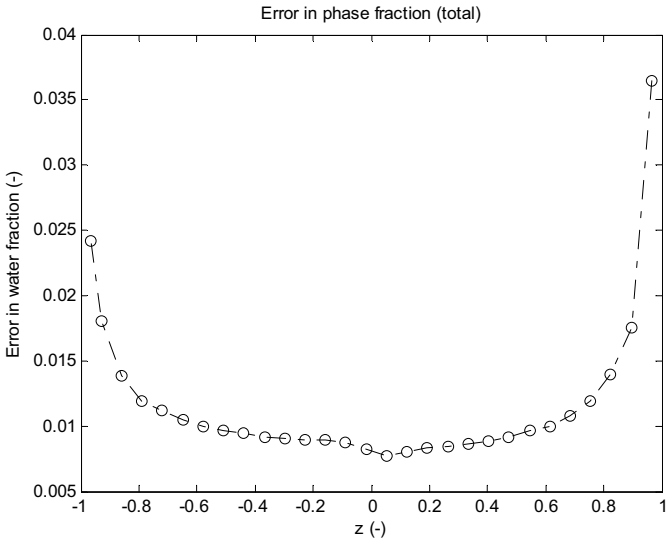

Figure 4.15 Measurement error at 0° angle and 50% input water cut, *d(z)* equal to 0 mm, position -1 is bottom of the pipe.

4.7 Experimental setup and procedure

The gamma instrument in Figure 4.16 is used to produce phase-distribution profiles. The experimental procedure and operation of the gamma instrument are executed in the same way for each experimental run. The measurement positions are programmed and controlled from a PC and the sequence is used in calibration and measurements. The angular position of the instrument is measured and corrected if necessary and single-phase oil and water calibrations are conducted before each experimental run. This is to minimize eventually measurement error. The gamma instrument traverses in both vertical and angular direction by use of step motors. The source collimator collimates the radiation to produce a beam. The source collimator is a 3 mm circular slot and the detector collimator is a rectangular slot of 3 mm height and 12 mm width. The radioactive source is Am^{241}, 45 millicurie (mCi) with 59.5 keV energy and the detector is a 1 in. x 6 mm NaI. The gamma test pipe is made of polypropylen instead of steel to reduce the absorption through the wall. The pipe has an inner diameter of 0.056 m and an outer diameter of 0.0643 m. The pipe is 0.4 m long and is located 10.3 m downstream the mixing unit. A computer programme called LabVIEW^{TM} operates the gamma instrument.

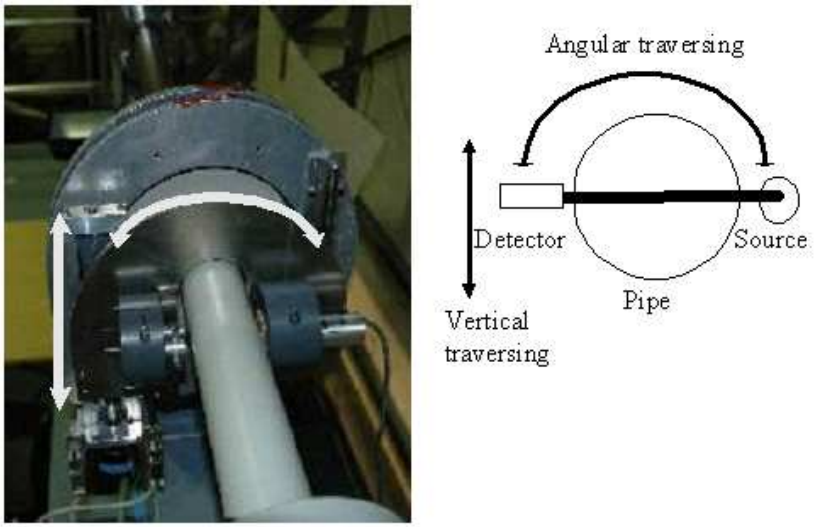

Figure 4.16 The gamma densitometry instrument.

Figure 4.17 shows the overall setup of the gamma instrument. The instrument contains:

- Gamma source (Am^{241}, 45 mCi, 59.5 keV)
- Photomultiplier tube (PMT)
- Spectroscopy amplifier and delay line amplifier (DLA)
- Single channel analyzer (SCA)
- Multichannel analyzer (MCA)
- Detector (1 in. x6 mm NaI detector)
- Counting system (PC with a specific data acquisition card)

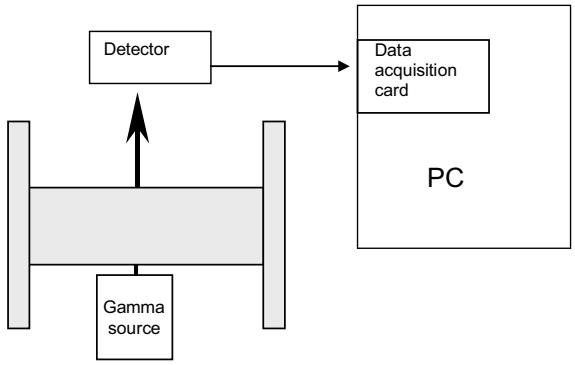

Figure 4.17 Setup of the gamma instrument.

The detector is a scintillation detector, which use crystals that emit light when gamma rays interact with the atoms in the crystals. The intensity of the light emitted is proportionally to the energy absorbed in the crystal by the gamma ray. The main interaction mechanism is the photoelectric effect, which absorbs all of the energy of the incident beam. The detector is connected to a photomultiplier that convert the light into electrons and amplifies the signals enabling individual photons to be detected. Each photon that enters the multiplier tube (PMT) creates a step peak in the output voltage. The voltage pulse is then re-shaped by the single channel analyser into a Gaussian shape and converted into a digital signal. The digital signal is sent to a computer, which stores, displays and analyzes the data. The measured count rates are well within the linear response region of the detector.

The instrument has to be calibrated with both oil and water to be able to calculate the in-situ fractions for stratified and dispersed flow. During the calibration, the pipe is first filled with single-phase water and the beam is traversed vertically (from top to bottom of the pipe) every mm close to the wall and every second mm further away from the wall. The calibration time in each measurement position is set to 60 seconds. Then the same procedure is done with the pipe filled with single-phase oil. When the calibration is done, two-phase experiments are done by using equal traversing setup as in the calibration with a measurement time of 30 seconds.

Figure 4.18 presents the scans produced by the gamma densitometer, the intensity (counts/s) vs. position (mm). The scans present calibration of single-phase oil, single-phase water and two-phase oil and water flow. In the two-phase experiment, the input water cut is equal to 50 % and the pipe angle is 0°. The calibration data for single-phase oil has higher intensity than water. This is because the density of oil is lower than the density for water. The calibration and the two-phase experiment starts 7 mm above the pipe in position 40 mm. The intensity (counts/s) above the pipe is constant and has its maximum value, due to the low density of air. There is a significant drop in the intensity when the beam goes through the wall. The intensity drops from 30800 to 21500, when the position changes from air at 33 mm to the inner wall at 29 mm. The vertical doted lines crossing position +29 mm and -29 mm represent the inner pipe boundaries. This is the intersection point of the calibration curves of oil and water. In this intersection point, the beam passes the inner pipe diameter and starts to penetrate inside the pipe where the fluid is. The beam is at the top of the pipe at beam position +29 mm and is at

the bottom of the pipe at position -29 mm. The intensity at these positions is equal provided the pipe thickness is the same at the top and at the bottom of the pipe, which is the case in these measurements. The oil in the top of the pipe absorbs the gamma beam, and follows the oil calibration curve. The gamma intensity decreases steeply at the interface between oil and water. Here the intensity values lie between the two calibration curves, because there is a mixture of oil and water at the interface. The beam traverses through the interface, and then through the water phase. In the water phase, the curve follows the single-phase water calibration curve to the bottom of the pipe.

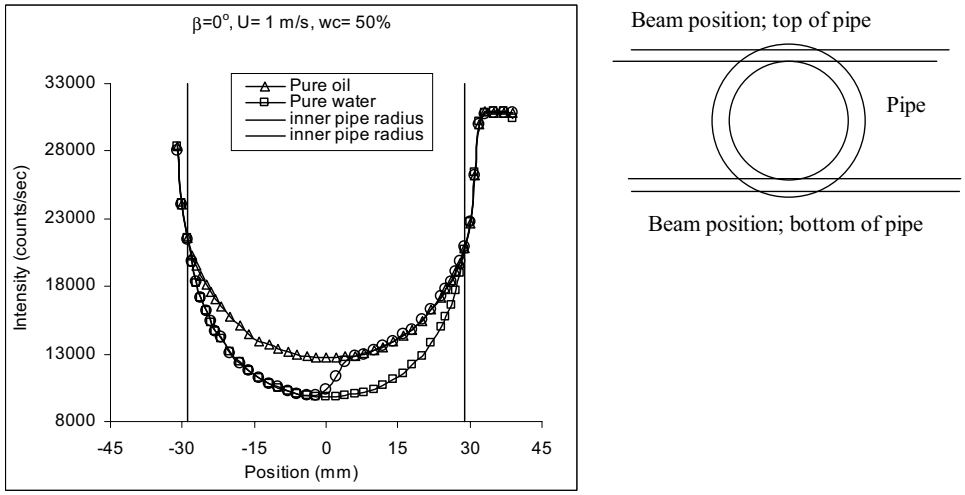

Figure 4.18 Gamma scans of single-phase and two-phase oil-water flow, 50% input water cut and 0° angle.

Eq. (4.15) converts the raw data into water fractions. Figure 4.19 presents the position in the pipe vs. water fraction. Position 1 is at the top of the pipe and position -1 is at the bottom of the pipe. The oil phase is located between position 1 (at the top of the pipe) and position 0.2 and the interfacial region between position 0.2 and -0.1. The gradient of the curve is very steep in the interfacial region due to low mixing of oil and water and/or because no or small waves at the interface. Below position -0.1 the single-phase water regime dominates the flow.

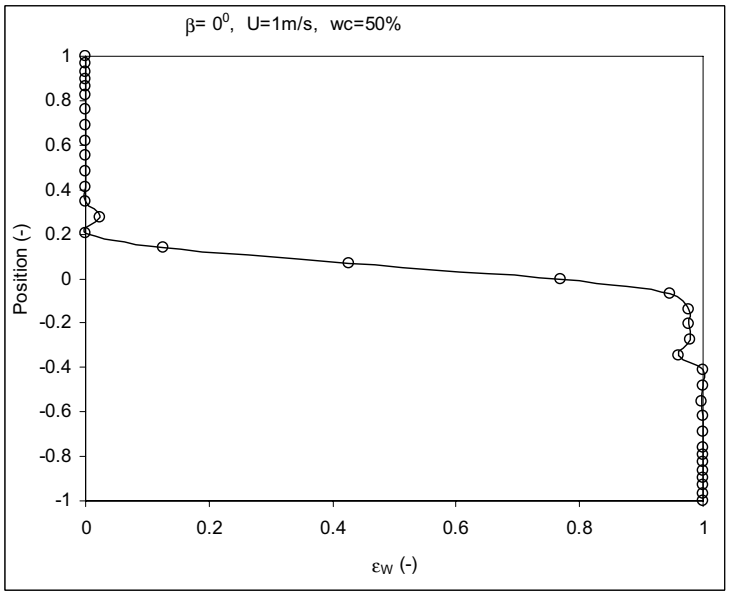

Figure 4.19 Gamma measurements of two-phase oil and water flow.

4.8 Flow pattern classifications

The flow is classified as stratified flow when two continuous phases flow simultaneously inside the pipe. One or both of the continuous phases could be either partially or fully dispersed. The flow pattern definitions in this thesis are similar to classifications used by Trallero (1995). The difference is five additional flow regimes called stratified wavy (SW), dispersion of water in oil and oil (Dw/o & o), plug flow (PG), dispersion of water in oil and water (Dw/o & w) and dispersion of oil in water and oil (Do/w & o). The dispersion of water in oil and oil (Dw/o & o) is part of the water in oil emulsion (w/o) flow pattern given by Trallero (1995). Several of the listed flow regimes in Table 4.3 have not been measured in the parameter range studied in present work, but the flow regimes have been measured by previous researchers as Elseth (2001) by use of another classification approach.

Table 4.3 Flow pattern classifications.

Flow pattern	**Abbrevation**
Stratified flow	ST
Stratified flow with mixing at the interface	ST & MI
Stratified wavy	SW
Dispersion of water in oil and oil	Dw/o & o
Dispersion of oil in water and water	Do/w &w
Dispersion of water in oil and water	Dw/o & w
Dispersion of oil in water and oil	Do/w & o
Dispersion of water in oil and dispersion of oil in water	Dw/o & Do/w
Plug flow	PG
Water in oil emulsion	w/o
Oil in water emulsion	o/w

Figure 4.20 to Figure 4.29 show the configuration of oil and water for the ten classified flow regimes. The flow regimes are divided into three main categories; stratified, plug flow and dispersed flow. The criteria for two-phase stratified flow is existence of two continuous phases at the same time inside the pipe. Five stratified flow regimes are presented in Figure 4.20 to Figure 4.24. The plug flow regime is presented in Figure 4.25 and the dispersed flow regimes are presented in Figure 4.26 to Figure 4.29. The flow configuration and degree of mixing in the stratified flow regime varies a great deal. Outside the stratified flow regime, different types of dispersions occur. There are two main dispersions; fully dispersed flow (Figure 4.28 and Figure 4.29) and partially dispersed flow (Figure 4.26 and Figure 4.27).

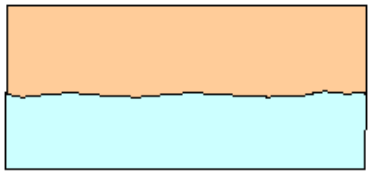

Figure 4.20 Stratified flow (ST).

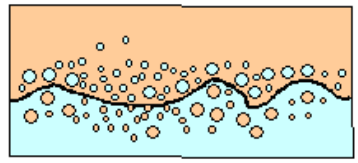

Figure 4.21 Stratified flow with mixing at the interface (ST & MI).

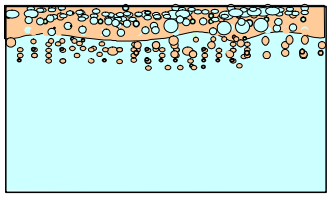

Figure 4.22 Dispersion of water in oil and water (Dw/o & w).

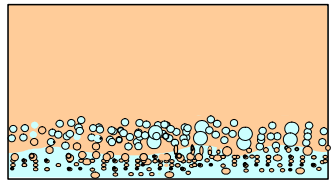

Figure 4.23 Dispersion of oil in water and oil (Do/w & o)

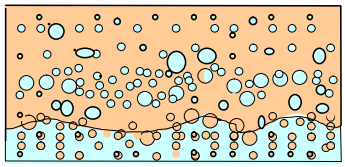

Figure 4.24 Dispersion of water in oil and dispersion of oil in water (Dw/o & Do/w).

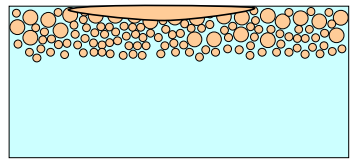

Figure 4.25 Plug flow (PG).

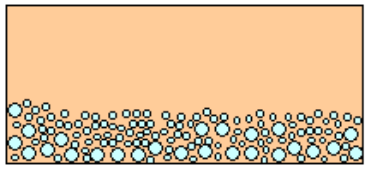

Figure 4.26 Dispersion of water in oil and oil (Dw/o & o).

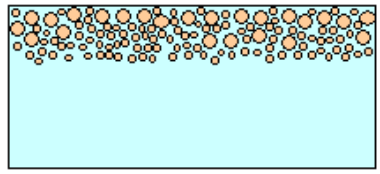

Figure 4.27 Dispersion of oil in water and water (Do/w & w).

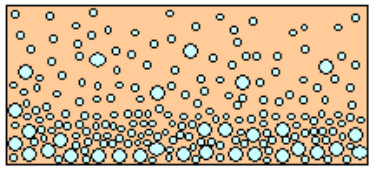

Figure 4.28 Water in oil emulsion (w/o).

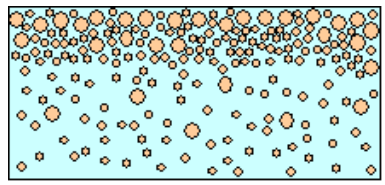

Figure 4.29 Oil in water emulsion (o/w).

4.8.1 Stratified flows

In the stratified flow regime (ST) the interface is smooth with no dispersed oil and water droplets, but long waves can be present. The gravity force is dominating and tends to segregate the phases. Figure 4.20 presents the ST flow regime. The stratified flow pattern

usually appears at low mixture velocities (≤ 1 m/s) and intermediate water fractions from 30 to 70 % [Elseth (2001)].

Figure 4.21 presents the stratified flow with mixing at the interface (ST & MI). An increase in the mixture velocity makes the interface more turbulent and wavier, which leads to droplet formation. The turbulent interfacial forces disperse the phases and spread the droplets throughout the pipe cross section, while the buoyant forces act in the opposite way and try to settle the droplets. This vortex motion at the boundary of the two liquids was observed by Guzhov et al. (1973). Water droplets exist in the oil layer and oil droplets in the water layer. Both kinds of droplets are usually located close to the interface. The degree of droplet entrainment can vary, but as long as there are two continuous layers in the flow and a clear oil and water layer the flow pattern classifies as ST & MI.

The dispersion of water in oil and water (Dw/o & w) flow regime in Figure 4.22 consists of two continuous phases, with a clear water phase in the lower part of the pipe and a dispersed phase in the top of the pipe. In the dispersed layer, both oil droplets in water and water droplets in oil exist. The flow regime occurs at high input water cuts. Soleimani (1999) identified this flow regime by use of conductivity probes and gamma densitometry.

In the dispersion of oil in water and oil (Do/w & o) as shown in Figure 4.23 a dispersed phase in the bottom of the pipe occurs and a clear oil layer in the top of the pipe is seen. The dispersion in the bottom of the pipe consists of oil droplets in water and water droplets in oil. The flow regime occurs at low input water cuts. Soleimani (1999) also identified this flow regime.

Figure 4.24 presents the dispersion of water in oil and dispersion of oil in water (Dw/o & Do/w) flow regime. In present study, Dw/o & Do/w flow regime is classified as stratified flow since two continuous phases of water and oil flows simultaneously inside the pipe. The interfacial mixing region in the ST & MI grows with an increase in mixture velocity, and for small input water cuts, a dual dispersion of Dw/o and Do/w can occur. The turbulent forces increase due to the increased velocity and spread the droplets across the entire cross section. Two types of dispersions occupy most of the pipe cross section. In the upper part of the pipe, there is water in oil dispersion and in the lower part of the pipe, an oil in water dispersion

occurs. Rodriguez and Oliemans (2006) treated the Dw/o & Do/w and water in oil emulsion (w/o) as equal flow pattern, since speed and resolution limitations of the video recording system made it impossible to distinguish between the two flow regimes.

4.8.2 Plug flow

The plug flow (PG) shown in Figure 4.25 is a time dependent flow pattern, characterized by a plug of oil flowing at the top of the pipe. The plug gradually disperses, until it is fully dispersed and then reappears again. In pictures taken of the PG flow regime the plug is not as visible as in Figure 4.25. Alkaya (2000) and Lum et al. (2006) observed the PG flow during the transition from ST & MI to Do/w & w. Lum et al. (2006) discovered the PG flow at pipe inclinations +5° and +10° at velocities between 0.6 to 1.0 m/s, which is similar to present study.

4.8.3 Dispersed flows

In Figure 4.26 a dense packed layer of water droplets is located near the bottom of the pipe in the oil continuous phase. The oil flow energy is insufficient to distribute larger water droplets over the cross section of the pipe. The flow is a dispersion of water in oil and oil (Dw/o & o) and is oil continuous. This flow pattern only appears at low input water cuts and sufficiently high mixture velocity to form the water droplets. The thickness of the dense packed layer varies with time and has usually a wavy character.

If the velocity is constant and the input water cut increases sufficiently, a similar dense packed layer of oil drops occurs over the single-phase water flow. The definition of this flow regime is a dispersion of oil in water and water (Do/w & w). Figure 4.27 shows the configuration of this flow regime. The velocity has to be high enough to disperse the oil droplets, but low enough to avoid the oil droplets to be distributed over the pipe cross-sectional area.

The water in oil emulsion (w/o) and oil in water emulsion (o/w) shown in Figure 4.28 and Figure 4.29 are fully dispersed flow regimes. The water in oil emulsion regime is oil dominated and the oil in water emulsion is water dominated. The oil or water droplets can be either homogenous or inhomogeneous distributed in the continuous phase. The emulsion is

only homogenous at sufficiently high mixture velocities. In the inhomogeneous distribution, there is a vertical concentration gradient.

4.9 Flow pattern experiments

Flow pattern identification in the multiphase flow loop at Telemark University College was executed by use of still pictures of the flow and vertical phase fraction gamma measurements.

4.9.1 Experimental conditions and procedure

The number of flow pattern and phase fraction measurements is equal to 91 runs. Table 4.4 gives the ranges of the experimental conditions. The measurements are conducted at mixture velocity equal to 1 m/s with increasing inclination angle from -10° to +10° and input water cut from 10 to 90%. The measurements start by filling the pipe with oil and then increasing the input water cut from 10 to 90%. Two measurements conducted at -10° angle at input water cut equal to 85% and 90% are not included due to air in the test pipe. The air was detected visually and in the phase fraction measurements as shown in Appendix 11, Figure A 9.

Table 4.4 Ranges of experimental conditions.

Parameter	**Value**
Pressure	1 atmosphere
Temperature	22 °C
Input water cut	10, 15, 20, 25, 35, 45, 50, 55, 65, 75, 80, 85, 90 %
Mixture velocity	1 m/s
Pipe inclinations	Horizontal, 1°, 5°, 10° upward, -1°, -5°, -10° downward

Both visual and gamma ray attenuation measurements are conducted in the flow pattern studies. Observations with a Nikon D70 reflex camera in front of a plexiglas section, located 10.1 m downstream the mixing unit, provide unique information about the flow structure. The observation represents a snapshot of a vertical plane inside the oil-water flow. The pictures are taken from the side of the pipe, such that the gamma ray phase fraction measurements can be superimposed on the pictures. To measure local phase fractions, a gamma densitometer is mounted 11.3 m downstream the mixing unit. In contrast to the visual observations, the gamma ray measurements are time and volume averaged values. The inclination angles are set

equal to 0º, ±1º, ±5º, and ±10º and input water cuts from 10 to 90% to study the impact they have on the flow behaviour.

The mixture velocity, physical fluid properties (density, viscosity and surface tension), flow geometry (pipe diameter, mixing unit), wetting properties (pipe material), surfactants and operating temperature and pressure are constant parameters. Some variations in temperature and surfactants can be present, but since the variations are small it is assumed that they are insignificant. Eq. (4.21) presents the mixture velocity and is set equal to 1 m/s in all the two-phase experiments presented in present study.

$$U_m = \frac{Q_o + Q_w}{A} = U_{SO} + U_{SW} \tag{4.21}$$

Figure 4.30 gives a schematic description of the main forces acting in downward pipe flow. The main forces affecting the flow behaviour are gravity, wall shear and interfacial forces.

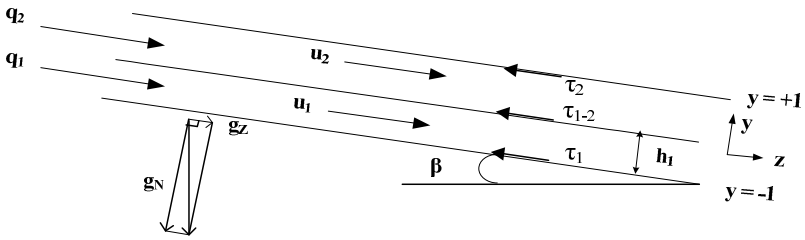

Figure 4.30 Stratified flow configuration and coordinates -10° ≤ α ≤ +10°.

Where,

u_1 = actual fluid 1 velocity (m/s)

u_2 = actual fluid 2 velocity (m/s)

h = interfacial height (m)

β = inclination angle (downward flow, (°)

Q_1, Q_2 = fluid 2 (light phase) and fluid 1 (heavy phase) flow rates (m^3/h)

g_N,g_z = normal and parallel gravity components (m/s^2)

h_1 = fluid 1 height (m)

τ_1, τ_2 = fluid 1 and 2 wall shear stresses (N/m^2)

$\tau_{1\text{-}2}$= interfacial shear forces (N/m^2)

Stratified flow regime (ST) where two layers of water and oil flow separately are chosen as a case description. Similar descriptions can also be made for dispersed flow. The gravity force in inclined pipe flow has two components: normal and parallel to the pipe axis. The normal gravity component enhances segregation of the liquids, similar to horizontal flow and the parallel component acts in the mean flow direction (downward or upward). In downward flow, the heavy phase accelerates and u_1 increases, which result in a decrease in the heavy phase holdup. Conversely, the velocity of the heavy phase in upward flow decreases and accumulates in the pipe. The wall shear forces for the respectively light (oil) and heavy (water) phase are due to the boundary layer at the inner wall of the pipe where the fluids are in contact with the pipe material. The wall shear forces act in the opposite direction of the flow. The interfacial shear force between oil and water can influence the curve of the interface, droplet break-up and coalescence rates.

4.9.2 Flow regime identification

Table 4.5 presents the flow regimes identified in this experimental campaign, which is located within the stratified, and plug flow regimes.

Table 4.5 Identified flow regimes in present study.

Flow pattern	**Abbrevation**
Stratified flow with mixing at the interface	ST & MI
Dispersion of water in oil and water	Dw/o & w
Dispersion of oil in water and oil	Do/w & o
Plug flow	PG

Present classification approach uses the measured phase distributions together with visual observations to determine the flow regime. The scaled y-axis fits closely the inner pipe diameter of the pictures. To distinguish between stratified and dispersed flow a pre-defined phase inversion water cut is used. Since phase inversion in flowing systems using Exxsol D60 is not reported in the literature, the phase inversion point for Exxsol D80 is used since the fluids has very similar fluid properties. Soleimani (1999) measured the phase inversion point to be at input water cut between 34 and 37% by use of Exxsol D80. The point where phase inversion occurs is set equal to 30% input water cut in present flow pattern identification. An inversion water cut of 50% were also tested giving equal classification.

The flow classifies as stratified flow when the measured phase fraction values are below and above the point of inversion, with the feature of having two continuous phases. Below the inversion point, the flow is oil continuous and above, the flow is water continuous. Three criteria have two be fulfilled in the classification of ST & MI. The first criteria is that the phase fraction has to be measured below the point of inversion in the upper part of the pipe and above in the lower part of the pipe. The second criterion is that there must exist droplets near the interface, which can be determined by both still pictures and by the phase fraction gradient in the interfacial region. The third criterion is that a clear oil and water phase must be present. The measured phase fraction must have values equal to zero in the top of the pipe and equal to one in the bottom of the pipe.

In the dispersion of water in oil and water flow regime (Dw/o & w) in Figure 4.22 the measured phase fractions are equal to one in the lower part of the pipe and in the upper part of the pipe the measured phase fractions are larger than zero and lower than the inversion point. The dispersion of water in oil and water (Dw/o & w) in Figure 4.22 and the dispersion of oil in water and water (Do/w & w) in Figure 4.27 are both characterized by a dispersed phase in the top of the pipe. Present measurements have no information of the fluid of the continuous phase, which is needed to distinguish between the stratified (Dw/o & w) and dispersed (Do/w & w) flow regimes. Instead, the point of inversion is used to determine whether the flow is stratified or dispersed.

In the dispersion of oil in water and oil (Do/w & o) in Figure 4.23 the measured phase fractions are equal to zero in the upper part of the pipe and in the bottom of the pipe the measured phase fractions are lower than one and above the point of inversion. The point of inversion is used to distinguish between the stratified (Do/w & o) and the dispersed (Dw/o & o).

The phase fractions alone cannot identify the plug flow regime. Visual observations are needed to observe the plugs in top of the pipe.

The radial distribution and the curvature of the interface of the configurations demonstrated are not measured in present study. The dispersion in the top of the pipe can be homogenous dispersed as shown in Figure 4.31 or a radial distribution could occur as shown in Figure

4.32. When a radial distribution occurs there can exist an oil continuous core flow in the centre of the pipe, which are not visually seen, since the continuous flow could be surrounded by a dispersed phase. Pictures taken by Soleimani (1999) of flow experiments conducted at 1.2 m/s and 60% input water cut, indicate a stratified mixed/water layer configuration, but looking at the gamma tomography and high frequency probes (reveals an oil core in the upper part of the pipe encapsulated by a water continuous dispersed phase as shown in Figure 4.31. Valle and Kvandal (1995) also measured a high water fraction around the edge of the pipe at lower mixture velocities and high input water fraction. Tomography profiles with use of gamma, presented by Soleimani (1999) also show that the curve in the vertical plane of the interface can vary as function of input water cut.

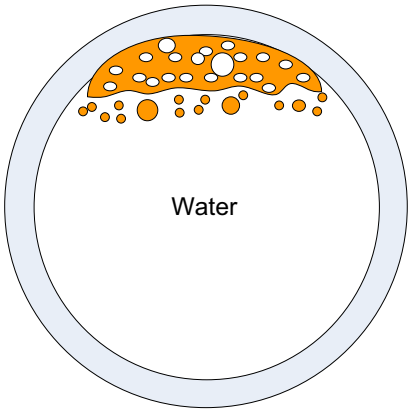

Figure 4.31 ST & MI flow regime

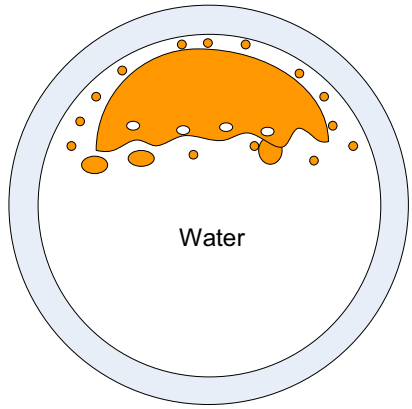

Figure 4.32 ST & MI flow regime

4.9.3 Stratified flow with mixing at the interface (ST & MI)

Figure 4.33 to Figure 4.34 represent the ST & MI flow regime with different amount of mixing. The measurements are taken at 50 and 20% input water cut and at pipe inclination equal to 0° angle. Since the position of the interface determined by still pictures is dependent on the positioning and setting of the camera, the still pictures cannot give you a precise description of the interface. In dispersed flow, it is even more difficult to determine the interface from still pictures. The exact position of the interface between oil and water can however be determined from the measured phase fractions using the point of phase inversion. The flow regimes are easy to interpret since two continuous layers of oil and water can be seen in the still pictures, and the phase fractions are equal to zero in the top and equal to one

in the bottom of the pipe. The gradient of the phase fraction curve at the interface describes the amount of mixing of oil and water at the interface and the size and frequency of the waves. The interface at 20% input water cut in Figure 4.34 is more turbulent and consists of more droplet break-up compared with the interface at 50% input water cut. Since the velocity is constant, the reason for the difference in the degree of mixing at the interface is most likely a consequence of the decrease in input water cut. The larger degree of mixing of droplets can lead to an asymmetric velocity profile. The LDA measurements in Chapter 5 shows that oil phase flows faster than the water phase at 25% input water cut, leading to an asymmetric velocity profile. Elseth (2001) measured also an asymmetric velocity profile at both 15 and 25% input water cut. Since the interface is much closer to the wall, the shear forces will contribute to turbulent mixing. The degree of waves and mixing at the interface is not only dependent on the input water cut but varies also depending on the inclination angle and mixture velocity for a given experimental setup.

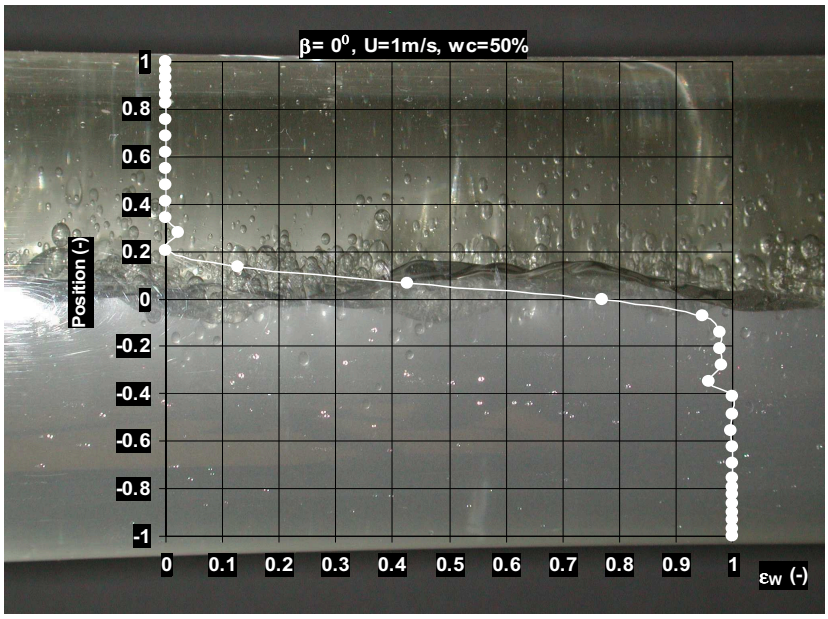

Figure 4.33 Stratified flow with mixing on the interface (ST & MI) at 0° angle and 50% input water cut. The mixture velocity is equal to 1m/s.

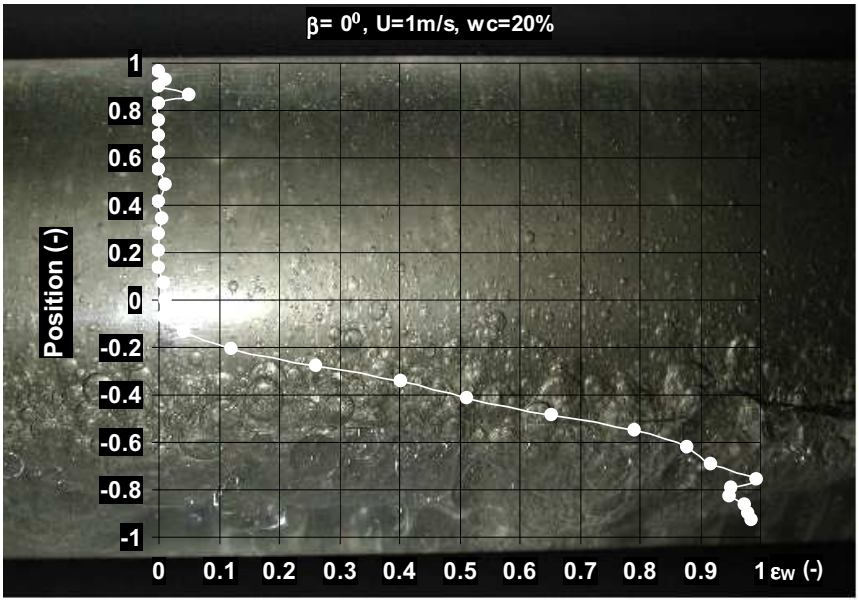

Figure 4.34 Stratified flow with mixing on the interface (ST & MI) at 0° angle and 20% input water cut. The mixture velocity is held constant equal to 1m/s.

4.9.4 Dispersion of water in oil and water (Dw/o & w)

Figure 4.35 presents the dispersion of water in oil and water (Dw/o & w) flow regime, where the input water cut is equal to 80% and pipe inclination equal to 0° angle. The still pictures gives the impression that the flow regime is a dispersion of oil in water and water (Do/w & w) as shown in Figure 4.27, however the measured phase fractions in the top of the pipe are measured to be very low, which indicates that there exists an oil continuous phase. The measured water fraction in the top of the pipe is above zero and below the phase inversion point. In the bottom of the pipe, a clear water phase exists. In the study of Elseth (2001) the flow is classified as dispersion of oil in water and water (Do/w & w).

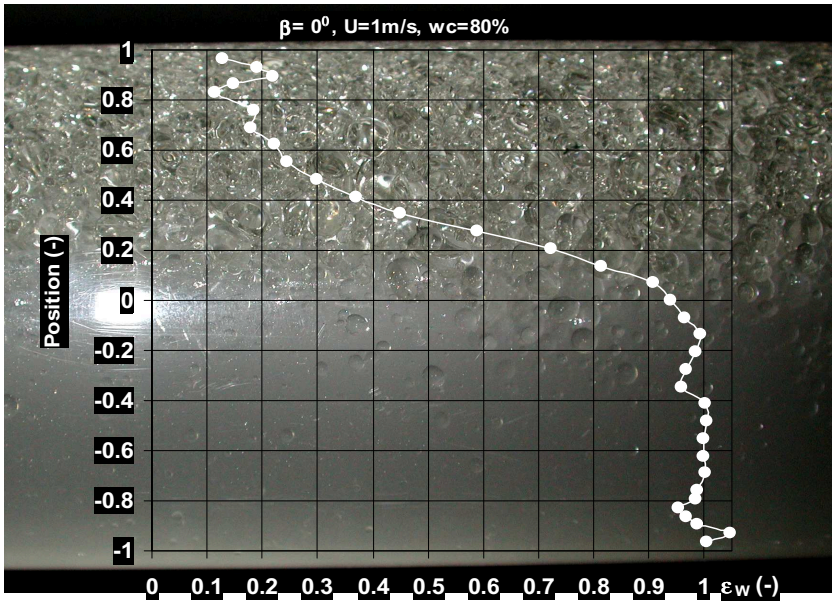

Figure 4.35 Dispersion of water in oil and water (Dw/o & w) at inclination angle equal to 0° and input water cut of 80%. The mixture velocity is equal to 1m/s.

4.9.5 Dispersion of oil in water and oil (Do/w & o)

Figure 4.36 represents the dispersion of oil in water and oil (Do/w & o) flow at +1° upward pipe angle and input water cut of 10%. The still picture shows a dispersed phase in the bottom of the pipe. Whether the dispersed phase is oil or water dominated is not possible to interpret from the pictures. However, since the phase fractions are both below and above the point of phase inversion (0.30) the flow consists of two continuous phases. The phase fractions are above the inversion point in the lower part of the pipe, which tells us that the fluid of the continuous phase is water. The water continuous phase is dispersed with oil droplets. In the upper part of the pipe, a clear oil layer is measured. Other investigators e.g. Elseth et al. (2000) and Kvandal et al. (2000) have classified this flow pattern as dispersed water in oil and oil (Dw/o & o). The picture also shows small water droplets in the oil phase in the centre of the pipe, but the gamma instrument does not capture this. The concentration of water droplets must hence be lower than the accuracy of the instrument.

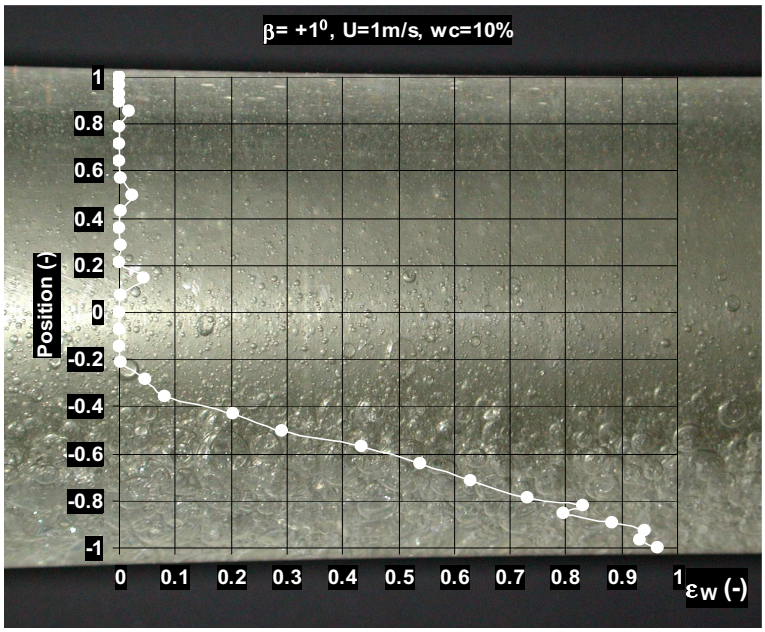

Figure 4.36 Dispersion of oil in water and oil (Do/w & o) at +1° angle and input water cut of 10%. The mixture velocity is equal to 1m/s.

4.9.6 Plug flow

Figure 4.37 presents the characteristics of the oil plug flow regime (PG) at +10° pipe inclination angle and 80% input water cut. The pictures of the flow are taken with a time step of approximately 2 seconds. The plug flow has a continuous water phase in the bottom of the pipe in position -1 to 0.2. Above the water layer, there is a dispersion of oil droplets in water, with interruption of long thin oil plugs in top of the pipe. In the first picture, which is taken at time equal to zero seconds, an oil plug is visually seen by the appearance of a more transparent phase in the top of the pipe. The plug is easier to observe in the experimental study than in the pictures. Two seconds later the plug is replaced with a dispersed phase. Similar flow patterns are described and measured by Russel et al. (1959), Angeli (1994) in horizontal flow and Alkaya (2000) in inclined flow.

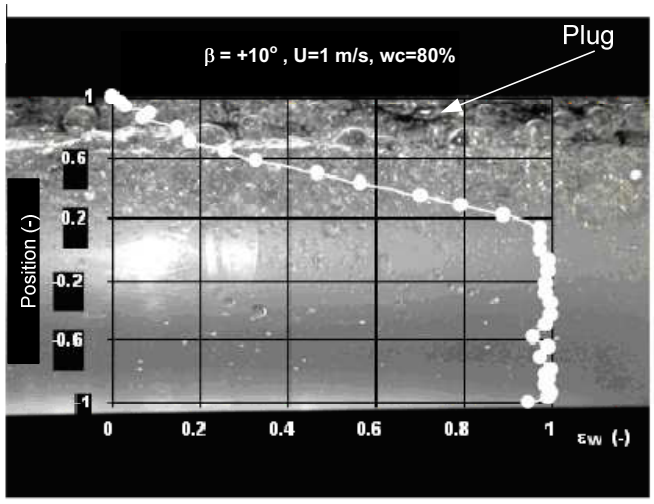

0s

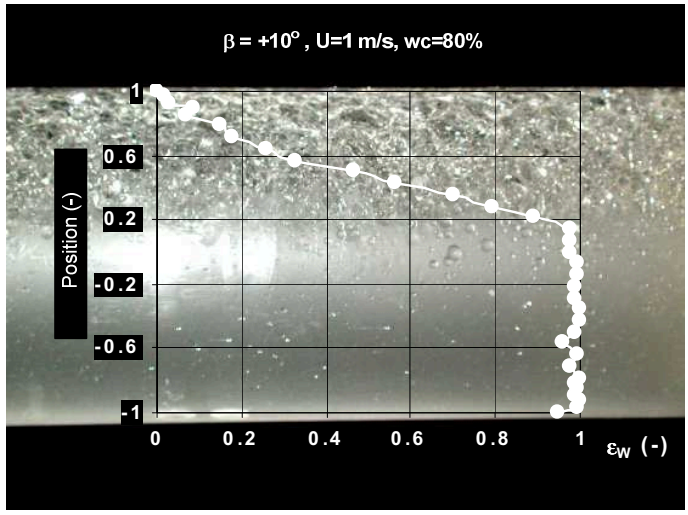

2 s

Figure 4.37 Sequence of pictures taken of the oil plug regime (PG) at +10° angle and 80% input water cut.

4.9.7 Flow pattern map

A flow pattern map for different angles and input water fractions are constructed to highlight the effect of pipe inclination in Figure 4.38. The mixture velocity is constant equal to 1m/s, the angle varies from –10° to +10° and the input water cut varies from 10 to 90%. The flow

pattern map is constructed by use of pictures and analysis of the phase fraction measurements as described in the sections above. An inversion water cut equal of 30% is used. Increasing the inversion water cut does not influence the flow pattern classification, but decreasing it below 30% will change the transition boundaries.

The two main flow regimes observed are stratified flow (ST & MI, Dw/o & w and Do/w & o) and plug flow (PG). The ST & MI regime dominates the flow regime map at medium input water cuts and at large input water cuts the Dw/o & w flow regime is most pronounced. The Do/w & o is identified at low input water cuts and low inclinations (±1°). The PG flow regime is only measured at +10° pipe angle and at 80% input water cut. The degree of mixing is most pronounced at high water cuts compared to low water cuts. The transition boundaries from ST & MI flow to Dw/o & w shifts too a higher input water cut from 75 to 80%, when the pipe inclination angle changes from ±1° to ±5°. Decreasing the pipe inclination from -5° to -10° decreases the transition boundaries from ST & MI from 80% to 75% input water cut. The pipe inclination also effects the transition from ST & MI to Do/w & o. The Do/w & o flow appears when the pipe inclination changes from horizontal to ±1° and disappears when the pipe inclines from ±5° and ±10°.

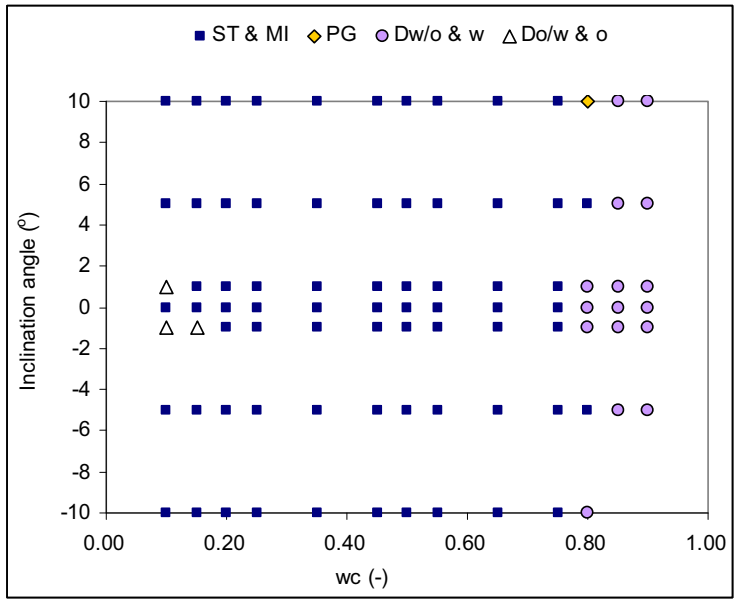

Figure 4.38 Flow patterns as function of inclination angle and input water cut.

4.9.8 Phase fractions as function of inclination angle at constant input water cut

This section presents a detailed analysis of the flow structure using the flow pattern map, still pictures and phase fractions. The measurements show that different flow configurations will form, depending on the inclination angle. Large variation in the interfacial region exists within the same flow regime. The gradient of the phase fraction curve at the interface describes the degree of dispersion of either oil in water or water in oil and/or the amplitude of waves. It is not possible to distinguish between the degree of dispersion and waves from the phase fraction measurement, but in conjunction with pictures taken of the flow, some conclusions can be drawn. Figure 4.39 shows the interfacial region. When the gradient of the interface is steep the interface region is broader and the interface can be either wavy or dispersed with oil and water droplets or a combination of both.

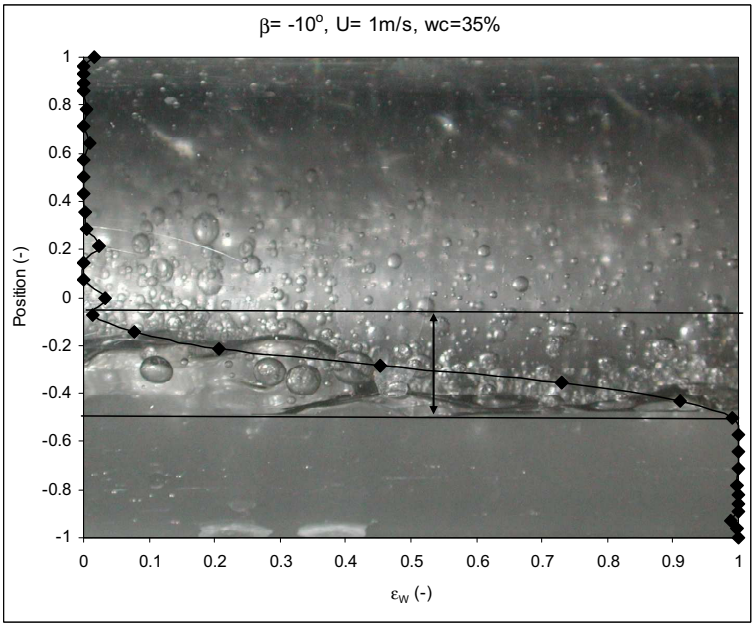

Figure 4.39 Gradient of the interfacial curve.

Figure 4.40 to Figure 4.54 present the measurements of the local phase fraction as function of inclination angles at different input water cut. Further analysis assumes an inversion water cut equal to 30%.

The position of the interface between oil and water, which is set equal to 30%, is varying with pipe inclination and input water cut. The altering location of the interface at constant input water cut implies that there is slip between the oil and water phase. The difference in interfacial position can be found in e.g. Figure 4.46. The interfacial position as function of inclination angle is decreasing from +10° to -10°, which indicates a larger holdup at +10° than at -10°. This is due to gravity forces, which is most pronounced at large upward inclinations and tends to retard the heavy water phase in upward flow. In downward flow, the water is the fastest moving phase and the holdup decreases. The difference in the position of the interface seems to increase with increasing input water cut from 10% (Figure 4.40) up to approximately 65% input water cut (Figure 4.47). The calculated slip ratio from the phase fraction distribution is presented in the section below.

Input water cut equal to 10%

The phase distribution curves at 10% input water cut (see Figure 4.40) show that there is a clear layer of oil in the upper part of the pipe, starting from below the centre of the pipe of the normalised radial position. At some inclinations, there is a dispersion of oil and water in the lower part of the pipe and at other inclinations, there is a clear water layer, indicating Do/w & o and ST & MI flow patterns respectively. Changing the inclination angle from 0° to ±1° increases the dispersion of oil in water in the bottom of the pipe and the Do/w & o flow regime appears. The largest effect is seen at -1°. The height of the water continuous phase at 30% input water cut is largest at +5° to +10° and lowest at -10° pipe inclinations. This is due to the gravitational force working in the opposite direction of the flow in upward inclination leading to accumulation of water. A water layer in the bottom of the pipe appears when the inclination changes from ±1° to ±5° and ±10°. Both still pictures and measured phase fractions equal to one reveals a water layer in the bottom of the pipe. The largest interfacial region is seen in upward flow, indicating that a larger degree of mixing and/or interfacial waves occur at these inclinations.

Input water cut equal to 15%

Figure 4.41 shows a clear oil layer above a dispersion of oil in water at 0° and -1° inclination angle, but at 0° angle the still pictures captures a water layer in the bottom of the pipe. The phase fractions below one at 0° angle in the bottom of the pipe is due to a wavy dispersed phase, which at times touches the bottom of the pipe. Since a water phase is observed in the

still pictures the flow is classified as ST & MI at 0° angle. But at -1° angle the flow is classified as Do/w & o. Decreasing the pipe further down to -5° and -10° a water layer occurs in the bottom of the pipe and the flow changes from being Do/w & o to ST & MI. The height of the interfacial region is largest at +10°, +5° and -1° angle.

Input water cut from 20 to 75%

Figure 4.42 to Figure 4.49 show the influence of pipe inclinations on the phase distributions curves at input water cut ranging from 20 to 75%. The phase fractions are equal to zero in the upper part of the pipe and equal to one in the lower part of the pipe. The flow from 20 to 75% input water cut is therefore classified as ST & MI. The gradient of the phase fraction curve is steepest for upward moving flow at high inclinations. This implies a larger amount of mixing and/or waves at the interface at +5° and +10° inclination angles compared to horizontal and downward flow. Measurements conducted by Oddie et al. (2003) indicate that upward inclinations (+2°) led to larger degree of dispersion between oil and water compared with downward (-2°). Lum et al. (2006) measured a more dispersed and wavy flow in the dual continuous (DC) flow regime in both upward and downward flow compared with horizontal flow. Many more drops were measured in downward inclination (-5°) compared with upward inclination, indicating that the degree of dispersion was most pronounced in downward flows. Kumara et al. (2009a) measured a wavier interface and larger Reynolds stresses at +5° than at -5° using the same experimentally facility and fluids, but with use of a lower mixture velocity (0.25 m/s) at constant input water cut equal to 25%. However, a larger degree of dispersion was measured at -5° pipe angle. The opposite trend was measured at lower inclinations, where a smooth interface with no mixing was measured at -1° pipe angle, while mixing was seen at +1°. Present measurements show the opposite. A larger degree of dispersion and/or waves is observed in the bottom of the pipe at -1° angle than at +1° angle at 20% input water cut. The difference is probably due to a larger mixture velocity in present study.

The flow structure in Figure 4.50 and Figure 4.51 at 50% input water cut demonstrates the difference between -10° and +10° inclination angle. Larger amplitude waves, and more dispersed droplets are seen at +10° angle. In the phase distribution profile, this is measured as a larger interfacial region at +10° compared to -10°.

Input water cut equal to 80%

The oil layer at 80% input water cut is totally dispersed with water droplets for most inclinations (see Figure 4.52).. The dense dispersion of oil and water in the top of the pipe increases the effective viscosity, which is reflected in the sudden increase in the pressure gradient measurements. At ±5° a clear oil layer is still measured and hence the flow classifies as ST & MI. Comparing visual observations and phase fractions reveals a PG regime at +10º angle and 80% input water cut. Since the gamma densitometer is not able to measure the dynamic behaviour of the flow, the PG flow regime cannot be detected in the phase distribution profiles.

Input water cut equal to 85 - 90%

An increased amount of mixing is seen at 85 and 90% input water cut in the upper layer (see Figure 4.53 and Figure 4.54) and the oil phase is fully dispersed. For the inclination range studied, the flow classifies as Dw/o & w. From the centre of the pipe and up to the top of the pipe, a dense dispersion of oil and water droplets exists. No large differences are seen between the inclination angles. The curves indicate an increase in water fraction near the top wall for all inclinations. A possible explanation could be seen in measurements conducted by Soleimani (1999) and Valle and Kvandal (1995). They reported a higher water fraction around the edge of the pipe at approximately 1 m/s and high input water cut. The measurements indicated an oil core encapsulated by water with a strongly curved interface. Soleimani (1999) used both high frequency probe and gamma densitometry system and Valle and Kvandal (1995) used conductance probes mounted around the inner periphery of the pipe. Since the accuracy of the measurements in present study is poorer close to the wall, the sudden increase in the top of the pipe could also be due to inaccurate measurements. If the inversion water cut where set equal to 20% at 85% input water cut, the flow would change from stratified (Dw/o & w) to dispersed (Do/w & w) at -5° and +5 inclination angle and at 90% input water cut all of the flow regimes would classify as dispersed flow (Do/w & w).

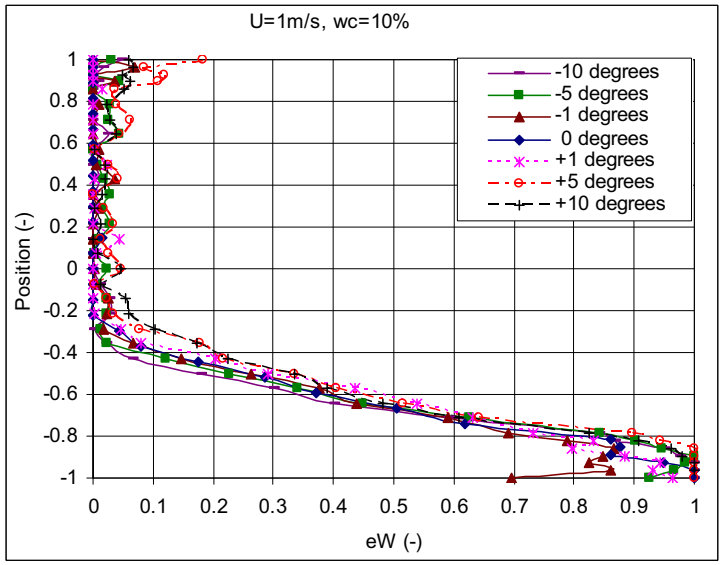

Figure 4.40 Local phase fraction vs. position at 10% input water cut and inclination angles from -10° to +10°.

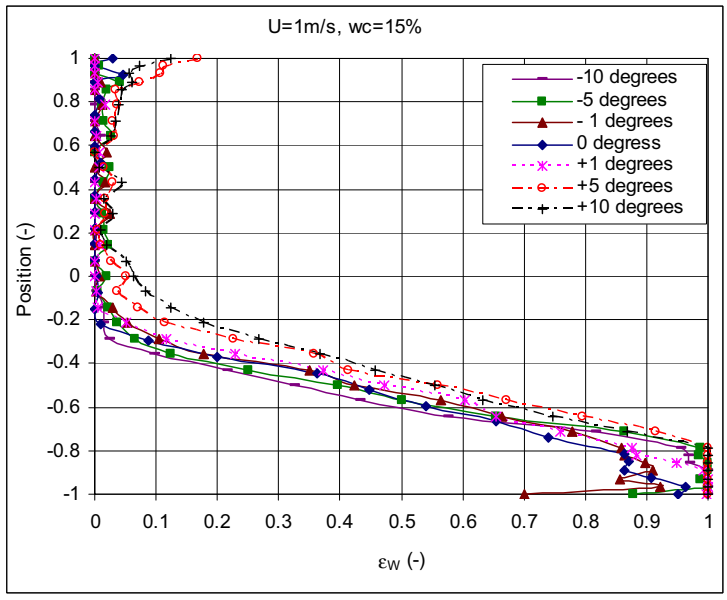

Figure 4.41 Local phase fraction vs. position at 15% input water cut and inclination angles from -10° to +10°.

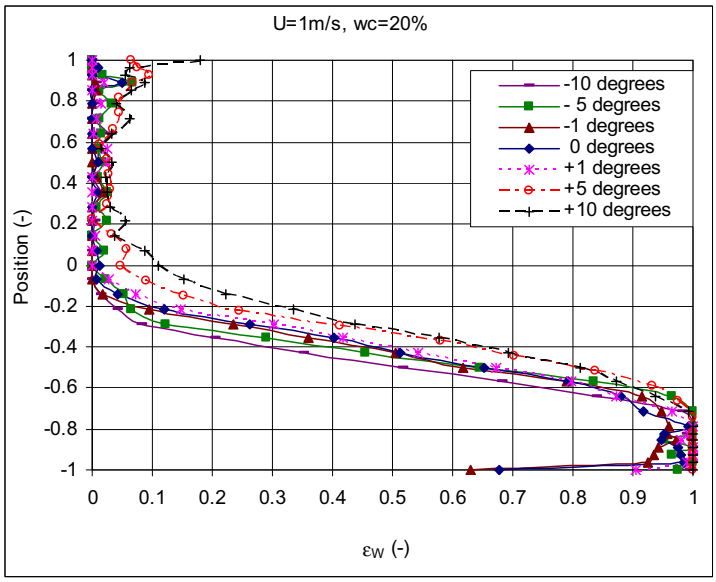

Figure 4.42 Local phase fraction vs. position at 20% input water cut and inclination angles from -10° to +10°.

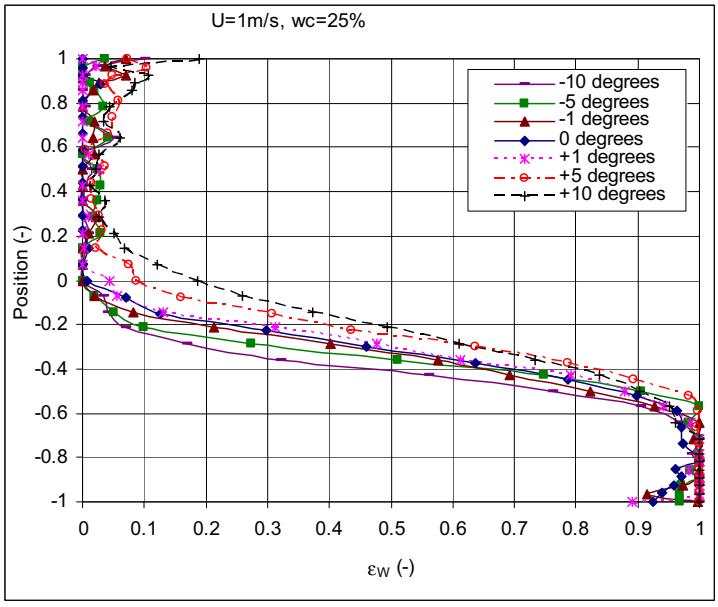

Figure 4.43 Local phase fraction vs. position at 25% input water cut and inclination angles from -10° to +10°.

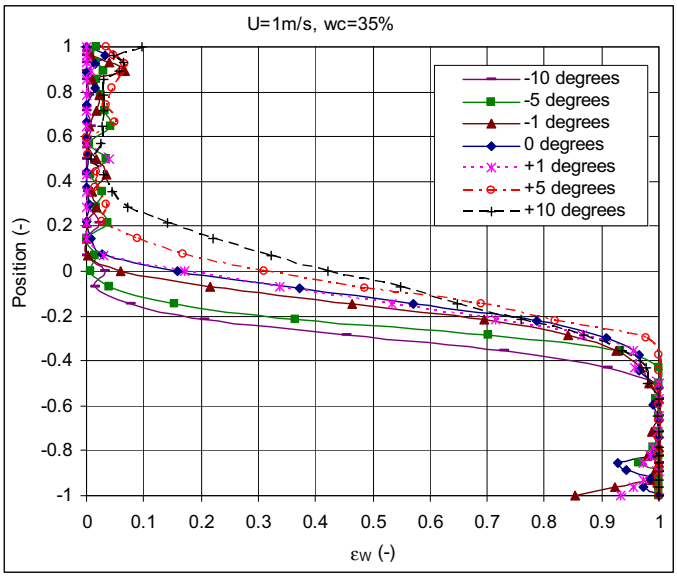

Figure 4.44 Local phase fraction vs. position at 35% input water cut and inclination angles from -10° to +10°.

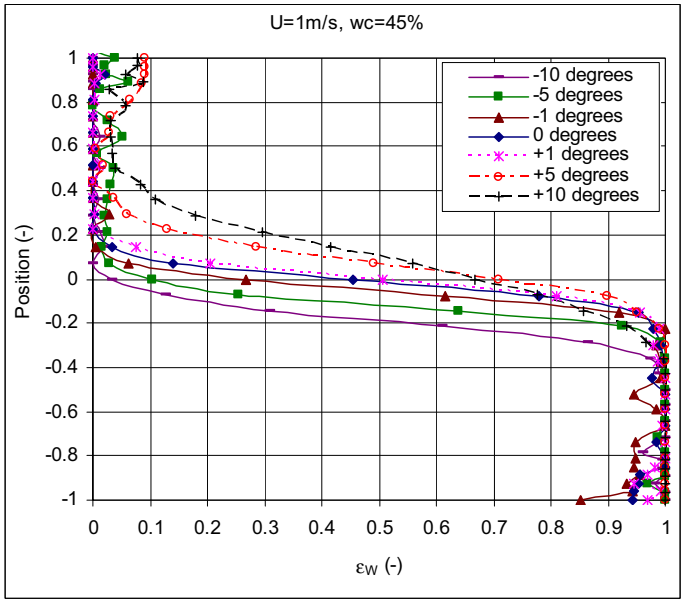

Figure 4.45 Local phase fraction vs. position at 45% input water cut and inclination angles from -10° to +10°.

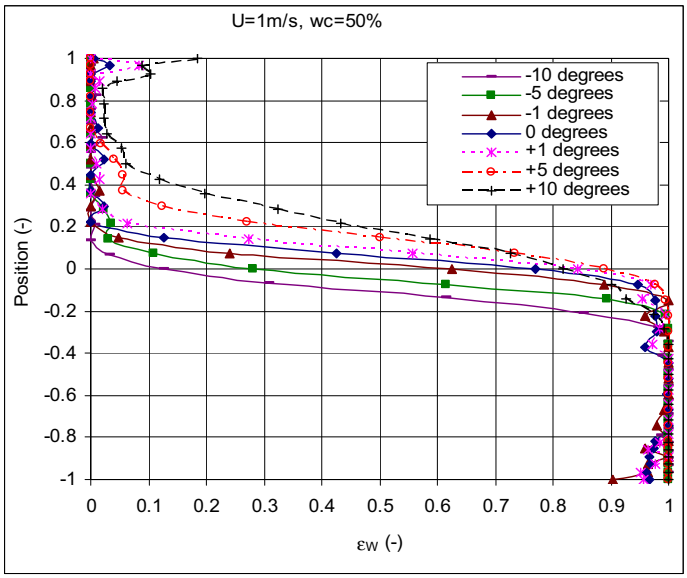

Figure 4.46 Local phase fraction vs. position at 50% input water cut and inclination angles from -10° to +10°.

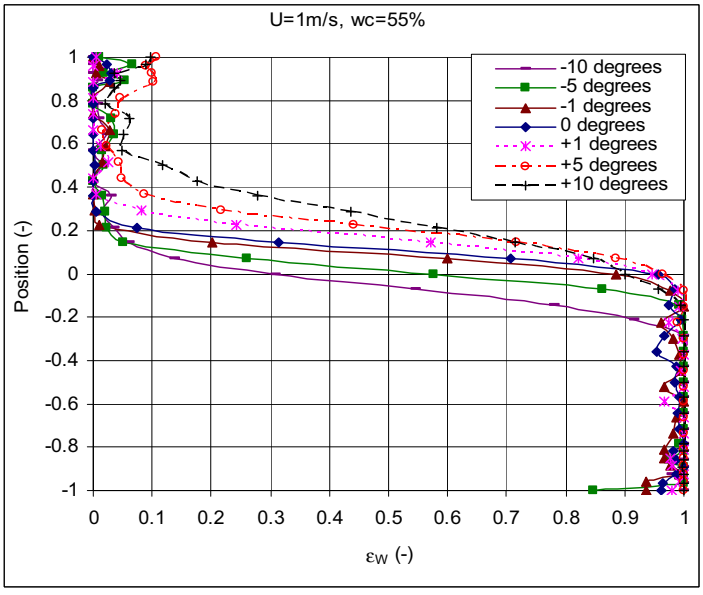

Figure 4.47 Local phase fraction vs. position at 55% input water cut and inclination angles from -10° to +10°.

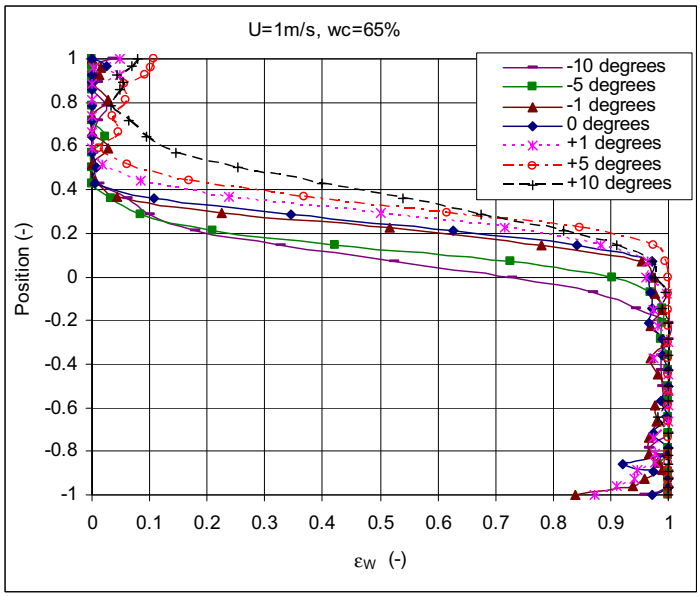

Figure 4.48 Local phase fraction vs. position at 65% input water cut and inclination angles from -10° to +10°.

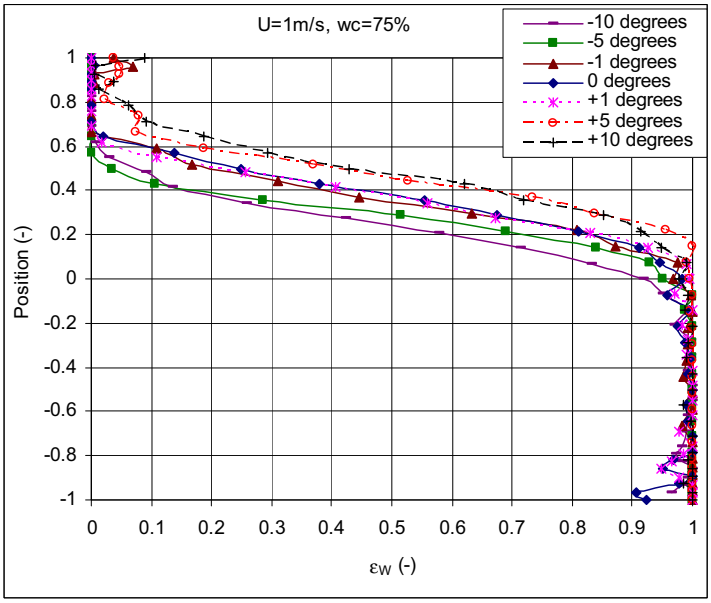

Figure 4.49 Local phase fraction vs. position at 75% input water cut and inclination angles from -10° to +10°.

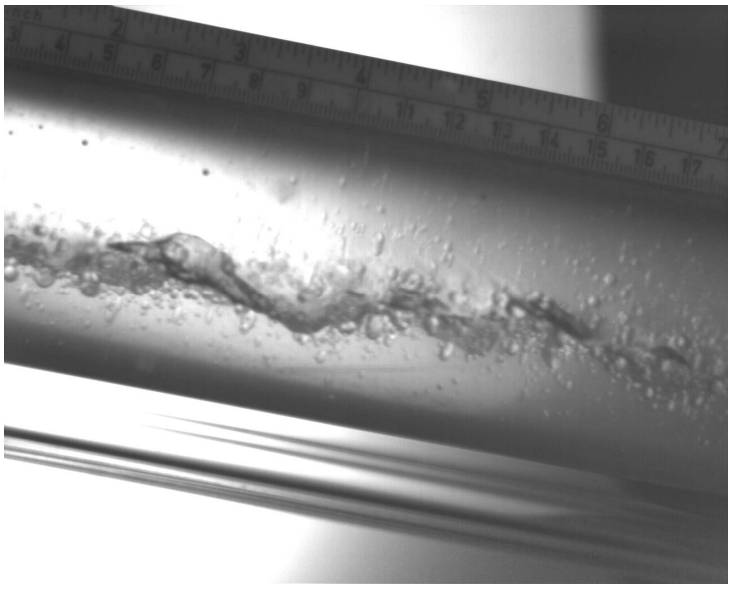

Figure 4.50 Flow structure at 50% input water cut at -10° inclination angle.

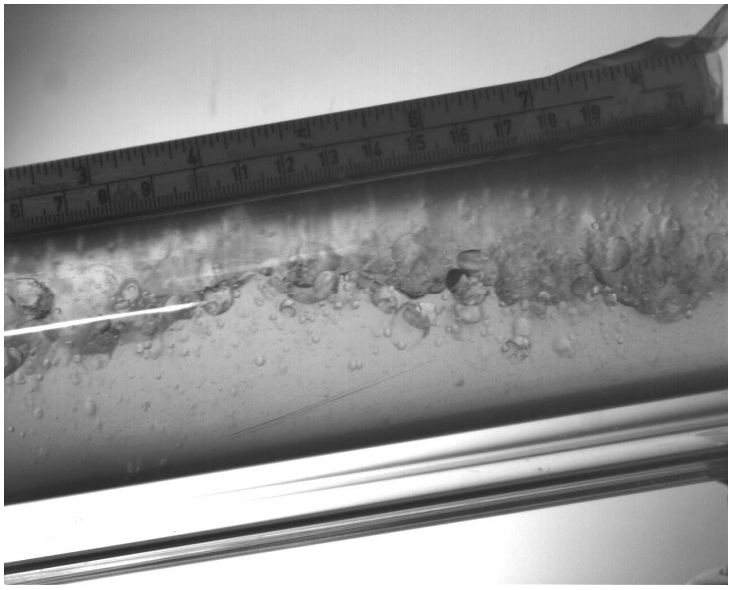

Figure 4.51 Flow structure at 50% input water cut at +10° inclination angle

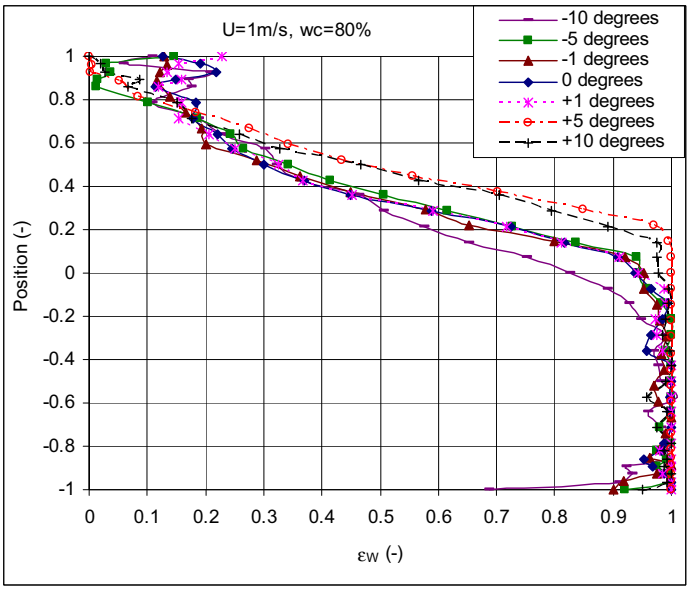

Figure 4.52 Local phase fraction vs. position at 80% input water cut and inclination angles from -10° to +10°.

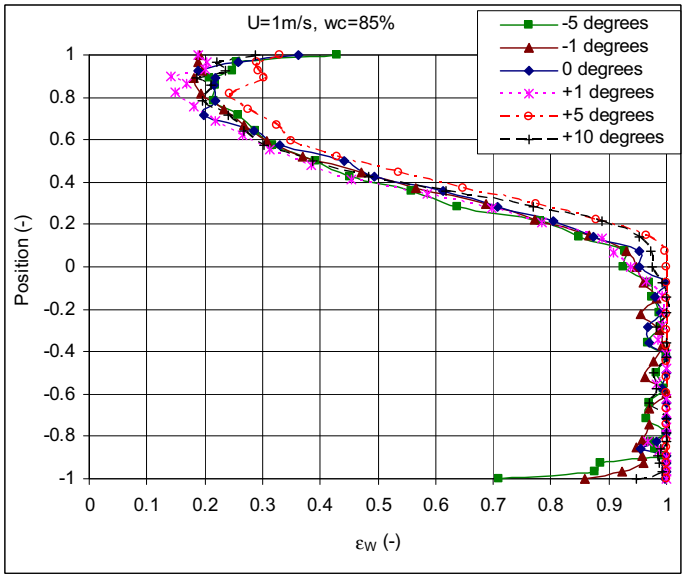

Figure 4.53 Local phase fraction vs. position at 85% input water cut and inclination angles from -5° to +10°.

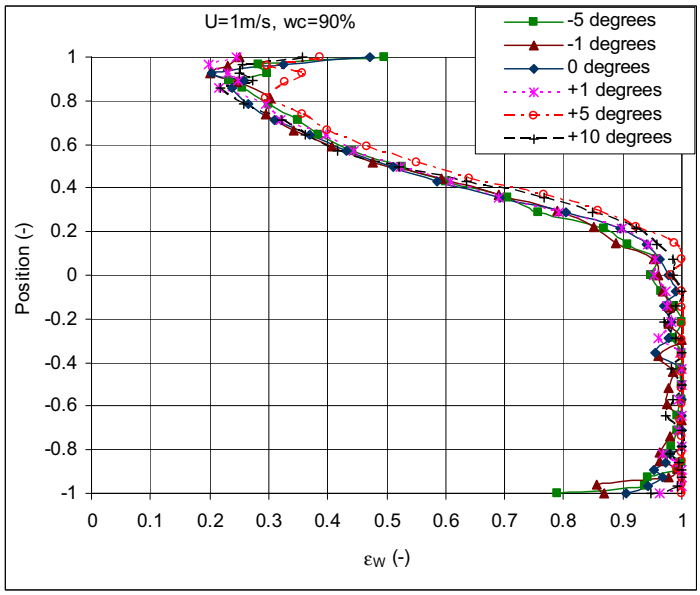

Figure 4.54 Local phase fraction vs. position at 90% input water cut and inclination angles from -5° to +10°.

4.10 Comparison with previous flow patterns

Classification of flow patterns often involves different experimentally techniques, different definitions and names for the same flow regimes. The first step when comparing with other publications is therefore to make sure that the classifications used are equivalent.

4.10.1 Flow pattern classifications

Elseth (2001) studied horizontal oil and water pipe flow with equal instrumentation and fluids as in present study. Elseth (2001) used visual observations in the classification of flow regimes. An equivalence table between flow regimes defined by present work and Elseth (2001) is presented in Table 4.6. The stratified smooth (SS) and stratified wavy (SW) flow patterns defined by Elseth (2001) is equivalent with the stratified (ST) flow pattern in present work and the stratified mixed (SM) is equivalent with the stratified flow with mixing at the interface (ST & MI). Elseth's (2001) water continuous dispersion with dense packed layer of oil droplets (Dw-DP) flow regime classifies as dispersed oil in water and water (Do/w & w) in present work and the oil continuous dispersion with dense packed layer of water droplets (Do-DP) as dispersed water in oil and oil (Dw/o & o). The homogenous oil continuous dispersion

(Do-H) and the inhomogeneous oil continuous dispersion (Do-I) are equivalent with the water in oil emulsion (w/o) defined in present study and the homogenous water continuous dispersion (Dw-H) and inhomogeneous water continuous dispersion (Dw-I) are equivalent with the oil in water emulsion (o/w). The dispersion of water in oil and oil in water (Dw/o & Do/w), dispersed water in oil and water (Dw/o & w), dispersed oil in water and oil (Do/w & o) and plug flow (PG) were not classified by Elseth (2001).

Table 4.6 Equivalence between present and Elseth (2001) flow patterns.

Present work		**Elseth (2001)**	
Stratified flow	ST	SS	Stratified smooth
Stratified flow	ST	SW	Stratified wavy
Stratified flow with mixing at the interphase	ST & MI	SM	Stratified wavy Stratified mixed
Dispersion of oil in water and water	Do/w & w	Dw-DP	Water continuous dispersion with dense packed layer of oil droplets
Dispersion of water in oil and oil	Dw/o & o	Do-DP	Oil continuous dispersion with dense packed layer of water droplets
Water in oil emulsion	w/o	Do-H Do-I	Oil continuous dispersion, homogenous Oil continuous dispersion, inhomogeneous
Oil in water emulsion	o/w	Dw-H Dw-I	Water continuous dispersion, homogenous Water continuous dispersion, inhomogeneous
Dispersion of water in oil and oil in water	Dw/o & Do/w	-	-
Plug flow	PG	-	-
Dispersionof water in oil and water	Dw/o & w	-	-
Dispersion of oil in water anad oil	Do/w & o	-	-

Table 4.7 shows that the stratified wavy flow classified by Lum et al. (2006) is consistent with the ST flow pattern in present study. The dual continuous flow regime (DC) of Lum et al. (2006) is consistent with the stratified flow regimes in present study ST & MI, Dw/o & Do/w, Dw/o & w and Do/w & o). Lum et al. (2006) does not distinguish between the level of dispersion of one phase into the other. The dispersed oil-in-water (Do/w) flow regime of Lum

et al. (2006) is equivalent with the Do/w & w and o/w flow patterns and the dispersed water-in-oil (Dw/o) is consistent with the Dw/o & o and w/o.

Table 4.7 Equivalence between present and Lum et al. (2006) flow patterns.

Present work		**Lum et al. (2006)**	
Stratified flow	ST	SS	-
Stratified flow	ST	SW	Stratified wavy
Stratified flow with mixing at the interface Dispersion of water in oil and oil in water Dispersionof water in oil and water Dispersion of oil in water and oil	ST & MI Dw/o & Do/w Dw/o & w Do/w & o	DC	Dual continuous flow
Dispersion of oil in water and water Oil in water emulsion	Do/w & w o/w	Do/w	Dispersed oil-in-water
Dispersion of water in oil and oil Water in oil emulsion	Dw/o & o w/o	Dw/o	Dispersed water-in-oil
Plug flow	PG	PG	Plug flow

4.10.2 Horizontal flow

Table 4.8 lists the flow regimes measured by present work, Elseth (2001) and Lum et al. (2006) in horizontal pipe flow at mixture velocity equal to 1 m/s. Application of present classification approach on the measured phase distribution of Elseth (2001) leads to a re-classification of some of the flow regimes (see Table 4.8). Elseth (2001) used still pictures to classify the flow regime and present study used a combination of still pictures and phase fraction measurements. The SW flow regime of Elseth (2001) was re-classified to ST & MI since the flow regime always contained some droplets at the wavy interface. The dispersed flow regimes (Dw/o & o and Do/w & w) measured in the top and in the bottom of the pipe were re-classified into stratified flows (Do/w & o and Dw/o & w).

Comparing the re-classified flow regimes of Elseth (2001) with present experiments shows small discrepancies. Present study measures ST & MI and Dw/o & w at 10 and 80% input water cut, while Elseth (2001) measures Do/w & o and ST & MI at the same input water cuts.

The reason to the observed differences could be that Elseth (2001) used a slightly larger mixture velocity compared with present study.

Lum et al. (2006) measured a DC (ST & MI, Dw/o & Do/w, Dw/o & w or Do/w & o) flow at input water cut ranging from 10 to 90%, which is equal to the experimental findings in present work. Lum et al. (2006) observed large structure variations in the DC. The dispersion was not necessarily uniform within each layer and the level of dispersion varied as function of input water cut and inclination angle. Lum et al. (2006) used a smaller pipe diameter (38 mm) and larger oil viscosity (5.5 cp) than present study.

Table 4.8 Flow regimes in horizontal pipe flow measured by present work, Elseth (2001) and Lum et al. (2006)

Water cut [%]	**Present work**	**Elseth (2001) Measured flow patterns**	**Elseth (2001) Re-classified flow patterns**	**Lum et al. (2006)**
10	ST & MI	Do-DP (Dw/o & o)	Do/w & o	DC
15	ST & MI	SM (ST & MI)	-	DC
20	ST & MI	SM (ST & MI)	-	DC
25	ST & MI	SM (ST & MI)	-	DC
40	ST & MI	SW (ST)	ST & MI	DC
50	ST & MI	SW (ST)	ST & MI	DC
60	ST & MI	SW (ST)	ST & MI	DC
70	ST & MI	SW (ST)	ST & MI	DC
75	ST&MI	SM (ST & MI)	-	DC
80	Dw/o & w	SM (ST & MI)	-	DC
85	Dw/o & w	Dw-DP (Do/w & w)	Dw/o & w	DC
90	Dw/o & w	Dw-DP (Do/w & w)	Dw/o & w	DC

4.10.3 Inclined pipes

In Table 4.9 the measured flow patterns at ±5° and +10° are compared with measurements of Lum et al. (2006). The flow patterns are identical from 10 to 60% input water cut. In contrast to the dispersed flow (Do/w) measured by Lum et al. (2006) at -5° angle and 80% input water cut, present study measures a stratified flow (ST & MI). However, the phase distribution measurements of Lum et al. (2006) in the upper part of the pipe are very similar to present measurements. Both studies measured a low water fraction in the upper part of the pipe.

Despite the low water fraction, Lum et al. (2006) measured the fluid of the continuous phase to be water. While present study measures a stratified flow (Dw/o & w) at inclination angles equal to +5º and +10º angle and input water cut equal to 90%, Lum et al. (2006) measured a dispersed flow (Do/w). Since the fluid of the continuous phase has not actually been measured in present study, it is difficult to determine whether the deviations in observed flow regimes at both 80 and 90% input water cut are due to different classification approaches or due to actual flow behaviour. Lum et al. (2006) observed a dispersed flow regime (Do/w) at 70% input water cut in the region where present measurements show a stratified (ST & MI) flow pattern. This indicates a larger degree of dispersion in downward flow in the measurements of Lum et al. (2006) compared with present study, which can be due to the lower pipe diameter of Lum et al. (2006). Lum et al. (2006) observed the plug flow (PG) regime at the same input water cut as present study and at lower input water cut equal to 70%.

Table 4.9 Flow regimes in inclined pipe flow by present work and Lum et al. (2006)

Water cut [%]	**Flow pattern in present work**			**Flow pattern in Lum et al. (2006)**		
	+5° angle	-5° angle	+10° angle	+5° angle	-5° angle	+10° angle
10	ST & MI	ST & MI	ST & MI	DC	DC	DC
15	ST & MI	ST & MI	ST & MI	-	-	-
20	ST & MI	ST & MI	ST & MI	DC	DC	DC
25	ST & MI	ST & MI	ST & MI	DC	DC	DC
35	ST & MI	ST & MI	ST & MI			
40	-	-	-	DC	DC	DC
45	ST & MI	ST & MI	ST & MI	-	-	-
50	ST & MI	ST & MI	ST & MI	DC	DC	DC
55	ST & MI	ST & MI	ST & MI			
60	-	-	-	DC	DC	DC
65	ST & MI	ST & MI	ST & MI	-	-	-
70	-	-	-	DC	Do/w	PG
75	ST&MI	ST&MI	ST&MI	DC	-	-
80	ST & MI	ST & MI	PG	DC	Do/w	PG
85	Dw/o & w	Dw/o & w	Dw/o & w	DC	-	-
90	Dw/o & w	Dw/o & w	Dw/o & w	Do/w	Do/w	Do/w

4.11 Slip ratio

The in situ phase fractions determined by use of gamma densitometer are used to calculate the slip ratio. Oddie et al. (2003) compared the holdup from the quick closing valves (QCV) measurements and the holdup computed from the gamma densitometer. Oddie et al. (2003) showed good agreement between the techniques. The difference between the two techniques was approximately within ±20% for 93% of the data points. The gamma densitometer was aligned on a vertical diameter in a fixed position and the accuracy of the measured density was estimated to be within 1%.

In present study the beam is assumed infinitely thin. The in situ phase fractions can therefore be area averaged instead of volume averaged. Since the area of the beam changes as function of beam position, the measured phase fractions in the different position are area averaged. Calculations of the area averaged in situ water phase fraction (ε_w) are shown in Eq. (4.22) and the holdup ratio (slip ratio) are presented in Eq. (4.23). The area of the beam is derived from Eq. (4.24).

$$\varepsilon_w = \sum \frac{\varepsilon_i A_i}{A_{tot}} \tag{4.22}$$

$$S_{ow} = \frac{\varepsilon_w U_{so}}{(1-\varepsilon_w) U_{sw}} \tag{4.23}$$

The area of the beam in different position in the pipe is calculated from Eq. (4.24), where R is the inner pipe radius, D_g is the beam diameter and z is the position in the pipe.

$$A_i = 2R \int_{R-z}^{R-z_i+D_g} \sqrt{1-\left(\frac{z_i}{R}\right)^2}\, dz \tag{4.24}$$

4.11.1 Horizontal and downward pipe inclinations

Figure 4.55 presents the slip ratio between oil and water from -10° to 0° inclination angle. For horizontal and downward flow, the slip ratio has large values at 10% input water cut and has a decreasing trend down to 90% input water cut. At low water cuts the slip ratio is measured to

be above one, meaning oil is travelling faster than water. The water phase experience larger shear compared with the oil phase, since the water-wetted perimeter is large compared to the volume occupied by the water. At high water cuts, the oil-wetted perimeter is large compared with the volume of oil leading to a slip ratio below one. Then, water is the fastest moving phase. When the slip ratio is equal to one, the oil and water flows with equal velocities. At 0° pipe inclination the slip ratio is equal to one at 55% input water cut and above one at 50% input water. The oil flows therefore faster than water at 50% input water cut. A possible explanation for this can be found in the measurements of Lovick and Angeli (2004a), which also measured a higher oil velocity than water at 50% input water cut, even the viscosity was 6 times that of water. The reason was due to an upward curved measured interface at 50% input water cut, which led to an increased water-wall contact compared to its volume. The water phase therefore experienced larger frictional forces, which resulted in a larger slip ratio. Another explanation is that the current wall shear is lower in the oil phase compared with the one in the water phase (see Chapter 6). A slip ratio equal to one occurs at quite different input water cuts dependent on the pipe inclination. A slip ratio equal to one occurs at decreasing input water cuts as the pipe inclination decreases. The no slip condition starts at 55% input water cut for 0° angle and decreases down to 30% input water cut when the pipe inclination decreases to -10° angle. At 0° pipe inclination Lum et al. (2006) measured a slip ratio equal to one at a much lower input water cut (between 20 and 25%) than present study shows and at -5° the slip ratio was equal to one over a range of input water cut (40-75%). Lum et al. (2006) observed a higher degree of mixing in the dual continuous flow regime in downward flow, which in addition to the effect of gravity explained the slip ratios close to one in many cases.

The especially low oil-water slip ratios measured at large input water cuts are attributed to the increase in effective viscosity in the dispersed layer in top of the pipe. This phenomenon was also measured by Valle (2000) by use of Exxsol D60.

Large differences in slip ratios between the angles are generally seen at medium input water cut, ranging from 30% to 75 %, while they are very similar at low and high input water cuts. At medium input water cut the slip ratio decreases with decreasing inclination angle (0 to -10°), which means that water phase velocity increases due to the increase in gravitational effect. Lum et al. (2006), Abduvayt et al. (2006), Rodriguez and Oliemans (2006) and Atmaca

et al (2008) also measured an increasing water phase velocity with increasing downward inclination.

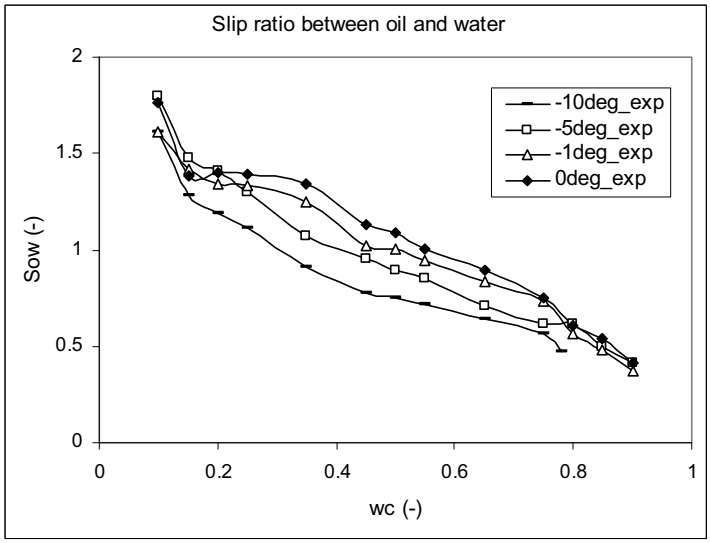

Figure 4.55 Slip ratio vs. input water cut at downward inclinations (-10° to 0°).

4.11.2 Horizontal and upward pipe inclination

Figure 4.56 shows the slip ratios trends in horizontal and upward moving flow. The slip ratios at low to medium input water cuts are larger in upward inclined flow compared to horizontal flow and have an increasing trend with increasing inclination angle. This is in agreement with the measurements conducted by Alkaya (2000), Lum et al. (2004), Abduvayt et al. (2006), Rodriguez and Oliemans (2006) and Atmaca et al. (2008), which measured a higher slip ratio in inclined flow compared to horizontal flow.

The slip ratio is large and above one at 10% input water cut. Increasing the water cut decreases the slip ratio to below one. This is the same trend as was observed in downward inclinations, but in upward flows the slip ratio is equal to one at much higher input water cuts, which means that the oil flows faster than the water phase at a larger number of input water cuts. In upward moving flow, the slip ratio is equal to one at 55% input water for 0° angle and increases up to 75% input water cut for +5° and +10° angle. Lum et al. (2006) also measured

a slip ratio equal to one at large input water cut equal to approximately 80% in upward inclinations (+5° and +10°).

Minor differences in slip ratios is seen between 0° and +1° angle and between +5° and +10° angle, while inclining the pipe from +0° to +5° has large effect on the slip ratio. Lum et al. (2006) also measured that the increase in slip ratio was larger from 0° to +5° than from +5° to +10° and explained this by the increased mixing at +10° angle. Kumara et al. (2009a) measured the opposite trend, where the largest effect in slip ratio was observed between 0° and +1° inclination angle. This is probably due to a much lower mixture velocity equal to 0.25 m/s in the work of Kumara et al. (2009a). The transition from ST & MI to PG flow do not influence the slip ratio in present study. In contrast, Lum et al. (2006) measured a large increase in the slip ratio.

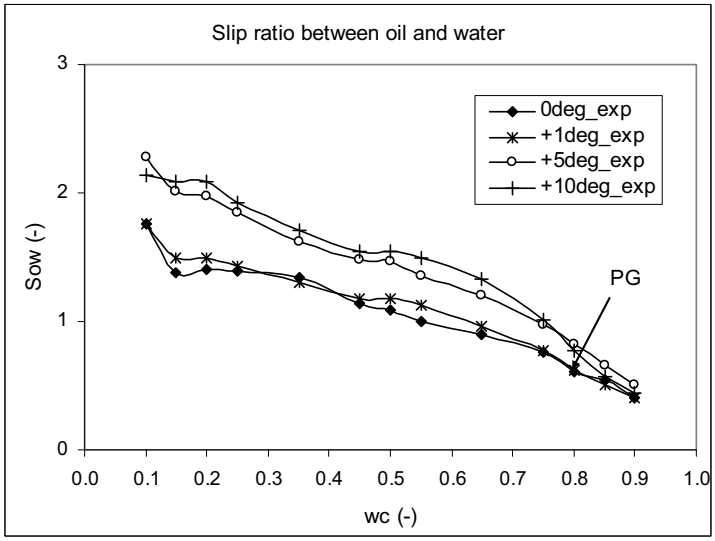

Figure 4.56 Slip ratio vs. input water cut at upward inclinations (0° to +10°).

4.11.3 Downward compared with upward pipe flow

Figure 4.57 to Figure 4.59 show that the slip ratio is larger in upward flow compared to downward flow, which means that the oil is the fastest moving phase in upward flow and water in downward flow. In upward flow, the gravity works opposite of the flow direction and retards the high-density phase (water) which leads to a higher slip ratio compared with

downward flow. In downward flow, the gravity works in the flow direction and favours the high-density phase, which leads to a faster moving water phase and a lower slip ratio compared with upward. Kumara et al. (2009a) also reported a larger slip ratio in upward flow compared to downward flow. The difference between the slip ratio increases with increasing inclination angle.

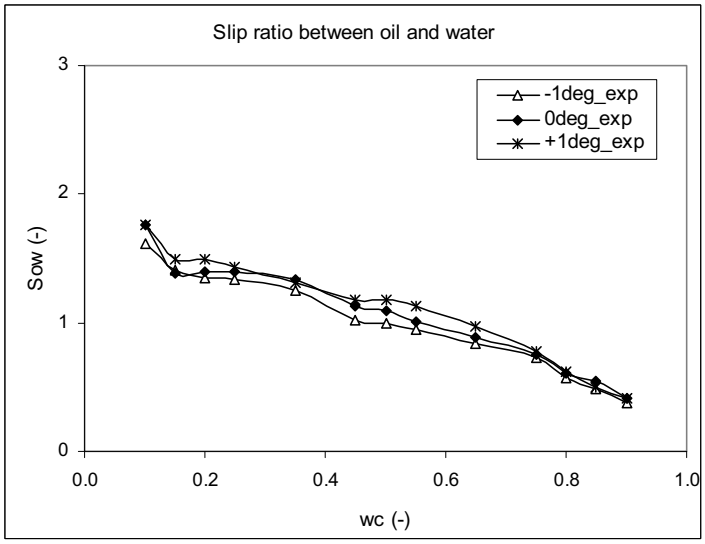

Figure 4.57 Slip ratio vs. input water cut at -1°, 0° and +1°.

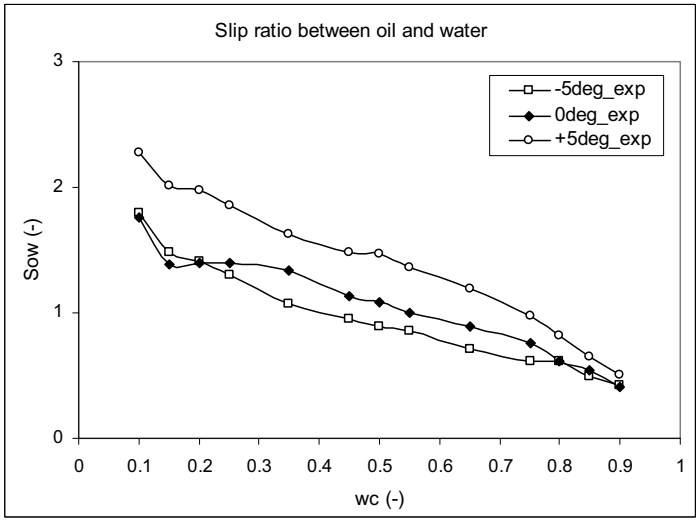

Figure 4.58 Slip ratio vs. input water cut at -5°, 0° and +5°.

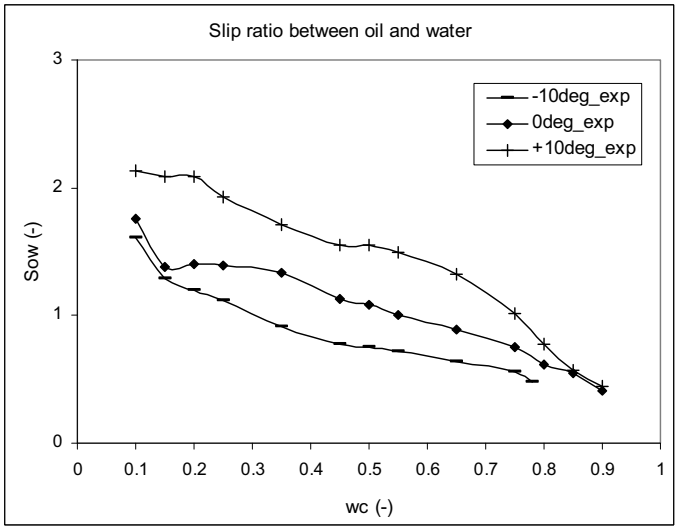

Figure 4.59 Slip ratio vs. input water cut at -10°, 0° and +10°.

4.12 Summary

- The gamma instrument produces vertical phase fraction measurements, which provides important characteristics of the flow behaviour.
- A new classification approach is introduced which makes the classification more objective. The method uses the measured phase fractions and a pre-defined phase inversion water cut to distinguish between stratified and dispersed flow.
- The flow regimes identified in present study in the parameter range studied (1 m/s, -10º to +10° inclination and 10 to 90% input water cut) are:
    - Stratified flow with mixing at the interface (ST & MI).
    - Dispersion of water in oil and water (Dw/o & w).
    - Dispersion of oil in water and oil (Do/w & o).
    - Plug flow (PG).
- The ST & MI flow regime dominates the flow pattern map at medium input water cuts, the Dw/o & w flow regime at high input water cut and the Do/w & o at low input water cuts and low inclinations (±1°). The PG flow regime is only measured at one experimental condition equal to +10° angle and 80% input water cut.

- Local measurement techniques like e.g. impedance probes can be inserted to measure the fluid of the continuous phase and hence determine the local phase inversion water cut.
- Additional gamma measurements in other directions can provide valuable information about the interfacial curve and the radial phase distribution.
- Different measurement techniques and interpretation of the data can result in different flow regimes, which can give large deviations when comparing with other publications (see section 4.10).
- The slip ratio is calculated from the measured phase fractions and has a large ratio at 10% input water cut and decreases to below one as the input water cut increases for all inclinations studied.
- The slip ratio is above one at 50% input water cut and 0° angle, indicating that oil is moving faster than water. A faster moving oil phase agrees well with the maximum velocity measured with the Laser Doppler instrument.
- The slip is larger in upward flow compared to downward flow.
- The accuracy in the phase fraction measurements is best in the centre of the pipe. The accuracy decreases when approaching the wall (Figure 4.9). The error in single-phase water ranges from ±0.77% in the centre of the pipe to ±18% near the wall.
- The measurement error can be reduced by increasing the calibration time to from 1 to 10 min. This will improve the pulse-counting statistic. The total error in the centre of the pipe decreases with 30% when the calibration time goes from 1 to 10 min in single-phase water flow (see Section 4.6.1).
- The accuracy and reproducibility of the positioning of the traversing gamma instruments has large influence on the measurement accuracy. If the accuracy of the positioning is set equal to zero, the total error will decrease considerably (see Section 4.6.3).

5 TWO PHASE PRESSURE GRADIENT

The total pressure drop influences the rate of production and is therefore a crucial parameter in multiphase flow behaviour. This chapter presents the total and the frictional pressure drops for both horizontal and inclined pipes.

5.1 Experimental conditions and procedure

The number of pressure drop experiments is equal to the number of phase fraction experiments (see Table 4.4). The differential pressure two-phase flow measurements are measured across the shortest distance equal to 5.38 m. The differential pressure transmitters are adjusted to zero in horizontal pipe flow. The impulse lines are filled with water during all the experiments and the measurements start always by filling the pipe with oil and then increasing the input water cut from 0 to 100%.

5.2 Pressure drop calculations

The frictional pressure drop is calculated from the measured pressure drop and holdup. The pressure gradient is the pressure drop divided by the measurement length.

5.2.1 Inclined single-phase flow

In single-phase water inclined pipe flows, the frictional pressure drop is measured directly since the impulse lines are filled with water as shown in Eq. (5.1), where dp_m is the measured pressure drop. The frictional pressure drop is negative in the direction of the flow.

$$dp_f = dp_m \tag{5.1}$$

In single-phase inclined oil flow, the static head of the oil flow must be accounted for. For a given experiment, the static head is the product of the density difference (ρ_w - ρ_o), gravity (g), length between the impulse lines (L) and vertical height ($sin\beta$). The static head (dp_s) is expressed in Eq. (5.2) when no fluid flow.

$$dp_s = (\rho_w - \rho_o) \cdot g \cdot L \cdot \sin\beta \tag{5.2}$$

The frictional pressure loss is found in Eq. (5.3), where dp_m is the measured pressure drop.

$$dp_f = dp_m - (\rho_w - \rho_o) \cdot g \cdot L \cdot \sin\beta \tag{5.3}$$

The total pressure drop over a length L is shown in Eq. (5.4). The total pressure drop is the sum of the frictional and gravitational pressure losses.

$$dp_T = dp_m - \rho_w \cdot g \cdot L \cdot \sin\beta \tag{5.4}$$

5.2.2 Inclined two-phase flow

Eq. (5.5) expresses the frictional pressure loss in two-phase oil-water experiments in inclined pipes, where the mixture density (ρ_m) is the average density of the oil and water flowing inside the pipe.

$$dp_f = dp_m - dp_s = dp_m - (\rho_w - \rho_m) \cdot g \cdot L \cdot \sin\beta \tag{5.5}$$

The mixture density (ρ_m) can be calculated from Eq. (5.6) or (5.7), where α is the input water cut. Eq. (5.6) assumes no slip between the phases, which means that the oil and water phase moves with equal velocities. This is not used in present study.

$$\rho_m = \alpha \cdot \rho_w + \alpha_o \cdot \rho_o = \alpha \cdot \rho_w + (1-\alpha) \cdot \rho_o \tag{5.6}$$

If there is slip between the phases, the mixture density (ρ_m) has to be calculated from the measured in situ volume fractions (ε_i) as shown in Eq. (5.7). Area averaging of the calculated mixture density is used since the beam is assumed infinitely thin. Area averaging is important since the area of the beam changes as function of beam position. The measured density at different position is calculated in accordance with Eq. (5.7).

$$\rho_m = \sum \frac{(\rho_w \varepsilon_i + \rho_o (1-\varepsilon_i)) A_i}{A_{tot}} \tag{5.7}$$

5.3 Frictional pressure gradient

5.3.1 Horizontal flow

Figure 5.1 shows the normalized frictional pressure gradient at 0° angle as function of input water cut, respectively. The frictional pressure gradients are normalized with the single-phase oil gradient and is presented as positive in the flow direction. The two-phase frictional pressure gradient is equal or larger than single-phase oil values. The frictional pressure

gradient stays constant and equal to that of pure oil from 0 to 15% input water cut. Then a small peak occurs between 15 and 35% input water cut followed by a weak increasing trend up to 80% input water cut. The variations in pressure gradient could be a result of a concave interfacial curve and due to increased mixing at the interface. At 80% input water cut a sudden increase in the pressure gradient arises, which is 1.7 times larger than that of pure oil. The peak occurs when the flow goes from being ST & MI to Dw/o & w. The pressure gradient stays at this level up to 90% input water cut in the Dw/o & w flow regime. Since the pressure gradient increase is quite severe, the peak is most likely a result of an increased effective viscosity in the upper dispersed layer. The increase in effective viscosity is probably due to formation of clusters of droplets (flocculation). This phenomenon is very similar to the phase inversion process, where clusters and multiple drops are formed [Piela et al. (2008)]. Another explanation could be that the presence of the interface and entrained droplets will affect the single-phase shear stress correlations as was seen in the parametric study performed by Hadziabdic and Oliemans (2007). The phase fraction measurements show that the degree of dispersion increases in the upper layer as the input water cut increases from 80 to 90%, while the pressure gradient is constant. Valle (2000), Elseth (2001) and Wahumpurage et al. (2008) also measured this peak in pressure gradient by use of the same oil (Exxsol D60). This peak in pressure gradient is not always observed, even though the experimental conditions are very similar (see Chapter 2). Lum et al. (2006) measured a increase in frictional pressure gradient at approximately 70% input water cut, but the increase was not as steep as observed in present study. Lum et al. (2006) used Exxsol D140 and a 1 in. stainless steel pipe. In contrast to present study Lovick and Angeli (2004a) measured a lower pressure gradient in two-phase flow compared to single-phase oil.

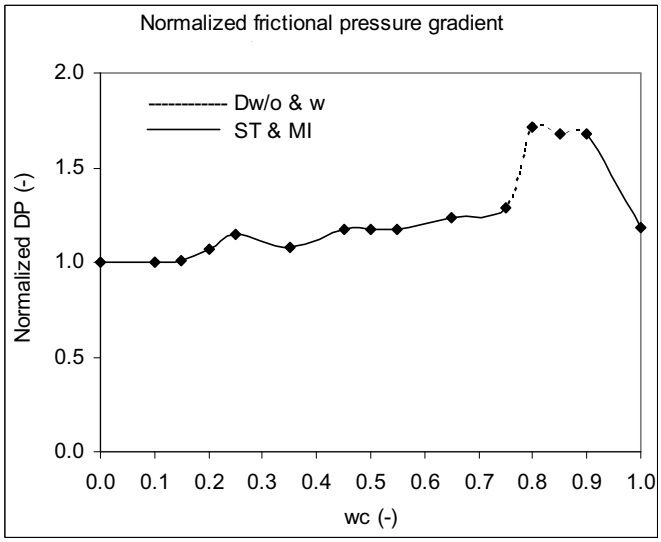

Figure 5.1 Normalized frictional pressure gradient vs. input water cut at 0° angle.

5.3.2 Pipe inclination from -10° to +10°

Figure 5.2 and Figure 5.3 show how the normalized frictional pressure gradient varies as the input water cut increases from 0 to 1 and the inclination increases from -10° to 0° and from 0° to +10°, respectively. A steep increase in pressure gradient is observed at approximately 80% input water cut for nearly all inclinations studied (-5° to +10°), where the flow transition from ST & MI to Dw/o & w occurs. The measurements at -10°C stopped at 78% input water cut due to air bubbles at larger water cuts. The peak is in the same order of magnitude for all inclinations studied. The transition from Do/w & o to ST & MI at low input water cuts and at low inclination angles (±1º) does not seem to have any significant influence on the frictional pressure gradient. The variations in the normalized frictional pressure gradient between different angles are small and within 20%.

Figure 5.2 shows the normalized frictional pressure gradient trends in horizontal and downward flow. The gradient is generally above that of pure oil, which is opposite of the measurements conducted by Lum et al. (2004) and Lum et al. (2006). Lum et al. (2006) measured a lower frictional pressure gradient in downward flows compared with horizontal flow.

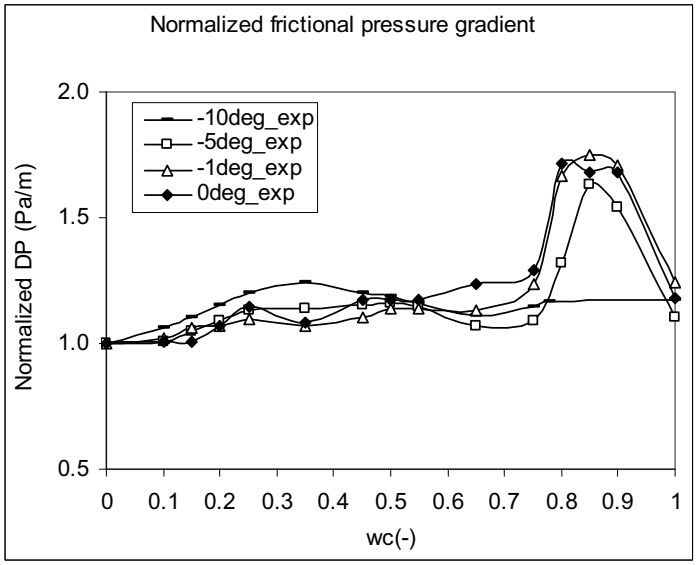

Figure 5.2 Normalized frictional pressure gradient vs. water cut from -10° to 0° angle.

Figure 5.3 shows that the normalized pressure gradient in upward flow is generally very similar, in terms of both trends and absolute values, which was also observed in downward flow. The pressure gradient is lower in upward flow compared with horizontal flow, which is most likely due to the higher measured in situ water fraction (see Chapter 4). Lum et al. (2006) also measured that the frictional pressure gradient trend and absolute value were similar at 0°, +5° and +10° inclination angle and that the frictional pressure gradient was lowest in upward flow compared to horizontal flow. The reduction in pressure gradient was attributed to the increased in-situ water fraction. A decrease in normalized frictional pressure gradient is observed from 0 to 10% input water cut at +1°, +5° and +10° angle. The two-phase gradient is lower than of single-phase oil. Increasing the amount of water from 10% to pressure gradient is in this region lower than that of single-phase oil. Increasing the amount of water from 10% to approximately 80% input water cut in present study, leads to an gentle increase, which is probably due to an gradually increase in the effective viscosity. An abrupt increase in normalized frictional pressure gradient is seen at 80% input water cut for upward inclinations. The size of the peak is of the same order of magnitude as for downward flow. The largest observed gradient is measured at 0° angle and 80% input water cut and the lowest at +10° angles between 0 and 35% input water cut.

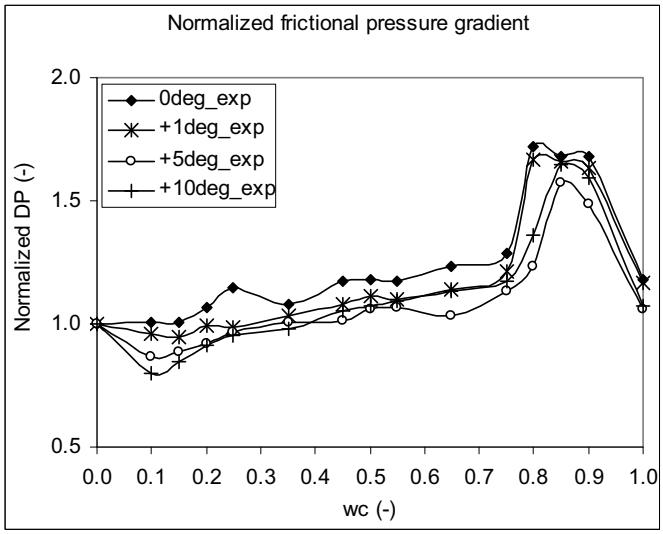

Figure 5.3 Normalized frictional pressure gradient vs. water cut from 0° to +10° angle.

The difference in normalized frictional pressure gradient between downward and upward inclinations increases with increasing inclination as seen in Figure 5.4 to Figure 5.6. In general, the normalized frictional pressure gradient is measured to be lower in upward flow compared to downward flow, especially at medium to low input water cuts. This is mainly due to the gravity forces working in the opposite direction of the flow in upward inclinations, leading to accumulation of the high-density water phase. Lum et al. (2006) measured an opposite trend, the frictional pressure gradient was slightly lower in downward flow (-5°) compared to upward flow (+5°). This was attributed to the increased mixing in downward flow. The viscous oil was dispersed instead of accumulated in the pipe.

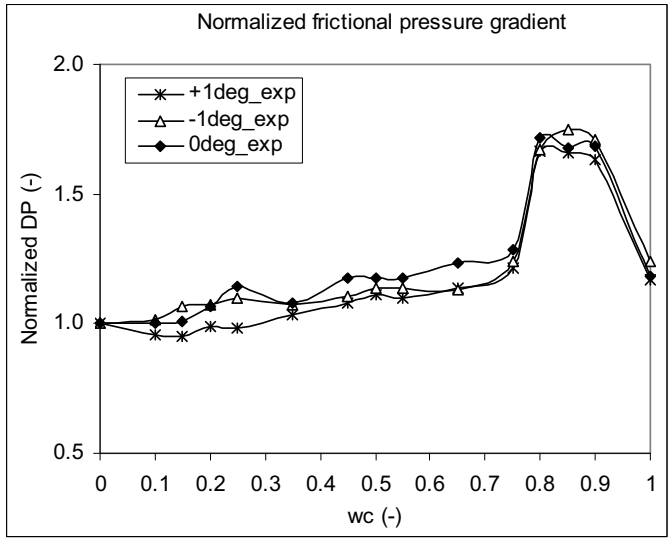

Figure 5.4 Normalized frictional pressure gradient vs. input water cut at -1°, 0° +1°angle.

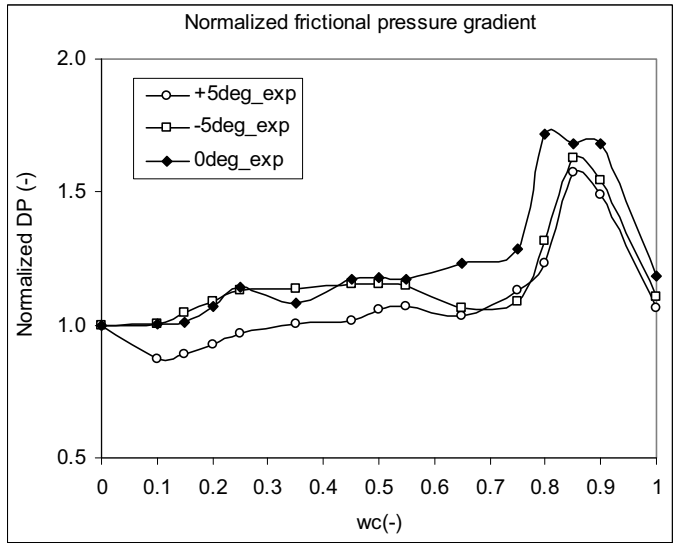

Figure 5.5 Normalized frictional pressure gradient vs. input water cut at -5°, 0° and +5°angle.

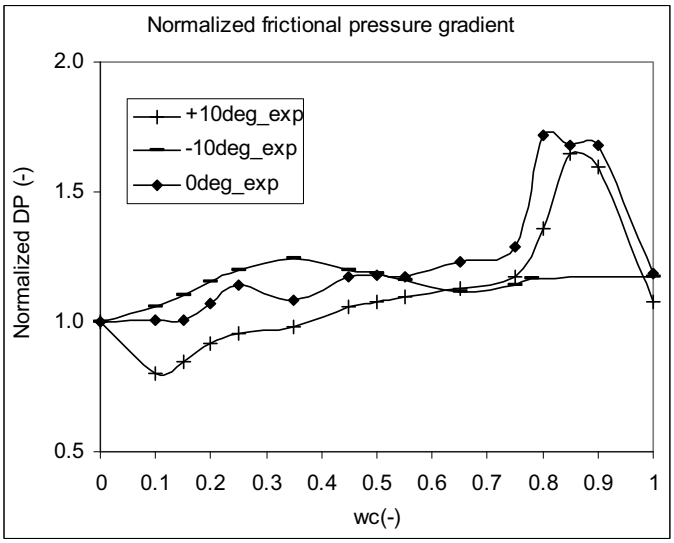

Figure 5.6 Normalized frictional pressure gradient vs. input water cut at -10º, 0° and +10° angle.

5.4 Summary

- The frictional pressure gradient in horizontal, downward and upward moving flow is in general larger in two-phase flow compared with single-phase oil flow, except in upward flow at low input water cut.
- An abrupt increase in normalized frictional pressure gradient was observed at all inclinations, except at -10° angle, which is due to lack of experimental data. The increase is attributed to the increase in effective viscosity of the upper dispersed layer and/or due to affect of the oil-water interface and entrainment of droplets on the single-phase and interfacial shear stress correlations.
- The normalized frictional pressure gradients at inclinations ranging from -10° to +10° are similar in terms of both trend and absolute value.

6 LASER DOPPLER ANEMOMETRY

Identification of velocity and turbulence distributions are important for instance in developing computer models for two-phase liquid-liquid flow. If computer models can predict the flow characteristics, the oil and gas industry can produce the oil and gas more safely and increase the income significantly. Laser Doppler Anemometry is applicable for obtaining detailed information about velocity and turbulence distributions providing that the optical conditions are good.

6.1 Laser Doppler theory

Laser Doppler Anemometry uses the frequency shift of light waves scattered by moving particles, i.e. the Doppler shift. Figure 6.1 presents the basic principle in the Laser Doppler measurement technique. The light source produces coherent light and optical fibers transfer the light to a beam splitter, where a prism splits the beam into two parts. From the beam splitter two optical fibers transfer the laser light into the transmitting optics. A transmitting lens focuses and changes the direction of the beams causing them to intersect in a measurement volume. Flow velocity information comes from light scattered by tiny particles carried in the fluid as they move through the probe volume. The tiny particles could be either naturally present or seeded in the flow and they should be of microscopic size and have density close to the surrounding fluid. In the probe volume, interference pattern forms and produces parallel planes of high and light intensity, so called fringes. A measurement is made when a tiny particle being carried by the flow passes through these fringes. The distance between the fringes is termed (d_f). By measuring the transit time across a given number of fringes, the velocity can be determined.

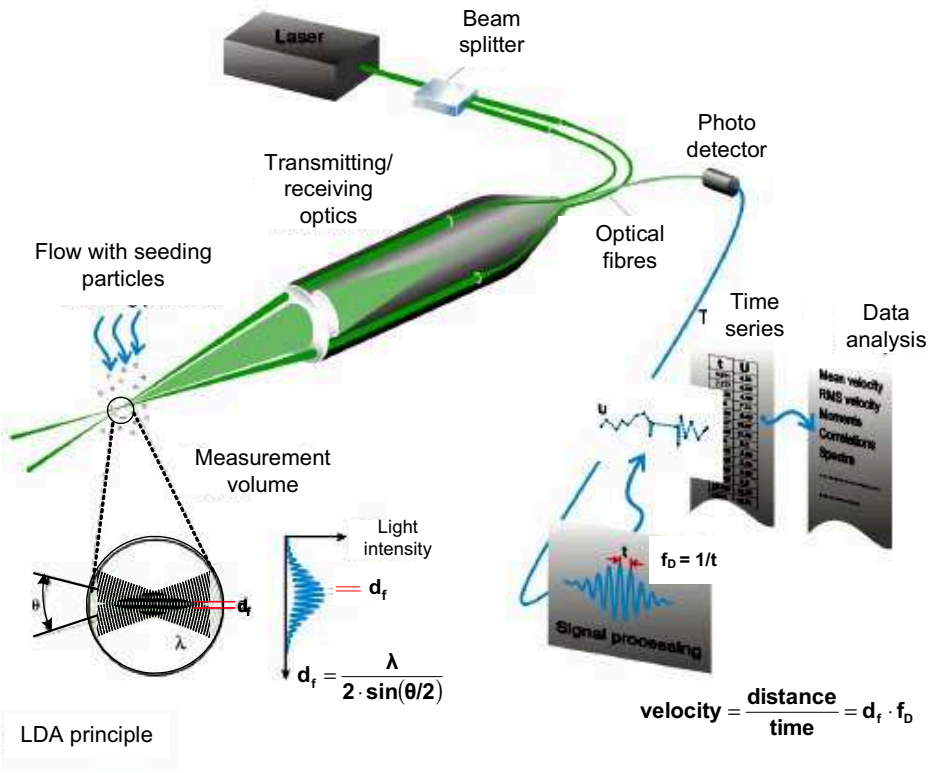

Figure 6.1 The principle of Laser Doppler measurement technique [Dantec reference guide (2000)].

The fringe distance (d_f) given in Eq. (6.1) is a function of the wavelength of the light (λ) and the angle (θ) between the beams. An illustration of the fringe pattern is presented in Figure 6.2, where b1 and b2 are the two intersecting beams.

$$d_f = \frac{\lambda}{2\sin(\theta/2)} \tag{6.1}$$

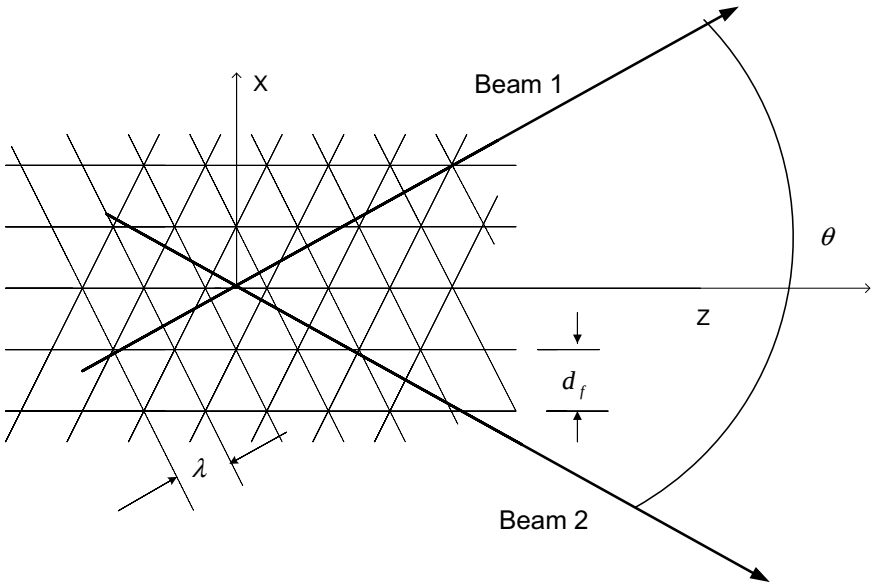

Figure 6.2 Determination of the fringe spacing.

The velocity given in Eq. (6.2) can be calculated from the fringe distance (d_f) and the measured Doppler shift (f_d, Doppler frequency) in the scattered light. The Doppler shift is the change in frequency of a wave due to the relative movement between the wave source and the wave receiver and provides the transit time across a given number of fringes ($t = 1/ f_d$).

$$u = \frac{\text{distance}}{\text{t}} = \text{d}_\text{f} \cdot f_d \tag{6.2}$$

To detect the Doppler frequency, the light scattered by the particle is collected by a receiving lens and focussed onto a photo detector, which converts the fluctuations in light intensity into fluctuations in a voltage signal. Since the transmitting- and the receiving optics in Figure 6.1 are in the same unit, this is called a backscatter system. The light can both backscatter and forward scatter when it hits a particle passing the probe volume. Figure 6.3 presents three modes of scattering that are mostly used in LDA measurements. The three modes are the reflected light, the 1st order refracted light and the 2nd order refracted light. The detection of reflected and 2nd order refracted light refers to backscattered mode and 1st to forward scattered mode.

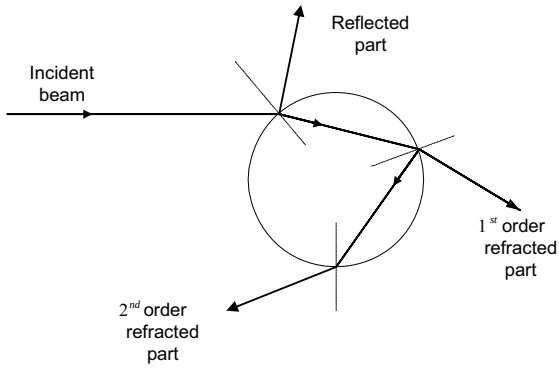

Figure 6.3 Light scattering by a particle [Dantec reference guide (2000)].

The voltage signals are fed to a signal processor, which determines the frequency of the signal which gives the velocity of the flow. Special software processes the raw data, axial and radial velocities, into statistical values like mean velocities, rms-velocities (root mean square) and cross-moments.

Using Laser Doppler Anemometry with the present setup as a method to measure velocity and turbulence profiles in pipe flow has several advantages, which are listed below:

- Non intrusive
- High spatial (due to small measurement volume) and temporal resolution
- Non calibration needed: Method is based on the stability and linearity of optical electromagnetic waves, which are unaffected by physical parameters like pressure and temperature
- Velocities from 0 to supersonic can be measured
- Ability to measure reversible flow
- One, two or three velocity components can be measured simultaneously
- Measurement distance can vary from cm to meters
- Measures both instantaneous and time averaged velocities

Among the disadvantages of LDAs are:

- Expensive (typically $40,000 for a simple system)
- The need for a transparent flow through which the light beams can pass

- Crude oils cannot be used (non transparent)
- Do not give continuous velocity signals.
- Refraction of signals, especially near the pipe walls
- Time consuming to use

6.2 Data analysis

Software from Dantec processes the axial (u) and radial (v) velocities into mean velocities, rms values and turbulent quantities. Eq. (6.3) presents the axial and radial mean velocities.

$$\bar{u} = \sum_{i=1}^{N} \eta_i \, u_i \qquad\qquad \bar{v} = \sum_{i=1}^{N} \eta_i \, v_i \tag{6.3}$$

In Eqs. (6.3) to (6.8) a weighting factor η_i is used. If the samples are statistically independent the weighting factor is equal to the arithmetic mean factor, which is presented in Eq. (6.4). Statistically independent samples can be obtained by using low concentrations of seeding particles in the flow, but this will increase the sampling time. Possible interactions between the particles and timing events are ignored when using Eq. (6.4) .

$$\eta_i = \frac{1}{N} \tag{6.4}$$

Eq. (6.5) expresses the variance of the velocity measurements.

$$\sigma^2 = \sum_{i=1}^{N} \eta_i \, (u_i - \bar{u})^2 \qquad\qquad \sigma^2 = \sum_{i=1}^{N} \eta_i \, (v_i - \bar{v})^2 \tag{6.5}$$

Eq. (6.6) presents the axial and radial rms-velocities or the velocity fluctuations. The rms values are also referred to as standard deviation and describe the spread of data about the mean.

$$u_{rms} = \sqrt{\sigma^2} = \sqrt{\sum_{i=1}^{N} \eta_i \, (u_i - \bar{u})^2} \qquad v_{rms} = \sqrt{\sigma^2} = \sqrt{\sum_{i=1}^{N} \eta_i \, (v_i - \bar{v})^2} \tag{6.6}$$

The turbulence intensity in Eq. (6.7) is the velocity fluctuations divided by the mean velocity.

$$Tu = \frac{u_{rms}}{\bar{u}} * 100\% \qquad Tv = \frac{v_{rms}}{\bar{v}} * 100\% \tag{6.7}$$

Eq. (6.8) gives the cross-moments, which are proportional to the Reynolds stresses.

$$\overline{u'v'} = \sum_{i=1}^{N} \eta_i (u_i - \bar{u})(v_i - \bar{v}) \tag{6.8}$$

6.3 Experimental setup

The laser beams consists of four beams, two green and two blue beams. The two colour system enables simultaneous measurement of axial and vertical velocity components. Figure 6.4 and Table 6.1 present the Laser Doppler characteristics and setup. The beams are generated from a water-cooled 3 W Lexel 80 Argon-ion laser. The laser produces coherent light, which first enters the beam splitter and splits the beam into two parts. Then the beams go through a brag cell, where one of the beams is frequency shifted to be able to distinguish between negative and positive velocity components. The Four Beam Module is a colour beam splitter which splits the two beams into two blue and two green beams, one shifted and one non-shifted beam. The green laser beams measures the axial velocities ($\bar{u}$) and the blue laser beams measures the vertical velocities ($\bar{v}$) as shown in Eq. (6.3). The wavelength for the green beams is 514.5 nm and 488 nm for the blue beams. The green beams are perpendicular to the blue beams. The beams are transferred by optical fibres to a lens inside the laser probe. The transmitting lens focuses the four beams to intersect in a measurement volume. The focal length of the front lens was 400 mm. The probe volume of the green beams is equal to 5.52 x 0.262 x 0.262 mm^3 (length x height x width) and the volume of the blue beams is equal to 5.24 x 0.249 x 0.249 mm^3 [Dantec reference guide (2000)]. The transmitting unit, the laser probe, receives the scattered light from the particles passing the probe volume. This is called a backscattered mode and detects reflected and 2nd order refracted light as shown in Figure 6.3. The light scattered by the particles is focused using a special lens into receiving optics, which transports the light to a colour separator. The colour separator separates and re-collimates the green and the blue beams, before they are focused into each photo multiplier (PM1 and PM2). The photo multipliers convert the light into electrical signals. A signal processor receives the

electrical signals and determines the frequency shift (f_d) and determines the instantaneous local velocities as shown in Eq. (6.2). The signal processor is a Burst Spectrum Analyser. A

PC is connected to the signal processor and a traversing system. Software designed by Dantec analysis the raw data into statistical values like mean velocities, rms-velocities and cross-moments as shown in Eq. (6.3), (6.6) and (6.8) respectively. The traversing system is a Dantec lightweight system, which makes it possible to traverse the laser probe 0.0125 mm in three directions.

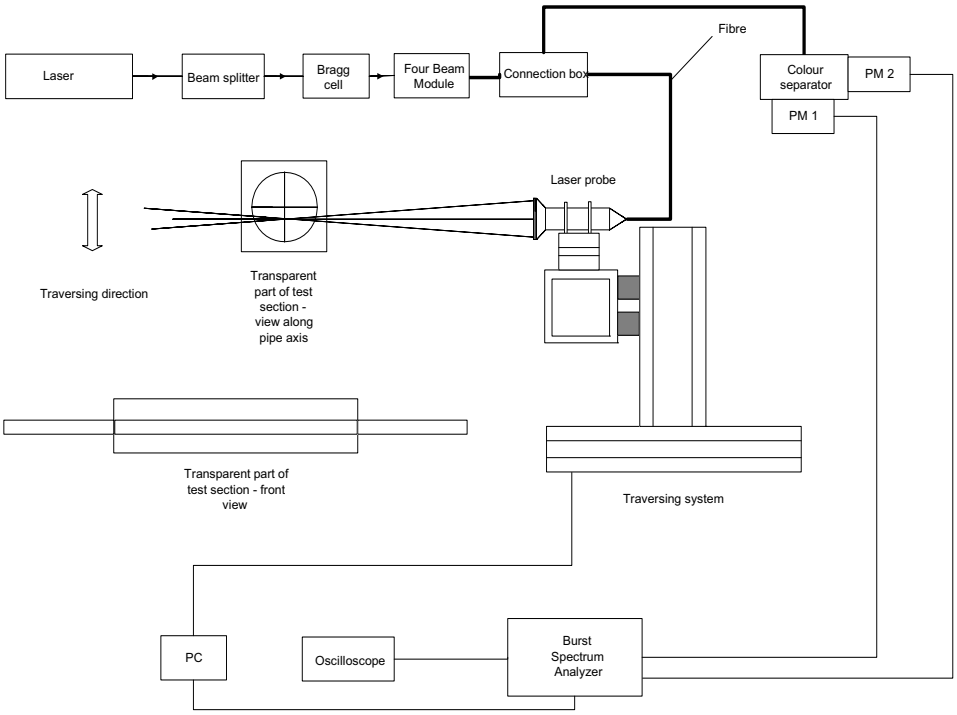

Figure 6.4 LDA setup [Elseth (2001)].

Table 6.1 Characteristics of the Laser Doppler Anemometer

Laser and optics	**Values**
Laser	3 W Lexel 80 Argon-ion
Wavelength (green)	514.5 nm
Wavelength (blue)	488 nm
Lens focal length	400 mm
Number of fringes	48
Fringe spacing (green)	5.422 μm
Beam spacing	38 mm
Beam diameter	1 mm
Fringe spacing (blue)	5.143 μm
Size of measurement volume (green)	5.52 mm x 0.262 mm x 0.262 mm (Length x Height x Width)
Size of measurement volume (blue)	5.24 mm x 0.249 mm x 0.249 mm (Length x Height x Width)
Mode	Backscattered

6.4 Simplified Refractive Index Matching (RIM) procedure

The RIM procedure is a method that involves selection of pipe material and fluids with equal or nearly equal refractive indices to accomplish velocity and turbulence measurements along the vertical diameter through the pipe centre. This method has been used by several investigators as e.g. Durst et al. (1995) and Budwig (1994). When light travels from one substance to another the light often changes direction, which is referred to as refraction of light. Snell's law of refraction defines the refractive index (n_r) of a substance according to Eq. (6.9), where c is the speed of light in vacuum and c_m is the speed of light in matter.

$$n_r = \frac{c}{c_m} \tag{6.9}$$

To avoid refraction of the laser beams the refractive index of the pipe should be chosen to be similar to that of oil and water. Table 6.2 shows the refractive indexes for air, water, Exxsol D60 and plexiglas. The plexiglas material has a refractive index close to that of Exxsol D60, which makes plexiglas suitable material for LDA measurements. The difference in refractive indexes and due to the curvature of the pipe will cause some experimental limitations, which are discussed below.

Table 6.2 Refractive indices for different substances at 20°C [Fischer and Jovanović (1998)].

Substance	**Refractive index (n_r)**
Air	1.00045
Water	1.333
Exxsol D-60	1.434
Plexiglass	1.51

In addition to difference in refractive index, refraction also occurs when passing a curved interface. Since the green beams measure the axial (horizontal) velocity and the blue measure the vertical velocities the green beams are aligned in the horizontal plane and the blue in the vertical plane. The green beams will be refracted equally since the beams enter the pipe wall at the same angle of incidence. The blue beams will enter the pipe wall at different angles of incidence, except for in the pipe centre. The green beams follow very closely the centre line through the entire pipe, while the blue beams are refracted to a larger degree close to the inner pipe wall. A rectangular box is built around the plexiglas section, to reduce the refraction of light, caused by the low refractive index of air compared to plexiglas and beams passing a curved interface. In that way the difference in refractive index is smaller and refraction of light smaller, provided that the rectangular box is filled with the same fluid as in the plexiglas section. Elseth (2001) reported simulations of the refractive index matching setup and showed that the control volume of the vertical velocity component changes direction from the vertical pipe diameter when the control volume approaches the wall. Since the overlap of the control volumes decrease toward the wall the sampling rate falls drastically.

Figure 6.5 presents the RIM system in the flow facility. The instrument is aligned along the vertical centre line and the measurements start in single-phase water. In two-phase experiments, the measurements start in the water phase at the lower pipe inner wall and traverses a few millimetres into the oil phase. The rectangular box is filled with water or oil, depending on the fluid used in the plexiglas section. Interchanging the water with oil, leads to a displacement of the probe volume. The intersection point lies off-centre, but in the same horizontal plane. The measurement volume is adjusted to the centre line by traversing the probe backwards with 2.5 mm, which was approximately the same factor as Elseth (2001)

used. The measurements in the oil phase starts at the upper inner pipe wall and traverses vertically down into the water phase. The RIM procedure is equal to that of Elseth (2001).

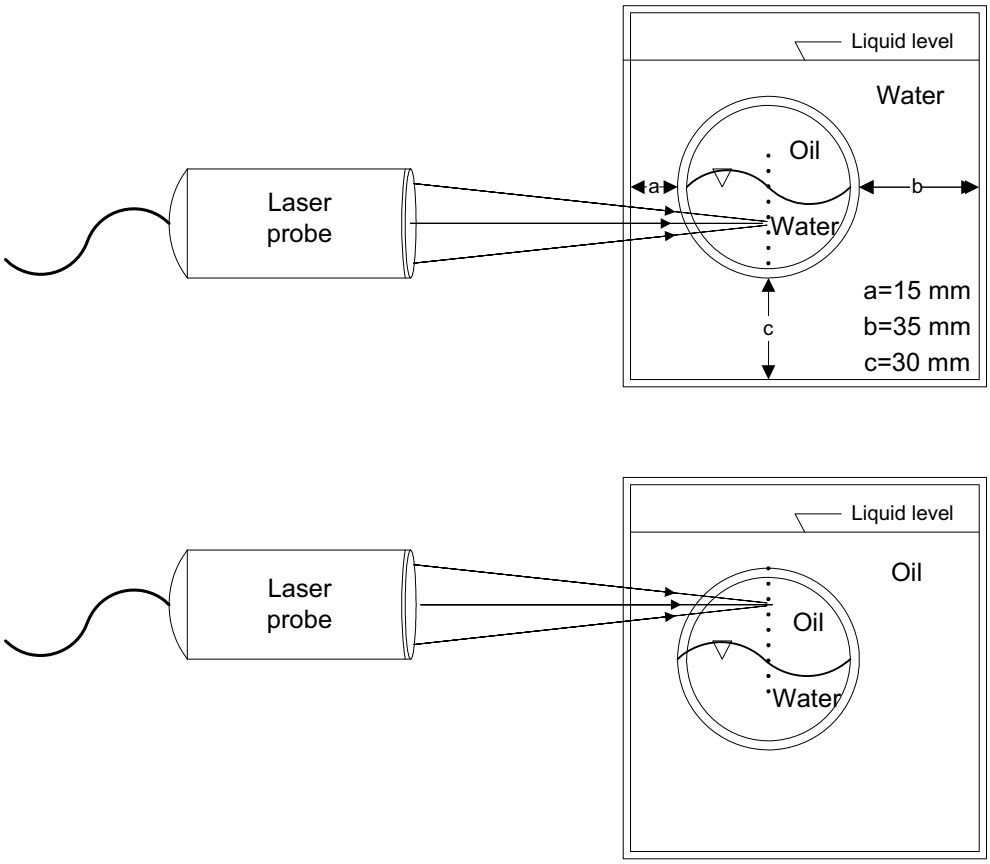

Figure 6.5 System for measurements in water-phase (above) and oil-phase (below).

The RIM system in the flow facility is presented in Figure 6.6. The laser beams intersect in a measurement volume inside the inclined two-phase flow.

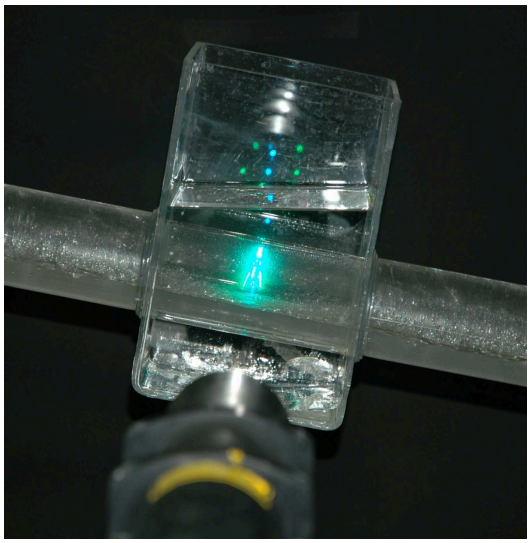

Figure 6.6 LDA measurements in inclined oil-water flow.

Laser Doppler measurement in the interface region between oil and water is challenging due to waves and dispersed droplets. Since the interface often is wavy the measurements conducted in the water phase has to move above the largest wave and into the oil phase and opposite for measurement in the oil phase. The fluid inside a small measurement volume in the interface region can alternate between a water continuous flow with dispersed oil droplets and oil continuous flow with dispersed water droplets as shown in Figure 6.7. This will cause refraction of the laser beams. Refraction of the laser beams leads to poorer signals and the number of samples becomes lower. Based on experience [Dantec reference guide (2000)] a thousand to a few thousand samples are sufficient when measuring the mean velocity. When it comes to measuring quantities like cross-moments, the number of samples must often exceed 10 000 and sometimes 100 000. It is very time consuming to measure such a high number of samples if the optical conditions are poor. The highest number of signals in present experiments is equal to 25 000. Lower values are measured close to the wall and in the interfacial region, where the number of signals can be as low as 100. The maximum number of signals is set to 25 000, the measurement interval is set equal to 240s and the dead time equal to 5ms. This means if 25 000 signals is measured within the measurement interval, the measurements stops or else it stops when the time has reached the measurement interval (240s). The shortest possible measurement time is equal to 125s ($5ms \cdot 25\ 000\ \ signals$).

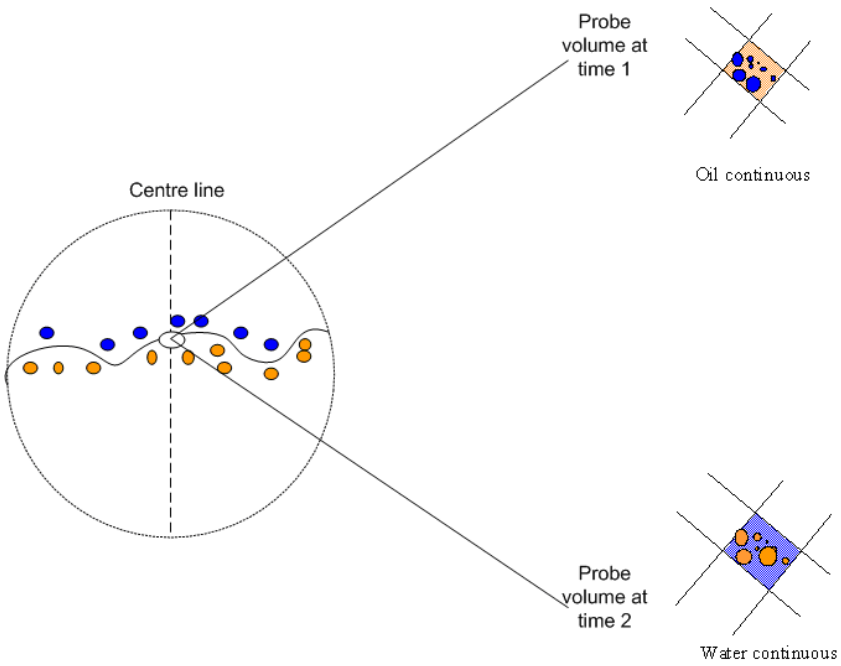

Figure 6.7 Illustration of laser measurements in wavy ST & MI flow.

6.5 Data validation

Validation of LDA experiments involves errors due to statistics, refraction of beams, traversing system and reproducibility. Several different methods are used to validate the accuracy and reproducibility of the measurements in current experimental campaign.

By use of the RIM procedure as shown in section 0 the refraction of beams is severely reduced. The vertical orientated beams, which measure the radial velocities, will experience most refraction due to the curved pipe interface. The radial mean velocities and v-rms will therefore be less accurate. Refraction due to poor optical conditions contributed to a low and random sampling rate. This was observed when there were dispersions and waves near the interfacial region and when the inner plexiglas wall was coated with organic deposits and droplets. Fringe distortion can occur due to tracer particles and droplets, which can lead to a higher measured turbulence level. Fringe distortion was reported by e.g. Zhang and Eisele (1998). They reported that overestimation of turbulence and mean velocity normally was

negligible, except for flow with very low turbulence. The accuracy of the traversing system is very good and will only have minor influence on the measurements. The accuracy of the traversing system is 0.0125 mm [Elseth (2001)].

6.5.1 Comparison of flow rates obtained from LDA and flow meter

Comparison between the flow rate obtained from the integrated velocity profile and flow rates measured by flow meters are done in both single-phase and two-phase flow. Nigmatulin et al. (2000) reported an uncertainty in the mean water and oil flow rate within 1.5 and 3.5 percent respectively by use of similar set-up as in present study. They assessed the accuracy of the LDA system by comparing the flow rates obtained from the integrated velocity profile with the flow rates measured by rotometers. They concluded that the accuracy of the rotometers was much less than the LDA measurements. The comparison of the flow rates obtained from the integrated velocity profiles in single-phase flow with the flow meter readings in present study (Chapter 3, Table 3.9) shows good agreement and the deviation between the two measurements is lower than the accuracy of the flow meters.

6.5.2 Model comparison

A comparison of the single-phase water velocity profile with the $1/7^{th}$ power law in Chapter 3 (Figure 3.13) shows negligible deviations. The nice match between the experimental data and the model confirms that the trend and the measurement accuracy in each measurement point are of high-quality.

The axial velocity profile in single-phase oil is normalized with the friction velocity as shown in Eqs. (6.12) and (6.13), giving the non-dimensional wall coordinates for the velocity (U^+) and position (Z^+). The friction velocity in Eq. (6.14) is calculated from the measured mean axial velocity and from the measured pressure gradient as shown in Eq. (6.15) and Eq. (6.16) respectively. In Figure 6.8 the normalized axial velocity profile is compared with the law of the wall model presented in Eqs. (6.10) and (6.11). The good agreement between the normalized axial velocity profile and the law of the wall model shows that the LDA measurements are accurate and that the current set-up works satisfactory. The laminar viscous sub layer extends from $Z^+ = 0$ to $Z^+ = 5$ and the fully turbulent region starts from $Z^+ = 30$. The region between the laminar and turbulent region is often called the buffer layer. The deviation

at the outer edge of the boundary layer is well described in the literature [e.g. Kays et al. (2005)] and was also measured by Elseth (2001). This region is referred to as the wake region.

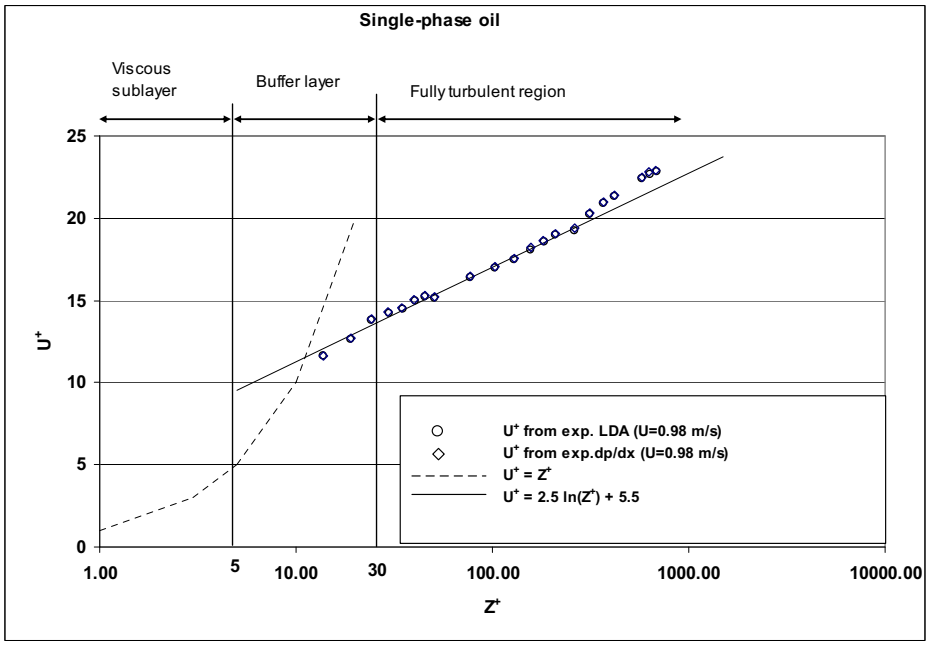

Figure 6.8 Axial velocity profile (LDA) and the law of the wall model.

Eq. (6.10) expresses the model for the viscous sub layer. The model assumes that the kinematic viscosity is much larger than the eddy diffusivity.

$$U^+ = Z^+ \tag{6.10}$$

Eq. (6.11) is an experimental fitted law of the wall model [Nikuradse (1932)] for the fully turbulent region, where the eddy diffusivity is assumed to be much larger than the kinematic viscosity.

$$U^+ = 2.5\ln\left(Z^+\right) + 5.5 \tag{6.11}$$

Eqs. (6.12) to (6.16) show the calculations of the non-dimensional wall coordinates for the velocity (U^+) and position (Z^+) from the experimental pressure gradient and axial time-mean velocity (LDA) data. Eq. (6.12) expresses the definition of the non-dimensional wall

coordinate (Z^+), where z is the vertical centre position in the pipe and υ is the kinematic viscosity.

$$Z^+ = \frac{zu_\tau}{\upsilon} \tag{6.12}$$

The normalized velocity with the friction velocity is expressed in Eq. (6.13), where $\bar{u}$ is the axial time-mean velocity and u_τ is the friction velocity as shown in Eq. (6.14).

$$U^+ = \frac{\bar{u}}{u_\tau} \tag{6.13}$$

The friction velocity is a function of the wall shear stress (τ_0) and the density (ρ)

$$u_\tau = \sqrt{\tau_0 / \rho} \tag{6.14}$$

Eqs. (6.15) and (6.16) give the wall shear stress (τ_0) calculated from the measured mean axial velocity (LDA) and from the measured pressure gradient, respectively. The friction factor (f) is expressed in Eq. (3.5), U is the velocity obtained from the integrated velocity profile and $\frac{dp}{dx}$ is the measured pressure gradient.

$$\tau_0 = \frac{f}{8}\rho U^2 \tag{6.15}$$

$$\tau_0 = \frac{D}{4}\left|\frac{dp}{dx}\right| \tag{6.16}$$

The largest number of samples in present study is 25 000 and the lowest is 1000. The accuracy of the velocity measurements as function of number of samples has been validated by comparing single-phase experiments with the $1/7^{th}$ power law and law of the wall models as shown above. The good agreement between the measured velocity profile and models shows that the number of samples is statistically good.

The number of independent samples, N in Eq. (6.4), for obtaining statistically reliable measurements must be fulfilled. Statistically independent measurements can be obtained by

using low concentration of seeding particles in the flow and by use of a dead-time mode in the processor. Durrani and Greated (1977) reports that for ordinary tap water there is an abundance of naturally occurring particles that follows precisely the flow and that seeding particles is generally unnecessary with liquids. In present study, no seeding particles where used and a dead time modus was set equal to 5ms to achieve statistically reliable measurements.

6.5.3 Reproducibility

Three independent measurement series of the velocity, u-rms, v-rms and cross-moments profiles in single-phase water are shown in Figure 6.9 to Figure 6.12. The number of samples in the experiments is above 1000 and below 25 000. Generally, the measurements follow the same trend. The velocities vary within ±1.4% in the centre of the pipe, which is probably caused by error in pump speed and/or flow meter. Some spread in the u-rms, v-rms and in the cross-moments are seen in the upper and lower part of the pipe region (z/R =0.6 to 1 and -0.7 to -1) for the three measurement series. The scattering is most pronounced for v-rms and cross-moments in the upper part of the pipe and is approximately equal to ±8%. This is most likely due to poor optical conditions caused by refraction of the beams.

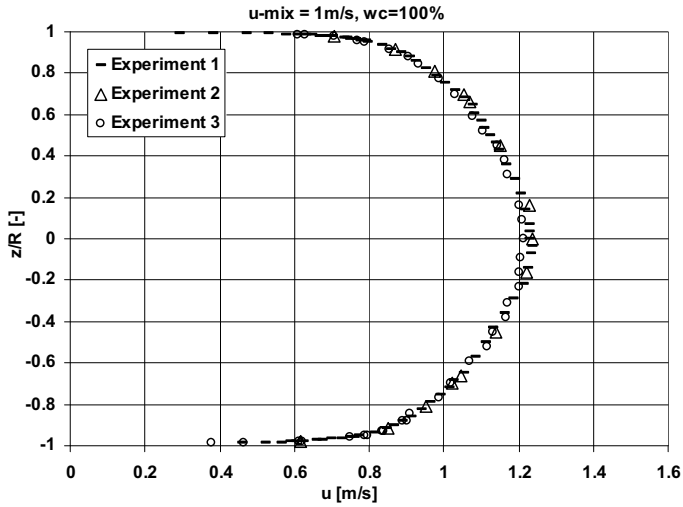

Figure 6.9 Three measurement series of velocity profile in single phase water.

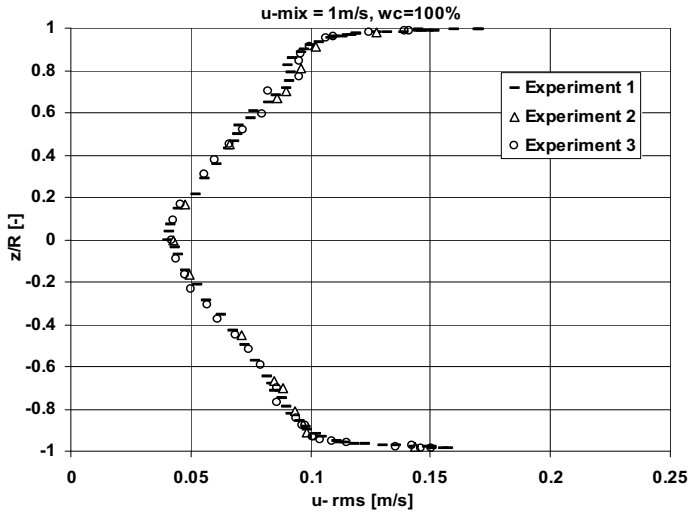

Figure 6.10 Three measurement series of u-rms in single phase water.

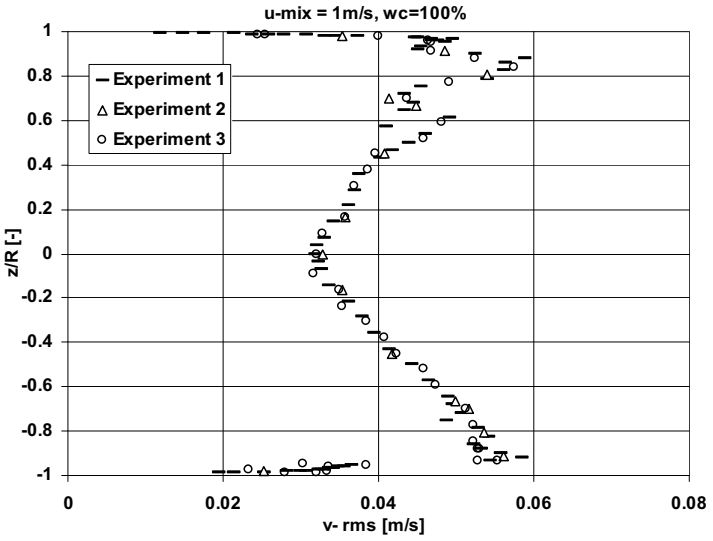

Figure 6.11 Three measurement series of v-rms in single phase water.

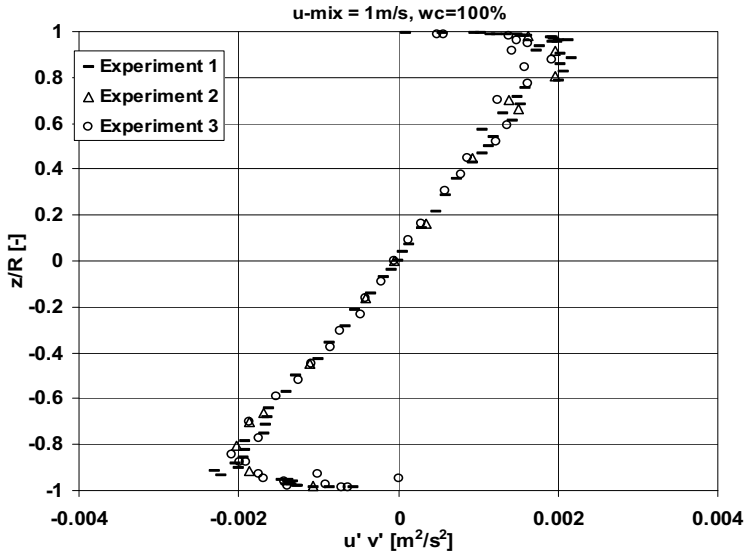

Figure 6.12 Three measurement series of cross-moments in single phase water.

In Figure 6.13, four independent measurements of the velocity distribution in horizontal pipe flow at 50% input water cut and 1 m/s is presented. In the raw data the number of samples varies from 10 to 25000, but in the presented data the measurements points with lower number of samples than 1000 is removed to increase the statistical accuracy. The number of samples in the water phase is normally equal to 25000, except for very close to the wall (z/R>0.90). In the oil and interfacial region the number of samples is lower than that of water and varies between 1000 and 25000. This could be due to a less transparent oil phase compared with water which gives a poorer optical condition. Most of these measurements have larger number of samples than 3000.

As seen in Figure 6.13, there is a larger spread between the four experiments near the interfacial region and in the oil phase. The velocity can vary with approximately ±2.5% in the interfacial region and in the oil phase. Close to the wall in the oil phase the deviations are larger and can be up to ±5%. These variations are probable due to variable pump speed, errors in the flow meter readings and variations in the optical conditions. The number of samples is lower in the interfacial region due to refraction of the beams caused by dispersed droplets and

a wavy interface. However, the trends of the velocity profile are equal in the four independent experiments.

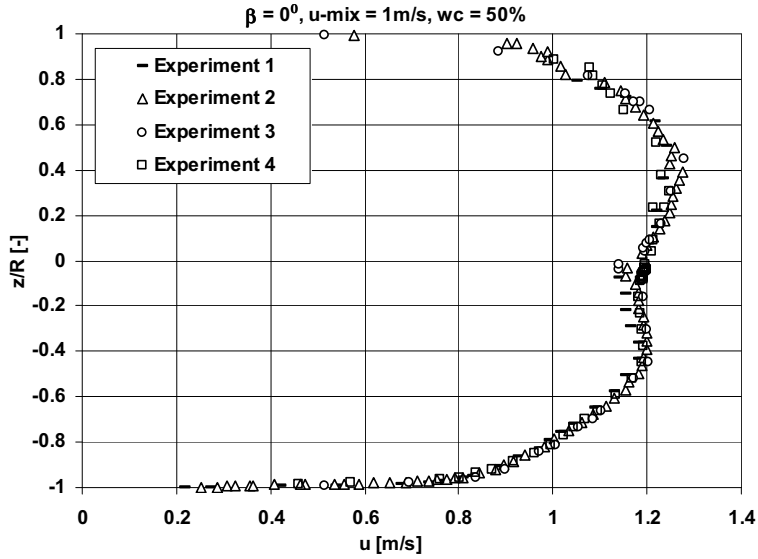

Figure 6.13 Velocity profiles in two-phase flow at 50% input water cut and 0° angle.

The good comparison between the velocity, rms-velocity and cross-moment trends observed in present study and that of Elseth (2001) also implies a good reproducibility.

6.6 Laser Doppler experiments

A Laser Doppler Anemometer measured the velocity and turbulence distributions in single and two-phase oil-water flow in horizontal and inclined pipe flow. The effect of increasing the input water cut and the effect of inclination on the measured axial mean velocity, axial rms-velocity, vertical rms-velocity, cross-moments and the Reynolds stresses are studied. The fluids in the experiments were Exxsol D60 and tap water. Table 6.3 gives the experimental conditions in the LDA measurements. The experiments were conducted at input water cuts equal to 0, 25, 50 and 100% and with a constant mixture velocity equal to 1 m/s. The inclination angle varied between –10° to +10°.

Table 6.3 LDA experimental conditions.

Parameter	Value
Pressure	1 atmosphere
Input water cut	0, 25, 50, 100 %
Mixture velocity	1 m/s
Pipe inclinations	Horizontal, +1°, +5°, +10° upward, -1°, -5°, -10° downward
LDA: Maximum number of samples	25000
Dead time modus	5 ms
Measurement time	240 s

6.6.1 Axial mean velocity

The velocity distribution in single-phase flow differs from the distribution in two-phase flow. In single-phase flow the profile is symmetrical around the pipe centre (z/R=0) and has high gradients close to the wall, in the viscous sub layer and into the region of turbulent flow, and lower gradient when approaching the centre of the pipe. In contrast to the symmetrical single-phase flow, the velocity distribution in two-phase flow is non-symmetrical. The velocity distribution is non-symmetrical for both 50% and 25% input water cut at the inclination angles studied (0º, ±1º, ±5º and ±10º). Figure 6.14 to Figure 6.23 show the asymmetric axial velocity distributions for two-phase oil-water flow. When the inclination angle increases or decreases the asymmetry increases accordantly. The local water fraction indicates the position of the interfacial region and the degree of dispersion and/or waves. Present measurements show that the axial velocity distribution is affected by the input water cut and inclination angle. This was also measured by Shi et al. (2000), Shi et al. (2001), Elseth (2001), Kumara et al. (2008) and Kumara et al. (2009a).

In horizontal two-phase flow at 50% input water cut, the oil phase moves faster than the water phase, even the viscosity of oil (1.6 cP) is higher than that of water (see Figure 6.14). One possible explanation can be found by comparing the wall shear in the oil phase with the wall shear in the water phase as shown in Eq. (6.17), where the friction factor of Blasius is used.

$$\frac{\tau_{wall,oil}}{\tau_{wall,water}} = \frac{\mathrm{Re}_o^{-0.25}}{\mathrm{Re}_w^{-0.25}} \cdot \frac{\rho_{oil}}{\rho_{water}} = 0.4962^{-0.25} \cdot \frac{790}{995} = 0.946 \qquad (6.17)$$

Since the wall shear in the oil phase is lower than the wall shear in the water phase, the oil phase moves faster than the water phase. Eq. (6.17) shows that the density ratio counteracts the viscosity effect in present study. In addition to the measurements conducted by Elseth (2001) and Kumara et al. (2008), a measured slip ratio above one (see Chapter 4), confirms that the oil velocity is higher than that of water at 50% input water cut.

6.6.2 Effect of inclination on the axial mean velocity at 50% input water cut

Figure 6.14 to Figure 6.18 present the axial mean velocity distribution together with the local water fraction at input water cut equal to 50% and inclination angles from -10º to +10º.

Figure 6.14 presents the velocity profiles at 50 and 100% input water cut and local phase fractions for pipe inclinations equal to 0° and ±1°. The two-phase flow has larger maximum velocities in both the oil and water phase and slightly lower velocities in the centre of the pipe compared with single-phase water flow. The oil phase in +1° upward pipe flow moves faster than the water phase, due to gravitational forces, while at -1° angle the oil and the water phase have almost equal maximum velocity. The maximum velocity is measured in the oil phase at +1º inclination. In Chapter 4, the calculated slip ratios is calculated to be above one and equal to one at +1º and -1º respectively, which supports the trends observed in the LDA measurements. The velocity of the oil phase is increasing from -1° to +1° inclination angle, while the water phase has the opposite trend. The measured velocity is more scattered at -1° near the interfacial region, which is probably caused by poorer optical conditions.

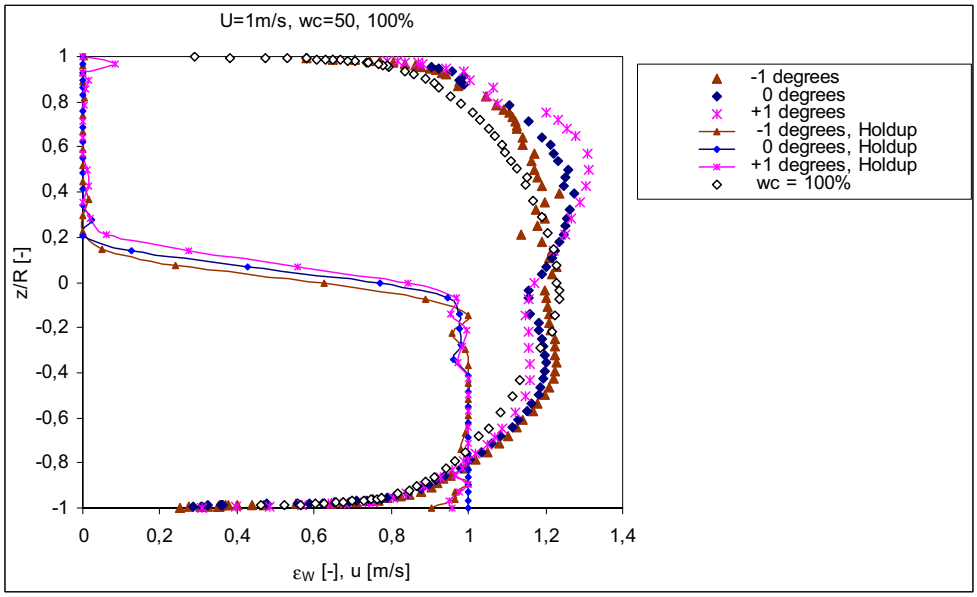

Figure 6.14 Axial velocity distributions at 1.0 m/s mixture velocity, 50% input water cut and pipe inclinations equal to 0° and ±1°.

Figure 6.15 presents the axial mean velocity distributions and local phase fractions for inclination angles equal to 0° and ± 5° angle at 50% input water cut. The oil phase moves substantial faster than the water phase at inclination angle equal to +5° and at inclination angle equal -5° the water phase moves faster than the oil phase, due to gravity forces. The observations agree well with the slip ratios presented in Chapter 4. The largest local velocity (1.45 m/s) in axial direction is in the oil phase at +5° angle. Larger variations in the measured velocity near the interfacial region and into the oil phase are seen at -5° angle. This implies that the accuracy of the measurements is reduced, which could be due to larger degree of waves and dispersed droplets giving refraction of the beams.

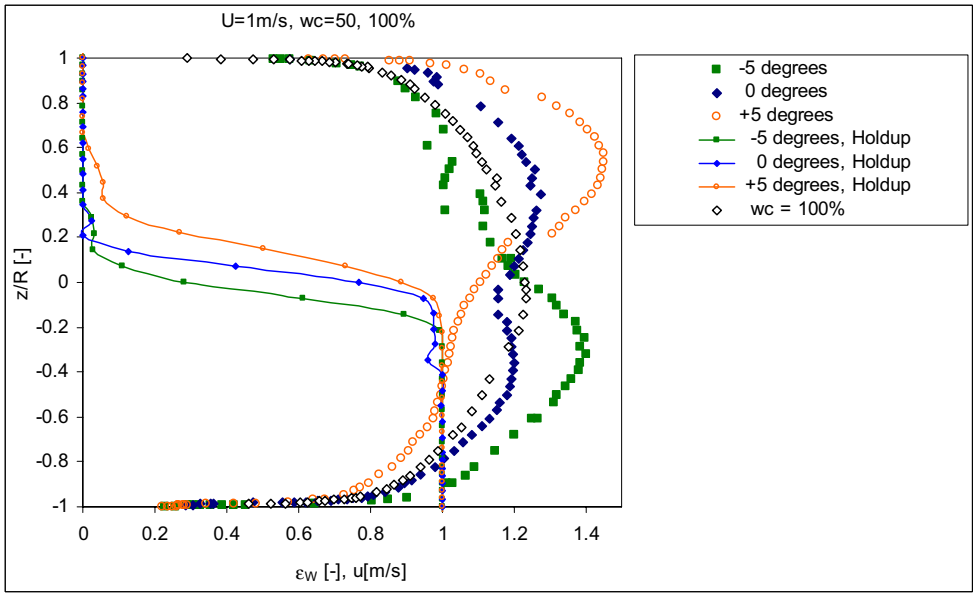

Figure 6.15. Axial velocity distributions at 1.0 m/s mixture velocity, 50% input water cut and pipe inclinations equal to 0° and ± 5°.

Figure 6.16 presents the axial velocity distributions and local phase fractions for pipe inclinations equal to 0º and ±10º at 50% input water cut. For inclination angle equal to ±10º there exists only one maximum velocity, which are located above the interfacial region (z/R=0.6) for +10º angle and below the interfacial region (z/R= -0.35) for -10° angle. As was observed in the measured slip ratio, the velocity profile shows that the oil phase is moving much faster than the water phase in upward moving flow at +10°. In downward moving flow, water is the fastest moving phase. The largest local velocity in axial direction is in the water phase and is measured at -10° angle, but the maximum velocity at +10º angle is nearly equal. Only a few measurement points exist in the interfacial region at -10° angle, which is probably due to small amplitude waves (see Chapter 4) and poorer optical conditions.

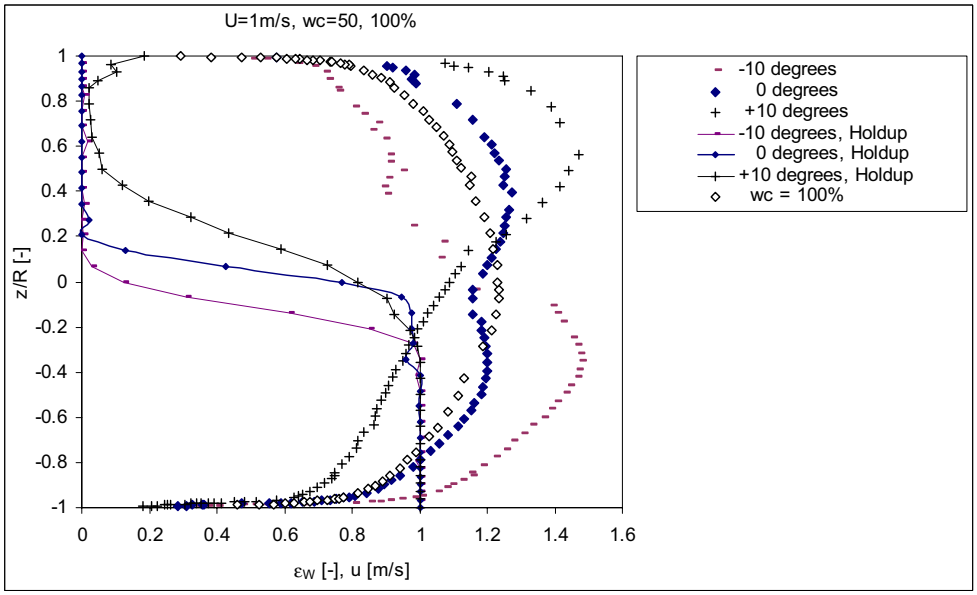

Figure 6.16. Axial velocity distributions at 1.0 m/s mixture velocity, 50% input water cut and pipe inclinations equal to 0° and ±10°.

Figure 6.17 shows the effects of inclining the pipe downward from horizontal to -10º angle. The large differences in the axial mean velocity profiles and the local water fractions show that the inclination angle has large effect on the two-phase oil-water flow. For downward moving flow, the oil phase velocity is decreasing with decreasing inclination angle (0° to -10°) and the water phase velocity is increasing. At -5° and -10° angle, the water is the fastest moving phase. The slip ratios presented in Chapter 4 also show equal trend.

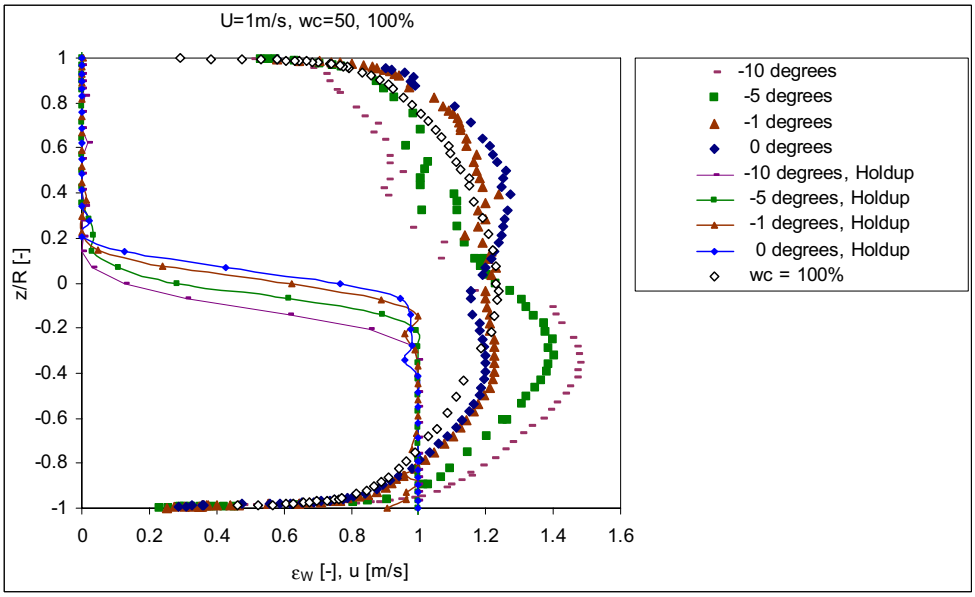

Figure 6.17. Axial velocity distributions at 1.0 m/s mixture velocity, 50% input water cut and downward pipe inclinations equal to 0°, -1º, -5º and - 10°.

Figure 6.18 shows the effects of inclining the pipe upward from horizontal to +10º angle. Small differences in the oil and water phase velocity are seen when increasing the inclination angle from 0º to +1º. The oil phase moves slightly faster at +1º angle than it does in horizontal flow and the water phase flows slightly slower. Changing the inclination angle from +1º to +5° results in larger differences in the velocity profiles, in both the oil phase and water phase. However, changing the inclination angle from +5º to +10º leads to smaller differences in the velocity profile. Generally, the velocity of the water phase is decreasing with increasing upward inclinations and the oil phase velocity increasing. The slip ratios also show small differences between 0° and +1° and between +5° and +10° and large variations when the pipe inclines from +1° to +5° angle.

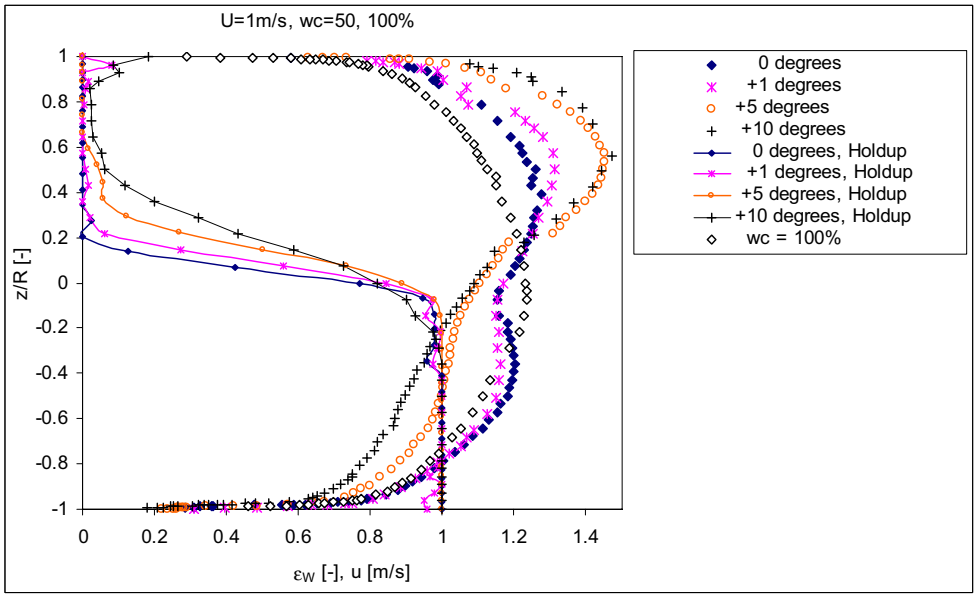

Figure 6.18. Axial velocity distributions at 1.0 m/s mixture velocity, 50% input water cut and upward pipe inclinations equal to 0°, +1º, +5º and + 10°.

6.6.3 Effect of inclination on the axial mean velocity at 25% input water cut

Figure 6.19 shows that the oil phase is moving faster than the water phase when the input water cut is equal to 25% and inclination angle equal to 0° and ±1°. This is in agreement with the calculated slip ratio from the gamma measurements in Chapter 4. There exists only one maximum velocity, which is located in the oil phase for all inclination angles. The highest velocity is found in upward moving flow at +1º inclination angle. Inclining the pipe with ±1º has small effect on the velocity profiles. The oil phase velocity decreases slightly from +1° to -1° inclination and the water phase velocity increases due to gravity.

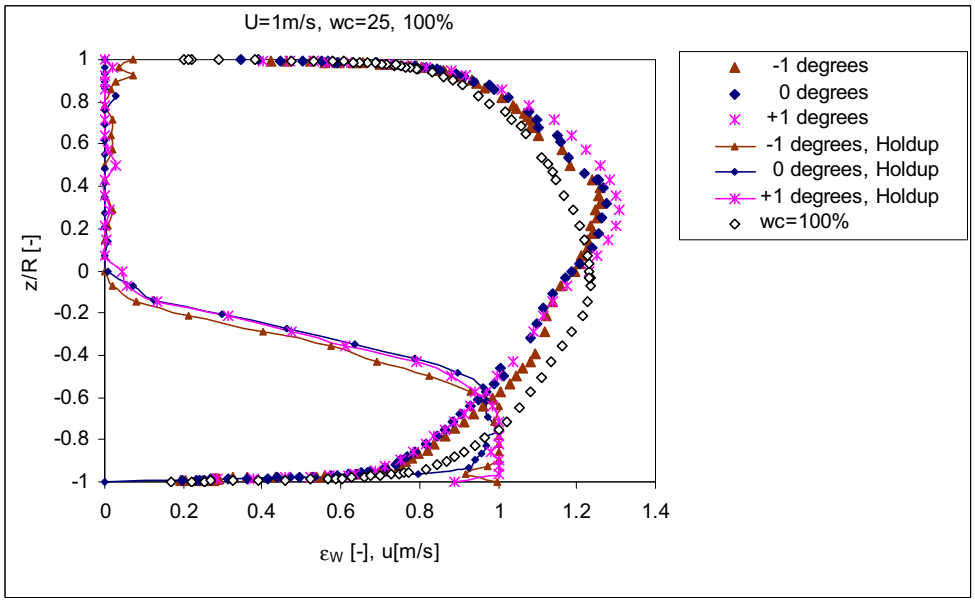

Figure 6.19 Axial velocity distributions at 1.0 m/s mixture velocity, 25% input water cut and pipe inclinations equal to 0° and ±1°.

Figure 6.20 shows that changing the angle from 0º to ±5º has large effect on the velocity profile. The velocity of the oil phase has a decreasing trend when the inclination angle changes from +5º to -5º, while the velocity of the water phase has an increasing trend. The maximum velocity of the oil and water phase is nearly equal at -5° inclination angle. The highest velocity is observed at +5° inclination and is located in the oil phase, which is in agreement with the slip ratios obtained from the measured phase fractions.

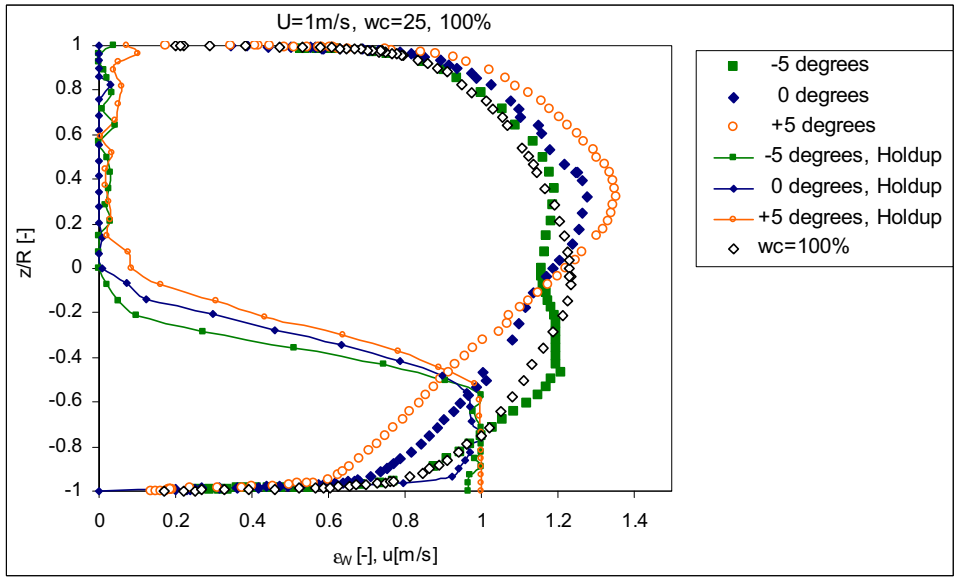

Figure 6.20. Axial velocity distributions at 1.0 m/s mixture velocity, 25% input water cut and pipe inclinations equal to 0° and ±5°.

Figure 6.21 presents the effect on velocity profiles by changing the inclination angle from 0º to ±10°. The changes in the velocity profiles by varying the inclination angle from 0° to ±10° are similar to the observation made at 0° and ±5° angle. The oil phase velocity decreases from +10° to -10° inclination angles and the water phase velocity increases. The highest observed velocity is in upward moving flow and is located in the oil phase, which was also observed at lower inclinations. A very low sampling number (<1000) is seen in the interfacial region at +10° inclination angle, which is probably due to the large rolling waves and dispersion of drops. The maximum velocity at -10° is measured in the lower part of the pipe very close to the interface between oil and water.

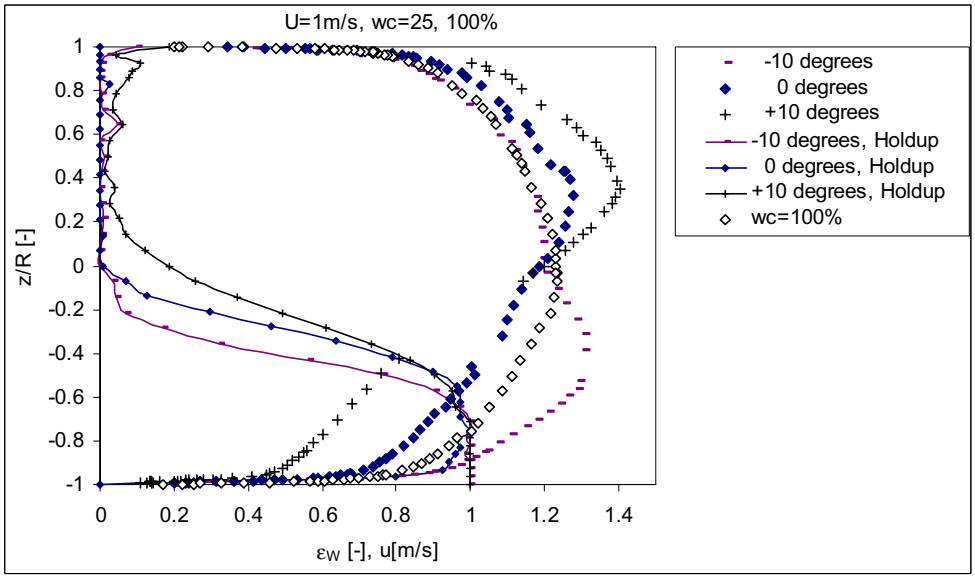

Figure 6.21. Axial velocity distributions at 1.0 m/s mixture velocity, 25% input water cut and different pipe inclinations (0° and ± 10°).

Figure 6.22 shows the velocity profiles in downward inclinations from -10° to 0º angle. Generally, the water phase velocity decreases from -10° to 0° inclination and the oil phase velocity increases. This trend was also observed in the calculated slip ratios in Chapter 4. Changing the angle from 0° to -1° angle shows only small differences in the velocity profile, but when the angle decreases from -1º to -5º the velocity of the oil phase decreases and the water phase velocity increases significantly. Decreasing the inclination angle from -5º to -10º angle leads to a larger water phase velocity compared to the oil phase velocity. The maximum velocity is located in the water phase at -10° inclination angle in the interfacial region (z/R = -0.4) and the maximum oil velocity is found in horizontal pipe flow.

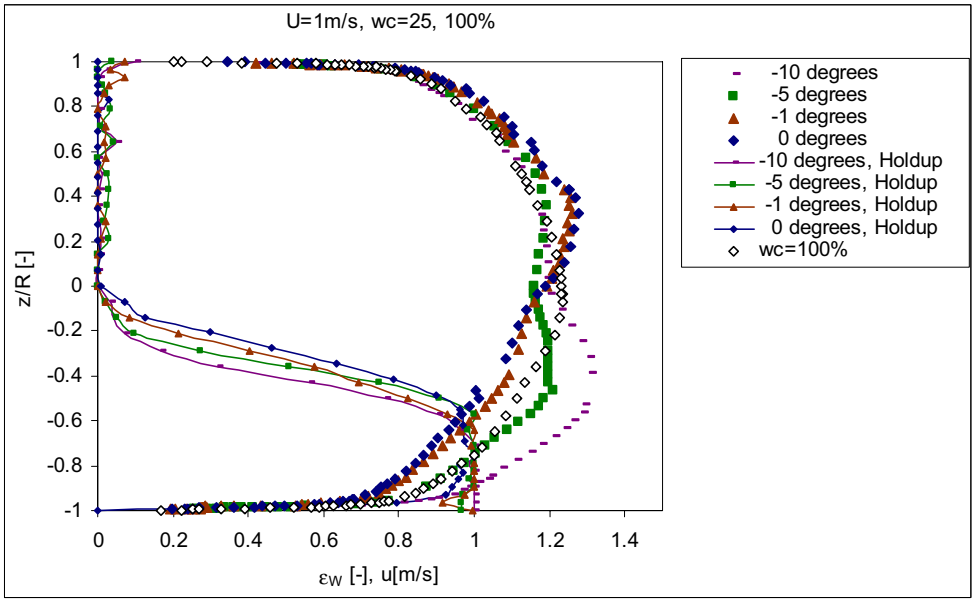

Figure 6.22. Axial velocity distributions at 1.0 m/s mixture velocity, 25% water cut and pipe inclinations from 0° to -10°.

Figure 6.23 presents the influence on the velocity profiles by changing the inclination angle upwards from 0° to +10°. The oil phase is the fastest moving phase in upward flow. This is in agreement with the calculated slip ratios in Chapter 4. The oil phase velocity increases when inclining the pipe from 0° to +10°, while the water phase stays nearly constant from 0° to +1° angle and decreases from +1° to +10° angle. The measurements show minor differences between the velocity profiles at 0° and +1° inclination angle, as was also the case in downward moving flow between 0° and -1° angle. The oil phase at +10° angle is the fastest moving phase with a maximum velocity of 1.4 m/s.

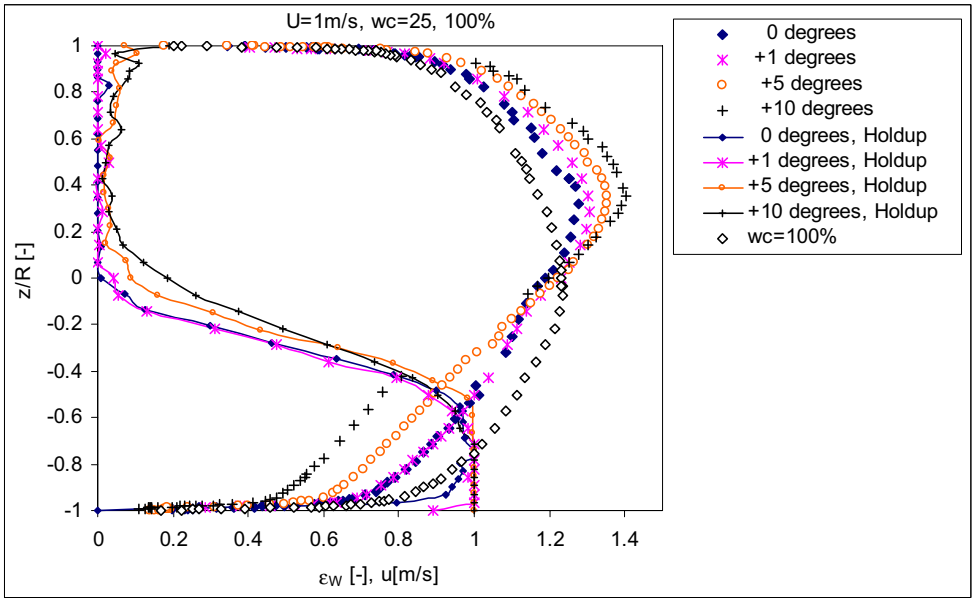

Figure 6.23. Axial velocity distributions at 1.0 m/s mixture velocity, 25% water cut and pipe inclinations from 0° to +10°.

6.6.4 Axial rms-velocity

This section presents the axial rms-velocities for input water cut equal to 0, 25, 50 and 100% at pipe inclinations equal to 0°, ±1°, ±5° and ±10°. The description of the rms-velocity distribution profiles is mainly concentrated between the wall peaks, from approximately -0.95 to +0.95 of the pipe diameter. The number of signals is poorer close to the wall and in the interface region, which makes the interpretation less reliable. Generally, in two-phase flow the u-rms velocities are decreasing from the upper and lower wall peaks to the interfacial region.

Figure 6.24 shows the distribution of u-rms in single-phase oil and water flow at velocity equal to 1.0 m/s. The trend of u-rms velocities for single-phase oil and water is nearly equal, with the exception of the smoothness of the curves. The oil-phase measurements are more scattered than the water-phase measurements, which are due to a much lower number of samples in the oil compared to water. The u-rms values are most scattered in the upper and lower region of the pipe. A data point, which is clearly off the trend is located at z/R = 0.65. This is most likely due to locally refraction of the laser beams due to poor optical condition. A lower sample rate in oil was also reported by Elseth (2001).

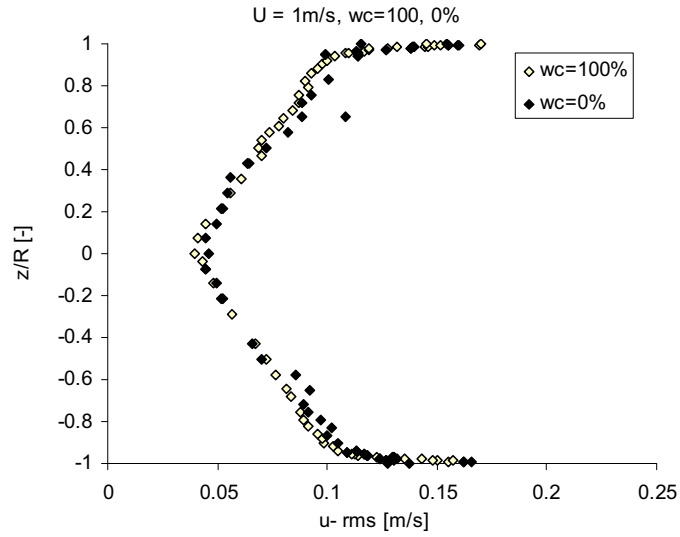

Figure 6.24. Axial rms-velocity distributions at 1.0 m/s velocity, input water cut equal to 0 and 100%.

6.6.5 Effect of inclination on the u-rms velocities at 50% input water cut

Figure 6.25 shows that the u-rms in the water phase increases with increasing downward inclination. The u-rms at 0º and -1º pipe inclinations is lower than the ones observed in single-phase flow, except for the interfacial region. When the pipe decreases from 0º to -5º and -10° angle the u-rms velocities become larger than the single-phase flow measurements in the lower part of the pipe. The local peaks in the u-rms profile seem to be caused by the interfacial waves and droplets. Elseth (2001) also measured a lower u-rms velocity above and below the interface at 50% input water cut and 0º pipe inclination, except for very close to the wall. A clear trend is difficult to see in the upper part of the pipe (z/R = 0.4 - 0.8) at -5° angle due to the large variation in the measured u-rms, which is most likely due to poor optical conditions.

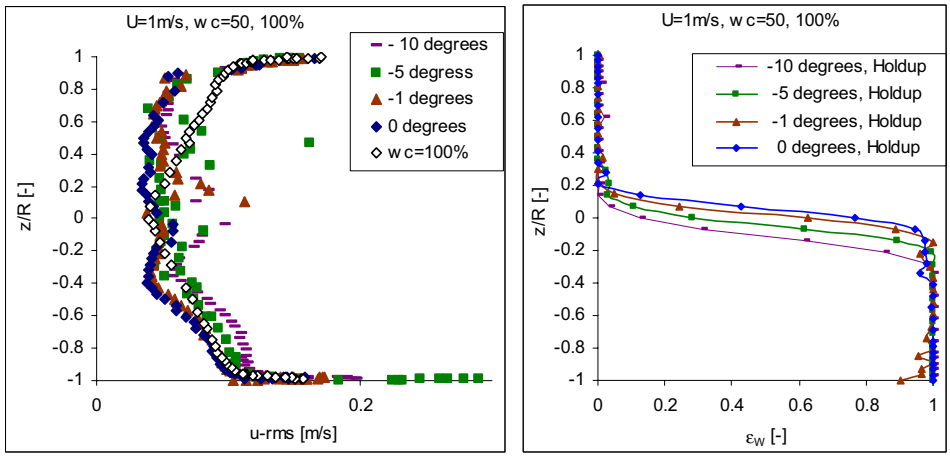

Figure 6.25. Axial rms-velocity distributions and holdup at 1.0 m/s mixture velocity, input water cut equal to 50% and pipe inclination angles from -10º to 0°.

Figure 6.26 shows the effect of inclining the flow upward from 0° to +10° on the u-rms velocities at 50% input water cut. The u-rms values are increasing in the centre of the pipe with increasing inclination (0° to +10°) and at +10° angle the u-rms is much larger compared with the single-water phase values. The effect of going from 0° to +1° has minor influence on the u-rms velocities, while a further increase to +5° and then to +10° increase the u-rms velocities significantly.

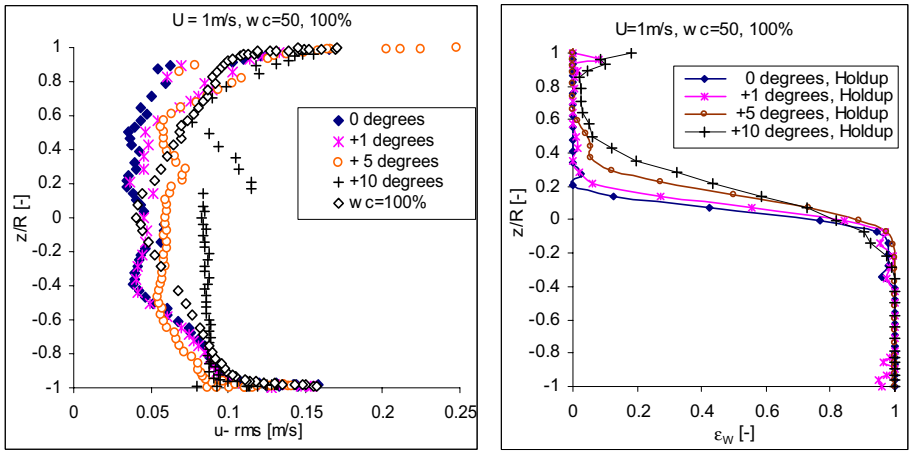

Figure 6.26. Axial rms-velocity distributions and holdup at 1.0 m/s mixture velocity, input water cut equal to 50% and pipe inclination angles from 0° to +10º.

6.6.6 Effect of inclination on the u-rms velocities at 25% input water cut

Figure 6.27 shows that the u-rms values above and below the interfacial region are mostly lower than the single water-phase values. The u-rms values in the water phase increase when the pipe inclines from 0° to -10° angle, which is the same trend as was observed at 50% input water cut, but to a much lower degree. Inclining the pipe downward from 0° to -1° has minor effect on the u-rms distributions. The u-rms values at 25% input water cut in inclined and horizontal flow differ much less from the single-phase water values compared to the ones measured at 50% input water cut.

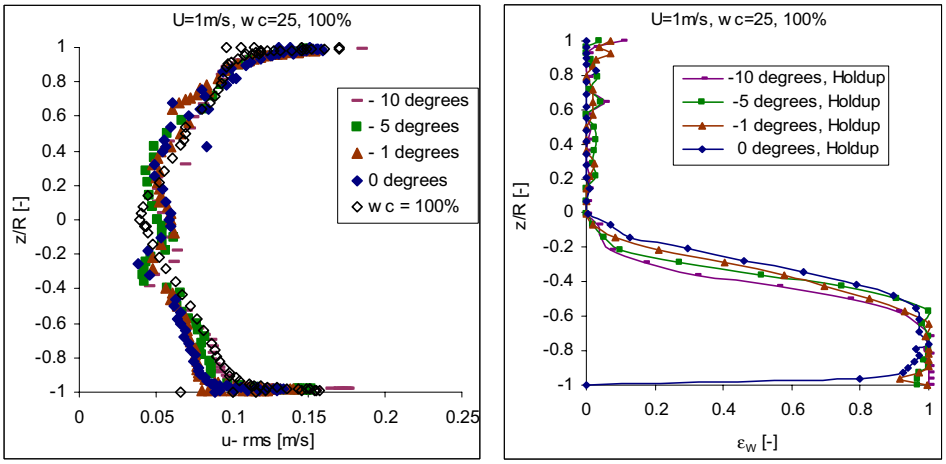

Figure 6.27. Axial rms-velocity distributions and holdup at 1.0 m/s mixture velocity, input water cut equal to 25% and pipe inclination angles from -10º to 0°.

Figure 6.28 shows an increase in u-rms in the interfacial region with increasing upward inclination. This was also measured in upward flow at input water cut equal to 50%. Larger variations in the u-rms are observed in upward moving flow compared to downward flow, which may be an indication of a more disturbed interface.

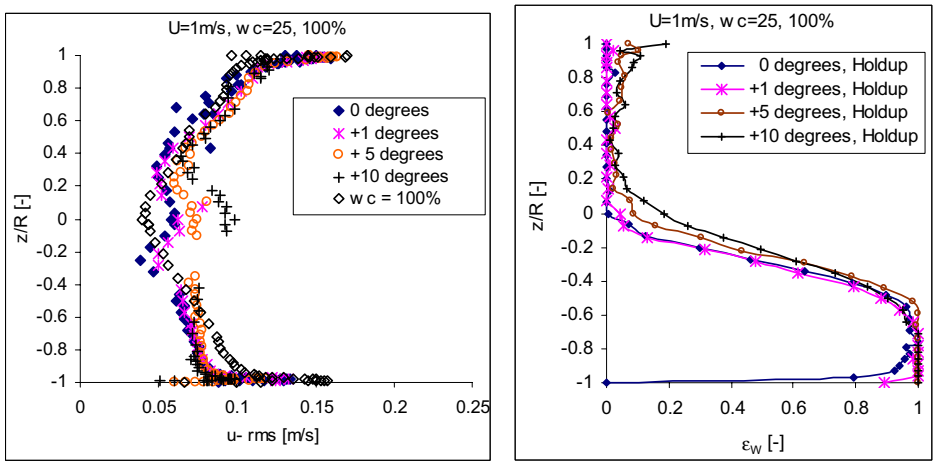

Figure 6.28. Axial rms-velocity distributions and holdup at 1.0 m/s mixture velocity, input water cut equal to 25% and pipe inclination angles from 0° to +10º.

6.6.7 Vertical rms-velocity

In two-phase flow the v-rms profile is generally decreasing from the wall peaks (z/R = +0.9 and -0.9) to the interfacial region. The larger degree of waves and dispersed droplets in the interface region at large inclination angles lead to low sampling number. The low sampling number causes discontinuities in the centre of the pipe in some of the measurements (Figure 6.30 and Figure 6.31).

Figure 6.29 shows a comparison between the v-rms-velocities of single-phase oil and water. The water v-rms velocities show an increasing trend from the inner walls to the wall peaks and then the values decrease towards the centre of the pipe. The oil v-rms velocities, generally follows the same trend, but deviates from the water v-rms trend at some locations in the pipe, due to optical disturbances. Deviations from the water v-rms trend are especially noticeable in the lower part of the pipe. Elseth (2001) reported higher v-rms values in oil compared with water, which do not agree with present measurements. This could be due to the inaccuracy in the flow meter and pump speed measurements.

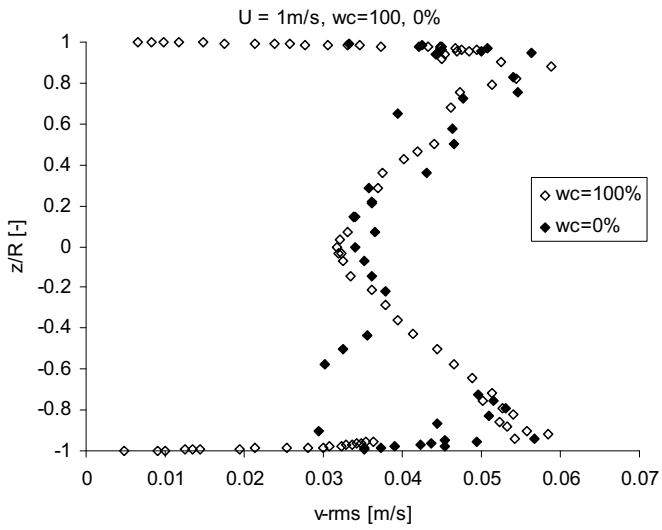

Figure 6.29. Vertical-rms velocity distributions at 1.0 m/s and input water cut from 0 to100%.

6.6.8 Effect of inclination on the v-rms velocities at 50% input water cut

Figure 6.30 presents the vertical-rms velocity and holdup distributions at 50 and 100% input water cut and downward inclination angles from -10° to 0°. Decreasing the inclination angle from 0° to -1° has minor effect on the v-rms measurements, but inclining the pipe further down to -5° and -10° leads to an increase in the v-rms in the water phase. While an increase is seen in the water phase, the v-rms in the oil phase does not seem to change much. In the upper part of the pipe, the v-rms is below the single-phase water values, while in the lower part of the pipe the v-rms measurements exceed the single-phase water values at inclinations equal to -5º and -10°.

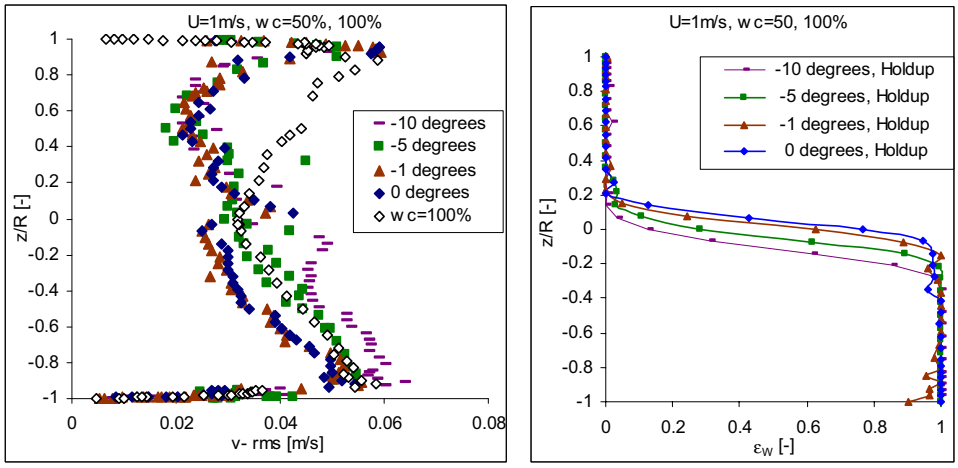

Figure 6.30. Vertical rms-velocity and holdup distributions at 1.0 m/s mixture velocity, input water cut equal to 50% and pipe inclination angles from -10 to 0°.

Figure 6.31 presents the v-rms velocity distributions and phase distribution profiles at 50% input water cut with the effect of increasing the pipe from 0° to +10°. As was also seen in downward moving flow the influence of inclining the pipe with +1° angle has minor effect on the flow. The v-rms velocities at +1° angle are slightly larger in the upper side of the pipe and slightly lower in the lower part of the pipe compared to the v-rms velocities at 0° angle. Increasing the pipe further up to +5° and +10° angle increase the v-rms values above the single-phase values in the interfacial region.

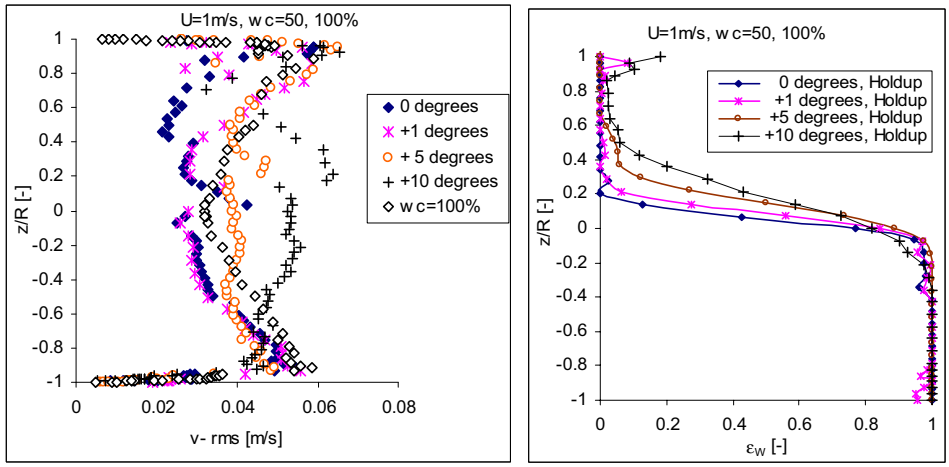

Figure 6.31. Vertical rms-velocity and holdup distributions at 1.0 m/s mixture velocity, input water cut equal to 50% and pipe inclination angles from 0° to +10º.

6.6.9 Effect of inclination on the v-rms velocities at 25% input water cut

Figure 6.32 presents the vertical rms-velocity and holdup distributions at 25 and 100% input water cut and the effect of decreasing the inclination angle downward from 0° to -10°. Generally, the two-phase values are lower than the single-phase values, except at -10° inclination where the v-rms is higher in the centre of the pipe, just above and in the interfacial region. In the water continuous phase the v-rms increases with decreasing inclination angle from 0° to -10°. It is not possible to observe a trend in the oil continuous flow region due to scattering caused by optical disturbances.

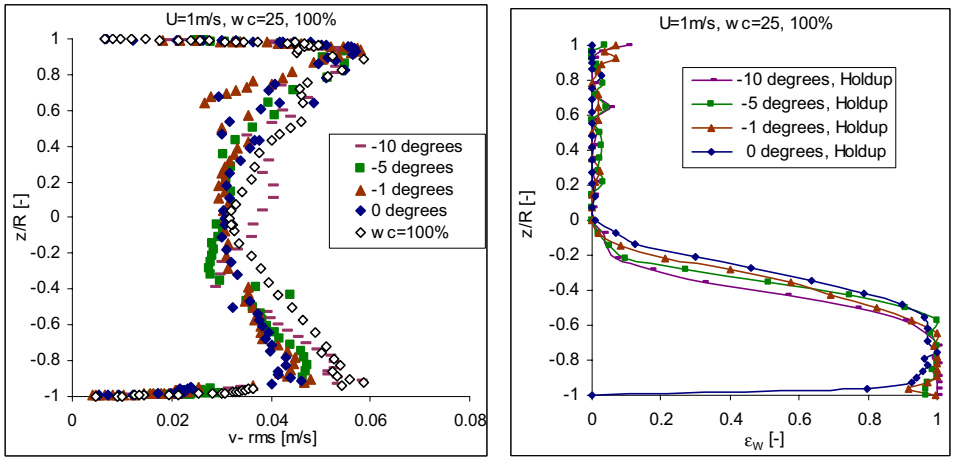

Figure 6.32. Vertical rms-velocity distributions and holdup at 1.0 m/s mixture velocity, water cut equal to 25% and pipe inclination angles from -10º to 0°.

Figure 6.33 presents the vertical rms-velocities and the effect of increasing the pipe upwards from 0° to +10° at 25% input water cut. The phase distribution curves are presented on the right hand side. Inclining the pipe from 0° to +1° has minor effect on the v-rms profile, but increasing the inclination up to +5° and +10° leads to increased v-rms values in the interfacial region as was observed at 50% input water cut. The v-rms values increase above the single-phase values.

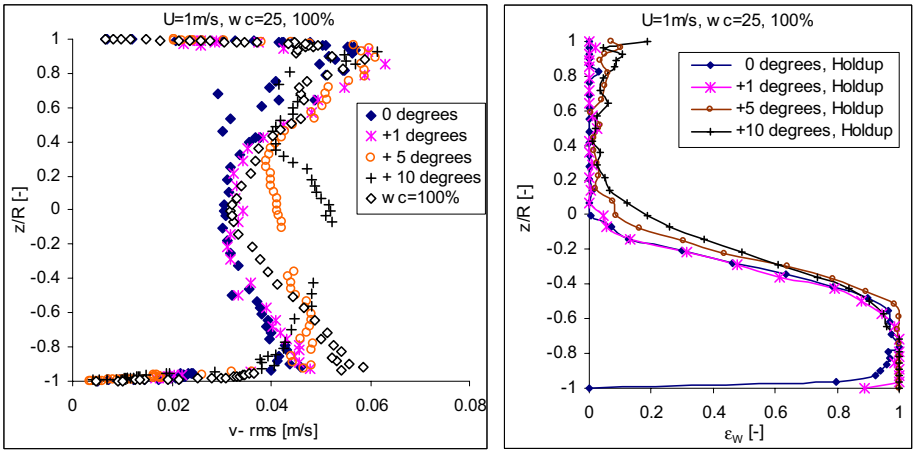

Figure 6.33. Vertical rms-velocity distributions and holdup at 1.0 m/s mixture velocity, water cut equal to 25% and pipe inclination angles from 0° to +10º.

6.6.10 Cross-moments

Cross-moment distributions calculated from Eq. (6.8) are presented for single-phase oil and water flow and for two-phase flow at input water cuts equal to 25 and 50% at pipe inclinations equal to 0°, ±1°, ±5° and ±10°.

Figure 6.34 shows the cross-moments for single-phase oil and water. The single-phase water values increases from the inner walls up to a maximum and decreases towards the centre of the pipe. The single-phase oil values deviates from this trend in the upper and lower part of the pipe, where scattering occurs due to poor optical conditions and refraction of the beams.

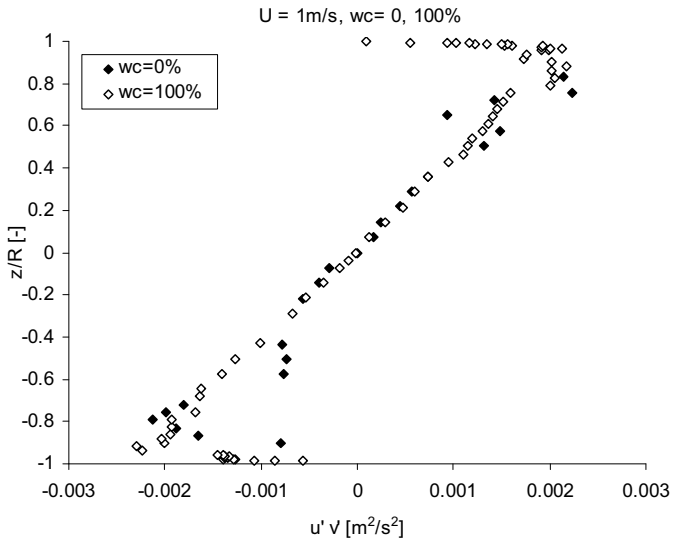

Figure 6.34. Cross-moment distributions in single-phase oil and water flow at 1.0 m/s.

6.6.11 Effect of inclination on the cross-moments at 50% input water cut

Figure 6.35 presents the cross-moments, holdup distributions and the effect of decreasing the inclination angle downward from 0° to -10° at 50% input water cut. The effect of adding 50% water to single-phase oil flow leads to a reduction of the cross-moments close to zero in the interfacial region and a distance above and below the interface. The dampening effect is observed in both horizontal and downward moving flow (-1° to -10° angle). The dampening effect at -10° inclination takes place above the interfacial region and less below. It seems like the waves and dispersed droplets in the interfacial region dampen the cross-moments. Elseth (2001), Kumara et al. (2009a) and Kumara et al. (2009b) reported a dampening of the Reynolds stresses in horizontal pipe flow. Elseth (2001) observed this phenomena in horizontal pipe flow at mixture velocities lower than 1.71 m/s. Kumara et al. (2009a) measured a dampening effect in both downward inclinations (-1° and -5°) and in horizontal pipe flow at a mixture velocity of 0.25 m/s and 25% input water cut. Solbakken and Schüller (2001) reported a lower pressure drop for three-phase gas/condensate/water than gas/condensate systems. An explanation for this behaviour was turbulence reduction due to interfacial dampening in the liquid-liquid system as were measured by Elseth (2001). The largest impact on the cross-moments is seen when the angle decreases from 0° to -10° angle. This is observed as a decrease in the water continuous phase in the lower part of the pipe. In

two-phase flow, the wall peaks are higher in the oil phase compared to single-phase flow, while in the water phase at lower inclinations (0° and -1°) the cross-moments are lower than the single-phase moments.

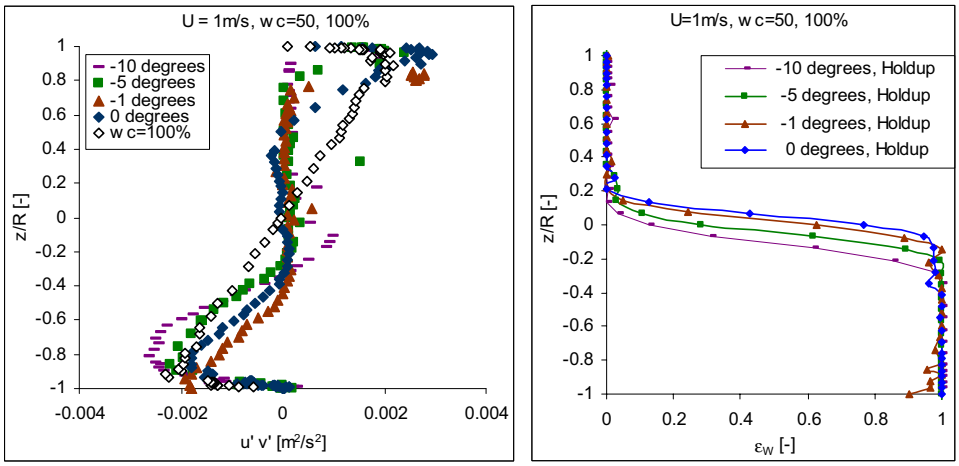

Figure 6.35. Cross-moments at 1.0 m/s mixture velocity, water cut equal to 50% and pipe inclination angles from -10º to 0°.

Figure 6.36 presents the cross-moments, holdup distributions and the effect of increasing the inclination angle upward from 0° to +10° at 50% input water cut. The influence of increasing the inclination angle has larger impact on the cross-moments than decreasing the inclination angle, which is probably due to more waves and/or dispersion of droplets in the interface region. The cross-moments increase significantly in the interfacial region, when the pipe inclines to +5° and +10° angle. Kumara et al. (2009a) measured an increase in the Reynolds stresses in the interfacial region at +5° inclination angle. The velocity and input water cut was equal to 0.25 m/s and 25%, and the increase in Reynolds stresses were explained by the increased turbulence fluctuations due to the rolling motion of the interface. Inclining the pipe from 0° to +1° affects the cross-moments insignificantly as observed when inclining the pipe from 0° to -1°. The dampening effect is significant at +1° angle and becomes less important when the inclination angle increases to +5° and +10°.

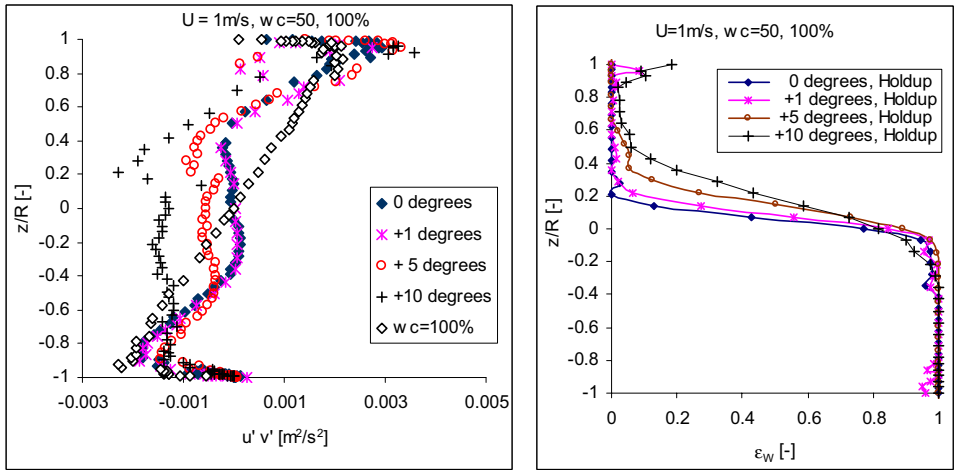

Figure 6.36. Cross-moments at 1.0 m/s mixture velocity, water cut equal to 50% and pipe inclination angles from 0° to +10º.

6.6.12 Effect of inclination on the cross-moments at 25% input water cut

Figure 6.37 presents the cross-moments, holdup distributions and the effect of decreasing the pipe downward from 0° to -10° angle at 25%. The cross-moments in downward flow are measured to be very close to zero in and above the interfacial region as was also measured at 50% input water cut. No large differences are seen between the pipe inclinations. The cross-moments values in the lower part of the pipe increases slightly to larger negative values when the pipe inclines from 0° to -10º angle.

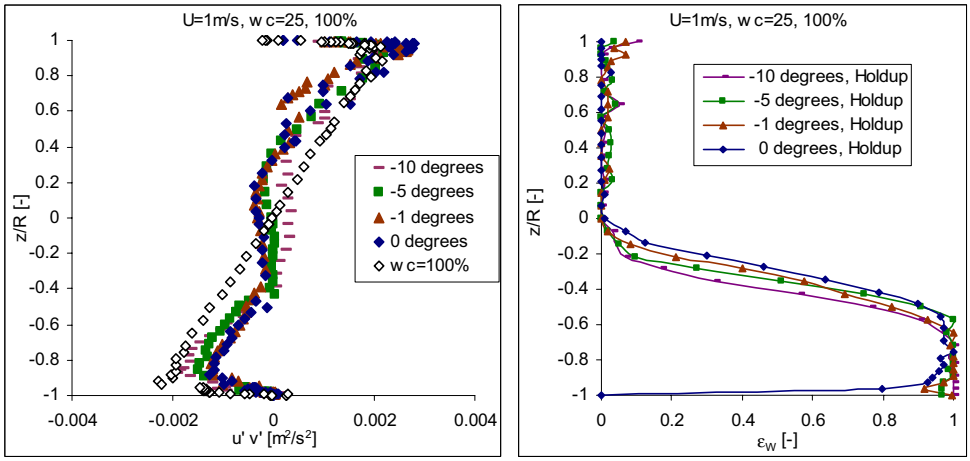

Figure 6.37. Cross-moments at 1.0 m/s mixture velocity, water cut equal to 25% and pipe inclination from -10° to 0º.

The trends observed in upward moving flow at 50% input water were also seen at 25% input water cut. Figure 6.38 shows an increasing trend (larger negative cross-moments) in the interfacial region when the pipe inclines upwards from 0° to +10° angle. This may be due to larger rolling waves in upward moving flow as was measured by Kumara et al. (2009a). The cross-moments changes insignificantly, when the pipe angle increases from 0° to +1°.

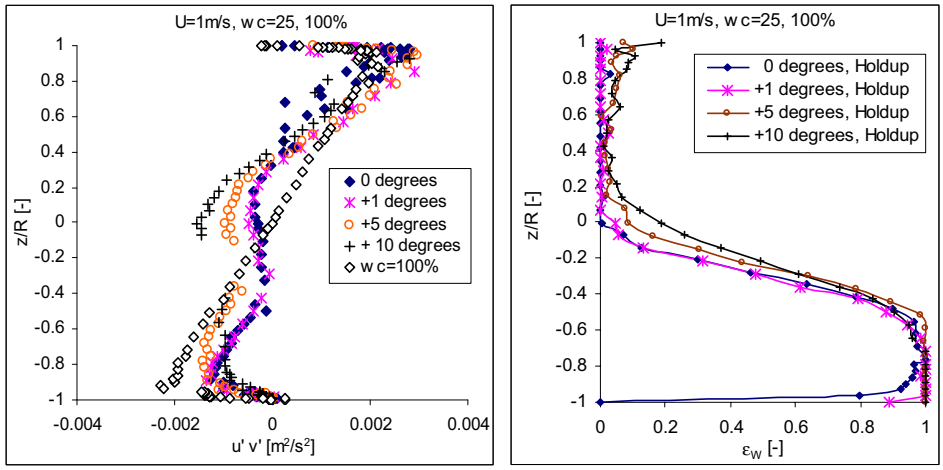

Figure 6.38. Cross-moments at 1.0 m/s mixture velocity, water cut equal to 25% and 100% and pipe inclination angles from 0º to 10°

6.7 Summary

- Axial mean velocity
  - The velocity distribution is symmetrical in single-phase and non-symmetrical in two-phase flow.
  - In horizontal two-phase flow at 50% input water cut, the high viscosity phase (oil phase) has a higher maximum velocity than the low viscosity (water phase), which could be contributed to the larger wall shear in the oil phase because of lower density for oil (see section 6.6.1). The calculated slip ratio from the gamma measurements in Chapter 4 supports this observation. A slip ratio above one means that that oil is the fastest moving phase.
  - The effect of pipe inclination is larger at 50% input water cut than at 25% input water cut.
  - The effect of inclining the pipe with ±1° has minor effect on the velocity profile, especially at 25% input water cut, which also the calculated slip ratios from the gamma measurements reflects.
  - Inclining the pipe with ±5° and ±10° angle has large effect on the measured velocity profile.
  - In downward moving flow at 25 and 50% input water cut, the oil phase velocity is decreasing with decreasing inclination angle (0° to -10°) and the water phase velocity is increasing (see Figure 6.17 and Figure 6.22). This trend is also observed in the calculated slip ratio measurements from the gamma measurements in Chapter 4.
  - In upward moving flow at 50% input water cut, the velocity of the water phase is decreasing with increasing upward inclinations (0° to +10°) and the oil phase velocity increases (see Figure 6.18). At 25% input water cut the same trend is observed, especially from +1° to +10° angle (see Figure 6.23).

- Axial rms velocity
  - The inclination affects the u-rms velocity profiles to a larger degree in upward moving flow compared to downward moving flow.
  - The u-rms velocities increase in the interfacial region with increasing upward inclination at 25 and 50 % input water cut (see Figure 6.28 and Figure 6.26).

- There are minor differences between the u-rms velocities at 0° and ±1°.

- Vertical rms velocity
  - The v-rms velocities increase in the interfacial region with increasing upward inclination at 25 and 50% input water cut.
  - In the water continuous phase, the v-rms increases with decreasing downward inclination angle from 0° to -10° at 25 and 50% input water cut (see Figure 6.32 and Figure 6.30).
  - The effect of inclining the pipe with ±1° is small.
- Cross-moments
  - A dampening effect of the cross-moments occurs in horizontal and downward moving flow at both 25 and 50% input water cut (see Figure 6.37 and Figure 6.35).
  - The absolute value of the cross-moments increase in the interfacial region when the pipe inclines upward from +1° to +10° angle at 25 and 50% input water cut (see Figure 6.38 and Figure 6.36).

- Data validation (see section 6.5)
  - A comparison of the integrated velocity profiles in single-phase water and oil with the flow meter readings in present study in Chapter 3 (Table 3.8) shows that the deviation between the two measurements is lower than the accuracy of the flow meters.
  - Model comparison: A comparison between two different models ($1/7^{th}$ power model and the law of the wall model) and experimental data shows good agreement which indicates a good accuracy of the LDA measurements and that the experimental set-up works satisfactory.
  - Reproducibility: The reproducibility of the velocity profile in single-phase and two-phase flow is good and within the accuracy of the flow meters. The turbulence distribution (v-rms, u-rms and cross-moments) in single-phase flow follows the same trend, but is more scattered than the velocity data. The good comparison between the trends observed in present study and that of Elseth (2001) implies a good reproducibility.

7 MODEL COMPARISON

7.1 Introduction

In stratified gas-liquid flow it is usually possible to assume (at least for sufficiently small gas velocities) that relatively little liquid is entrained in the gas phase and relatively little gas is entrained in the liquid phase. The reason for the validity of this assumption is, of course, that in a gas-liquid system, the buoyancy force is so dominant that turbulence is unable to move a significant fraction of drops or bubbles away from the interface (except for the smallest drops or bubbles). In liquid-liquid systems this assumption is generally no longer valid, with the exception of very low velocities, see for example, Angeli and Hewitt (2000) and Elseth (2001). Again, the fundamental reason is obvious: the reduced density difference between the two liquid phases enables relatively weak turbulent forces to move drops away from the liquid-liquid interfaces This means that in almost all liquid-liquid systems a method is required which is able to model the fraction of the dispersed phase in each liquid layer.

Figure 7.1 Stratified oil-water flow in a 0.056m pipe ($u_{mix} = 1$ m/s, input water cut is equal to 25%).

A turbulent diffusion model of dispersed particles flowing in a pipe was outlined by Mols and Oliemans (1998). Valle (2000) has used a similar turbulent diffusion model to model dispersed liquid-liquid flows and has shown that concentration profiles can be predicted with reasonable accuracy. Within the framework of the two-fluid model it is also possible to model liquid-liquid flows but now a closure relation is required that determines the entrainment rate of droplets into the continuous phase (see e.g. Valle, 2000).

7.2 Two fluid model combined with a dispersion model

The model presented is developed by Schulkes (2000) and have features which are very similar to the models for fully-dispersed flow as presented by Mols and Oliemans (1998) and Valle (2000). Namely, the dispersed phase concentration profile is computed by balancing turbulent dispersive forces with buoyancy forces. This study gives a comparison of the model against the presented experimental data and a description of the model. The model has been published in Amundsen et al. (2009). Valle (2000) developed a two-dimensional model which computes a force balance on the dispersed phase drops and subsequently determines the spatial drop distribution in the cross section of the pipe. This two-dimensional model is computationally too expensive to be used in transient multiphase simulations. However, rather than obtaining a full radial description of the dispersed phase concentration, it is assumed that outside the near-wall boundary layers, the dispersed phase concentration is essentially one-dimensional and dictated by the direction of the gravitational vector. This means that the interface has a layered structure and do not have a curved interface. This assumption should be valid, at least for low velocities [see e.g. Soleimani (1999)]. This means that at the cost of reducing the accuracy of the model in the near-wall region a significant simplification is obtained. In addition, the model can readily be integrated in the two-fluid modelling concept. In the proposed model, the only closure parameter that cannot be obtained from mechanistic considerations, is the dispersed phase fraction at the liquid-liquid interface. It is tempting to relate this dispersed phase fraction to the inversion water cut but there is currently no experimental evidence that can support this assumption. The complexity of the inversion process is well-documented in e.g. Piela et al. (2008) and even though some attempts have been made to model this process by e.g. Brauner and Ullmann (2002) this parameter is treated as a variable which can be specified.

7.2.1 Dispersion model

The defining feature of liquid-liquid flows is the fact that it is relatively easy to disperse one phase into the other. The reason for this is, of course, that the density difference between the phases is relatively small. Hence, the turbulent dispersive forces which are required to transport the dispersed phase in the direction opposite to the acting buoyancy forces are relatively large. The essential building blocks of the model are therefore clear: the concentration profile of the dispersed phase is modelled as a balance between turbulent and buoyancy forces.

Consider a cross section of a pipe a long distance downstream from the inlet of the pipe such that it is possible to assume that the flow has reached a steady state and is fully-developed. Let ε denote the concentration of the dispersed phase (oil droplets in water and water droplets in oil) in the cross section of the pipe. In general, the dispersed phase is a function of the vertical height z and the cross-wise coordinate y. However, being the dominant force, gravity imposes a dominant direction on the concentration gradient of the dispersed phase. Because of this, it is possible as a first approximation, to assume that concentration gradients perpendicular to the force of gravity can be neglected. This turns out to be a valid assumption, at least in the bulk of the flow. Close to the solid boundaries where significant velocity gradients lead to Safman lift effects, the model would have to be modified [see e.g. Valle (2000)].

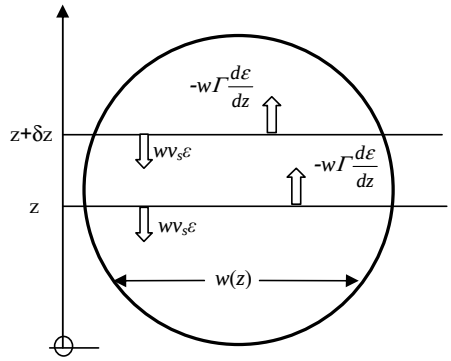

Figure 7.2 Schematic diagram of control volume and dispersed phase fluxes.

The flux of the dispersed phase in a control volume as shown in Figure 7.2 is expressed in Eq. (7.1). The dispersed phase is assumed to be heavier than the continuous phase so that the dispersed phase concentration increases towards the bottom of the pipe. For a fully-developed steady-state flow the flux of dispersed particles into the control volume must equal the flux out of the control volume.

$$wv_s\varepsilon\big|_{z+\delta z} - w\Gamma\left.\frac{d\varepsilon}{dz}\right|_z = wv_s\varepsilon\big|_z - w\Gamma\left.\frac{d\varepsilon}{dz}\right|_{z+\delta z} \tag{7.1}$$

Where $w(z)$ denotes the width of the control volume, v_s denotes the sedimentation velocity of the dispersed phase as a result of the action of gravity forces and Γ denotes the turbulent particle diffusion coefficient. By letting $\delta z \to 0$ in Eq. (7.1) and integrating once, Eq. (7.2) is derived.

$$w v_s \varepsilon + w\Gamma \frac{d\varepsilon}{dz} = C \tag{7.2}$$

Where C is an integration constant. At $z = 0$ it is clear that $w(0) = 0$ which implies that the integration constant $C = 0$. The equation which describes the vertical dispersed phase concentration profile becomes therefore Eq. (7.3).

$$v_s \varepsilon + \Gamma \frac{d\varepsilon}{dz} = 0 \tag{7.3}$$

In the case where the sedimentation velocity is constant, Eq. (7.3) has a trivial exponential solution. However, as will be shown below, the sedimentation velocity is a function of the dispersed phase fraction, that is $v_s = v_s(\varepsilon)$, and hence Eq. (7.3) will in general have to be solved numerically.

The model for the vertical dispersed phase concentration as given in Eq. (7.3) requires closure relations for the sedimentation velocity (v_s) and for the turbulent diffusion coefficient (Γ).

Sedimentation velocity (v_s)

A fluid particle falling in an infinite, homogeneous medium has a well-known sedimentation velocity [Batchelor (1967)] which is determined by the balance of buoyancy and drag forces as shown in Eqs. (7.4) and (7.5).

$$F_g = \frac{4\pi}{3} a^3 \left(\rho_f - \rho_p\right) g \cos\theta \tag{7.4}$$

$$F_D = \frac{\pi}{2} a^2 \rho_f C_D v_\infty{}^2 \tag{7.5}$$

The sedimentation velocity can be written as shown in Eq. (7.6).

$$v_\infty = -sign(\Delta\rho)\sqrt{\frac{8a\,|\,\Delta\rho\,|\,g}{3\rho_f C_D}} \tag{7.6}$$

Where a denotes the radius of the fluid particle, $\Delta\rho = \rho_p - \rho_f$ with ρ_p and ρ_f denoting the particle and fluid density respectively, g denotes the gravitational acceleration. The sedimentation velocity of the dispersed phase is low so an estimate of the drag coefficient for particle Reynolds numbers $\mathrm{Re}_p \le 100$ is needed. The approximation of the drag coefficient [Jayanti and Hewitt (1991)] is shown in Eq. (7.7).

$$C_D = \frac{18.5}{\mathrm{Re}_p^{0.6}} \tag{7.7}$$

Where the particle Reynolds number is defined via Eq. (7.8).

$$\mathrm{Re}_p = \frac{2av_\infty\rho_f}{\mu_f} \tag{7.8}$$

Determination of the sedimentation velocity in Eq. (7.6) requires information about the dispersed phase particle size a. Hinze's (1955) classical model is used to compute the maximum drop size. Experimental work by Simmons and Azzopardi (2001) with air and water shows that in a dilute system the Hinze (1955) model gives a good approximation of the maximum drop size while in a non-dilute system the maximum drop size tends to be under-predicted. Oil-water flow experiments conducted by Vielma et al. (2007) also show that the model of Hinze (1955) under predicts the maximum droplet size. Once the maximum drop size is known, the drop size distribution is calculated by use of a Rosin-Rambler distribution. Then a mean drop size can be computed, which is related to the maximum drop size via Eq. (7.9).

$$d_{mean} = 0.557 d_{\max} \tag{7.9}$$

The mean drop size as given in Eq. (7.9) is subsequently used in the computation of the sedimentation velocity. When a fluid particle moves in the presence of other particles, the sedimentation velocity reduces due to the action of particle-particle interactions. It is this sedimentation velocity that is required in Eq. (7.3). A common way to write the sedimentation

in such a system is shown in Eq. (7.10), where the exponent n_s has to be specified [Richardson and Zaki (1954)].

$$\frac{v}{v_\infty} = (1-\varepsilon)^{n_s} \tag{7.10}$$

Batchelor (1972) and Batchelor and Wen (1982) have shown that in the limit of dilute suspensions ($\varepsilon << 1$) the exponent n_s = 6.5 for the case of mono-dispersed suspensions while it decreases to n_s = 5.5 for suspensions with slightly-varying solid particles. Classical experiments by Richardson and Zaki (1954), and a more recent experiments by Di Felice (1999), show that in the low Reynolds number limit, the exponent n_s is in a similar range, namely $4.8 < n_s < 6.5$. Calculations with the model described here show that the best match with experimental profiles is obtained when n_s = 3. The reason why the exponent (n_s) used in present calculations is lower than that of Di Felice (1999) could be that the larger elasticity to the droplets compared to solid particles will increase the sedimentation velocity. Another aspect that will influence the sedimentation velocity is that the dispersion in present experiments is inhomogeneous with a dilute and dense dispersion in different parts of the pipe. The sedimentation velocity can therefore vary as function of position of the pipe.

Turbulent diffusion coefficient

Mols and Oliemans (1998) suggest modelling the turbulent particle diffusion coefficient in dilute systems as shown in Eq. (7.11), where Γ_f denotes the turbulent fluid diffusivity.

$$\Gamma = \gamma_p \Gamma_f \tag{7.11}$$

The constant $\gamma_p < 1$ accounts for the fact that the particle diffusivity is less than the fluid diffusivity due to particle inertia effects. Following Mols and Oliemans (1998) the turbulent fluid diffusivity is expresses as shown in Eq. (7.12).

$$\Gamma_f = (0.7u^*)^2 \times T_{\text{int}} \tag{7.12}$$

In which u^* denotes the friction velocity and T_{int} denotes the integral fluid time scale. The friction velocity is given as $\sqrt{\tau_w / \rho_m}$, where τ_w is the mean wall shear stress and ρ_m is the

mixture density of the fluid zone. Eq. (7.13) shows how the integral fluid time scale can be approximated, where D_h denotes the hydraulic diameter of the oil or water layer.

$$T_{\text{int}} \approx 0.1 D_h / u^* \tag{7.13}$$

For simplicity the γ_p constant in Eq. (7.11) is set equal to one ($\gamma_p = 1$), which may be justified by the fact that the densities of the oil and water phase are not very different. This means that the particle diffusivity is approximated via Eq. (7.14).

$$\Gamma = 0.049 u^* D_h \tag{7.14}$$

It is to be expected that the particle diffusivity is modified by the presence of dispersed-phase particles. However, it is difficult to quantify this modification, in particular when the dispersed phase fraction increases beyond the dilute limit. For this reason the particle diffusivity as given in Eq. (7.14) is chosen.

With the sedimentation velocity and the diffusivity specified, the profile Eq. (7.3) can be solved. However, one additional condition needs to be specified in order to obtain a unique solution of Eq. (7.3). The dispersed phase concentration at $z = 0$ or $z = D$ is unknown, so an initial boundary condition cannot be given.

In the fully dispersed flow regime assuming no slip, the area-averaged volume fraction of the dispersed phase (ε) as shown in Eq. (7.15) is equal to the input water cut. Eq. (7.3) is now solved subject to the condition in Eq.(7.15) being fulfilled.

$$\varepsilon = \frac{1}{A} \int_A \varepsilon_i dA \tag{7.15}$$

In the case of stratified flow, the profile of the dispersed phase fraction in each layer is still found using Eq. (7.3). However, in this case the fraction of dispersed phase in each layer is not known (this is something the model should provide) so that we can not use Eq. (7.15) to close the problem. Instead an assumption which states that the volume fraction of the dispersed phase at which phase inversion occurs, is a well-defined quantity. This dispersed phase fraction, denoted by ε_{inv}, then defines the maximum fraction of the dispersed phase at

the liquid-liquid interface. It is not unreasonable to assume that ε_{inv} is related to the inversion water cut but at the moment this is just a hypothesis.

Suppose that the flow is stratified and the oil-water interface (h) is positioned at $z = h < D$, then in the oil-layer ($h < z < D$), Eq. (7.3) is solved by using $\varepsilon(h) = \varepsilon_{inv}$ while in the water layer ($0 < z < h$) the profile equation is solved with $\varepsilon(h) = 1 - \varepsilon_{inv}$. In both cases, the numerical integration of Eq. (7.3) starts at the liquid-liquid interface.

7.2.2 Two fluid model

When the profile of the dispersed phase in each of the layers has been computed, the area-averaged fraction of the dispersed phase in each layer, similarly to Eq. (7.15) can be calculated. This averaged fraction of the dispersed phase is subsequently used in the computation of the mixture density and the emulsion viscosity in each layer as shown in Eqs. (7.16) and (7.17), where ε denotes the volume fraction of the dispersed phase and ρ_c and ρ_d denote the densities of the continuous and dispersed phases respectively.

$$\rho_m = \rho_c(1-\varepsilon) + \rho_d\varepsilon \tag{7.16}$$

Various models for the emulsion viscosity have been proposed in the literature [see e.g. Pal (2000)] and here the model as proposed by Valle (2000) is used, in which the constants c_1 and c_2 are dependent on the continuous phase according to: c_1=1.558 and c_2=1.66 for oil continuous flow and c_1=1.307 and c_2=1.18 for water-continuous flow.

$$\mu_m = \mu_c\left(1 + \frac{c_1\varepsilon}{c_2 - c_1\varepsilon}\right)^{2.5} \tag{7.17}$$

Once the mixture density and mixture viscosity are specified, these mixture properties are in the friction factors to compute the wall and the interfacial shear stresses in the oil and water layers. The shear stresses for the different zones of oil (τ_o), water (τ_w) and the interface (τ_{ow}) are expressed in (7.18) to (7.20).

$$\tau_o = \frac{1}{8} f_o \rho_o u_o^2 \tag{7.18}$$

$$\tau_w = \frac{1}{8} f_w \rho_w u_w^2 \tag{7.19}$$

$$\tau_{ow} = \frac{1}{8} f_{ow} \rho_o (u_o - u_w)|u_o - u_w| \tag{7.20}$$

Three friction factors are specified; the wall friction factors (f_o and f_w) and interfacial friction factor (f_{ow}). Haaland's (1983) friction factor correlation is used to calculate the wall friction factors (f_o and f_w) with a roughness parameter equal to that of smooth pipes. The hydraulic diameter must be used when calculating the wall frictions, as shown in Eq. (7.21).

$$D_o = \frac{4A_o}{S_o}, D_w = \frac{4A_w}{S_w} \tag{7.21}$$

The interfacial friction factor is a difficult parameter to specify and is calculated by following Taitel et al. (1995), as shown in Eq. (7.22).

$$f_{\text{int}} = \max(f_{co}, 0.054) \tag{7.22}$$

In which f_{co} denotes the Darcy friction factor [e.g. Haaland (1983)] in the oil-continuous phase. With all the friction factors specified, the usual equations describing force balance in a stratified flow as shown in Eqs. (7.23) and (7.24) [see e.g. Ullmann and Brauner (2006)] are applied to determine the pressure drop, the in-situ velocities and position of the liquid-liquid interface.

$$A_w\left(\frac{dP}{dx}\right) - \tau_w S_w - \tau_i S_i - \rho_w A_w g \sin\beta = 0 \tag{7.23}$$

$$A_o\left(\frac{dP}{dx}\right) - \tau_o S_o + \tau_i S_i - A_o \rho_o g \sin\beta = 0 \tag{7.24}$$

Where S_w denotes the perimeter of the pipe surface in contact with the water, S_o the perimeter of the pipe surface in contact with the oil and S_i the width of the interface. The pressure gradient can be eliminated by substituting the pressure gradient in Eq. (7.23) into Eq. (7.24),

which yields Eq. (7.25). The next step is to express Eq. (7.25) as function of the interface height (h) as shown in Appendix 12.

$$F(h_w) = -\frac{\tau_o S_o}{A_o} + \frac{\tau_w S_w}{A_w} + \tau_i S_i \left(\frac{1}{A_w} + \frac{1}{A_o} \right) + (\rho_w - \rho_o) g \sin\beta = 0 \tag{7.25}$$

Eq. (7.26) expresses the in situ velocities of oil and water.

$$u_w = \frac{A}{A_w} U_{sw}, \; U_{sw} = \frac{Q_w}{A} \tag{7.26}$$
$$u_o = \frac{A}{A_o} U_{so}, \; U_{so} = \frac{Q_o}{A}$$

The mass balance of the continuous and dispersed phase can be expressed as shown in Eqs. (7.27) and (7.28).

$$U_{so} = U_{sco} + U_{sdo} \tag{7.27}$$

$$U_{sw} = U_{scw} + U_{sdw} \tag{7.28}$$

Where U_{so} denotes the superficial oil velocity, U_{sco} the superficial velocity of the oil-continuous layer and U_{sdo} the superficial velocity of the dispersed oil phase and likewise for the water phase.

Assuming no slip between the dispersed phase and the continuous phase (u_{co}=u_{dw} and u_{cw}=u_{do}) the superficial velocities of the dispersed phases (U_{sdo} and U_{sdw}) can be expressed as in Eqs. (7.29) to (7.32), where ε_{do} and ε_{dw} are the area averaged dispersed volume fractions of oil and water.

$$U_{sdo} = \frac{\varepsilon_o}{1-\varepsilon_o} U_{scw} \tag{7.29}$$

$$U_{sdw} = \frac{\varepsilon_w}{1-\varepsilon_w} U_{sco} \tag{7.30}$$

$$U_{sdo} = \varepsilon_{do} u_{cw} \tag{7.31}$$

$$U_{sdw} = \varepsilon_{dw} u_{co} \tag{7.32}$$

The superficial velocities of the continuous phase are expressed in terms of the in situ phase fractions as shown in Eq. (7.33).

$$U_{sco} = \varepsilon_{co} u_{co}, \; U_{scw} = \varepsilon_{cw} u_{cw,} \tag{7.33}$$

Substituting Eqs. (7.29) to (7.33) into Eqs. (7.27) and (7.28) yields Eqs. (7.34) and (7.35).

$$U_{so} = \varepsilon_{co} u_{co} + \frac{\varepsilon_o}{1-\varepsilon_o} \varepsilon_{cw} u_{cw} \tag{7.34}$$

$$U_{sw} = \varepsilon_{cw} u_{cw} + \frac{\varepsilon_w}{1-\varepsilon_w} \varepsilon_{co} u_{co} \tag{7.35}$$

7.2.3 Iterative procedure

With all the equations in place the iterative procedure to solve the problem is shown below (see Figure 7.3).

- The first step is to assume a dispersed phase fraction (ε) in each layer identically to zero. The hold-up equation [Eq. (7.25)] is then solved with respect to liquid height (h).
- The in situ velocities of oil and water phase are calculated as shown in Eq. (7.26).
- Next step is to compute the quantities required in the dispersion model in Eq. (7.3). The sedimentation velocity (v) in Eqs. (7.6) to (7.10) and the turbulent diffusion coefficient (Γ) in Eqs. (7.11) to (7.14).
- After that the concentration profile of the dispersed phase in each layer is computed by solving Eq. (7.3) with use of the inversion water cut (ε_{inv}) condition. Then the area-averaged dispersed phase concentration in each layer is determined by use of Eq. (7.15).
- Then the mixture density (ρ_m) and viscosity (μ_m) in each layer is computed according to Eqs. (7.16) and (7.17).
- The mixture velocities in each layer is subsequently computed from Eq. (7.27) to (7.35), ensuring that total mass for each fluid is conserved.

- The new position of the liquid-liquid interface is re-computed by solving the hold-up equation but now with mixture properties.

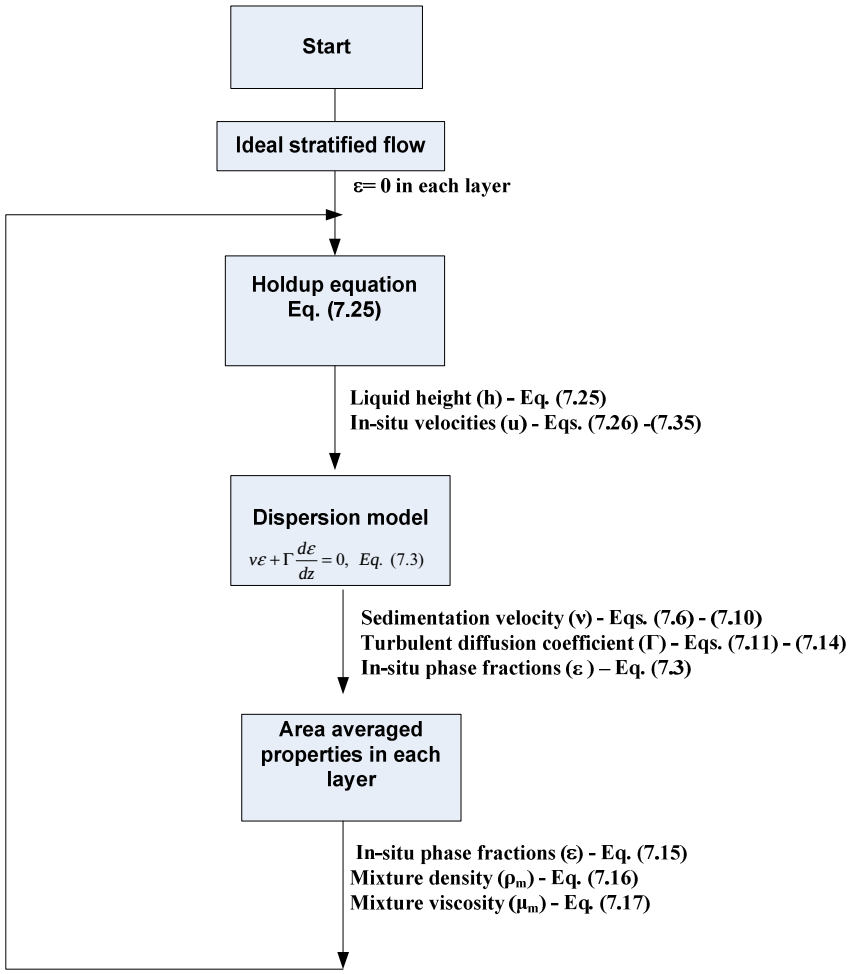

Figure 7.3 Iterative procedure.

Convergence of the iterative procedure is tracked by computing:

$$E_c = (\varepsilon_o^{(n+1)} - \varepsilon_o^{(n)}) / \varepsilon_o^{(n+1)} + (\varepsilon_w^{(n+1)} - \varepsilon_w^{(n)}) / \varepsilon_w^{(n+1)} \tag{7.36}$$

The solution is considered to be converged when the error $E_c < 10^{-3}$ and then the pressure gradient is calculated from Eqs. (7.23) or (7.24). During the iterative process it may occur that one of the continuous phases completely disappears and is turned into the dispersed phase.

When this happens, the hold-up equation is, obviously, no longer required. In this case the flow is fully dispersed flow and the condition presented in Eq. (7.15) is used to solve Eq. (7.3). The mixture properties are computed as outlined above and the concentration profile of the dispersed phased is computed as outlined in section 7.2.1.

7.3 Model vs. experiments in horizontal pipes

Comparisons between experiments and model predictions are shown for horizontal pipe flow. The experimental flow regimes, phase fractions, slip ratio and pressure gradients are compared with the predictions from the presented two-fluid dispersion model. Present horizontal data at 1 m/s and data of Elseth (2001) at 2 and 3 m/s are used in the model comparison.

7.3.1 Input data

The input data is the fluid properties of oil and water, pipe geometry, experimental variables and numerical parameters. The experiments were conducted at 1 bar pressure and temperature equal to approximately 20°C.

Table 7.1 Input data to oil-water model

Fluid properties	
Density oil, water	790,1000 (kg/m^3)
Viscosity oil, water	1.64, 1.02 (cP)
Oil-water surface tension	0.043 (N/m)
Inversion water cut	50 (%)
Pipe geometry	
Pipe diameter	0.0563 (m)
Inclination	0 (°)
Wall roughness	$1 \cdot 10^{-5}$ (m)
Experimental variables	
Mixture velocities	1, 2, 3 (m/s)
Water cuts	10-90 (%)
Numerical parameters	
Accuracy of solution	$1 \cdot 10^{-4}$

7.3.2 Flow regimes in horizontal pipe flow

Since the classification by Elseth (2001) is different from present study, the flow regimes of Elseth (2001) is re-classified by interpretation of the measured phase fraction profiles (see Table A7 in Appendix 13). The inversion input water cut is set equal to 50% in the model predictions; hence all the experimental flow regimes are classified in accordance to this. Figure 7.4 presents the experimental flow pattern map at velocities ranging from 1 to 3 m/s and input water cut from 10 to 90%. Increasing the velocity increases the degree of mixing. Increasing the velocity from 1 to 2 m/s at low and high input water cuts the flow pattern goes from being stratified to dispersed flow. The flow regime changes from ST & MI to o/w at 10% input water cut and at 85 and 90% the flow regime transforms from Dw/o & w to o/w. Increasing the velocity from 2 to 3 m/s at medium input water cuts the flow regime changes from ST & MI to Dw/o & Do/w. The flow pattern at 3 m/s and high input water cuts is classified as o/w. Figure 7.5 presents the flow pattern predictions. The flow patterns are classified by interpreting the phase distribution curves as was done for the measured phase fractions. The model fails predicting Dw/o & w flow regime at low velocity (1 m/s) and large input water cuts. The predictions compares well at low and large input water cuts when the velocity increases from 1 to 2 m/s, while at medium input water cut (50%) the model does not predict a ST & MI flow, but a Dw/o & Do/w. The predictions match the experimental values perfectly at large velocity equal to 3 m/s.

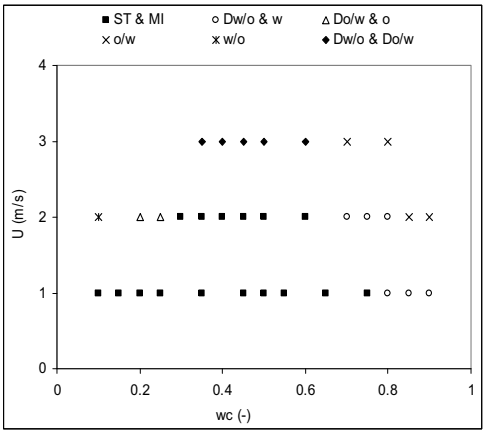

Figure 7.4 Experimental flow pattern map.

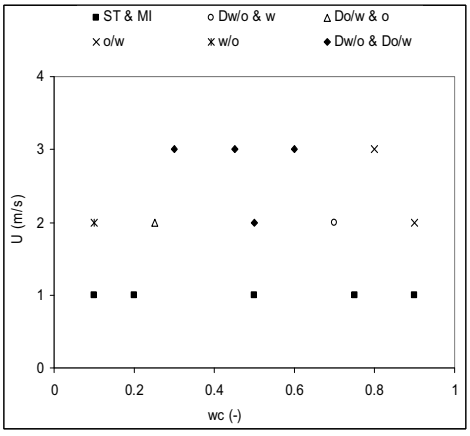

Figure 7.5 Computed flow pattern map.

7.3.3 Phase fraction predictions vs. experiments

Figure 7.6 shows a plot of the measured and computed water concentration profiles for various water cuts at a mixture velocity of 1m/s and Figure 7.7 presents the computed vs. experimental phase fractions. In Figure 7.6 on the vertical axis the dimensionless height is shown while on the horizontal axis the water fraction is plotted. The concentration profiles are generally predicted well by the model with the exception of the case with 50 and 90% input water cut. At 50% input water cut the model predicts a larger degree of dispersion at the interface than the experiments show and at 90% input water cut the model predicts a clear oil layer in the top of the pipe with almost no dispersed water while the experimental results show a dispersed layer in the top of the pipe. The model fails to predict the flow regime at 90% input water cut. Figure 7.7 shows that 87% of the phase fractions are predicted within ±60%. Large deviations are seen when the predictions are equal to zero and the measurements are larger than zero and the other way around (see e.g. 20, 50 and 90% input water cuts).

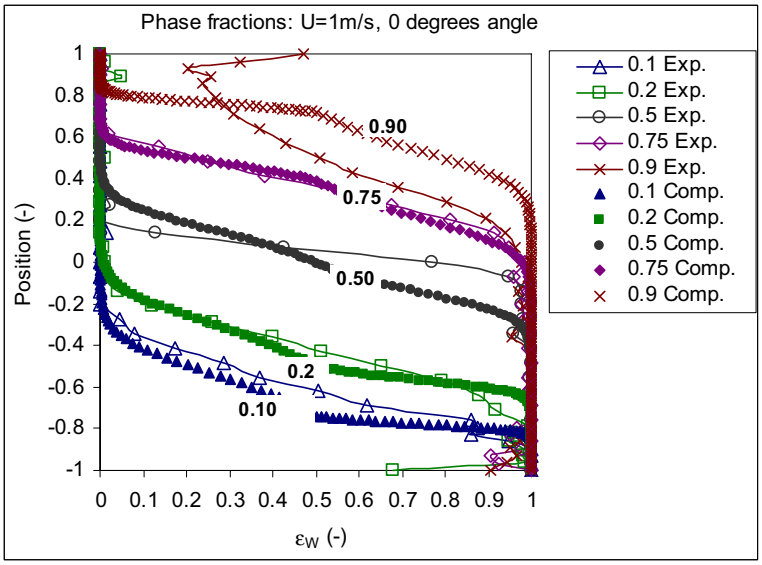

Figure 7.6 Water fraction as a function of the height in the pipe (U = 1 m/s).

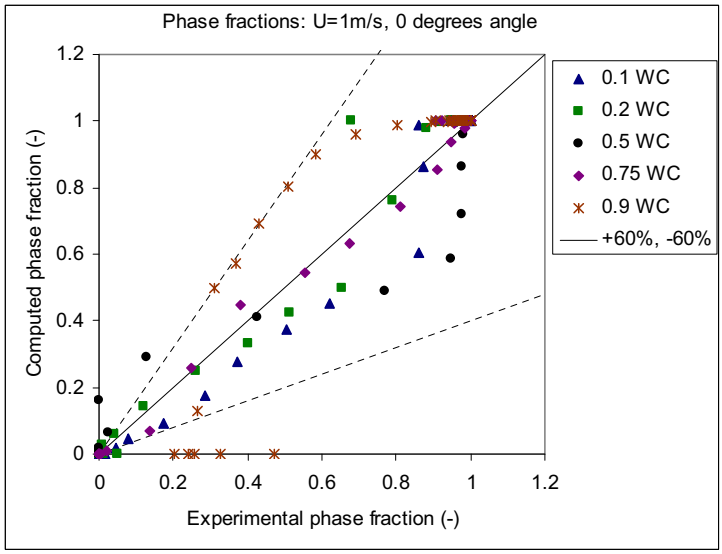

Figure 7.7 Experimental vs. computed water fraction at 1 m/s.

The model comparison at mixture velocities equal to 2 and 3 m/s is done by use of Elseth's (2001) published experimental data. The experimental setup used by Elseth (2001) is essentially the same as present study (same fluids, same pipe dimensions, same instrumentation). Figure 7.8 presents the measured and computed water fractions as function of vertical centre positions in the pipe and Figure 7.9 shows the predicted vs. experimental for the case with $U = 2$ m/s. The model is able to predict the increased amount of dispersion with increasing the velocity (see Figure 7.6 and Figure 7.8), but the quality of the model predictions gets poorer at higher velocities. In particular in the case of 50% input water cut, a large difference between model predictions and experiments are seen. The experiment shows less degree of dispersion than the predictions. The model over-predicts the phase fraction in the lower part of the pipe at 10 and 90% input water cut and under-predicts the phase fraction in the upper part of the pipe. At medium input water cut (25 – 70%) the model under-predicts the phase fractions in the lower part of the pipe. Good comparison between model and predictions are seen in the upper part of the pipe for 25 and 70% input water cut. Figure 7.9 shows that approximately 80% of the predictions are within ±60%, which is 7% lower compared to the experiments with velocity equal to 1 m/s. The largest deviations are seen at

50% input water cut, in the interfacial region, where the computed phase fractions are equal to zero.

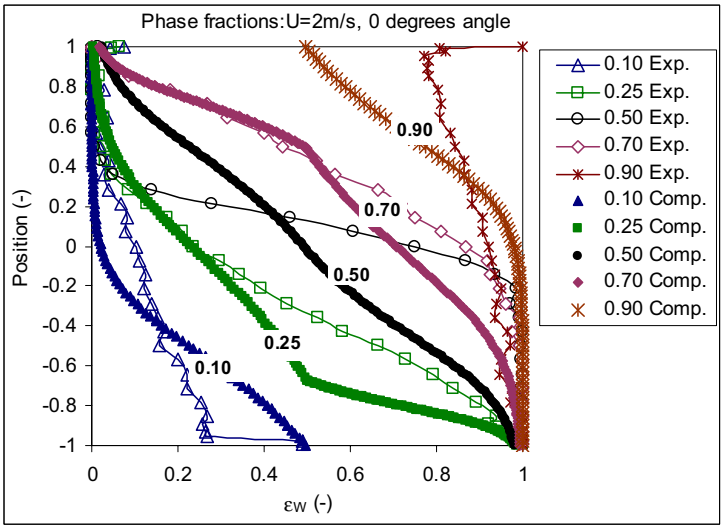

Figure 7.8 Water fraction as a function of the height in the pipe (U = 2 m/s).

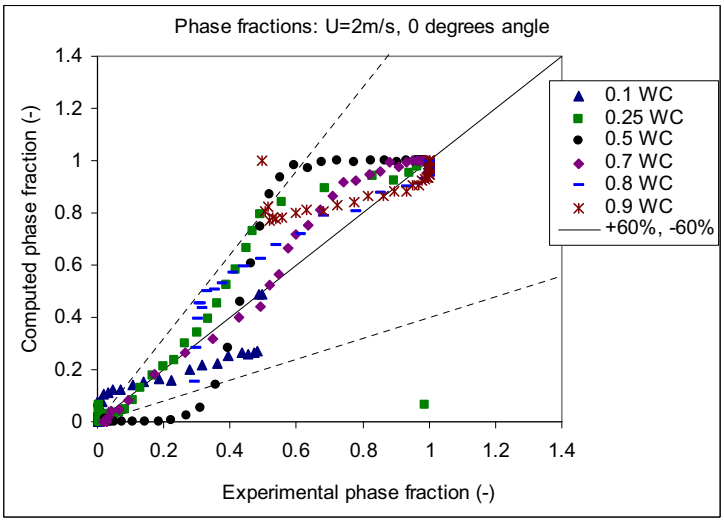

Figure 7.9 Experimental vs. computed water fraction at 2 m/s.

When the mixture velocity increases to 3 m/s, the quality of the predictions becomes even worse (Figure 7.10). Deviations occur now in both the lower and upper part of the pipe. At input water cuts from 30 to 60%, the model under-predicts the phase fractions in the lower part of pipe, and tends to over-predict in the upper part. The opposite trend is seen at input water fraction equal to 80%. Figure 7.11 shows that 76% of the phase fractions are predicted within ±60%, which is slightly worse than the predictions at 2 m/s.

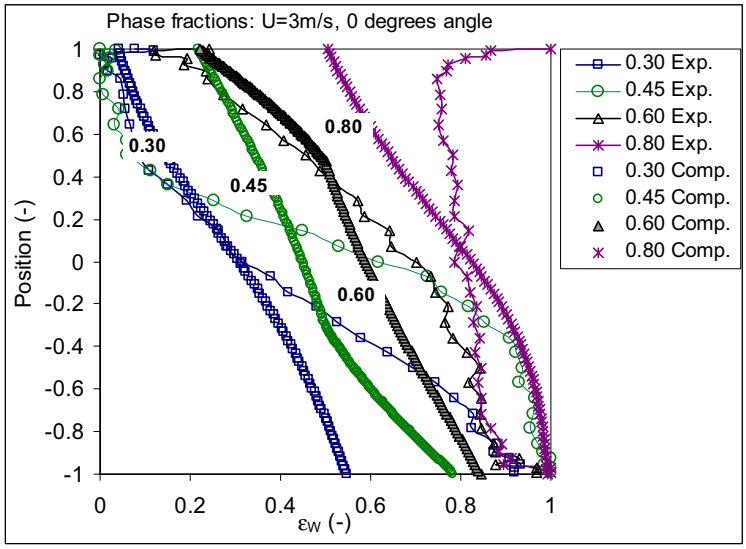

Figure 7.10 Water fraction as a function of the height in the pipe (U = 3 m/s).

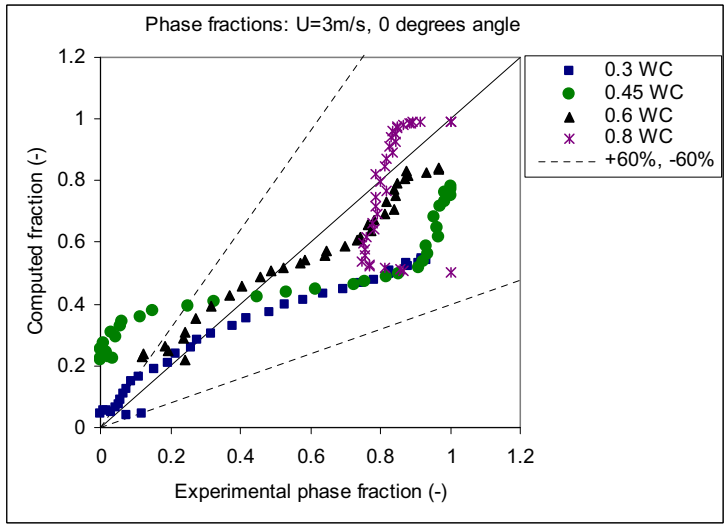

Figure 7.11 Experimental vs. computed water fraction at U = 3 m/s.

At low mixture velocities the predicted cross sectional phase fractions agree well with observed values, except at input water cut equal to 50 and 90%. As the mixture velocity increases, the quality of the predictions becomes gradually worse. One reason to the poor model predictions could be that the model assumption of non-radial concentration distributions is wrong. Soleimani (1999) observed that the concentration profile of the dispersed phase fraction has a definite stratified character for low mixture velocities, which is in line with the central modelling assumption. As the mixture velocity increases, Soleimani (1999) observed that the dispersed phase fraction took on an increasingly radial profile (see Chapter 2). This means that when the turbulent dispersive forces start to dominate the gravitational forces, the layered structure visible for lower velocities is being destroyed and the interface can either be concave or convex. Another possible reason to the deviations could be due to inaccurate closure parameters as sedimentation velocity (v), turbulent diffusion (Γ) and the viscosity (μ_m) in the dispersion model. Additional mechanisms as interfacial waves, surfactants, lift forces and flocculation that are not included in the model could also cause the difference between experimental and predicted phase fraction distributions.

7.3.4 Pressure gradient prediction vs. experiments

A comparison of the measured and computed pressure gradients as a function of the input water cut at 1 m/s in horizontal flow is shown in Figure 7.12. The predictions compares well with the experiments from 0 to 70% input water cuts, while large deviations are seen at higher input water cuts where the flow regime changes from being ST & MI to Dw/o & w. During the flow transition the experiments show a sharp increase in the pressure gradient at input water cut equal to 75%, while the model predicts a slightly decrease up to 90% input water cut and then an increase up to approximately the value of single-phase water. The model also fails to predict the dispersed flow in top of the pipe as shown in sections 7.3.2 and 7.3.3. Figure 7.13 shows that the measured and computed pressure gradients agree reasonable (within +5 and -15%) for input water cuts from 10 to 75%. However, for the higher input water cuts the computed values are under-predicted by 37% of the measured values.

The sudden peak in pressure gradient could be due to two physical phenomenon; droplet-droplet interactions and phase inversion. The large increase of dispersed droplets at higher input water cuts in the experiments could lead to an increase in the effective viscosity due to droplet-droplet interactions. The fluid in the upper-part of the pipe will then move significantly slower than the water-continuous fluid in the lower part of the pipe, which leads to a strong asymmetry in the velocity profile with associated increase in the pressure gradient. This is confirmed in Figure 7.14 where Elseth (2001) presents measured velocity profiles together with phase fraction measurements. Another physical explanation of the peak in pressure gradient is occurrence of a local phase inversion. If a local phase inversion takes place, the oil continuous phase in the stratified flow with mixing at the interface regime will then be replaced by a water continuous phase with dispersed oil droplets, and flow would go from being stratified to dispersed flow. This is not likely to happen, since the measured water fraction is measured both below and above the point of inversion. The flow is still stratified (Dw/o & w) and hence a local phase inversion should not occur. Another feasible explanation that was proposed by Hadziabdic and Oliemans (2007) is that the closure relations are greatly affected by the nature of the interface as waviness and position and the rate of entrainment.

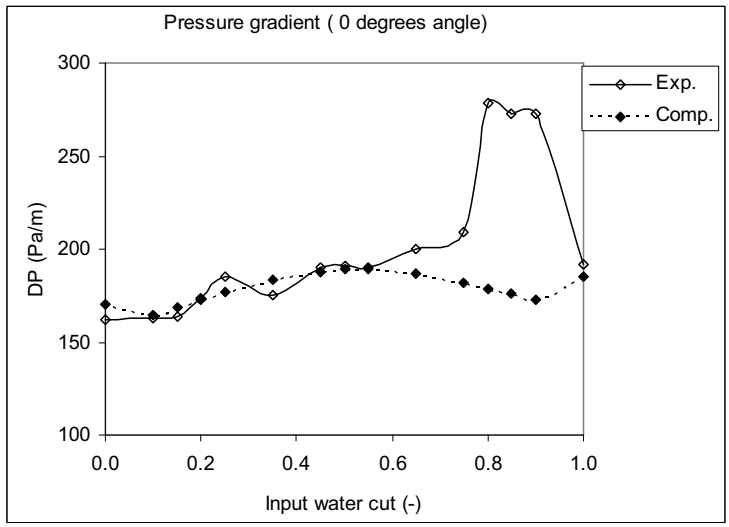

Figure 7.12 Pressure gradient as function of input water cut (U = 1 m/s).

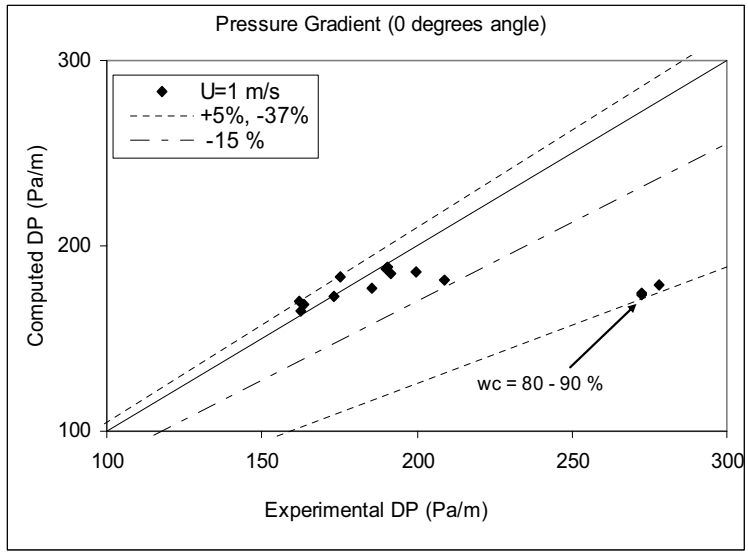

Figure 7.13 Experimental vs. computed pressure gradient at U = 1 m/s.

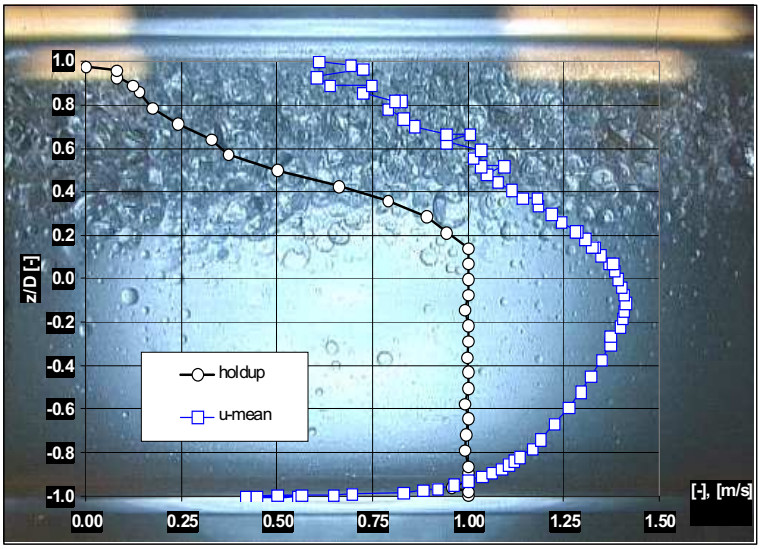

Figure 7.14 Oil-water flow pattern with super-imposed measured local phase fractions and velocities as function of the height at 85% input water cut and 1.02 m/s [Elseth (2001)].

Increasing the velocity from 1 to 3 m/s the pressure gradient predictions are getting worse as shown in Figure 7.15 to Figure 7.17. Poorer predictions with increasing velocity agree well with the results presented by Arirachakaran et al. (1989) and Atmaca et al. (2008). The model predictions deviate to a larger extent at 2 m/s compared to the predictions at 1 m/s. At medium input water cuts (15 to 70%) the deviations increases from ±15% at 1 m/s to +45% at 2 m/s. Even larger deviations between the model predictions and experiments are seen at 3 m/s. Here, the deviations from the experimental results are up to 60% at medium input water cuts (35 to 50%). The pressure gradient measured at 2 and 3 m/s are from Elseth (2001).

The cause of these deviations could be due to the difference in phase fraction distributions between the model and experimental data. The largest deviations in pressure gradient predictions compare well with the largest deviations in phase fraction predictions. Atmaca et al. (2008) observed similar trends at larger velocities, when comparing the model of Zhang and Sarica (2005) with both horizontal and inclined pipe flow data. They observed that the model over-predicted the pressure gradient and that the predictions were worsened with increasing mixture velocity.

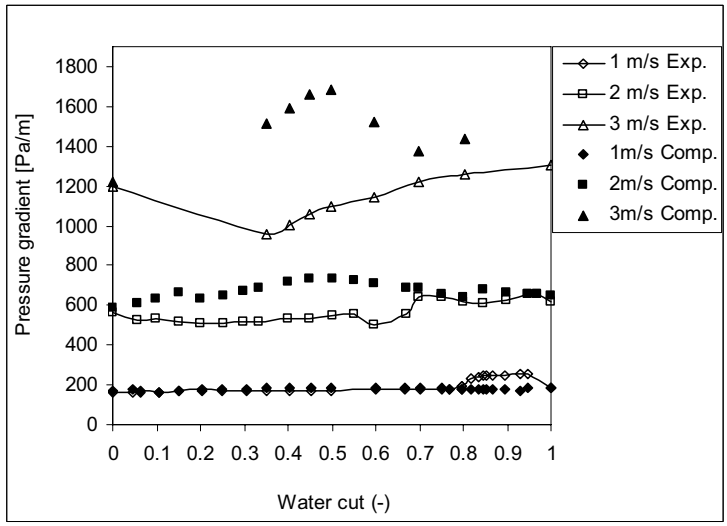

Figure 7.15 Pressure gradient as function of input water (U = 1-3 m/s). The pressure gradient at 2 and 3 m/s are measured by Elseth (2001).

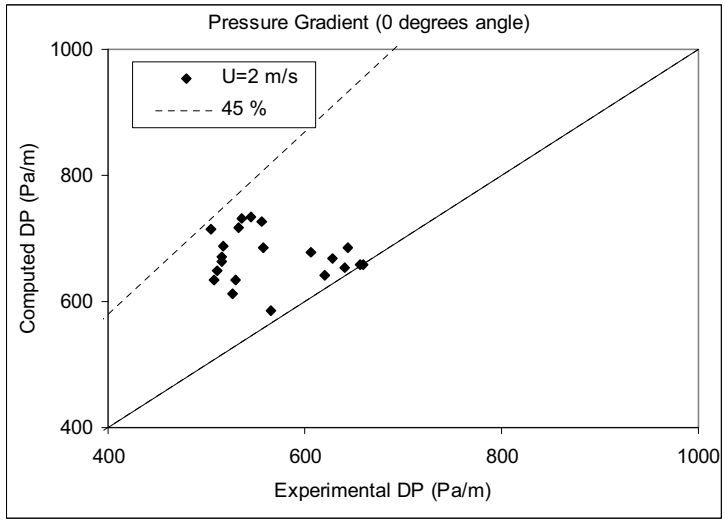

Figure 7.16 Experimental vs. computed pressure gradient at U = 2 m/s.

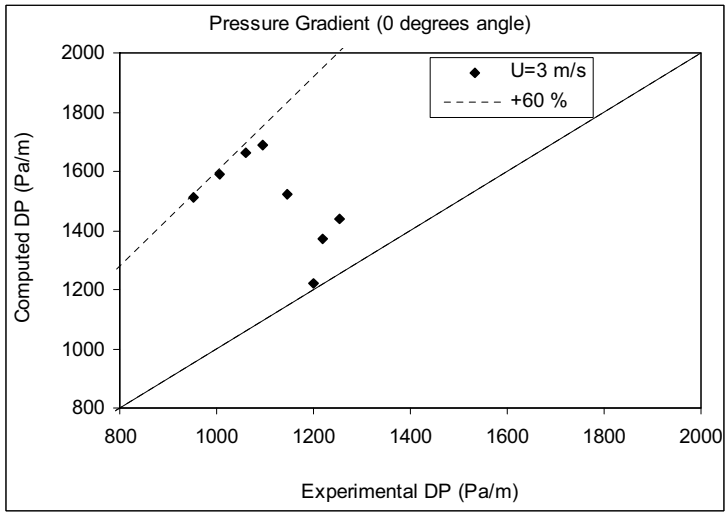

Figure 7.17 Experimental vs. computed pressure gradient at U = 3 m/s.

7.3.5 Slip ratio

In Figure 7.18 and Figure 7.19 the experimental oil-water slip ratio as presented in Chapter 4, section 4.11 is compared with the model predictions. The largest difference between predicted and measured slip ratio is observed at 1 m/s at high input water cuts, where also large deviations in the phase fraction and pressure gradient predictions exist. At higher input water cuts the model predicts a slip ratio closer to one, while the experimental results show that the water flows much faster than the oil phase leading to a higher pressure gradient compared to the model predictions. Here, the upper oil continuous layer was fully dispersed which caused an increase in the effective viscosity. The slip ratio predictions at 2 and 3 m/s are in general better compared to the predictions at 1 m/s. The model tends to under-predict the slip ratios from 1 to 3 m/s. Lovick and Angeli (2004b) also showed that the two-fluid model under-predicted the velocity ratio and concluded that the most likely reason was due to the interface curvature which were found experimentally in three-layer flows.

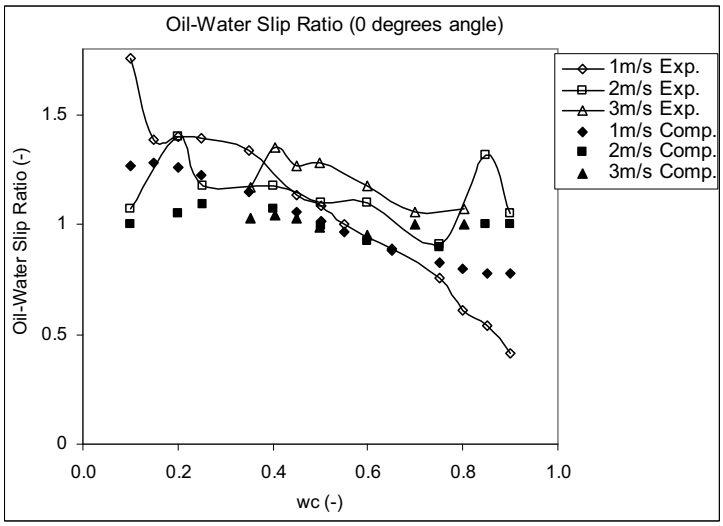

Figure 7.18 Experimental and computed oil-water slip ratio as function of input water cut and velocity (U = 1 – 3 m/s).

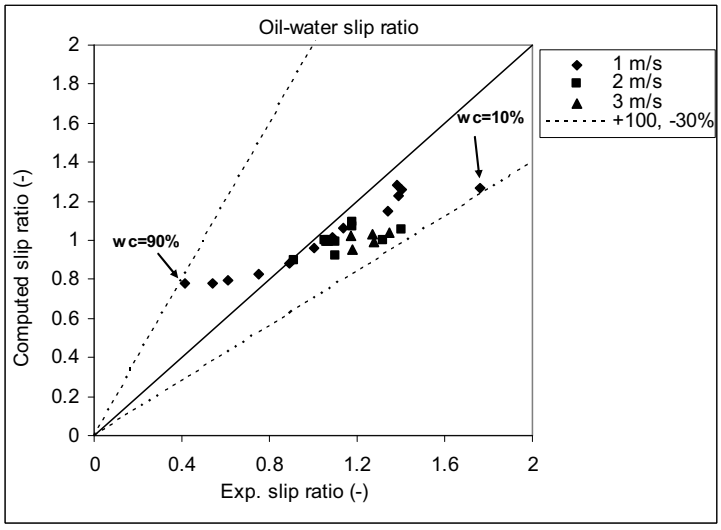

Figure 7.19 Experimental vs. computed slip ratio at velocity equal to 1, 2 and 3 m/s.

7.4 Parametric study

Since the exact location of the interface cannot be determined from the phase fraction measurements, the dispersed phase fraction at the interface between the oil and water continuous fluids is unknown. The dispersed phase fraction (inversion point) at the interface is set equal to $\varepsilon_{inv} = 0.5$ in all the simulations presented above. While the model predictions are, of course, dependent on the value of the interfacial dispersed phase fraction ε_{inv}, it is found that the dependence on ε_{inv} is rather weak. This is shown in Figure 7.20, Figure 7.21 and Figure 7.22 where only small differences are observed in the pressure gradient and phase fraction predictions. The computed pressure gradients with interfacial fraction equal to 30 and 50% show small deviations (Figure 7.20). The largest deviations are seen at the largest velocities. Figure 7.21 and Figure 7.22 show the influence of varying the inversion water cut ε_{inv} from 20 to 50% on the computed phase fractions. The input water cut is equal to 30 and 40% and the mixture velocity is equal to 3 m/s. The differences in phase fraction predictions with increasing ε_{inv} is larger at 30% input water cut than at 40%, but cannot explain the large deviations between the model and measurements.

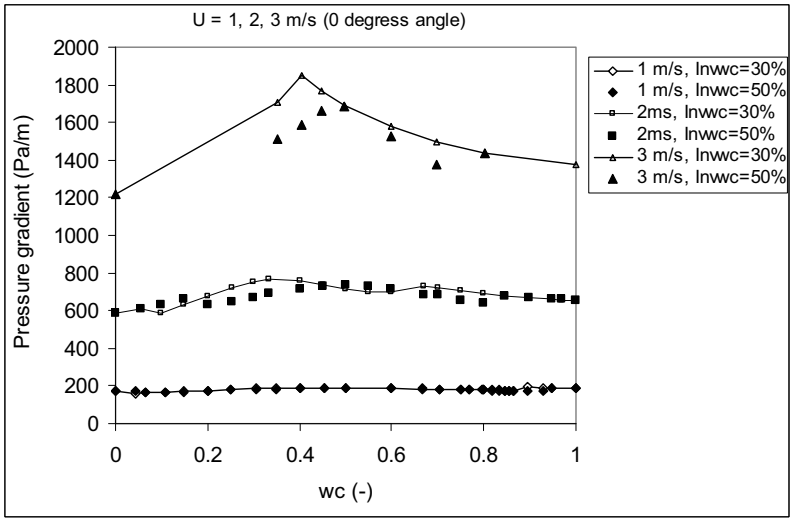

Figure 7.20 Pressure gradient as function of input water cut (U = 1-3 m/s) using interfacial phase fraction (ε_{inv}) equal to 30 and 50%.

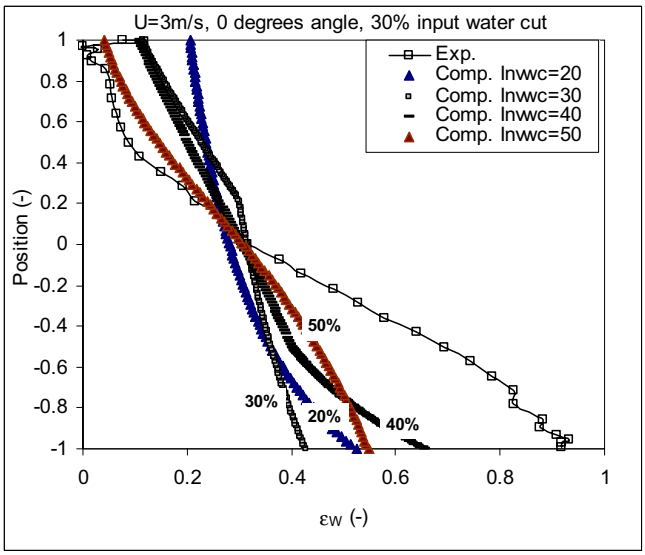

Figure 7.21 Water fraction as a function of the height in the pipe (U = 3 m/s) at 30% input water cut, interfacial phase fraction (ε_{inv}) equal to 20, 30, 40 and 50%.

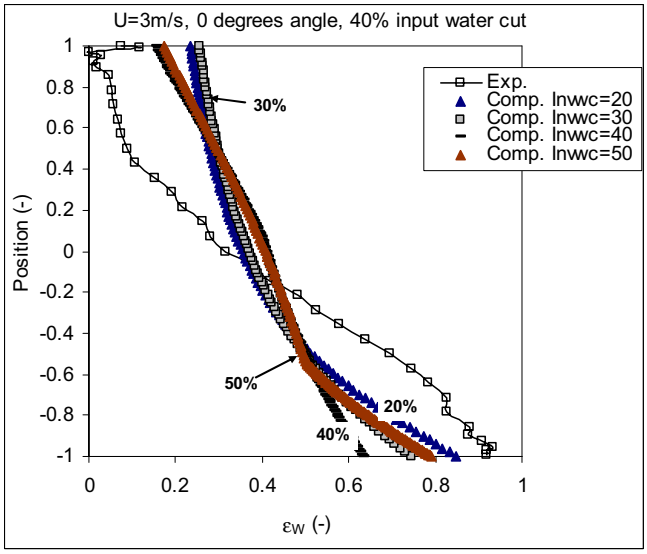

Figure 7.22 Water fraction as a function of the height in the pipe (U = 3 m/s) at 40% input water cut, interfacial phase fraction (ε_{inv}) equal to 20, 30, 40 and 50%.

The influence on model predictions of the interfacial surface tension has also been investigated since this parameter was regarded as one of the most uncertain physical parameters in the model. Changing the interfacial tension influences the modelling results: lowering oil-water surface tension (σ) leads to smaller drops and hence a more uniform distribution of the dispersed phase. However, the model predictions are only weakly dependent on the interfacial surface tension.

7.5 Summary

- The model is able to predict the flow regimes at 3 m/s, but fails to predict the transition from ST & MI to Dw/o & w at 1 m/s and the ST & MI flow regime at medium input water cuts at 2 m/s (see Figure 7.4 and Figure 7.5).
- The model can reproduce important trends as increasing mixing with increasing mixture velocity.
- The two-fluid model performs best at a low mixture velocity equal to 1 m/s. Reasonable predictions of the pressure gradient, phase fractions and slip ratio are observed, except at input water cut larger than 75% and phase fraction predictions at 50% input water cut (see Figure 7.6 and Figure 7.12 and Figure 7.18).
- As the mixture velocity increases from 1 to 3 m/s the phase fractions and pressure gradient predictions become gradually worse (see Figure 7.8, Figure 7.10 and Figure 7.15).
- The slip ratios comparisons do not seem to follow the trend with increasing deviations with increasing mixture velocity as observed for the phase fractions and pressure gradients comparisons. The largest deviations are seen at the lowest velocity (1 m/s) and high input water cuts (75 – 90%).
- The observed under-prediction of the pressure gradient at 1 m/s at 75% input water cut and higher in Figure 7.12 is most likely due to the failure in prediction of the phase fraction distributions, due to the increased effective viscosity or due to the poor prediction of the single-phase and interfacial shear stresses.
- As shown in Figure 7.20 to Figure 7.22 the sensitivity of the inversion water cut is too low to explain the observed deviations between model predictions and measurements. Since the model is weakly dependent on both the inversion water cut and the

interfacial surface tension the deviations between the predictions and experiments are not due to fault in these input parameters.

- Possible explanation for the deviations in pressure gradient, phase fraction and slip ratio predictions could be:
    - That the model assumption of a layered structure gradually breaks down as the velocity increases. This is supported by the conclusion made by Lovick and Angeli (2004b) and Atmaca et al. (2008).
    - Inadequate closure relations for the viscosity, single-phase and interfacial shear stresses in the two-fluid model
    - Inadequate closure relations for the sedimentation velocity and turbulent diffusion coefficient in the dispersion model.
    - Additional mechanisms as
        - Flocculation which can lead to increase in the effective viscosity [Valle 2000)]
        - Interfacial waves [Al-Wahaibi and Angeli (2007)]
        - Surfactants

8 CONCLUSIONS AND FURTHER WORK

In this chapter the main conclusions and recommendations for further work on the experimental and modeling part are presented.

8.1 Conclusions

Production of accurate and high-quality experimental data is essential to understand the behaviour of multiphase flow. The experimental data in present study provides the basis for further model development and validation of existing models. The models that are within reasonable accuracy and better than the existing models are implemented in commercial simulation tools used in field development and operation. Models that are able to predict the multiphase flow behaviour decrease the uncertainties in the design and construction of new fields and can lower the operational costs greatly.

In this study a flow facility is built to generate high-quality experimental data used to validate a two-phase flow model. Addition of water to single-phase oil flow at a mixture velocity of 1 m/s has pronounced effect on the measured pressure gradient, phase fraction, velocity and turbulence profiles. The influence of water is most pronounced at high water cut for the frictional pressure gradient where a sudden increase is observed. The effect of small inclinations, -1° and +1° angle, has minor effect on the measured phase fractions, velocity and turbulence profiles, but large differences from horizontal pipe flow are observed at higher inclinations equal to ±10° and ±5° angles. The inclination angle has however minor effect on the measured frictional pressure gradient.

The model presented is an improvement of the existing commercialised multiphase models due to the ability to predict the phase distribution profile and the increased degree of mixing with increasing velocity. To achieve good prediction, the fluid characterization must be done properly since the fluid properties are input to the flow models. The measured fluid properties are viscosity, density and oil-water surface tension. The phase inversion water cut has not been measured, but is assumed to be equal to 50% water cut based on values reported in the literature. The model comparison shows that accurate predictions of the degree of mixing in two-phase flow are strongly dependent on reliable closure relations of the viscosity of the mixed phase, shear stresses, turbulent diffusion sedimentation velocity. The presence of the interface and its characteristics along with the dispersed droplet concentration must be

accounted for when calculating the closure relations. More experimental studies are needed to develop reliable closure relations for multiphase flow behaviour.

8.1.1 Flow facility

The basic instrumentation in the new two-phase inclinable test loop proves to work satisfactorily in the parameter range studied. Initial experiments and analysis of the pump, flow meters and pressure transducers show that the measurements are accurate, at steady state condition and in the fully developed region.

8.1.2 Gamma densitometry

A new classification approach to determine the flow regime is established. The method uses the measured phase fractions together with a pre-defined phase inversion water cut to distinguish between stratified (two continuous phases) and dispersed flow (one continuous phase). The flow classifies as stratified flow when the measured phase fraction values are below and above the point of inversion. Additional criteria are used to distinguish between the different appearances in the stratified flow regimes. The identified flow regimes in present study are three different stratified flows with different degrees of dispersion and a plug flow regime as shown below. The most occurring flow regime in horizontal and inclined pipes is the ST & MI flow.

- Stratified flow with mixing at the interface (ST & MI).
- Dispersion of water in oil and water (Dw/o & w)
- Dispersion of oil in water and oil (Do/w & o)
- Plug flow (PG)

The effect of inclination on phase distribution and slip ratio is most pronounced at larger inclinations equal to ±10° and ±5° angle, especially at medium input water cuts. The slip ratio is calculated from the phase fraction measurements and generally it has a value above one at 10% input water cut and decreases to below one as the input water cut increases. The slip is larger in upward flow compared to downward flow and the differences between the slip ratios increases with increasing inclination angle. The effect is most pronounced at medium input water cuts. In upward flow the gravitational force works in the opposite directions of the flow and retards the heavy phase. The oil phase moves therefore faster than the water phase in upward moving flow and hence the slip is larger.

The error propagation analysis shows that the accuracy is best in the centre of the pipe and decreases towards the wall due to the increase in wall absorption length compared with liquid. The error in single-phase water flow ranges from ±0.77% in the centre of the pipe to ±18% near the wall (see Figure 4.9).

8.1.3 Two-phase pressure gradient

The frictional pressure gradient is derived from the measured and the static pressure gradient. The static pressure gradient is calculated from the measured holdup calculated by area averaging the measured phase fractions.

The trends and absolute value of the frictional pressure gradients at pipe inclinations from -10° to +10° angle does not show any significant differences. All of the studied inclinations show an abrupt increase in the frictional pressure gradient at approximately 80% input water cut. The increase is attributed to the increased effective viscosity of the upper dispersed layer. The frictional pressure gradient in two-phase flow is in general larger than the single-phase values, except in upward flow at low input water cut.

8.1.4 Laser Doppler Anemometry

A Laser Doppler Anemometer measures the axial mean velocity and turbulence profiles in the vertical center-line of the pipe. The experimental results show the differences between single and two-phase flow and the effect of inclining the pipe from -10° to +10° inclination angle at 25 and 50% input water cut.

The flow behavior in single-phase flow is very different from two-phase flow with regards to both velocity and turbulence distributions. The velocity distribution is symmetrical in single-phase flow and non-symmetrical in two-phase flow and the turbulence trends are different in single-phase compared with two-phase flow.

In horizontal flow at 50% input water cut, the maximum velocity is measured to be in the oil phase, which is in accordance with the slip ratio calculated from the measured phase fractions. The slip ratio is measured to be above one meaning that the oil phase is flowing faster than the water phase.

The effect of pipe inclination on the velocity and turbulence profiles is larger at 50% input water cut compared with 25%. Inclining the flow with ±1° angle has minor influence on the velocity and turbulence profiles, while inclining the pipe further with ±5° and ±10° affects the measured profiles significantly.

The velocity and turbulence data in single-phase flow have been validated against the law of the wall model and the reproducibility has been validated by comparing three different experiments conducted with the same experimental conditions. The experimental data compare well with the law of the wall model and the repeated experiments follow generally the same trends. The sample statistics is best in single-phase water compared with single-phase oil, which is due to poorer optical conditions in the oil phase. A comparison of four two-phase experiments conducted at equal conditions shows that the trends are equal implying a good reproducibility. The accuracy of the measurements is poorest close to the wall in the oil phase and in the interfacial region, where the statistical accuracy is low. Here, the number of samples could be as low as 1000, but most of the samples is above 3000.

8.1.5 Model comparison

Predictions of the flow regime, pressure gradient, in-situ phase fraction and slip ratio using a two-fluid model combined with a dispersion model is compared with experimental data.

The model is able to reproduce the experimental flow regimes at high velocity (3 m/s) at the input water cuts studied (35 to 80%). There is reasonable agreement between model predictions and experimental flow regimes also at lower velocities, but with some exceptions. The predictions matches the data well at low and high input water cut for mixture velocity equal to 2 m/s, but fails to predict the ST & MI flow regime at medium input water cuts. Here, the model predicts a Dw/o & Do/w regime. The predictions at low velocity (1 m/s) match the experimental data from 10 to 75% input water cuts, but the model is not able to predict the transition from ST & MI to Dw/o & w that occurs at 80% input water cut.

The two-fluid model performs well at low velocity (1 m/s). Here, the pressure gradient, phase fraction and slip ratio predictions compares well, except at input water cuts larger than 75%. Deviations are in addition seen in the phase fraction predictions at 50% input water cut, where

the model predicts larger degree of dispersion compared with the experiments. The under-predictions of the pressure gradient at input water cuts above 75% are most likely due to unsuccessful predictions of the phase fractions and due to the increase in the effective experimental viscosity in the dense upper dispersed layer. The model does not predict a dense dispersed upper layer which the experiments show, but instead the model predicts a ST & MI flow regime with a clear oil layer in the upper part of the pipe. Although, larger deviations are seen in the phase fraction predictions at 50% input water cut, the slip ratios and pressure gradient predictions shows good comparison with the experimental values.

As the mixture velocity increases, the predictions of the pressure gradient, and phase fractions become gradually worse. However, the model is able to predict the trend of increasing degree of mixing with increasing mixture velocity as was observed in the experiments. The model predictions are poorest when the degree of mixing between the phases is largest, which implies that the features of the dispersed layer are not captured by the model. The model over-predicts the pressure gradient from 10 to 70% input water cut at velocity equal to 2 m/s and gives reasonable agreement at higher input water cuts. The largest deviations are seen at medium input water cuts, which could be explained by the phase fraction predictions showing more dispersed flow behaviour giving rice to larger pressure gradients. A peak in the experimental pressure gradient also occurs at 2 m/s, where the flow regime transforms from ST & MI to Dw/o & w at approximately 75% input water cut. The peak in pressure gradient is not captured by the model, which could be due to the failure in flow regime predictions. The model predicts a transition from Dw/o & Do/w to Dw/o & w at 75% input water cut. Even larger pressure gradient over-predictions are seen at 3 m/s, especially at input water cuts from 35 to 60%. Here, the gradient of the phase fraction curves show that the flow is more dispersed in the model predictions than in the experiments, as was also the case at 2 m/s. This could be the reason for the large over-predictions of the pressure gradient.

One of the main reasons for the observed deviations could be that the relations for the viscosity and single-phase and interfacial shear stress in the two-fluid model are inadequate or that the closure relations for the sedimentation velocity and turbulent diffusion coefficient in the dispersion model are insufficient. The dispersion mechanisms between the phases is modelled as a balance between turbulent and buoyancy forces. The deviation between predictions and experiments implies that additional mechanisms as flocculation, interfacial

waves and surfactants could be present. These mechanisms are not included in the model. Another possible explanation for the observed deviations is that the model assumption of a layered structure gradually breaks down as the velocity increases. Several investigators like e.g. Lovick and Angeli (2004b) and Atmaca et al. (2008) have reported that the interface is not flat, but has a convex or concave curvature. The position of the interface is not is not measured in current study and could give rice to large uncertainties in the predictions.

8.2 FURTHER WORK

8.2.1 Flow facility

The basic instrumentation was proven to work satisfactorily in the parameter range studied, but at low and high input water cuts the accuracy of the flow meters could be improved. Decreasing the uncertainty in the measurements within reasonable limits, make the model comparison more reliable. The uncertainties in the basic instrumentation, the flow meters and the pressure transducers, can be reduced by replacing the flow meters with e.g. Coriolis meters and the pressure transducers with 16 bit resolution membrane transducer on a field bus logging system. Too exclude differences in fluid properties caused by temperature variations a procedure which make sure that the temperature of the water and oil are equal between each experimental run can be implemented. The flow development should be measured along the pipe length for verification of fully developed flow. Additional pressure transducers, gamma densitometer and Laser Doppler Anemometer can be implemented along the pipe length.

8.3 Experimental campaign

Current experimental campaign is conducted using only one mixture velocity (1 m/s). It is expected that increasing or reducing the mixture velocity will effect the flow behaviour, so experiments should be run at different velocities as function of input water cut and inclination angle.

The effect of a wavy interface is not well understood. Thus the frequency and amplitude of the waves should be measured to find the effect they have on the flow parameters like e.g. interfacial shear stress. A parametric study done by Hadziabdic and Oliemans (2007) shows that both interfacial waves and entrainment can influence the shear stresses greatly. The effect of waves on droplet formation and entrainment should also be covered.

The fluid properties in a real production pipe line or well will change along the pipe length due to pressure loss. The influence of different fluid properties should therefore be investigated. The density, viscosity and interfacial surface tension can be changed by either varying the temperature or pressure or a different fluid can be chosen. Different concentrations of surfactants added to the flow can be used to study the effect of interfacial surface tension. A comparison between Exxsol D80 and Exxsol D60 will reveal if the small differences in fluid and chemical properties influences the flow parameters. The fluid properties and chemistry of Exxsol D60 and a real crude oil is very different. A real crude is therefore expected too behave differently from Exxsol D60. To be able to simulate a production system the differences between a synthetic oil system and a crude oil need to be quantified.

Another important issue is the scale-up from a small experimental pipe diameter to a larger production pipeline. The diameter in the well is approximately 2 -3-in., while a production pipe could have diameters up to 16-in. Since it is impossible to have similar conditions (e.g. velocity, Reynolds number and shear stress) in the 2-in. pipe as in a production pipeline it is important to quantify which of the scale-up laws that should be used when performing experiments. The most common way to down-scale is to use equal superficial velocities. This gives rice to a much higher shear stress and lower Reynolds number compared with a production pipeline.

Additional instrumentation should be included to measure the exact position of the interface between oil and water and measurement of the droplet size distribution should be included since this can have a great influence on the closure relations in the dispersion model.

8.3.1 Gamma densitometry

The classification approach uses the phase inversion water cut to determine whether the flow is stratified or dispersed. The phase inversion water cut has not been measured in current set up and may vary with the experimental parameters like e.g. flow velocity and input water cut. The use of the pre-defined phase inversion water cut should therefore be validated. One way to validate the present approach is to measure the fluid of the continuous phase by e.g. impedance probes and compare the measurements with the pre-defined phase inversion water cut. These measurements are directly input to the classification of flow regimes. Another way

to measure the phase inversion water cut is to measure the transition from oil continuous to water continuous by gradually increasing the input water cut in the dispersed flow regime. The point of inversion in present study is used in the classification of flow regime and as input to the oil-water flow model. The measurement techniques should consist of gamma densitometry (phase fractions), pressure gradient and e.g. impedance probes (fluid of the continuous phase).

The gamma instrument traverses vertically from the top to the bottom of the pipe and measures an average phase fraction of the liquid content covered by the beam. The radial distribution is therefore not captured and will not reveal an eventual convex/concave interfacial curve, which can influence the pressure gradient and slip ratio. To find out if the deviations between the model prediction and experiments are due to a curved interface the radial phase fraction distribution should be measured by traversing the gamma densitometer by e.g. 45 and 90° radial directions.

The accuracy can easily be improved by increasing the calibration time from 1 to 10 minutes (see section 4.6.1.) This will improve the pulse-counting statistics and decrease the large uncertainties close to the wall. The accuracy in the vertical gamma profiles can be improved by measuring the exact position of the laser beam inside the pipe with a laser system. This will decreases the uncertainties in the traversing system and hence decrease the error of phase fractions, slip ratios and gravitational pressure gradient.

8.3.2 Two-phase pressure gradient

The uncertainties in the pressure gradient measurements become large when the gravitational force balances the frictional force and the measured pressure gradient becomes close to zero. This occurs in large upward inclination at approximately 35% input water cut. When the pressure gradient becomes below zero the impulse lines are exchanged with each other to be able to measure in the whole pressure gradient range. This can introduce an additional error in the measurements, so it is recommended to implement a more accurate transducer which can be used in the whole parameter range without having to change the set up of the instrument. An additional pressure transducer with a membrane which separates the fluid in the pipe and the fluid in the impulse lines can eliminate eventual disturbances due to mixing of oil and

water in the impulse entrance and disturbances due to air. A membrane based transducer will in addition reduce the experimental time since the impulse lines do not have to be flushed.

8.3.3 Laser Doppler Anemometry

The wall shear stresses in two-phase flow should be calculated from the velocity profiles and compared with the single-phase values. This can reveal eventual influences of the water-phase on the oil shear stresses or vice versa. In two-phase flow calculations, single-phase expressions for the wall shear stresses are used and eventual effects of an additional phase is not accounted for. The velocity profiles should be integrated so that the average velocity of the oil and water phase can be compared with the calculated values.

Current measurements are located in the vertical centre-line of the pipe. Radial velocity distributions will give additional information about the velocity distribution in the pipe cross-sectional area and give the distribution of the wall shear along the pipe circumferences.

Measurements in dispersed flow could be improved by using a refractive index matching method as Kvandal et al. (2000) describes. This can improve the sample statistics in the ST & MI flow regime and make measurements possible in the dispersion of water in oil and water (Dw/o & w) and in the dispersion of oil in water and oil (Do/w & o).

The Laser Doppler Anemometer should be calibrated in present experimental set-up to determine the measurement accuracy in single-phase flow and one should increase the sample statistics near the interfacial region and in the oil phase, especially near the wall. The sample statistics may be improved by e.g. implementing a new laser source.

8.4 Model comparison

The model comparison shows deviation at both low and large velocities. The deviations observed at 1 m/s occur at large input water cuts, where the model is not able to predict the sudden increase in pressure gradient observed in the experiments. The phase fraction predictions at 90% input water cut does not match the experimental values. To find out if the failure in phase fraction predictions is causing the large deviations in pressure gradient predictions, the measured phase fractions can be used as input to the two-fluid model. A comparison of the predicted and experimental pressure gradient will then show the validity of

the closure relations for viscosity and shear stresses. A similar approach was used by Lovick and Angeli (2004b), where the measured phase fractions was used as input to the fluid two-fluid model to predict the measured pressure gradient. The sudden pressure gradient increase at 80% input water cut is addressed to the increase in effective viscosity of the upper dispersed layer. There exists several closure relations for both the viscosity and the interfacial shear stress in the literature and these should be validated to find out how sensitive the model is to the various expressions. A similar parametric study as was done by Hadziabdic and Oliemans (2007) should be done to find the most sensitive parameter and reveal the effect of two-phase flow on the shear stress correlations.

The flow regime is determined by using a phase inversion water cut and the predicted phase fractions. Both values have to be correct to predict the flow regime. The inversion water cut should therefore be measured in present study by use of e.g. conductivity probes for determination of the fluid of the continuous phase in each experimental condition.

The closure relations for the sedimentation velocity (v) in the dispersion model can be validated by measuring the droplet size and distribution and compare the values with the model of Hinze (1955) and Rosin-Rambler distribution. Since the effect of the dispersed-phase on the turbulent particle diffusion coefficient (Γ) is not accounted for in present model, the sensitivity of different turbulent diffusion coefficient, should be checked.

The velocity profile can be calculated from the two-fluid model and compared with the measured velocity distributions. The effect of radial distribution should also be studied.

Additional dispersion mechanisms and droplet-droplet interactions as generation of droplets due to interfacial waves, flocculation and lift forces should be implemented to the model and the predictions should be compared with experimental values.

Computational fluid calculations can also be used to find the main mechanisms in oil-water flow by comparing the measured and predicted velocity distributions, cross-moments or Reynolds stresses.

The model should be validated against experimental data with different fluid properties and tested against full-scale experiments or field data to ensure that the model is capable to predict the flow behaviour in an oil production pipe.

The experimental data should also be tested against commercial available multiphase tools as e.g. OLGA which is used to simulate production of oil and water in real production pipelines. Validation of commercial multiphase tools will decrease the uncertainties related to field development and production and ensure a more safe and reliable production.

BIBLIOGRAPHY

Abduvayt, P.; Manabe, R.; Watanabe, T. and Arihara, N. (2006) Analysis of Oil/Water-Flow Tests in Horizontal, Hilly Terrain, and Vertical Pipes, SPE Production and Operations, 21, 123–133.

Alboudwarej, H.; Felix, J.; Taylor, S.; Badry, R.; Bremner, C.; Brough, B.; Skeates, C.; Baker, A.; Palmer, D.; Pattison, K.; Beshry, M.; Krawchuk, P.; Brown, G.; Calvo, R.; Triana, J. A. C.; Hathcock, R.; Koerner, K.; Hughes, T.; Kundu, D.; de Cardenas, J. L. & West, C. (2006) Highlighting Heavy Oil, Oilfield Review, 34-53.

Aleklett, K.; Höök, M.; Jakobsson, K.; Lardelli M.; Snowden S. and Söderbergh, B.; (2010) The Peak of the Oil Age - analyzing the world oil production Reference Scenario in World Energy Outlook 2008, Energy Policy, Vol. 38, Issue 3, 1398 -1414.

Alkaya, B. (2000) Oil-Water Flow Patterns and Pressure Gradients in Slightly Inclined Pipes, The University of Tulsa, Master thesis.

Alkaya, B.; Jayawardena, S. S. and Brill, J. P. (2000) Oil-Water Flow Patterns In Slightly Inclined Pipes, Proceedings of ETCE/OMAE2000 Joint Conference, Energy for the New Millenium, New Orleans, LA.

Al-Wahaibi, T.; Smith, M. and Angeli, P. (2007) Transition between stratified and non-stratified horizontal oil–water flows. Part II: Mechanism of drop formation Chemical Engineering Science, 62, 2929-2940.

Al-Wahaibi, T. and Angeli, P. (2007) A Transition between stratified and non-stratified horizontal oil–water flows. Part I: Stability analysis, Chemical Engineering Science, 62, 2915-2928.

Al-Wahaibi, T. and Angeli, P. (2008) Droplet size and velocity in dual continuous horizontal oil–water flows, Chemical engineering research and design, 86, 83-93.

Amundsen, L. Schulkes, R. and Melaaen M. (2009) Oil-water flow:experiments and model development, 14th International Conference on Multiphase Production Technology, Cannes, France, 183-195.

Angeli, P. (1994) Pressure Drop And Flow Patterns In Horizontal Liquid-Liquid Flow In Pipes, Department of Chemical Engineering & Chemical Technology Imperial College of Science, Technology and Medicine Prince Consort Road London.

Angeli, P. (1996) Liquid-liquid dispersed flows in horizontal pipes, Imperial College of Science, PhD thesis, Technology and Medicine, London, UK.

Angeli, P. and Hewitt, G. F. (1998) Pressure gradient in horizontal liquid-liquid flows, International Journal of Multiphase Flow, 24, 1183 – 1203.

Angeli, P. and Hewitt, G. F. (2000) Drop size distributions in horizontal oil-water dispersed flows. Chemical Engineering Science, 55, 3133-3143.

Arirachakaran, S.; Oglesby, K. D.; Malinowsky, M. S.; Shoham, O. and Brill, J. P. (1989) An Analysis of Oil-Water Flow Phenomena in Horizontal Pipes. SPE Production Operations Symposium, Oklahoma City, Oklahoma, March 13-14.

Aslina, H. S. (2006) Local volume fraction on liquid-liquid dispersion, The Eleventh Asian Congress of Fluid Mechanics, Kuala Lumpur, Malaysia, 434-443.

Aspen HYSYS, http://www.aspentech.com/core/

Atmaca, S.; Sarica, C.; Zhang, H. and Al-Sarkhi, A. S. (2008) Characterization of Oil Water Flows in Inclined Pipes, SPE Annual Technical Conference and Exhibition held in Denver, Colorado, USA, 21-24 September.

Bannwart, A. C.; Rodriguez, O. M. H.; Trevisan, F. G.; Vieira, F. F. and Carvalho, C. H. M. (2009) Experimental investigation on liquid–liquid–gas flow: Flow patterns and pressure-gradient, Journal of Petroleum Science and Engineering.

Barnea, D. (1987) A unified model for predicting flow-pattern transitions for the whole range of pipe inclinations, International Journal of Multiphase Flow, 13, 1-12.

Barnea, D. and Taitel, Y. (1993) Kelvin-Helmholtz Stability Criteria For Stratified Flow: Viscous Versus Non-Viscous (Inviscid) Approaches, Int. J. Multiphase Flow, 19, 639-649.

Batchelor, G. B. (1967) An introduction to fluid dynamics, Cambridge University Press.

Batchelor, G. K. (1972) Sedimentation in a dilute suspension of spheres. J. Fluid Mech. 52, 245-268.

Batchelor, G. K. and Wen, C. S. (1982) Sedimentation in a dilute polydispersed system of interacting spheres, Part 2. Numerical results J. Fluid Mech. 124, 495-528.

Beretta, A.; Ferrari, P.; Galbiati, L. and Andreini, P. A. (1997) Horizontal oil-water flow in small diameter tubes Flow patterns, Int. Comm. Heat Mass Transfer, 24, 223-229.

Berger, M. J.; Hubbell, J. H.; Seltzer, S. M.; Chang, J.; Coursey, J. S.; Sukumar R. and Zucker D. S. (2007) XCOM: Photon Cross Sections Database, National Institute of Standards and Technology (NIST).

Bouguer, P. (1929) Essai d'optique sur la gradation de la lumière.

Brinkman, H. C. (1952) The viscosity of concentrated suspensions and solutions, J. Chem. Hydrodynamics, 20, 571.

Brauner, N. and Maron, D. M. (1989) Two-Phase Liquid-Liquid Stratified Flow PhysicoChemical Hydrodynamics, 11, 487-506.

Brauner, N. and Maron, D. M. (1992) Stability Analysis of Stratified Liquid-Liquid Flow, International Journal of Multiphase Flow, 18, 103-121.

Brauner, N. and Maron, D. M. (1993) The Role of Interfacial Shear Modelling in Predicting the Stability of Stratified Two-Phase Flow, Chemical Engineering Science, 48, 2867-2879.

Brauner, N.; Maron, D. M. and Rovinsky, J. (1998) A two-fluid model for stratified flows with curved interfaces, International Journal of Multiphase Flow, 24, 975-1004.

Brauner, N. and Ullmann, A. (2002) Modeling Of Phase Inversion Phenomenon In Two-Phase Pipe Flows, International Journal of Multiphase Flow, 28, 1177-1204.

Brinkman, H. C. (1952) The viscosity of concentrated suspensions and solutions, J. Chem. Hydrodynamics, 20, 571.

Budwig R. (1994) Refractive index matching methods for liquid flow investigations, Experiments in Fluids Journal 17, 350-355.

Charles, M. E. and Lilleleht, L. U. (1966) Correlation of Pressure Gradients for the Stratified Laminar-Turbulent Pipeline Flow of Two Immiscible Liquids, The Canadian Journal of Chemical Engineering, 44, 47-49.

Charles, M. E.; Govier, G. W. and Hodgson, C. W. (1961) The Horizontal Pipeline Flow of Equal Density Oil-Water Mixtures, The Canadian Journal of Chemical Engineering, 39, 27-36.

Chester, A. K. (1991) The Modelling Of Coalescence Processes In Fluid-Liquid Dispersions: A Review Of Current Understanding, Trans IChemE, 69, 259-270.

Churchill, S. W.(1977) Friction-Factor Equation Spans All Fluid-Flow Regimes Chemical Engineering, 91, 91-92.

Clay, P. H. (1940) The mechanism of Emulsion Formation in Turbulent Flow, Proceedings, Akademie van Wetenschappen, Amsterdan, 43, 852.

Coleman, J. W. and Garimella, S. (1999) Characterisation of two phase flow patterns in small diameter round and rectangular tubes. Int. J. Heat and Mass Transfer, 42, 2869-2881.

Cox, A. L. (1985) A study Of Horizontal And Down Hill Two-Phase Oil-Water Flow, The Faculty Of The Graduate School Of The University Of Texas, Master thesis.

Dantec reference guide (2000).

Di Felice, R. (1999) The sedimentation velocity of dilute suspensions of nearly monosized spheres, Int. J. Multiphase Flow 25, 559-574.

Doherty, J.; Ngan, P.; Monty, J. and Chong, M. (2007) The development of turbulent pipe flow, 16th Australian Fluid Mechanics Conference.

Durrani, T. S. and Greated C. A. (1977) Laser systems in flow measurements, Plenum Press New York.

Durst, F.; Jovanovic, J. and Sender, J. (1995) LDA measurements in the near-wall region of a turbulent pipe flow, J. Fluid Mech. 295, 305-335.

East, R. C.; Astle, M. J. and Beyer, W. H. (1984-1985) CRC Handbook of Chemistry and Physics, 65th edition, Library of Congress card No. 13-11056.

Ekman, V. W. (1910) On the change to from steady to turbulent motion of liquids, Ark. F. Mat. Astron. Och. Fys., Vol. 6, Nr. 12.

Elseth, G., (2001) An Experimental Study of Oil/Water Flow in Horizontal Pipes, Dr.ing, Norwegian University of Science and Technology (NTNU), Telemark University College.

Elseth, G.; Hanssen, R.; Kvandal, H. and Duchet-Suchaux, P. (2005) Investigation of three-phase gas-crude oil-water flow in inclined pipes, Multiphase Production Technology, 12, 37-51.

Elseth, G.; Kvandal, H. K. and Melaaen, M. C. (2000) Measurement of Velocity and Phase Fraction in Stratified Oil/Water Flow, MFTP, Antalya, Turkey.

Fairuzov, Y. V.; Arenas-Medina, P.; Verdejo-Fierro, J. and Gonzalez-Islas, R. (2000) Flow Pattern Transitions in Horizontal Pipelines Carrying Oil-Water Mixtures: Full-Scale Experiments, Journal of Energy Resources Technology, 122, 169-176.

Fisher, M. and Jovanvić J. (1998) Feasibility Study on the Applicability of an LDA System to Two-Phase Liquid-Liquid Pipe flows, Internal Report from Industrial Project for Norsk Hydro Research Centre, Porsgrunn, Norway.

Flores J. G., Chen X. T., Sarica C., Bril J. P. (1997) Characterization of Oil-Water Flow Patterns in Vertical and Deviated Wells, SPE 38810, Annual Technical Conference and Exhibition, San Antonio, Texas.

Flores, J. G.; Sarica, C.; Chen, T. X. and Brill, J. P. (1998) Investigation of Holdup and Pressure Drop Behavior for Oil-Water Flow in Vertical and Deviated Wells, Transactions of the ASME, Journal of Energy Resources Technology, 120, 8 – 14.

Frøystein, T.; Kvandal, K. H. and Aakre, H. (2005) Dual Energy Gamma Tomography System For High Pressure Multiphase Flow, Flow Measurement and Instrumentation, 16, 99-112.

Gao, H.; Gu, H. and Guo, L. (2003) Numerical study of stratified oil-water two-phase turbulent flow in a horizontal tube, International Journal of Heat and Mass Transfer, 46, 749–754.

Guzhov, A. I.; Grishin, A.P; Medredev, V. F. and Medredeva O. P. (1973) Emulsion Formation During the Flow of Two Immiscible Liquid in a Pipe, Neft, 8, 58-61.

Hadziabdic, M. and Oliemans, R. V. A. (2007) Parametric study of a model for determining the liquid flow-rates from the pressure drop and water hold-up in oil-water flows, International Journal of Multiphase Flow 33, 1365-1394.

Hapanowicz, J. (2008) Slip between the phases in two-phase water–oil flow in a horizontal pipe, International Journal of Multiphase Flow, 34, 559–566.

Hapanowicz, J.; Troniewski, L. and Witczak, S. (1997) Flow Patterns of Water-Oil Mixture Flowing in Horizontal Pipes, International Symposium on Liquid-Liquid Two-Phase Flow and Transport Phenomena, Antalya, Turkey.

Hasson, D. and Mann, U. (1970) Annular Flow Of Two Immiscible Liquids I. Mechanisms, The Canadian Journal of Chemical Engineering Science, 48, 514-520.

Hinze J. O. (1955) Fundamentals of the Hydrodynamic Mechanism of Splitting in Dispersion Processes., AICHE Journal Vol 1, 3, 289-295.

Hinze J. O. (1959) Turbulence, McGraw-Hill, New York.

Howarth, W. J. (1964) Coalescence Of Drops In A Turbulent Flow Field, Chemical Engineering Science, 19, 33-38.

Hussain, S. A.; Xu, X. Y. and Hewitt, G. F. (2008) Water Local Volume Fraction on Oil in Water Dispersion, Journal of Applied Fluid Mechanics, 1, 57-63.

Haaland, S.E. (1983) Simple and Explicit Formulas for the Friction Factor in Turbulent Pipe Flow, Journal of Fluids Engineering, Vol. 105, March.

Incropera, F. P. and DeWitt, D. P. (2002) Fundamentals of Heat and Mass Transfer, Fifth edition, p. 467.

Ioannou, K.; Nydal, O. J. and Angeli, P. (2005) Phase inversion in dispersed liquid-liquid flows. Experimental Thermal and Fluid Science, 29, 331-339.

Jayanti, S. and Hewitt, G. (1991) Review of literature on dispersed two-phase flow with a view to CFD modelling, AEA-APS-0099, AEA Petroleum Services, Harwell Laboratory, Oxon, UK.

Jayawardena, S. S.; Alkaya, B.; Redus, C. L. and Brill, J. P. (2000) A New Model For Dispersed Multi-Layer Oil-Water Flow, 2nd North American Conference Multiphase Technology, Department of Petroleum Engineering, The University of Tulsa, USA.

Johansen, G. A. and Jackson, P. (2004) Radioisotope Gauges for Industrial Process Measurements.

Johnson, G. W. (2005) A study of Stratified Gas-Liquid Pipe Flow, PhD thesis, Faculty of Mathematics and Natural Sciences, University of Oslo.

Karabelas, A. J. (1978) Droplet Size Spectra Generated Turbulent Pipe Flow of Dilute Liquid/Liquid Dispersions. AIChE Journal, 24, 170-180.

Kays, W. and Crawford, M. (1993) Convective Heat and mass Transfer, Third Edition.

Kays, W.; Crawford, M. and Weigand, B. (2005) Convective Heat and mass Transfer, Fourth Edition.

Khor, S. H. (1998) Three-Phase Liquid-Liquid-Gas Stratified Flow In Pipelines, Imperial College of Science, Technology and Medicine, London, UK.

Klein A. (1981) Review: Turbulent developing pipe flow, Journal of Fluid Engineering, Vol. 103, 243.

Kocianova, E.; Moore, I. P. T. and Carpenter, K. J. (1995) The Effect Of Inlet Design On The Horizontal Pipeline Flow Of Two Immiscible Liquids, The 1995 Icheme Research Event / First European Conference.

Kokal, S. (2005) Crude-oil emulsions: A state-of-the-art review, SPE 77497-PA, Production and Facilities.

Kolmogorov A. N. (1949) On the breaking of drops in turbulent flow, Doklaby Akad. Nauk. USSR, 66, 825-828.

Kouba, G. E. (2003) Mechanistic models for droplet formation and breakup, Proceedings of the ASME/JSME Joint Fluids Engineering Conference 2 B, pp. 1607-1615.

Kubie, J. and Gardner, G. C. (1977) Drop Sizes And Drop Dispersion In Straight Horizontal Tubes And In Helical Coils. Chemical Engineering Science, 32, 195-202.

Kumara, W.; Elseth, G.; Halvorsen, B. and Melaaen, M. (2008) Computational study of stratified two phase oil/water flow in horizontal pipes, 6th International Conference on Heat Transfer, Fluid Mechanics and Thermodynamics, Pretoria, South Africa.

Kumara, W.; Elseth, G.; Halvorsen, B. and Melaaen, M., (2009a) Velocity and turbulence measurements of oil-water flow in horizontal and slightly inclined pipes using PIV, Computational Methods in Multiphase Flow V, WIT transactions on Engineering Sciences, Vol. 63.

Kumara, W.; Halvorsen, B. and Melaaen, M., (2009b) Particle image velocimetry, gamma densitometry, and pressure measurements of oil-water flow, Multiphase Science and Technology, Vol.21, No. 1-2, pp.51-64.

Kurban, A. P. A.; Angeli, P. A.; Mendes-Tatsis, M. A. and Hewitt, G. F. (1995b) Stratified and dispersed oil-water flows in horizontal pipes, The. 7th International Conference on Multiphase production, Cannes, France on 7-9 June 1995, 277–291.

Kurban, A. P. A.; Mendes-Tatsis, M. A. and Hewitt, G. F. (1995a) Oil-Water Flows in Horizontal Tubes, Cheme Research Event, The 1995 ICheme Research Event / First European Conference, Vol 2, 757 –759.

Kvandal, H. K.; Elseth, G. and Melaaen, M. C. (2000) Measurement of Velocity and Phase Fraction in Dispersed Two-Phase Flow, MFTP 2000, Antalya, Turkey.

Kvandal, H.; Valle, A.; Robøle, B. and Arvesen, T. (1998) Comparison between Three-Phase Field Tests and Multiphase Simulation Code, Annual Technical Conference and Exhibition New Orleans, Louisiana.

Laflin, G. C. and Oglesby, K. D. (1976) An Experimental Study On The Effects Of Flow Rate, Water Fraction And Gas-Liquid Ratio On Air-Oil-Water Flow In Horizontal Pipes, The University Of Tulsa.

Langhaar, H. L. (1942) Trans. ASME 64, A55.

Latzko, H. and Angew, Z. (1921) Der Warmeubergang an einen turbulenten. Flussigkeits oder Gasstrom. Math. Mach., Vol. 1, pp. 268-290.

Levich V.G. (1962) Physiochemical Hydrodynamics, Prentice-Hall, Inc. H. J.

Liu, W.; Guo, L.; Wu, T. and Zhang, X. (2003) An Experimental Study on the Flow Characteristics of Oil-Water Two-Phase Flow in Horizontal Straight Pipes, Chinese J. Chem. Eng., 11, 491–496.

Lockard, R. W., and Martinelli, R. C. (1949) Proposed Correlation of Data for Isothermal Two-Phase, Two-Component Flow in Pipes. Chemical Engineering Progress, Vol. 45, No 1, pp. 39-48.

Lovick, J. (2004) Horizontal, oil-water flows in the dual continuous flow regime, Doctor of Philosophy thesis, Department of Chemical Engineering, University of London.

Lovick, J. and Angeli, P. (2001) Two phase liquid flows at partially dispersed flow regime, Proceedings of 4th International Conference of Multiphase flow-ICMF'01, New Orleans.

Lovick, J. and Angeli, P. (2004a) Experimental studies on the dual continuous flow pattern in oil–water flows, International Journal of Multiphase Flow, 30, 139–157.

Lovick, J. and Angeli, P. (2004b) Two-Phase Liquid Flows At The Partially Dispersed Flow Regime, The 4th International Conference on Multiphase Flow, New Orleans, USA, Department of Chemical Engineering, University College London, Torrington Place, London WC1E 7JE, UK.

Lovick, J. and Angeli, P. (2004c) Droplet size and velocity profiles in liquid–liquid horizontal flows, Chemical Engineering Science 59, 3105-3115.

Lum, J. Y. L.; Lovick, J. and Angeli, P. (2004) Low inclination oil-water flows. Canadian. Journal, Chem. Eng. 82, 303-315.

Lum, J.; Al-Wahaibi, T. and Angeli, P. (2006) Upward and downward inclination oil–water flows, International Journal of Multiphase Flow, 32, 413-435.

Malinowsky, M. S. (1975) An experimental Study of Oil-Water and Air-Oil-Water Flowing Mixtures in Horizontal Pipes, M. S Thesis, The University of Tulsa.

Mandal, T. K.; Chakrabarti, D. P. and Das, G. (2007) Oil Water Flow Through Different Diameter Pipes- Similarities And Differences, Institution of Chemical Engineers, 85, 1123-1128.

Martinez, A. E.; Arirachakaran, S.; Shoham, O. and Brill, J. P. (1988) Prediction of Dispersion Viscosity of Oil/Water Mixture Flow in Horizontal Pipes, The 63rd Annual Technical Conference and Exhibition of the Society of Petroleum Engineers, Houston.

Mols, B. and Oliemans, R. V. A. A (1998) Turbulent Diffusion Model For Particle Dispersion And Deposition In Horizontal Tube Flow, International Journal of Multiphase Flow, 24, 55-75.

Mukherjee, H.; Brill, J. P. and Beggs, H. D. (1981) Experimental Study of Oil-Water Flow in Inclined Pipes, Journal of Energy Resources Technology, Vol.103.

Mukhopadhyay, H. (1977) An experimental Study of Two-Phase Oil-Water Flow in Inclined Pipes, M.S thesis, The university of Tulsa.

Munaweera, S. J.; Kvandal, H. K.; Robøle, B. and Valle, A. (2002) Flow patterns in crude oil-water flow at low water cuts, 3rd North American Conference, Banff, Canada: 6-7 June.

Ng, T. S.; Lawrence, C. J. and Hewitt G. F. (2001) Two-phase stratified flow in horizontal and inclined circular pipe, Proceedings of the 4ht Int. Conf. On Muliphase Flow, New Orleans, USA.

Ngan, K. H.; Ioannou, K.; Rhyne, L. D. and Angeli, P (2009) Prediction Of Pressure Gradient In Dispersed Liquid-Liquid Flows During Phase Inversion, BHR Group Multiphase Production Technology 14th, 131-139.

Nigmatulin, T. R.; Bonetto, F. J.; Larreteguy, A. E.; Lahey, R. T. Jr. and McQuillen, J. B. (2000) An experimental study of dispersed liquid/liquid two-phase upflow in a pipe, Chemical Engineering Communications, 1563-5201, Volume 182, Issue 1, Pages 121-162.

Nikuradse, J. (1932) Gesetzmässigkeiten der turbulenten Strömung in glatten Rohren, VDI Forschnungsheft, 356.

Nädler, M. and Mewes, D. (1997) Flow Induced Emulsification in the Flow of Two Immiscible Liquids in Horizontal Pipes, International Journal of Multiphase Flow, 23, 55-68.

Nädler, M. and Mewes, D. (1995) The Effect of Gas Injection on the Flow of Immiscible Liquids in Horizontal Pipes, Chem. Eng. Tech., 18, 156-165.

Oddie, G.; Shi, H.; Durlofsky, L. J.; Aziz, K.; Pfeffer, B. and Holmes, J. A. (2003) Experimental study of two and three phase flows in large diameter inclined pipes, International Journal of Multiphase Flow, 29, 527-558.

Oglesby, K. D. (1979) An experimental study on the effects of oil viscosity, mixture velocity, and water fraction on horizontal oil/water flow, M.S. thesis, The University of Tulsa.

Orr, R. (1995) Part 4 – Model Oil – Density and Interfacial Tension of Base Oils, Technical report, Hydro, Research Centre Porsgrunn, Norway.

Orr R. (2009) Initial studies on model oils, Memo, StatoilHydro, Research Centre Trondheim, Norway.

Pal, R. (1993) Pipeline Flow of Unstable and Surfactant-Stabilized Emulsions AlChE Journal, 39, 1754-1764.

Pal, R. and Rhodes, E. (1985) A Novel Viscosity Correlation for Non-Newtonian Concentrated Emulsions, Journal of Colloid and Interface Science, *107*, 301-307.

Pal, R. and Rhodes, E. (1989) Viscosity/Concentration Relationships for Emulsions, Journal of Rheology, 33, 1021-1045.

Pal, R.; Bhattacharya, S. N. and Rhodes, E. (1986) Flow behavoiour of oil-in-water emulsions, The Canadian Journal Of Chemical Engineering, 64, 3-10.

Pan, L., (1996) High Pressure Three-Phase (Gas/Liquid/Liquid) Flow, Phd, University of London, Imperial College of Science, United Kingdom.

Persen, L. F. (1972) Boundary layer theory, Tapir forlag.

Piela, K.; Delfos, R.; Ooms, G.; and R. V. A. Oliemans, J. W.; Mudde, R. F. and Burgerscentrum, J. M. (2006) Pressure Drop Measurements During Phase Inversion In An Oil-Water Flow Through A Horizontal Pipe Loop, BHR Group Multiphase Technology 5, 363-370.

Piela, K.; Delfos, R.; Ooms, G.; Westerweel, J. and Oliemans, R. (2008) On the phase inversion process in an oil–water pipe flow, International Journal of Multiphase Flow, 34, 665-677.

Pilehvari, A.; Saadevandi, B.; Halvaci, M. and Clark, P. E. (1988) Pipeline Transport Of Heavy Crudes As Emulsions, Proc. 3rd Int. Symp. Liquid Solid Flows, ASME V, 161-168.

Plegue, T. H.; Frank, S. G.; Fruman, D. H. and Zarkin, J. L. (1989) Concentrated viscous crude oil-in-water emulsions for pipeline transport, Chem. Eng. Comm. 82, 111-122.

Poesio, P. and Beretta, G. (2008) Minimal dissipation rate approach to correlate phase inversion data, International Journal of Multiphase Flow, 34, 684-689.

Reichert, J. K. and Azad, R. S. (1976) Nonasymptotic behavior of developing turbulent pipe flow, Can. J. Phys. 54, 268.

Reynold, O. (1883) An experimental investigation of the circumstances which determine whether the motion of water shall be direct or sinuous, and of the law of resistance in parallel channels, Phil. Trans. Roy. Soc. Lindon A, Vol. 174, 935-982.

Richardson, J. F. and Zaki, W. N. (1954) Sedimentation and fluidisation. Part 1, Trans. Inst. Chem. Engrs 32, 35-53.

Rodriguez, O. M. H. and Oliemans, R. V. A. (2006) Experimental study on oil-water flow in horizontal and slightly inclined pipes, International Journal of Multiphase Flow, 32, 323–343.

Rosentsvaig, A. K. (1982) Turbulent pipe flow of concentrated emulsions with a non equilibrium dispersed phase, Inzhenerno-Fizicheskii Zhurnal, 42, 336-372.

Russell, T. W. F.; Hodson, G. W. and Govier, G. W. (1959) Horizontal Pipeline Flow of Mixtures of Oil and Water, The Canadian Journal of Chemical Engineering, 37 (1), 9-17.

Schulkes, R. (2000) Modelling concentration profiles in dispersed oil-water flow, Internal Report from Industrial Project for Norsk Hydro Research Centre, Porsgrunn, Norway.

Scott, G. M. (1985) A Study Of Two Phase Liquid-Liquid Flow At Variable Inclinations, The Faculty of the Graduate School of The University of Texas, Master thesis.

Segev A. (1984) Mechanistic Model For Estimating Water Dispersion In Crude Oil Flow. AIChE Annual Meeting, San Francisco USA.

Shi, H.; Cai, J. Y.; Gopal, M. & Jepson, W. P. (2000) The effect of surfactants on low water cut oil-water flows in large diameter pipelines, 2nd North American Conference Multiphase Technology, Canada.

Shi, H.; Cai, J. and Jepson, W. P. (2001) Oil-Water Two-Phase Flows in Large-Diameter Pipelines, Journal of Energy Resources Technology.

Shiller, L. (1922), Physik. Z. 23, 14, ZAMM 2, 96.

Shlicting, H. (1934), ZAMM 14, 368.

Shlichting, H. (1979) Boundary Layer Theory, McGraw-Hill, New York.

Shlichting, H. and Gersten K. (2000) Boundary Layer Theory, 8th revised and enlarged edition, Springer.

Simmons, M. and Azzopardi, B. (2001) Drop size distributions in dispersed liquid-liquid pipe flow, Int. J. Multiphase Flow 27, 843-859.

Simmons, M. J. H.; Zaidi, S. H. and Azzopardi, B. (2000) Comparison of laser based drop size measurements techniques and their application to dispersed liquid-liquid pipe flow, Optical Engineering 39 2, pp. 505-509.

Simmons, M. J. H.; Azzopardi, B. J. and Zaidi, S. H. (1998) Measurement Of Drop Sizes And Flow Patterns In Liquid-Liquid Pipe Flow, Third International Conference on Multiphase Flow, ICMF98, Lyon, France.

Sleicher, C. A. (1962) Maximum Stable Drop Size In Turbulent Flow. AIChE Journal, 8, 471-477.

Solbakken, T. and Schüller, R. B. (2001) Multiphase flow experiments on a high pressure recombined gas/condensate/water system, BHR Group 2001 Multiphase '01.

Soleimani, A. (1999) Phase distribution and associated phenomena in oil-water flows in horizontal tubes, PhD, Imperial College of Science, London.

Soleimani, A.; Lawrence, C. J. and Hewitt, G. F. (1997) Effect of mixers on flow pattern and pressure drop in horizontal oil-water pipe flow, International Symposium on Liquid-Liquid Two Phase Flow and Transport Phenomena.

Sotgia, G.; Tartarini, P. and Stalio, E. (2008) Experimental Analysis of Flow Regimes And Pressure Drop reduction In Oil–Water Mixtures, International Journal of Multiphase Flow, 34, 1161-1174.

Sparrow, E. M.; Lin, S. H. and Lundgren, T. S. (1964), Phys. Fluids 7, 338-347.

Spedding, P. L.; Donnelly, G. F. and Cole, J. S. (2005) THREE PHASE OIL–WATER–GAS HORIZONTAL CO-CURRENT FLOW I. Experimental and Regime Map, Institution of Chemical Engineers, Trans IChemE, Part A.

Stapelberg, H. H. and Mewes, D. (1989) Experimental Studies Of The Stratified Flow Of Two Immiscible Liquids And Air In A Horizontal Pipe. European Two-Phase Flow Group Meeting, Paris.

Stapelberg, H. H. and Mewes, D. (1990) The Flow Of Two Immiscible Liquids And Air In A Horizontal Pipe, Institut fur Verfahrenstechnik der Universitat Hannover Hannover, Federal Republic of Germany, Techreport.

Su H. and Hanzevack E. L. (1988) A Model for Drop Size Distribution and Maximum Drop Size in Two-Phase Liquid-Liquid Flow. AIChE Annual Meeting, Washington D. C.

Taitel, Y.; Barnea, D. and Brill, J. P. (1995) Stratified Three Phase Flow In Pipes Int. J. Multiphase Flow, 21, 53-60.

Taitel, Y. and Dukler, A. E. (1976) A Model for Predicting Flow Regime Transitions In Horizontal and Near Horizontal Gas-Liquid Flow, AIChE Journal, 22, 47-55.

Tande, M (2008) Viscosity to Exxsol D60 and water with (3% NaCl, 11% MEG), Technical report, StatoilHydro, Research Centre Porsgrunn, Norway.

Taylor, G. I. (1934) Proc. Roy. Soc., London, A153, 302.

Theissing, P. (1980) A generally Valid Method for Calculating Frictional Pressure Drop in Multiphase Flow. Chemie Ingenieur Technik, Vol 52, No. 4, pp. 344-345.

Trallero, J. L. (1995) Oil-water flow patterns in horizontal pipes, PhD, The University of Tulsa.

Trallero, J. L.; Sarica, C. and Brill, J. P. (1997) A Study of Oil/Water Flow Patterns in Horizontal Pipes, SPE Production and Facilities, 165-172.

Tsouris, C and Tavlarides, L. L. (1994) Breakage and coalescence models for drops in turbulent dispersions, AIChe J, 40, 395-406.

Ullmann, A. and Brauner, N. (2006) Closure relations for two-fluid models for two-phase stratified smooth and stratified wavy flows, Int. J. Multiphase Flow, 32, 82-105.

Utvik, H.O; Rinde, T. and Valle, A. (2001) An experimental Comparison Between a Recombined Hydrocarbon-Water Fluid and a model Fluid System in Three-Phase Pipe Flow, Journal of Energy Resources Technology, 123, 253-259.

Utvik, O. H.; Valle, A. and Rinde, T. (1998) Pressure drop, flow pattern and slip for a multi-phase crude oil-water-hydrocarbon gas system, Third International Conference on Multiphase Flow, Lyon, France, June 8-12.

Utvik, O. H.; Rinde, T. and Valle, A. (1999) An experimental comparison between a recombined hydrocarbon-water fluid and a model fluid system in 'three phase pipe flow, BHR Group 1999 Multiphase '99, 169-180.

Valle, A. (2000) Three phase Gas-Oil-Water Pipe Flow, PhD, Imperial College of Science, Technology and Medicine, London.

Valle, A. and Kvandal, H. K. (1995) Pressure drop and dispersion characteristics of separated oil/water flow, The First International Symposium on Two-Phase Flow Modelling and Experimentation, Rome, Italy.

Valle, A. and Utvik, O. H. (1997) Pressure drop, flow pattern and slip for two phase crude oil/water flow: Experiments and model predictions, International Symposium on Liquid-Liquid Two Phase Flow and Transport Phenomena, Antalya, Turkey.

Vedapuri, D.; Bessette, D. and Jepson, W. P. (1997) A Segregated Flow Model To Predict Water Layer Thickness In Oil-Water Flows In Horizontal And Slightly Inclined Pipelines, BHR Group Multiphase.

Vielma, M.; Atmaca, S.; Sarica, C. & Zhang, H. (2007) Characterization of Oil/Water Flows in Horizontal Pipes, SPE Annual Technical Conference and Exhibition, Anaheim, California, U.S.A., 11-14.

Vigneaux, P.; Chenais, P. and Hulin, J. P. (1988) Liquid-Liquid Flows in an Inclined Pipe. AIChE Journal, 34, 781-789.

Wahumpurage, A. S.; Halvorsen, B. M. and Melaaen, M. C (2008) An experimental investigation of oil-water flow in horizontal pipe using PIV and gamma measurements, 11th International conference on multiphase flow in industrial plants, Palermo, Italy.

Wallis, G. B. (1969) One-Dimensional Two-Phase Flow, McGraw-Hill.

Wang, Q. Y. (1999) Predictions of developing turbulent pipe flow by a modified K-ε-γ model, PhD, University of Manitoba, Mechanical and industrial engineering, Winnipeg.

Walvekar, R. G.; Choong, T. S. Y.; Hussain, S.; Khalid, M. and Chuah, T. (2009) Numerical study of dispersed oisl-water turbulent flow in horizontal tube, Journal of Petroleum Science and Engineering, 1-20.

Xu, X. (2007) Study on oil–water two-phase flow in horizontal pipelines, Journal of Petroleum Science and Engineering 59, 43-58.

Xu, J.; Wu, Y.; Feng, F.; Chang, Y. and Li, D. (2008) Experimental Investigation On The Slip Between Oil And Water In Horizontal Pipes, Experimental Thermal and Fluid Science, 33, 178-183.

Yao, H. Y. and Gong, J., (2004) An experimental investigation on flow patterns and pressure gradient of heavy oil–water flows in horizontal pipes, The 3rd Int. Symp. on Multiphase, Non-Newtonian and Reacting Flow, Hangzhou, China.

Yeo, L. Y.; Matar, O. K.; de Ortiz, E. S. P. and Hewitt, G. F. (2000) Phase inversion and associated phenomena, Multiphase Science and Technology, 12, 51-116.

Zhang, Z. H. and Eisele, K. (1998) On the overestimation of the flow turbulence due to fringe distortion in LDA measurement Volumes, Experiments in Fluids, 25, 371-374.

Zhang, H. and Sarica, C. (2005) Unified Modeling of Gas/Oil/Water Pipe Flow - Basic Approaches and Preliminary Validation, SPE Annual Technical Conference and Exhibitio, Dalas, Texas, U.S.A.

Zhang, H. and Sarica, C. (2006) Unified Modeling of Gas/Oil/Water-Pipe Flow - Basic Approaches and Preliminary Validation, SPE Projects, Facilities & Construction.

Zhou, G. and Kresta, S. M (1998) Correlation of mean drop size and minimum drop size with the turbulence energy dissipation and the flow in an agitated tank, Chemical Engineering Science 53, 2060-2079.

Zittel, W. and Schindler, J. (2008) Crude Oil: The supply Outlook, report to the Energy Watch Group, EWG –series No 3.

APPENDIX

Appendix 1:

Summary of experimental work on oil-water flow in small pipe inclinations

Table A 1 Experimental work on oil-water flows in small pipe inclinations (0°-30°).

Report	**Rig data**	**Velocities** **Water cut**	**Parameters investigated** **Instrument/**	**Fluid properties**	**Incl.**	**Oper. cond.**
Russel et al. (1959)	Smooth transparent L: 10.7 m ID: 20.3 mm	Uso : 0.013 - 1.0 m/s Usw : 0.04 - 1.08 m/s	Pressure drop Hold-up: Quick closing valves (QCV) Flow patterns: Visual	ρ_O: 834 kg/m^3; μ_O: 18 cp μ_W: 1 cp ρ_W : 1000 kg/m^3	0°	
Charles et al. (1961)	Smooth transparent L: 8 m ID: 26.4 mm	Uso : 0.015 - 0.91 m/s Usw : 0.02 - 1.07 m/s	Pressure drop Mean phase fractions: QCV Flow patterns: Visual	Three commercial oils ρ_O: 998 kg/m^3; μ_O: 6.29 cp, 16.8cp, 65cp ρ_W : 1000 kg/m^3	0°	
Sleicher (1962)	L: 11.9 m ID: 38.1 mm	Uso : Very small Usw : 0.56 - 2.4 m/s Dilute system	Drop size: Photographic	ρ_O: 700-1585 kg/m^3; μ_O: 0.5-32.1 cp μ_W: 1.0, 3.96 cp ρ_W : 1000 kg/m^3 σo_W : 8.1-45 mN/m	0°	
Charles and Lilleleht (1966)	L: 4.9 m ID: 15.9 mm	Uso : 0 - 2.3 m/s Usw : 0.7 - 5.3 m/s Dilute suspensions for most of the data	Pressure drop	ρ_O: 825 kg/m^3; μ_O: 5.5 cp μ_W: 1.0 cp ρ_W : 1000 kg/m^3	0°	
Guzhov et al. (1973)	L: 18.0 m ID: 39.4 mm	Umix : 0.2 - 1.7 m/s No-slip oil WC: 0.1 - 0.9	Flow pattern Pressure drop	ρ_O: 896 kg/m^3 μ_O: 18 cp μ_W: 1.0 cp ρ_W : 998 kg/m^3 σo_W : 44.8 mN/m	0°	
Malinowsky (1975)	L: 29.9 m ID: 38.4 mm	Uso : 0.26 - 1.36 m/s Usw : 0.19 - 2.08 m/s	Flow pattern: Visual	ρ_O: 848 kg/m^3	0°	

			Pressure drop	μ_O: 4 cp μ_W: 1.2 cp ρ_W : 998 kg/m^3 σo_W : 22.3 mN/m		
Laflin and Oglesby (1976)	Transparent (Lexan) L: 30.7 m ID: 67 mm	Uso : 0.17 - 1.16 m/s Usw : 0.17 - 1.16 m/s	Flow pattern: Visual Pressure drop	ρ_O: 828 kg/m^3 μ_O: 4.94 cp μ_W: 1.2 cp ρ_W : 999 kg/m^3 σo_W : 22.3 mN/m	0°	
Kubie and Gardner (1977)	L: 4 m ID: 17.2 mm	Uso : 0.85 - 3.4 m/s Dilute	Drop size and distribution: Photographic Drop concentration: Isokinetic probe	ρ_O: 828 kg/m^3 μ_O: 4.94 cp μ_W: 1.2 cp ρ_W : 999 kg/m^3 σo_W : 22.3 mN/m	0°	
Mukhopadhyay (1977)	Lexan L: 13. 7 m ID : 0.0381 m	Um: 0.60 - 0.70 m/s	Pressure drop Water holdup: QCV	Diesel / Water fluid system: ρ_O: 850 kg/m^3; μ_O: 4.5 cp μ_W: 1 cp ρ_W : 998 kg/m^3 σo_W : 22.3 mN/m	$\pm 30^0 \pm$ $50^0 \pm 6$ $5^0 \pm 80$ $^0 \pm 90^0$	P:1 bar T: 30 ^oC
Karabelas (1978)	L: 32.3 m ID: 50.4 mm	Uso : 1.18 - 3.0 m/s Usw : 0.05 - 0.12 m/s Dilute system	Drop size: Encapsulation technique with isokinetic sampling, Photographic Drop size distribution: Encapsulation technique with isokinetic sampling, Photographic	ρ_{OW}: 798, 898 kg/m^3 μ_O: 1.82, 15 cp μ_W: 1 cp ρ_W : 1000 kg/m^3 σo_W : 32-35 mN/m	0°	

Oglesby (1979)	L: 30.5 m ID: 41 mm	Uso : 0.03 - 3.19 m/s Usw : 0.07 - 2.71 m/s	Pressure drop Flow pattern: Visual	ρ_{OW}: 857, 861, 868 kg/m^3 μ_O: 32, 61, 167 cp μ_W: 1.0 cp ρ_W : 999 kg/m^3	0°	
Mukherjee et al. (1981)	Lexan L: 13.7 m ID: 38 mm	U_{SW}: 0.14 - 0.52 m/s U_{SO}: 0.17 - 0.52 m/s U_{SL}: 0.65 m/s	Pressure drop Water holdup: Valves	Diesel/Water ρ_O: 850 kg/m^3; μ_O: 4.5 cp ρ_W: 998 kg/m^3; μ_W: 1 cp σo_W: 0.0223 N/m	0° ±30° ±90°	P: Atm. T: 30 °C
Segev (1984)	ID : 1067 mm	U_{SW}: < 0.02 m/s U_{SO}: 0.84 - 2.04 m/s	Local dispersed phase fractions: Sample probes	ρ_{OW}: 858 kg/m^3; μ_O: 11.6 – 43.4 cp ρ_W: 1000 kg/m^3; μ_W: 1 cp	0°	
Cox (1985) (Taken from Jason Y et al)	Plexiglass L: 10.4 m ID : 0.0508 m	Um = 0.05 - 1.28 m/s Uws = 0.05 - 0.64 m/s Uos = 0.05 - 0.64 m/s WC: 0 - 100%	Flow pattern: Photography Hold-up: QCV	ρ_W: 998 ρ_O: 754 μ_w: 0.894 mPa s μ_O: 1.38 mPa s	0° -15° -30°	
Scott (1985)	Plexiglass L: 10.4 m ID : 0.0508 m	U_m = 0.05-1.28 m/s U_{ws} = 0.05-0.64 m/s U_{os} = 0.05-0.64 m/s WC: 0% -100%	Flow pattern: Visual observation Hold-up: QCV	ρ_W: 998 ρ_O: 754 μ_w : 0.894 mPa s μ_O: 1.38 mPa s	+15^0 and +30^0	
Vigneaux et al. (1988)	L: 14 m ID : 0.20 m Entrance length: 2 m	U_m = 0.027 - 0.35 m/s WC: 30 - 95%	Phase distribution: Local high frequency impedance probe	ρ_W: 998 ρ_O: 740 μ_w : 1 mPa s	90°, +85°+75°+65°+45° +25^0	
Martinez et al. (1988)	L: 12 m ID: 59 mm	Um: 0.76 - 4.7 m/s WC: 0 - 35% (Homogenous dispersed flow pattern)	Pressure drop	ρ_O: 860 kg/m^3; μ_O: 85 cp (26.7°C) μ_W: 1.0 cp ρ_W : 1000 kg/m^3	0°	1 bar, 15.6°C, 21.1°C, 26.7°C, 32.2°C
Su and Hanzevack (1988)	ID: 50.8, 76.2, 101.6 mm	Um: 0.95 - 3.38 m/s (Oil continuous)	Drop size and distribution and phase	μ_O: 1.79, 2.37, 2.94 cst ρ_W: 1000 kg/m^3;	0°	

			distributions: Pulsed laser combined with digital image processing	μ_W: 1cp		
Arirachakaran (1989)	Steel pipes, transparent pipes L_1:12.8 L_2: 6.1m ID_1: 41.0 mm ID2: 26.6 mm $(L/D)_{1,2}$: 292, 375 $(Exit\ length)_{1,2}$: 109, 22 m	Uso: 0.45 - 3.6 m/s WC: 5 - 90%	Pressure drop Flow pattern: Visual	Diesel fuel oil, tap water ρ_{O1}: 868 kg/m^3 ρ_{O2}: 898 kg/m^3 μ_{O1}: 4.7, 58, 84, 115 cp @ 21.1°C μ_{O2}: 237, 2116 cp @ 21.1°C ρ_W: 998 kg/m^3 μ_w : 1.06 mPa s σ_{ow}: 29 - 32 mN/m	0°	10° to 36.67°C
Stapelberg and Mewes (1989)	Transparent pipe L: 8 m ID: 25 mm	Uso: 0.04 m/s Usw: 0.04 - 0.06 m/s Oil-water stratified flow	Pressure drop	Mineral white oil ρ_O: 850 kg/m^3 μ_O: 30 cp ρ_W: 1000 kg/m^3 μ_w : 1 cp σ_{ow}: 50 mN/m	0°	
Angeli (1994)	Stainless steel Transparent L: 9.7 m ID : 24.3 mm	Uws = 0.05 - 1.2m/s Uos = 0.05 - 1.2 m/s WC: 0% -100%	Pressure drop Flow pattern: Visual (video)	Exxsol D80: ρ_O: 801 kg/m^3 μ_o : 1.6 mPas @ 25°C σ_{ow}: 17 mN/m @ 22°C	0°	
Kurban et al. (1995a)	Stainless steel Clear acrylic L: 10 m ID : 24 mm	Um = 1 - 3.9 m/s WC = 0.05 - 0.85 %	Flow pattern: Visual	ρ_O: 860 kg/m^3 μ_O: 1.6 cp ρ_W: 998 kg/m^3 μ_w : 1 cp	0°	
Kurban et al. (1995b)	Clear acrylic L: 10 m ID : 24 mm	U_m = 0.1 – 5 m/s WC = 10 - 90%	Flow pattern: Visual Oil-water interface level: High frequency impedance probe	Exxsol D80 ρ_O: 800 kg/m^3 μ_O: 1.6 cp @ 25°C ρ_W: 1000 kg/m^3 μ_w : 1 cp σ_{ow}: 17 mN/m @ 22°C	0°	

			Drop size distribution: Conductivity probe and photographic technique (Borescope)			
Nädler and Mewes (1995)	Acrylic resin L: 12 m ID : 59 mm	U_{ws} =0.0143 - 1.44 m/s U_{os} =0.0078 - 1.48 m/s $(L/D)_{1,2}$=225, 680	Pressure drop Flow pattern: Visual, impedance probe	ρ_O: 841 kg/m^3 μ_O: 31 cp ρ_W: 998 kg/m^3 μ_w : 1 cp	0°	
Valle and Kvandal (1995)	Glass pipe L: 2x5 m ID : 37.5 mm	Usw =0.2-1.2 m/s Uso =0.2-1.2 m/s	Pressure drop Flow pattern: Visually Oil-water distribution: Non isokinetic conductivity probes Phase exposure to the inner pipe wall: Conductivity probe	Exxsol D80 and water ρ_O: 794 kg/m^3 μ_O: 2.3 cp ρ_W: 1002 kg/m^3 μ_w : 1.02 cp σ_{ow}: 37.3 mN/m	0°	
Trallero (1995)	Acrylic L: 15.5 m ID: 50.1 mm	Usw =0.01 - 1.7 m/s Uso = 0.01 - 1.7 m/s	Flow pattern: 1.Camera 2. Differential pressure transducers 3. Conductance Local phase continuity: Conductance probe Holdup: QCV	ρ_O: 884 kg/m^3 μ_O: 28.8 cp ρ_W: 1037 kg/m^3 μ_w : 0.97 cp σ_{ow}: 36 mN/m	0°	P=1 bar T=25.6°C

Angeli (1996)	Stainless steel Acrylic pipe L_1: 9.7 m L_2: 9.2 m ID_1 : 24.3 mm ID_2 : 24 mm $(L/D)_{FP}$ = 370 $(L/D)_{DP}$ = 213 & 158	Um = 0.9 - 3.0 m/s Usw =0 - 3.6 m/s Uso =0 - 3.6 m/s WC = 25 - 85%	Pressure drop Flow pattern: 1. High speed video scope 2. Conductivity needle probe 3. Impedance probe Oil-water distribution: 1. Impedance probe Drop size distribution: 1. Photographic & endoscope 2. Conductivity needle probe	Exxsol D80 and Water ρ_O: 801 kg/m^3 @ 20°C μ_O: 1.6 cp @ 20°C ρ_W: 1000 kg/m^3 μ_w : 1 cp σ_{ow}: 17 mN/m @ 20°C	0°	Low pressure rig (Imperial College)
Valle and Utvik (1997)	Stainless steel L: 100 m ID : 77.9 mm	Usw =0-2.33 m/s Uso =0 - 2.33 m/s Um= 1.17, 1.74, 2.33 m/s	Pressure drop Flow pattern: Traversing conductivity probe In-situ phase fractions: gamma densitometer	Light crude oils, synthetic formation water ρ_O: 741 kg/m^3 μ_O: 1.0 cp ρ_W: 1000 kg/m^3 μ_w : 0.43 cp σ_{ow}: 28.5 mN/m	0°	70°C 105 bar
Nädler and Mewes (1997)	Perspex L: 48 m ID : 59 mm $(L/D)_{DP1}$ = 225 $(L/D)_{DP2}$ = 680	Um : 0.1 - 1.6 m/s WC: 0 - 100%	Pressure drop Flow pattern: 1. Visual 2. Electrical conductance Phase inversion: Electrical conductance	Mineral oil ρ_O: - kg/m^3 μ_O: 22, 27, 35 cp ρ_W: - kg/m^3 μ_w : - cp	0°	T:18-30°C
Hapanowicz et al. (1997)	Glass L: 1.5 m ID : 12, 16, 22 mm	Uso : 0.02 - 8 m/s Usw: 0.01 - 0.4 m/s WC: 7 - 98.3%	Pressure drop Flow pattern: Visual	Viz and tar oil ρ_{O1}: 1200 kg/m^3 μ_{O1}: 40 cp ρ_{O2}: 915 kg/m^3	0°	T: 20°C

				ρ_{O2}: 1200 kg/m^3 μ_{O2}: 40 cp		
Beretta et al. (1997)	Glas L: 1000 mm ID : 3 mm $(L/D)_{FP}$: 200	Qo: 0.32 - 3.3 l/h Qw: up to 33.9 l/h	Pressure drop Flow pattern: Photographs (stroboscope)	ρ_O: 866.48, 886.25, 865.50 kg/m^3 μ_O: 71.17, 51.325, 9.874 cp σ_{ow}: 31.5, 36.0, 37.4 mN/m	0°	
Flores et al. (1997)	Transparent L: 15.5 m ID : 0.0508 m	Um: 0.0908 - 2.542 m/s Uws: 0.0454 - 1.271 m/s Uos: 0.0454 - 1.271 m/s WC: 0 -100%	Flow pattern: 1.Visually 2. Electrical conductance 3. Pressure gradient Hold-up: Electrical conductance Phase distribution: Electrical conductance	Mineral oil and water ρ_W: 1000 ρ_O: 850 μ_w : 1 mPa s μ_O: 20 mPa s σ_{ow}: 33.5 mN/m @ 32.2 °C	+45° +60° +75° +90°	
Vedapuri et al. (1997)	Plexiglass L: 18 m ID: 101.6 mm	Usl: 0.1- 2 m/s Um1: 0.4 - 1.6 m/s Um2: 0.4 - 0.8 m/s WC: 20, 40, 60, 80%	Flow pattern: Visual Pressure drop: Manometer Phase distribution: Isokinetic sampling In situ velocity profiles: Pitot tube	Oil-Sea water μ_O: 2 cp & 96 cp Sea water	0° +2°	P:1.36 bar T: 40 °C
Simmons et al. (1998)	Transparent PVC L: m ID: 50.8 m	Uws: 0.0454, 0.04678, 1.2711 m/s Uos : 0 - 1.271 m/s Um: 0.0908 - 2.543	Flow pattern: Camera Drop size: Optical, Laser	Kerosene, 25% potassium carbonate	0° 90°	

		m/s WC: 0-100%	back-scatter (Par-Tec), Far-field diffraction (Malvern)			
Flores et al. (1998)	Transparent L: 15.3 m ID : 50.8 m	Uws: 0.0454, 0.04678, 1.2711 m/s Uos: 0 - 1.271 m/s Um: 0.0908 - 2.543 WC: 0 - 100%	Flow pattern: 1.Visual 2. Electrical conductance Pressure gradient Hold-up: QCV	Mineral oil/Water ρ_O/ρ_W: 0.85 kg/m^3 μ_O/μ_w: 20.0 mPa s σ_{ow}: 35.5 mN/m	+90° +75° +60° +45°	
Angeli and Hewitt (1998) (Imperial College)	1.Stainless steel 2.Acrylic resin L: 9.7 m ID : 24.3 mm (1 in.) 1.$(L/D)_{DP}$: 206 2. $(L/D)_{DP}$: 165	Umix: 0.3 - 3.9 m/s WC: 0 - 100%	Flow pattern: Visual Pressure gradient	Exxsol D80 and tap water ρ_W: 1000 kg/m^3 ρ_O: 801 kg/m^3 μ_w : 1 mPa s μ_O: 1.6 mPa s σ_{ow} : 17 mN/m	0°	P: 1bar T: 20°C Low pressure rig (Imperial College)
Soleimani (1999)	Stainless steel Acrylic resin tube L: 9.7 m ID: 1in.	U_L: 0.5 - 3.5 m/s WC: 0 - 100%	Flow pattern: 1.Visually (High speed camera) 2. Conductivity 3. Densitometer Local volume fractions: High frequency impedance probe [(Angeli (1996)], Gamma densitometer Behaviour of drops: Endoscope	Exxsol D80, Tap water ρ_O: 801 kg/m3 μ_O: 1.6 cp σ_{ow} :17 mN/m	0°	Low pressure rig (Imperial College)
Alkaya et al. (2000)	Acrylic L: 21m	Um: 0.025 - 1.75 m/s Usw : 0.025 - 1.75	Pressure drop Flow pattern:	Mineral oil/Water ρ_O: 848 kg/m^3;	0°, ±0.5°	P: 1.4 bar T: 35 ^oC

	ID: 50.8 mm 1.$(L/D)_{DP}$: 299 2. $(L/D)_{DP}$: 165	m/s Uso: 0.025 - 3.50 m/s WC: 0 -100%	Visual Conductance probes Hold-up: QCV Phase distribution: Conductance probes	μ_O: 12.9 cp ρ_W: 994 kg/m^3; μ_W: 0.72 cp σo_W: 16.7 mN/m	±5° ±1° ±2°	
Fairuzov et al. (2000)	ID: 16-in. 363.5 mm L/D: 688	Um: 0.05 - 2.11 m/s WC: 1.5 - 50%	Local water fraction: Multipoint sampling probe (MPSP) and centrifuge Flow pattern: MPSP	Crude oil/Fresh water ρ_O: 851 kg/m^3; μ_O: 5.96 cp @ 38°C	0°	1 bar
Angeli and Hewitt (2000)	Stainless steel Acrylic resin L: 8 m ID: 24 mm	U_{DP}: 0.05 - 0.11 m/s Ucp: 1.1 - 1.7 m/s	Droplet size distribution: Visual (Video recording with endoscope)	Mineral oil/Water ρ_O: 801 kg/m^3; μ_O: 1.6 cp ρ_W: 1000 kg/m^3 μ_w : 1 cp σ_{ow}: 17 mN/m	0°	
Kvandal et al. (2000)	Stainless steel Duran 50 glas L: 8 m ID: 2-in.: 56.3 mm	Um: 1.5 - 3.0 m/s WC: 0 -100%	Local phase fractions: Gamma densitometer Velocity profiles and fluctuations: Laser Doppler Velocimetry	Mineral oil/Water solvent ρ_O: 842 kg/m^3 μ_O: 3.6 cp ρ_W: 1101 kg/m^3 μ_w : 3.2 cp σ_{ow}: 30 - 35 mN/m	0°	
Shi et al. (2000)	Plexiglas L: 18 m ID: 100 mm	U_L: 0.4 - 3.0 m/s WC: 0, 5, 10, 15, 20%	Flow pattern: Visual Pressure drop-manometer Oil-water distribution profile: Pitot	Oil/ Sea water μ_O: 3.0 cp ρ_O: 820 kg/m^3 σo_W: 33.4 mN/m σo_W: 6.9 mN/m σo_W: 1.9 mN/m	0°	0.13 MPa 25°C

			tube Velocity profiles: Pitot tube			
Valle (2000)	Duplex steel L: 120 m ID: 3-in., 77.9 mm	Um: 1.17, 1.75, 2.33, 3.0 m/s WC: 0 -100%	Flow pattern: Two wire capacitance probe Pressure drop Phase fraction profiles: Fixed gamma densitometer	Mineral oil Exxsol D60/Water ρ_O: 756 kg/m^3; μ_O: 0.8 cp ρ_W: 1000 kg/m^3 μ_w : 0.4 cp	0°	P: 88 bar T: 74°C
		Um: 0.87, 1.75, 2.33 m/s WC: 0 -100%		Crude oil system 1 ρ_O: 796 kg/m^3; μ_O: 1.67 cp ρ_W: 1009.7 kg/m^3 μ_w : 0.5 cp σ_{ow}: 23.4 mN/m	0°	P: 90 bar T: 60°C
		Um: 0.87, 1.75, 2.33 m/s WC: 0 -100%		Crude oil system 1 ρ_O: 839.5 kg/m^3 μ_O: 2.42 cp ρ_W: 1009.7 kg/m^3 μ_w : 0.5 cp σ_{ow}: 32.0 mN/m	0°	P: 20 bar T: 60°C
		Um: 0.87, 1.75, 2.33 m/s WC: 0 -100%		Crude oil system 1 ρ_O: 809.7 kg/m^3 μ_O: 2.53 cp ρ_W: 1022.5 kg/m^3 μ_w : 0.85 cp σ_{ow}: 32.0 mN/m	0°	P: 90 bar T: 30°C
		Um: 0.87, 1.75, 2.33 m/s WC: 0 -100%		Crude oil system 1 ρ_O: 822.9 kg/m^3 μ_O: 2.67 cp	0°	P: 90 bar T: 20°C

				ρ_W: 1025.7 kg/m^3 μ_w : 1.05 cp σ_{ow}: 35 mN/m		
		Um: 1.17, 1.75, 2.33 m/s WC: 0 -100%		Crude oil system 2 ρ_O: 741.0 kg/m^3 μ_O: 1.03 cp ρ_W: 1000.4 kg/m^3 μ_w : 0.43 cp σ_{ow}: 28.5 mN/m	0°	P: 105 bar T: 70°C
		Um: 1.17, 1.75 m/s WC: 0 -100%		Crude oil system 3 ρ_O: 865 kg/m^3 μ_O: 3.7 cp ρ_W: 1010 kg/m^3 μ_w : 0.5 cp σ_{ow}: 28.5 mN/m	0°	P: 20 bar P: 60°C
		Um: 0.6 - 2.34 m/s WC: 0 - 100%		Crude oil system 4 ρ_O: 909 kg/m^3 μ_O: 0.8 cp ρ_W: 1000 kg/m^3 μ_w : 0.4 cp σ_{ow}: 28 mN/m	0°	P: 12 bar T: 60°C
Elseth (2001)	Stainless steel Plexiglas L: 10 m ID: 56.3 mm	Um: 0.67 - 3.0 m/s WC: 0 -100%	Flow pattern: Visual Pressure drop Phase distributions: Gamma densitometry Velocity and turbulence profiles: LDA	Exxsol D60/Water ρ_O: 790 kg/m^3 μ_O: 1.64 cp ρ_W: 1000 kg/m^3 μ_W: 1.02 cp σo_W: 43 mN/m	0°	P: 1 bar T: 25°C Telemark University College

Solbakken and Schüller (2001)	Duplex steel L: 120 m ID: 3-in., 77.9 mm	Um: 1.17 and 2.33 m/s WC: 0 -100%	Pressure drop Flow pattern: Traversing conductivity probes	Exxsol D60/Formation Water ρ_O: 756 kg/m^3 μ_O: 0.8 cp ρ_W: 1000 kg/m^3 μ_W: 0.4 cp σo_W: 32.5 mN/m Condensate/distilled water ρ_O: 656 kg/m^3 μ_O: 1.03 cp ρ_W: 1010.4 kg/m^3 μ_W: 0.43 cp σo_W: 28.5 mN/m	0° 0°	P:87.5 bar T: 74°C P:105 bar T: 70°C
Utvik et al. (2001)	Duplex steel L: 120 m ID: 3-in., 77.9 mm	Um: 1.17 and 1.75 m/s WC: 0 -100%	Pressure drop Flow pattern: Two-wire capacitance probe	Exxsol D60/Formation Water ρ_O: 756 kg/m^3 μ_O: 0.8 cp ρ_W: 1000 kg/m^3 μ_W: 0.4 cp σo_W: 32.5 mN/m Light crude oil/Distilled Water ρ_O: 741.0 kg/m^3; μ_O: 1.03 cp ρ_W: 1010.4 kg/m^3; μ_W: 0.43 cp σo_W: 28.5 mN/m	0° 0°	P:87.5 bar T: 74°C P:105 bar T: 30°C
Shi et al. (2001)	Plexiglas L: 18 m ID: 100 mm	U_L: 0.4 - 3.0 m/s WC: 0 - 100%	Flow pattern: Visual Pressure drop Oil-water distribution profile: Pitot tube	Oil/ Sea water μ_O: 3.0 cp ρ_O: 820 kg/m^3 σo_W: 33.4 mN/m σo_W: 6.9 mN/m σo_W: 1.9 mN/m	0°	P: 0.136MPa T: 25°C

			Velocity profiles: Pitot tube			
Munaweera et al. (2002)	Stainless steel L: 14 m ID: 56.3 mm	Um: 0.5 - 3.0 m/s WC: 2 -11%	Pressure drop Local phase distribution: Traversable gamma densitometer Flow pattern: Traversable gamma densitometer	Light crude oil and condensate mixture/Water ρ_O: 751 kg/m^3 @ 60°C, 1 bar μ_O: 0.73 cp @ 60°C, 1 bar ρ_W: 1004 kg/m^3 @ 60°C, 1 bar μ_W: 0.5 cp @ 60°C, 1 bar σo_W: 28.5 mN/m @ 60°C, 1 bar	0°	P: 1bar T: 60°C
Liu et al. (2003)	Plexiglas Stainless steel L: 20 m ID: 40 mm	Uso: 0.04 -1.2 m/s Usw: 0.04 - 2.2 m/s	Flow pattern: Visualization Transient fluctuation of differential pressure drop Pressure drop	Mechanical oil/tap water ρ_O: 893 + 0.614T kg/m^3 μ_O: 428.51e$^{-0.0593T}$ cp σo_W: 27.72 e$^{0.0018T}$ mN/m	0°	P: 1bar T: 5-20°C
Oddie et al. (2003)	Transparent L: 11 m ID: 150 mm	Um: 0.03 - 1.26 m/s WC : 0 -100%	Flow pattern: Visual Hold up: QCV Hold-up: Gamma densitometer Electrical conductivity probes (Transient and steady state)	Kerosene/tap water ρ_O: 828 kg/m^3 μ_O: 5.5 cp ρ_W: 998 kg/m^3 μ_W: 0.993 cp σo_W: 40 mN/m	0°, -2°, +2°, +20°, +45°, +85°	
Lum et al. (2004)	Stainless steel L: 8 m ID: 38 mm	U_M: 0.7 - 2.5 m/s WC: 10 - 90%	Pressure drop Flow pattern: 1. Visual observation 2. Conductivity probes	Exxsol D140/Water ρ_O: 828 kg/m^3 μ_O: 5.5 cp ρ_W: 998 kg/m^3 μ_W: 0.993 cp	0^0, +5°	T: 20 ^{o}C

			Hold up: QCV Phase distribution: Impedance probes	σo_W: 40 mN/m		
Lovick and Angeli (2004a)	Stainless steel L: 8 m ID: 38 mm	U_M: 0.8 - 3.0 m/s WC: 10 - 90%	Pressure drop Flow pattern: Visual Phase distribution: Impedance Phase continuity: Conductivity probes Hold-up-QCV	Mineral oil/Water ρ_O: 828 kg/m^3; μ_O: 6 cp σo_W: 39.6 mN/m	0°	P:1 bar T: 25°C
Lovick and Angeli (2004b)	Stainless steel L: 8 m ID: 38 mm	U_M: 1 - 2 m/s WC: 10% - 90%	Pressure drop Flow pattern: Visual Phase distribution: Impedance Phase continuity: Conductivity probes Hold-up: QCV	Mineral oil/Water ρ_O: 828 kg/m^3 μ_O: 6 cp σo_W: 39.6 mN/m	0°	P:1 bar T: 25°C
Lovick and Angeli (2004c)	Stainless steel L: 8 m ID: 38 mm	U_M: 1.5 - 2.5 m/s WC: 20 - 80%	Drop size and distribution: Impedance Drop velocity: Impedance Phase continuity: Conductivity and single impedance probe Phase	Mineral oil/Water ρ_O: 828 kg/m^3 μ_O: 6 cp	0°	

			distribution: Conductivity and single impedance probe Flow pattern: Conductivity and single impedance probe			
Abduvayt et al. (2006)	L: 120 m ID: 106.4 mm 1.(L/D): 305	Uso: 0.025 – 1.502 m/s Uso: 0.025 – 1.502 m/s	Pressure drop Flow pattern – video camera Hold up – conductance probes	Kerosene/Tap water ρ_O: 800 kg/m^3; μ_O: 1.88 cp σo_W: 40 mN/m	0°, ±0.5° ±3°	P:2.45 bar T: 35 (±5) ^oC
Lum et al. (2006)	Stainless steel L: 8 m ID: 38 mm	Um: 0.7 - 2.5 m/s WC: 10 - 90%	Pressure drop Flow pattern: Visual Conductivity probes (Fluid of continuous phase and position of interface) Hold up: QCV Phase distribution: Impedance probes (Lovick and Angeli (2001)]	Exxsol D140/Tap water ρ_O: 828 kg/m^3 μ_O: 5.5 cp ρ_W: 998 kg/m^3 μ_W: 0.993 cp σo_W: 40 mN/m	0°, ±5° +10°	T: 25 ^oC
Rodriguez and Oliemans (2006)	Stainless steel L: 15 m ID: 82.5 mm	Um: 0.04 - 5.55 m/s Usw = 0.02 - 2.55 m/s Uso = 0.02 - 3.00 m/s	Pressure drop Flow pattern: Visual Phase distributions: Gamma densitometer	Mineral oil/brine ρ_O: 830 kg/m^3 μ_O: 7.5 cp ρ_W: 1060 kg/m^3 μ_W: 0.8 cp σo_W: 20.4 mN/m	0° -1.5° 1° ±2° ±5°	

Vielma (2007)	Transparent pipes L: 21.13 m ID: 58.6 mm $(L/D)_{DP}$: 272 $(L/D)_{QCV}$: 108	Um: 0.025 - 1.75 m/s Usw: 0.02 - 2.55 m/s Uso: 0.02 - 3.00 m/s	Pressure drop Flow pattern: Visual Droplet size: High speed video camera Phase distributions: Conductivity probes Hold-up: QCV	Mineral oil (Tulco Tech 80)/Tap water ρ_O: 858.75 kg/m^3 @ 15.6°C μ_O: 13.5 cp @ 40°C σo_W: 16.38 mN/m @ 25.1°C	0°	T: 29 - 45°C
Mandal et al. (2007)	Transparent pipes ID: 25 mm ID: 12 mm $(L/D)_{DP}$: 80 $(L/D)_{QCV}$: 166	Um: 0.03 - 1.5 m/s	Flow pattern: Visual Effect of different mixers	Mineral oil (kerosene)/Tap water ρ_O: 787 kg/m^3 μ_O: 1.2 cp	0°	
Al-Wahaibi & Angeli (2007)	Stainless steel Transparent pipe L: 8 m ID: 38 mm	Um: 0.6, 0.9-1.10 m/s Uso: 0.05 - 0.55 m/s	Wave characteristics (instantaneous fluctuations of the Interface): Conductivity probe Onset of entrainment: High speed video camera	Mineral oil (kerosene)/Tap water ρ_O: 828 kg/m^3 μ_O: 5.5 cp	0°	
Al-Wahaibi et al. (2007)	Stainless steel Transparent pipe L: 3.5 m ID: 14 mm	Uso: 0.09 - 0.44 m/s Usw: 0.10 - 0.8 m/s	Wave characteristics (instantaneous fluctuations of the Interface): Conductivity probe Mechanisms of drop	Mineral oil (kerosene)/Tap water ρ_O: 828 kg/m^3 μ_O: 5.5 cp @ 25°C σo_W: 39.6 mN/m @ 25°C ρ_O:1000 kg/m^3 μ_O: 1.0 cp @ 25°C	0°	

			detachment: High speed video camera			
Xu et al. (2008)	Stainless steel and transparent pipe ID: 50 mm ID: 25 mm	Input oil volume fraction = 3 – 94%	Hold up: QCV Flow pattern: Visual	White oils/Tap water @ 20°C and 0.101MPa. ρ_{O1}: 860 kg/m^3 μ_{O1}: 50 cp σo_{W1}: 44.5 mN/m ρ_{O2}: 860 kg/m^3 μ_{O2}: 138 cp σo_{W2}: 45.2 mN/m ρ_{W}: 998 kg/m^3 μ_{W}: 1 cp	0°	T : Room temp. P : 1bar
Hussain et al. (2008)	Stainless steel L:1.0, 8.85, 7.72 m ID: 25.4 mm	Um: 1.8, 2.5 & 2.76 m/s WC: 40, 46, 60%	Phase fraction distribution and flow development: Gamma tomography	Exxsol-D80/water @ 25°C ρ_{O}: 801 kg/m^3 μ_{O}: 1.6 cp σo_{W}: 17 mN/m	0°	
Al-Wahaibi and Angeli (2008)	Stainless steel Transparent pipe L: 8 m ID: 38 mm See [Lovick & Angeli (2004a)]	Um: 0.6, 0.9 - 1.10 m/s Uso: 0.05 - 0.55 m/s	Droplet velocity and size: Dual impedance probe	Mineral oil/Tap water ρ_{O}: 828 kg/m^3 μ_{O}: 5.5 cp @ 25°C σo_{W}: 39.6 mN/m @ 25°C ρ_{O}: 1000 kg/m^3 μ_{O}: 1.0 cp @ 25°C	0°	
Atmaca et al. (2008)	Transparent pipe L: 21.1 m ID: 50.8 mm	Uso: 0.025 - 1.75 m/s Usw: 0.025 - 1.75 m/s	Flow pattern: Visual Pressure drop Water holdup: QCV Phase distribution and interface boundaries: Conductivity probes	Mineral oil (Tulco Tech 80^{TM})/Tap water ρ_{O}: 850 kg/m^3 μ_{O}: 15 cp @ 25°C σo_{W}: 29.15 mN/m @ 25°.1C	0°, ±1° ±2° -5°	

Wahumpurage et al. (2008)	Steel pipe Transparent pipe L: 15 m ID: 56mm	Um: 0.5, 1.06 m/s WC: 0.25, 0.5, 75%	Flow pattern: Visual Pressure drop Phase distributions: Gamma densitometry Velocity and turbulence profiles: PIV	Exxsol D60/Water ρ_O: 790 kg/m^3 μ_O: 1.6 cp ρ_W: 998 kg/m^3 μ_W: 1 cp σo_W: 43 mN/m	0°	1 bar, 25°C
Kumara et al. (2009a)	Steel pipe, Transparent pipe L: 15 m ID: 56mm	U_M: 0.25 m/s WC: 0.25%	Flow pattern: Visual Pressure drop Phase distributions: Gamma densitometry Velocity and turbulence profiles: PIV	Exxsol D60/Water ρ_O: 790 kg/m^3 μ_O: 1.64 cp ρ_W: 996 kg/m^3 μ_W: 1.0 cp σo_W: 43 mN/m	0°	1 bar, 25°C Telemark University College
Kumara et al. (2009b)	Steel pipe, Transparent pipe L: 15 m ID: 56mm	U_M: 0.25, 0.5, 1.06 m/s WC: 0.25, 0.5, 75%	Local velocity and turbulence distribution: PIV Phase distributions: Gamma densitometry Velocity and turbulence profiles: PIV Flow regime: Visual	Exxsol D60/Water ρ_O: 790 kg/m^3 μ_O: 1.64 cp ρ_W: 996 kg/m^3 μ_W: 1.0 cp σo_W: 43 mN/m	0°	1 bar, 25°C Telemark University College

Appendix 2 Flow pattern in horizontal pipes

Table A 2 Flow patterns in horizontal pipes.

Investigator	Flow patterns	Description
Russel et al. (1959)	Mixed flow	Two separated layers with a dispersed phase at the top of the pipe
	Stratified flow	Two continuous phases with different degree of mixing
	Bubble flow	Oil bubbles/plugs flowing in the top of the pipe together with a water layer
Oglesby (1979)	Segregated	Oil and water flow in two distinct layers with no mixing at the interface.
	Semi-segregated	Oil and water continuous phases with some mixing at the interface.
	Semi-mixed	Three segregated layers, with a dispersion in the middle and two pure phases
	Mixed	Dispersion occupies more than half the pipe volume
	Dispersed	Oil and water totally mixed with concentration gradient
	Homogenous	Totally homogenous dispersed flow
Angeli (1996)	SW	Stratified wavy
	SWD	Stratified wavy/drops
	3L	Three layer (water, mixed layer and oil layer)
	SM/oil	Stratified mixed/oil layer (oil continuous)
	SM/water	Stratified mixed/water layer (water continuous)
	M	Mixed (Completely dispersed flow)
Trallero (1995)	ST	Two phases completely separated
	ST & MI	stratified flow with mixing at the interface
	Do/w & w	Dispersion of oil in water and water
	o/w	Oil in water emulsion
	Dw/o & Do/w	Dispersion of water in oil and oil in water
	w/o	Water in oil emulsion
Soleimani (1999)	Stratified wavy	Two phases completely separated
	Stratified wavy/drops	Two layers, with droplets concentrated near the interface zone
	Stratified mixed/water layer	Two layers, lower clear water layer with an dispersion in the top of the pipe
	Stratified mixed/oil layer	Two layers, upper clear oil layer with and dispersion in the bottom of the pipe
	Three layer flow	Clear oil layer, a dispersed layer and a water layer
	Dispersed flow	One phases completely dispersed as droplets in the other
Kvandal et al. (2000)	SD	Stratified dispersed flow
	DIH-B	Dispersed flow with an inhomogeneous bulk mixture
	DIH-W	Dispersed flow with an inhomogenous wall mixture
	DH	Dispersed homogenous flow
Alkaya (2000)	Trallero et al. (1997)	
	Dw/o & o	Dispersed water in oil and oil

Valle (2000)	Separated Dispersed oil continuous Dispersed water continuous Slug	
Elseth (2001)	SS SW SM Do-Dp Dw-DP Do-I Dw-I Do-H Dw-H	Stratified Smooth Stratified Wavy Stratified mixed Oil continuous dispersion with dense packed layer of water droplets Water continuous dispersion with dense packed layer of oil droplets Oil continuous dispersion – inhomogeneous Water continuous dispersion – inhomogeneous Oil continuous – homogeneous Water continuous – homogeneous
Lovick and Angeli (2004a)	SW DC Dw/o Do/w	Stratified wavy. Two layers of oil and water with a wavy interface Oil and water continuous phases with different degree of dispersions Dispersed water in oil phase Dispersed oil in water phase

Appendix 3 Flow pattern in slightly inclined pipes (0-10°)

Table A 3 Flow pattern in slightly inclined pipes (0 – 10°)

Investigator	Flow patterns	Description
Vedapuri et al. (1997)	Semi-segregated	Oil and water continuous phases with some mixing at the interface.
	Semi-mixed	Oil and water continuous phases with mixing at the interface.
	Dispersed	Oil and water continuous phases with large degree of mixing.
Alkaya (2000)	See Figure A 8	See Figure A 8
Oddie et al. (2003)	Segregated	
	Semi-segregated	
	Semi-mixed	
	Mixed	
	Dispersed	
	Homogenous	
Lum et al. (2004)	SW	Completely separated layers with a wavy interface
	DC	Oil and water continuous phases with different degree of dispersions
	o/w	Oil in water dispersion. Oil is dispersed in a continuous water phase
	w/o	Water in oil dispersion. Water is dispersed in a continuous oil phase
Abduvayt et al. (2006)	ST-S	Segregated; No mixing and a smooth interface
	SW	Segregated; No mixing and a wavy interface
	SR	Segregated; No mixing and a concave-down curvature interface
	O/TP & W	Segregated; No mixing and water occupied most of the cross section
	O-WF & W	Segregated; No mixing with a thin water film around the upper pipe wall
	ST-WD/O & W	Semi segregated; Stratified with water droplets in oil and water
	ST-WD/O & OD/W	Semi segregated; Stratified with water droplets in oil and oil droplets in water
	SR-WD/O & W	Semi segregated; Stratified-roll wave with water droplets in oil and water
	SLR-OD/WD & WD/O	Semi segregated; Stratified long roll waves with dispersed water and oil droplets
	DW/O & W	Semi dispersed; Dispersion of water in oil and water
	ThO/TP & FDO/W	Semi dispersed; Thin oil line at the top of pipe and fine dispersion of oil in water
	FDW/O & FDO/W	Semi dispersed; Fine dispersion of water in oil and fine dispersion of oil in water
Lum et al. (2006)	Lum et al. (2004)	See Figure A 8
	PG	Plug flow; Time dependent oil plug in top of pipe with a water layer
Rodriguez and Oliemans (2006)	Trallero (1995)	Stratified wavy; Wavy interface with no mixing
	SW	

Appendix 4 Rig modifications

Initial oil and water experiments without the pre-separator installed revealed that stable emulsions and air bubbles where formed in the separator and in the test section. Two-phase experiments could not be run due to the emulsions in the separator which caused unclean phases out from the separator and into the test section (oil in the water phase and water in the oil phase). Effort was made to find the reason why stable emulsions were formed and how the rig had to be modified to be able to run oil-water flow experiments.

One possible explanation for the observed air bubbles is that air bubbles emerge from the oil due to a sub atmospheric pressure in the test section. A sub atmospheric pressure in the test section occurs mainly due to the location of the main separator, which is approximately 2 m below the test section. A ball valve was used to increase the pressure in the test section and hence remove the air bubbles. The ball valve was installed down streams the gamma section. The effect of increasing the pressure in the test section is clearly demonstrated in Figure A 1 and Figure A 2. Figure A 1 shows air bubbles in the top of the pipe, when the ball valve is open, while Figure A 2 shows no existence of air bubbles, when the ball valve is closed.

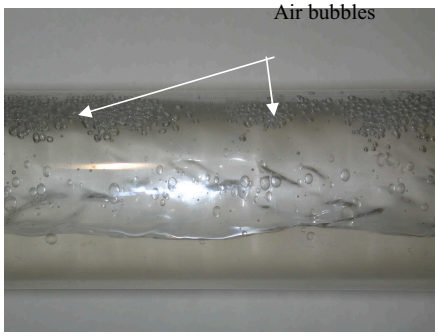

Figure A 1 Oil and water experiments with sub atmospheric pressure in the test section.

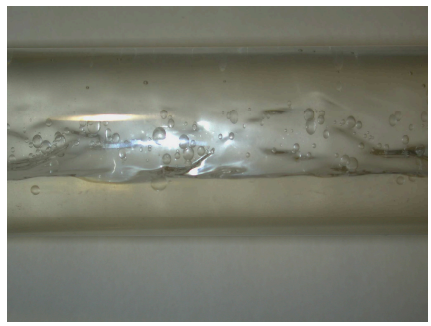

Figure A 2 Oil and water experiments without sub atmospheric pressure.

However in the two-phase oil-water flow experiments, the ball valve exerted too much shear which caused oil-water emulsion in the separator. The emulsions (white foam) formed are shown in Figure A 3.

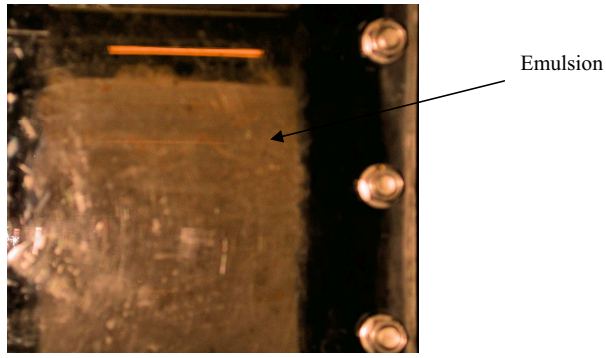

Figure A 3 Emulsions in separator.

The emulsion was formed when the velocity exceeded 0.5 m/s. At higher velocities the oil and water mixes more intensively and the retention time in the separator is lower. The formation of the emulsion is also dependent on the incoming water cut, surface tension of oil and water and temperature. The oil-water emulsion makes the optical conditions too poor for Laser Doppler experiments since the dispersion of oil drops in the water phase makes the water shady. A chemical emulsion breaker was tested, but the emulsion was even more stable.

Process simulations

The absorption of air into oil and water takes place in the oil and water tank at 1 atm. Equilibrium between oil and air causes the air to be absorbed in the oil. The solubility of air in oil is higher than of air in water. When the pressure decreases in the test section the air will emerge from the oil and cause air bubbles. Visual experiment of single-phase oil and water show that the single-phase oil flow contains more air-bubbles compared to the single-phase water flow. Dynamic process simulations (Aspen HYSYS®) also confirm that the sub atmospheric pressure in the test section can cause the absorbed air to separate. The sub atmospheric pressure in the test section is set equal to 0.9 atm. The simulations presented in Table A 4 show that the oil contains more air-bubbles than water.

Table A 4 Hysys simulations of amount of air in oil and water.		
Fluid	**Pressure [atm], test section**	**Separated air [vol%]**
Oil	0.9	2.4
Water	0.9	0.1

Use of different flow configurations

Different flow configurations were tried out to regulate the pressure in the test section and to avoid the formation of oil-water emulsions. The three flow configurations in Figure A 4 was implemented down streams the test section before the flow enters the separator. The three configurations are made of stainless steel and are 2.4 m high. The small pipe on the top of the U-bends is 0.52 m long and a rubber hose connects the small pipe to the oil tank. A valve is mounted at the end of the rubber hose, which enables air-entrance. The first and the second modifications are called U-pipe 1 and U-pipe 2 and the third is called a V-pipe configuration.

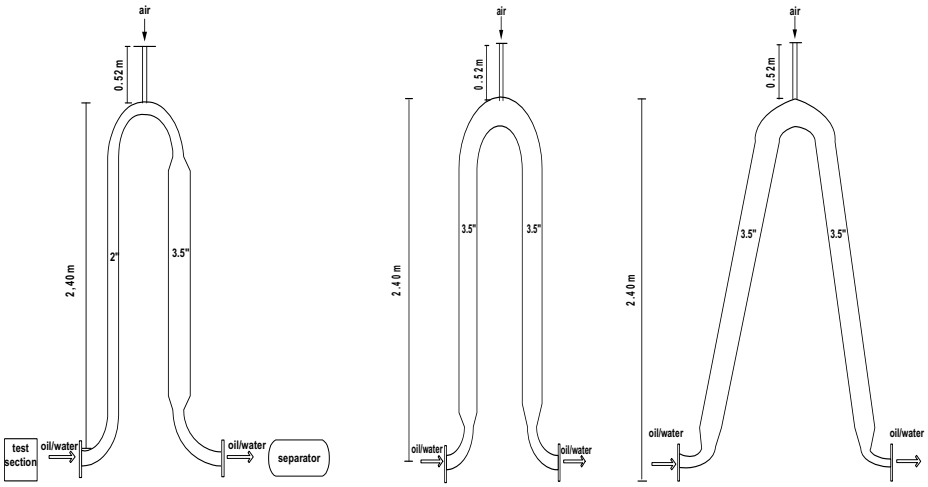

Figure A 4 Different flow configurations: U-pipe 1, U-pipe 2 and V-pipe.

In the U-pipe 1 configuration, the flow enters a 2-in. vertical pipe. The flow turns 180° in a 2-in. U-bend and flows into a 3.5-in. vertical pipe. Two-phase oil-water experiments showed that the U-pipe 1 configuration caused oil-water emulsion.

The U-pipe 2 configuration was modified by replacing the 2-in. pipe with a 3.5-in. pipe and replacing the 2-in. bend with a 3.5-in. bend. When the diameter is higher, the velocity is lower, which leads to less turbulence and mixing of oil and water. Experiments with this configuration revealed that the modifications are not enough to avoid oil-water emulsion to be formed. A probable cause for this is the height of liquid fall together with the contraction at the bottom of the pipe causing turbulence and mixing.

The V-pipe configuration was build to reduce the liquid fall and the shear at the bottom of the pipe. The dimensions of this configuration are 3.5-in. Experiments with the V-pipe did not reduce the formation of emulsion.

Conclusion

The ball valve and the three flow configurations caused emulsion that did not separate in the main separator, but it was proved that the increased pressure in the test section removed the air bubbles. The final solution was a pre-separator tank which was installed downstream the test section (see Chapter 3), which reduced the mixing and increased the separation time.

Appendix 5: Viscosity of Exxsol D60 and tap water

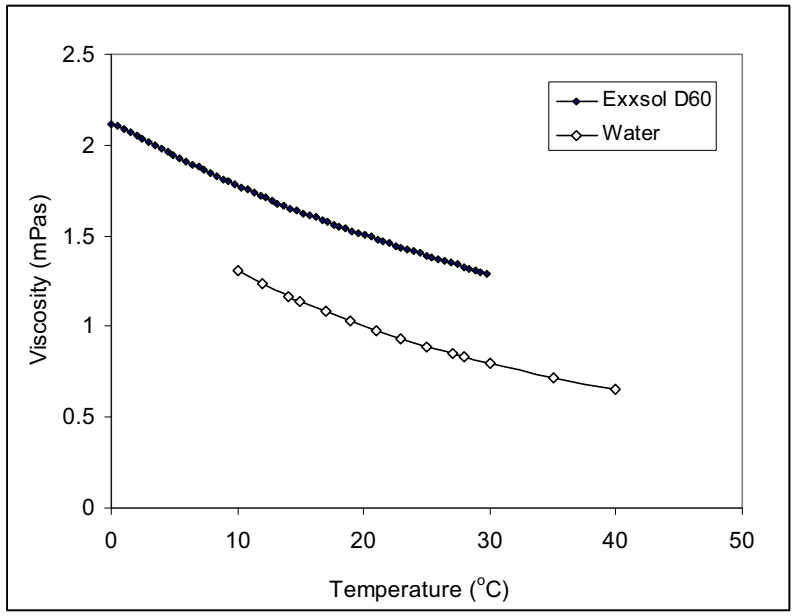

Figure A 5 Viscosity as function of temperature for Exxsol D60 and tap water.

Appendix 6: Density of Exxsol D60 and tap water

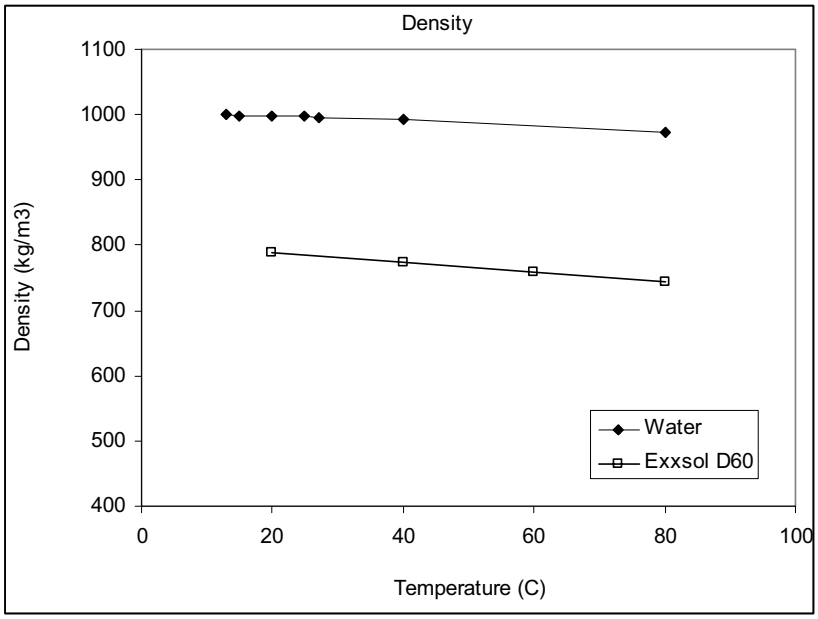

Figure A 6 Density as function of temperature for Exxsol D60 and tap water.

Appendix 7: Water calibration

Table A 5 Water calibration of turbine meter with use of Coriolis flow meter.

Mass flow meter Water [l/min]	Turbine meter Water [l/min]	Correlations: y = 1.0397x - 1.6017	difference between mass flow meter and correlation
16.1	16.5	17.4	1.35
16.8	16.6	17.6	0.79
24.1	23.8	24.4	0.33
32.0	31.8	32.1	0.13
40.2	40.2	40.2	0.03
54.5	54.6	54.1	-0.38
54.9	55.3	54.7	-0.23
69.2	69.6	68.5	-0.72
75.8	76.7	75.3	-0.49
84.7	85.9	84.1	-0.61
97.1	99.3	97.0	-0.13
112.6	115.2	112.4	-0.20
112.7	115.7	112.8	0.09
120.3	123.5	120.3	0.01
127.4	131.2	127.8	0.33
134.2	138.1	134.4	0.22
147.7	152.2	147.9	0.27
148.2	152.6	148.3	0.10
173.3	178.6	173.4	0.08
184.9	190.4	184.7	-0.16
198.3	204.6	198.4	0.01
230.9	238.4	230.8	-0.13
241.0	248.9	240.9	-0.06
266.8	275.9	266.9	0.05
268.1	276.8	267.8	-0.28

Appendix 8: Oil calibration

Table A 6 Water calibration of turbine meter with use of Coriolis flow meter.

Mass flow meter Oil [l/min]	Turbine meter Oil [l/min]	Correlation: y = 1.0531x - 3.7819:	difference between mass flow meter and correlation
22.2	17.4	20.1	-2.06
22.3	17.2	19.9	-2.43
27.6	24.8	27.2	-0.45
33.6	32.3	34.3	0.68
39.5	39.9	41.5	1.92
39.7	39.8	41.4	1.74
53.5	53.4	54.3	0.81
69.9	70.0	70.0	0.09
77.6	78.3	78.0	0.36
78.2	78.7	78.3	0.17
83.7	84.8	84.1	0.46
99.3	101.4	99.9	0.65
110.8	113.7	111.6	0.76
114.0	116.6	114.3	0.30
119.5	123.0	120.4	0.86
126.3	130.0	127.0	0.74
132.7	136.8	133.5	0.79
147.0	151.2	147.2	0.15
147.3	151.9	147.9	0.59
164.0	169.5	164.6	0.58
188.5	194.5	188.3	-0.19
204.2	211.2	204.2	-0.07
229.5	237.6	229.3	-0.25
242.6	251.3	242.2	-0.39
264.8	274.5	264.3	-0.54

Appendix 9 Derivation of error in phase fraction measurements

The error in phase fraction $d(\varepsilon_w)$ can be expressed as in Eq. (A1) by differentiating Eq. 4.9 with respect to I, I_0, γ_1, γ_2 and H.

$$d(\varepsilon_w) = \sqrt{\left(\frac{\partial \varepsilon_w}{\partial I}\right)^2 d(I)^2 + \left(\frac{\partial \varepsilon_w}{\partial I_0}\right)^2 d(I_0)^2 + \left(\frac{\partial \varepsilon_w}{\partial \gamma_1}\right)^2 d(\gamma_1)^2 + \left(\frac{\partial \varepsilon_w}{\partial \gamma_2}\right)^2 d(\gamma_2)^2 + \left(\frac{\partial \varepsilon_w}{\partial H}\right)^2 d(H)^2} \quad \text{(A1)}$$

Error in transmitted beam intensity I

The first step is to calculate the error in phase fraction due to error in transmitted beam intensity I (experimental fluids). The calculations are shown in Eqs. (A2) to (A4). This is done by differentiation of Eq. 4.9 with respect to I.

$$\left(\frac{\partial \varepsilon_w}{\partial I}\right) d(I) = \frac{\partial \left(\dfrac{\ln\left(\dfrac{I_0}{I}\right)/H - \gamma_2}{(\gamma_1 - \gamma_2)} \right)}{\partial I} d(I) = \frac{-1}{(\gamma_1 - \gamma_2)H} \frac{d(I)}{I} \quad \text{(A2)}$$

An expression for the relative error in the transmitted intensity $\frac{d(I)}{I}$ in Eq. (A2) is derived by substituting dn with $d(I \cdot T)$ in Eq. 4.16. The relative error in I is shown in Eq. (A3).

$$\frac{d(I)}{I} = \frac{\sqrt{n}}{n} = \frac{1}{\sqrt{n}} \quad \text{(A3)}$$

Eq. (A3) is then substituted into Eq. (A2) and a final equation for the measurement error in the phase fraction due to measurement error in the transmitted beam intensity I is derived. T is the measurement time of the transmitted beam (I) and H is the length of the fluids.

$$\left(\frac{\partial \varepsilon_w}{\partial I}\right) d(I) = \frac{-1}{(\gamma_1 - \gamma_2)H\sqrt{n}} = \frac{-1}{(\gamma_1 - \gamma_2)H\sqrt{I \cdot T}} \quad \text{(A4)}$$

The liquid length (H) is a function of the beam position as shown in Figure A 7.

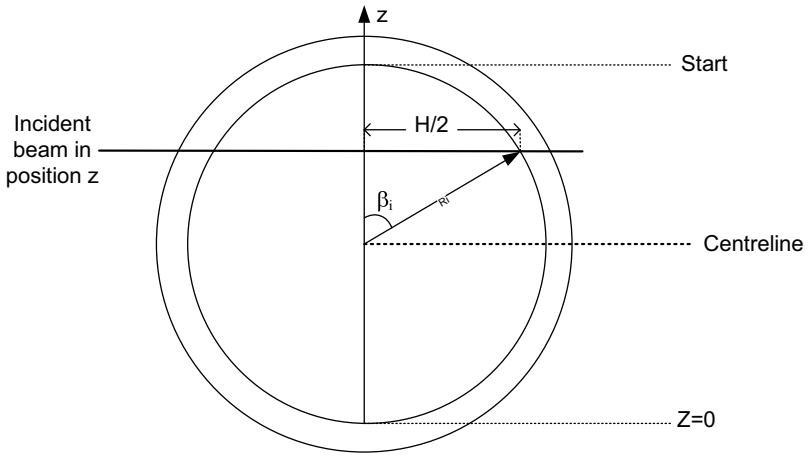

Figure A 7 Geometrical description of beam position (z) and liquid length (H).

The liquid length (*H*) can be derived from Eqs. (A5), where β_i is the angle as shown in Figure A 7.

$$H = 2R\sin(\beta_i) \tag{A5}$$

where

$$\beta_i = \arccos\left(\frac{z-R}{R}\right) \tag{A6}$$

Error in phase fraction due to error in incident beam I_0

By using same approach as shown above, the measurement error in phase fraction due to the incident beam I_0 (pipe filled with air), can be expressed as in Eq. (A7).

$$\left(\frac{\partial \varepsilon_w}{\partial I_0}\right) d(I_0) = \frac{1}{(\gamma_1 - \gamma_2)H\sqrt{n_0}} = \frac{1}{(\gamma_1 - \gamma_2)H\sqrt{I_0 \cdot T_0}} \tag{A7}$$

Error in phase fraction due to error in attenuation coefficients γ_1 and γ_2

The next step is to find the error in phase fraction due to error in the calibration of the attenuation coefficients (γ_1 and γ_2). Eq. 4.9 is differentiated with respect to the attenuation coefficient γ_1 and γ_2 as shown in Eqs. (A8) and (A9).

$$\left(\frac{\partial \varepsilon_w}{\partial \gamma_1}\right) d(\gamma_1) = \frac{\gamma_2 - \ln\left(\frac{I_0}{I}\right) \Big/ H}{(\gamma_1 - \gamma_2)^2} \cdot \gamma_1 \frac{d(\gamma_1)}{\gamma_1} \tag{A8}$$

$$\left(\frac{\partial \varepsilon_w}{\partial \gamma_2}\right) d(\gamma_2) = \frac{\ln\left(\frac{I_0}{I}\right) \Big/ H - \gamma_1}{(\gamma_1 - \gamma_2)^2} \cdot \gamma_2 \frac{d(\gamma_2)}{\gamma_2} \tag{A9}$$

An expression for γ_1 can be derived by substituting the intensities I_1 and I_0 with $I_1 = n_1/T_1$ and $I_0 = n_0/T_0$ into Eq. 4.12. This gives Eq. (A10).

$$\gamma_1 = \frac{\ln\left(\frac{n_0 T_1}{n_1 T_0}\right)}{H} \tag{A10}$$

To find the measurement error in the attenuation coefficient γ_1, Eq. (A10) must be differentiated with respect to n, n_0 and H as shown in Eq. (A11).

$$d(\gamma_1) = \sqrt{\left(\frac{\partial \gamma_1}{\partial n_1}\right)^2 d(n_1)^2 + \left(\frac{\partial \gamma_1}{\partial n_0}\right)^2 d(n_0)^2 + \left(\frac{\partial \gamma_1}{\partial H}\right)^2 d(H)^2} \tag{A11}$$

Eqs. (A12) and (A13) show the differentiation of expression (A10) with regard to number of counts (n_1) with calibration fluid 1 and number of counts (n_0) in empty pipe.

$$\left(\frac{\partial \gamma_1}{\partial n_1}\right) d(n_1) = \left(\frac{\partial \frac{\ln\left(\frac{n_0 T_1}{n_1 \tau_0}\right)}{H}}{\partial n_1} \right) d(n_1) = -\frac{1}{H n_1} d(n_1) \tag{A12}$$

$$\left(\frac{\partial \gamma_1}{\partial n_0}\right) d(n_0) = \left(\frac{\partial \dfrac{\ln\left(\dfrac{n_0 T_1}{n_1 \tau_0}\right)}{H}}{\partial n_0} \right) d(n_0) = \frac{1}{H n_0} d(n_0) \tag{A13}$$

The relative errors in pulse counting $\frac{d(n_1)}{n_1}$ and $\frac{d(n_0)}{n_0}$ are found from Eq. 4.16 and substituted into Eq. (A12) and (A13). The expression for the relative error in γ_1 is expressed more conveniently when the relationships $n_1 = I_0 T_1 \exp(-\gamma_1 H)$ and $n_0 = I_0 T_0$ are used as shown in Eqs. (A14) and (A15).

$$\left(\frac{\partial \gamma_1}{\partial n_1}\right) d(n_1) = -\frac{1}{H\sqrt{I_0 T_1 \exp^{-\gamma_1 H}}} \tag{A14}$$

$$\left(\frac{\partial \gamma_1}{\partial n_0}\right) d(n_0) = \frac{1}{H\sqrt{I_0 T_0}} \tag{A15}$$

The error in γ_1 due to error in liquid length H is shown in Eq. (A16).

$$\left(\frac{\partial \gamma_1}{\partial H}\right) d(H) = \left(\frac{\partial \dfrac{\ln\left(\dfrac{n_0 T_1}{n_1 \tau_0}\right)}{H}}{\partial H} \right) d(H) = -\frac{\ln\left(\dfrac{n_0 T_1}{n_1 \tau_0}\right)}{H} \frac{d(H)}{H} = -\frac{\ln\left(\dfrac{I_0}{I_1}\right)}{H} \frac{d(H)}{H} \tag{A16}$$

The relative error in liquid length $\frac{d(H)}{H}$ can be calculated from Eqs. (A17) and (A18). The derivation of the Eq. (A17) is shown in Appendix 10. The relative error in the liquid length is a function of the error in the position (z) and inner pipe radius (R). The expressions assume that the pipe is circular.

$$\frac{d(H)}{H} = \frac{1}{R} \cdot \frac{\dfrac{R-z}{R}}{1-\left(\dfrac{R-z}{R}\right)^2} d(z) \tag{A17}$$

The error in the positioning of the beam $d(z)$ can be quantified as in Eq. (A18), where dz_0 is the uncertainty in zero point and d_{step} is the uncertainty in the traversing device.

$$d(z) = dz_0 + d_{step} \tag{A18}$$

Substituting the expressions for the error in relative liquid length in Eq. (A17) and error in positioning in Eq. (A18) into Eq. (A16) gives the error in γ_1 due to liquid length H as shown in Eq. (A19). The same approach finding the error in γ_2 due to liquid length H is used and the result is presented in Eq. (A20).

$$\left(\frac{\partial \gamma_1}{\partial H}\right) d(H) = -\frac{\ln\left(\frac{I_0}{I_1}\right)}{H}\left(\frac{1}{R}\cdot\frac{\frac{R-z}{R}}{1-\left(\frac{R-z}{R}\right)^2}\left(dz_0 + d_{step}\right)\right) \tag{A19}$$

$$\left(\frac{\partial \gamma_2}{\partial H}\right) d(H) = -\frac{\ln\left(\frac{I_0}{I_2}\right)}{H}\left(\frac{1}{R}\cdot\frac{\frac{R-z}{R}}{1-\left(\frac{R-z}{R}\right)^2}\left(dz_0 + d_{step}\right)\right) \tag{A20}$$

The total measurement error in the attenuation coefficient γ_1 is now found by substituting Eqs. (A14) and (A15) for the error in pulse counting and Eq. (A19) for the error in liquid length into Eq. (A11), which is the total error in attenuation coefficient. The derived equation is then substituted into Eq. (A8) to give the total error in phase fraction due to error in the attenuation coefficient.

$$\left(\frac{\partial \varepsilon_w}{\partial \gamma_1}\right) d(\gamma_1) = \frac{\gamma_2 - \ln\left(\frac{I_0}{I}\right)\Big/H}{(\gamma_1-\gamma_2)^2 H}\sqrt{\frac{1}{I_0}\left(\frac{\exp(\gamma_1 H)}{T_1}+\frac{1}{T_0}\right)+\left(-\ln\left(\frac{I_0}{I_1}\right)\left(\frac{1}{R}\cdot\frac{\frac{R-z}{R}}{1-\left(\frac{R-z}{R}\right)^2}\left(dz_0 + d_{step}\right)\right)\right)^2} \tag{A21}$$

The total measurement error in phase fraction is found by substituting γ_2 into the derived Eq. for the relative error in attenuation coefficient for fluid 1 and substitute this expression into

Eq. (A9). The error in phase fraction due to error in attenuation coefficients for fluid 2 is shown in Eq. (A22).

$$\left(\frac{\partial \varepsilon_w}{\partial \gamma_2}\right) d(\gamma_2) = \frac{\ln\left(\frac{I_0}{I}\right) \Big/ H}{(\gamma_1 - \gamma_2)^2} - \gamma_1 \sqrt{\frac{1}{I_0}\left(\frac{\exp(\gamma_2 H)}{T_2} + \frac{1}{T_0}\right) + \left(-\ln\left(\frac{I_0}{I_2}\right)\left(\frac{1}{R} \cdot \frac{\frac{R-z}{R}}{1-\left(\frac{R-z}{R}\right)^2}\left(dz_0 + d_{step}\right)\right)\right)^2} \quad \text{(A22)}$$

Error in phase fraction measurements due to error in the liquid length *d*(*H*)

The error in phase fraction measurements due to error in the liquid length *d*(*H*) is shown in Eq. (A23). Eq. 4.9 is differentiated with respect to the liquid length *H*.

$$\left(\frac{\partial \varepsilon_w}{\partial H}\right) d(H) = -\frac{\ln\left(\frac{I_0}{I}\right)}{H(\gamma_1 - \gamma_2)} \frac{d(H)}{H} \quad \text{(A23)}$$

The expression for the relative error in liquid length $\frac{d(H)}{H}$ as presented in Eqs. (A17) and (A18) are substituted into Eq. (A23). The final expression is given in Eq. (A24).

$$\left(\frac{\partial \varepsilon_w}{\partial H}\right) d(H) = -\frac{\ln\left(\frac{I_0}{I}\right)}{H(\gamma_1 - \gamma_2)} \left(\frac{1}{R} \cdot \frac{\frac{R-z}{R}}{1-\left(\frac{R-z}{R}\right)^2}\left(dz_0 + d_{step}\right)\right) \quad \text{(A24)}$$

The total error in phase fraction measurements is now derived by substituting the equations for errors in phase fractions due to *I*, I_0, γ_1, γ_2 and *H* as presented in Eqs. (A4), (A7), (A21), (A22) and (A24) into Eq. (A1).

Appendix 10 Liquid length

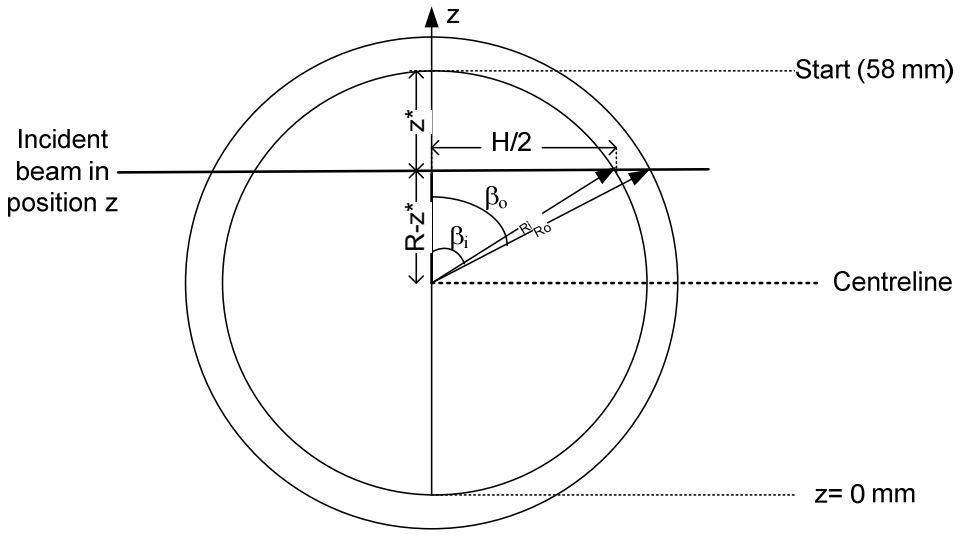

Figure A 8 Liquid length *H* as function of position *z* and wall thickness.

Calculation of error in liquid length *d(H)* assumes that the beam thickness is small compared to the geometry of the pipe, so that the beam can be expressed as a thin line. Eq. (A25) expresses the liquid length *H* as function of inner angle β_i.

$$H = 2R\sin\beta_i \tag{A25}$$

$$\frac{d(H)}{d(z)} = 2R\frac{d(\sin\beta_i)}{d(z)} = 2R\cos\beta_i\frac{d(\beta_i)}{d(z)} \tag{A26}$$

Derivation of an expression for $\frac{d(\beta_i)}{d(z)}$ is shown in eq. (A27) to (A32).

$$\cos\beta_i = \frac{R - z^*}{R} \tag{A27}$$

$$z^* = 2R - z \tag{A28}$$

$$\cos\beta_i = \frac{z-R}{R} \tag{A29}$$

$$\frac{d(\cos\beta_i)}{d(z)} = \frac{d}{d(z)}\left(\frac{z-R}{R}\right) \tag{A30}$$

$$-\sin\beta_i \frac{d(\beta_i)}{d(z)} = \frac{1}{R} \tag{A31}$$

$$\frac{d(\beta_i)}{d(z)} = -\frac{1}{R\sin\beta_i} \tag{A32}$$

Substituting Eq. (A32) into Eq. (A26) gives:

$$\frac{d(H)}{d(z)} = \frac{2R\cos\beta_i}{R\sin\beta_i} = -\frac{2}{\tan\beta_i} \tag{A33}$$

The relative error in *H* can now be expressed as shown in Eq. (A34).

$$\frac{d(H)}{H} = -\frac{2}{\tan\beta_i}\frac{d(z)}{H} \tag{A34}$$

Substituting the expression for *H* in Eq. (A25) into Eq. (A34) gives:

$$\frac{d(H)}{H} = -\frac{2}{\tan\beta_i}\frac{d(z)}{2R\sin\beta_i} = -\frac{1}{R}\cdot\frac{\cos\beta_i\ d(z)}{\sin^2\beta_i} \tag{A35}$$

The expression for $\cos\beta_i$ in Eq. (A27) and the relationship $\sin^2\beta_i = 1-\cos^2\beta_i$ is substituted into Eq. (A35). The relative error in liquid length $\frac{d(H)}{H}$ is now expressed as function of R and *d(z)*.

$$\frac{d(H)}{H} = -\frac{\frac{z-R}{R}}{R(1-\cos^2\beta_i)}d(z) = -\frac{\frac{z-R}{R}}{R\left(1-\left(\frac{z-R}{R}\right)^2\right)}d(z) \tag{A36}$$

Calculation of wall length is shown in Eqs. (A37) to (A 40) below.

$$H = 2R\sin\beta_i \tag{A37}$$

$$H_o = 2R\sin\beta_o \tag{A38}$$

$$\beta_o = \arccos(\frac{R-z}{R_o}) \tag{A39}$$

$$\Delta x_{wall} = H_o - H \tag{A 40}$$

Appendix 11: Detection of air in the test section

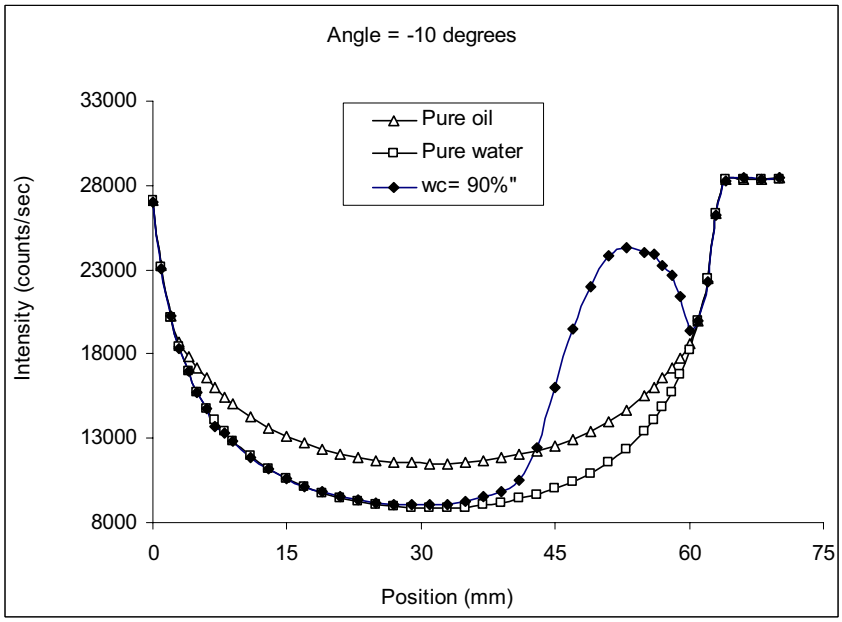

Figure A 9 Gamma measurements of oil, water and air at -10º angle and 90% input water cut

Appendix 12 Geometrical relationships

The water and oil area can be calculated from Eq. (A41):

$$A_w = \frac{A}{2\pi}(\delta - \sin\delta), \quad A = \frac{\pi D^2}{4}$$
$$A_o = A - A_w \tag{A41}$$

The wetted perimeters of oil, water and the oil-water interface are expressed as in Eq. (A42):

$$S_o = \left(\pi - \frac{\delta}{2}\right)D$$
$$S_w = \frac{\delta D}{2} \tag{A42}$$
$$S_i = D\sin\left(\frac{\delta}{2}\right)$$

The wetted angle is expressed in Eq. (A43).

$$\delta = 2\arccos\left(1 - \frac{2h}{D}\right) \tag{A43}$$

Figure A 10 shows the pipe geometry, the wetted angle (δ) and the height (h).

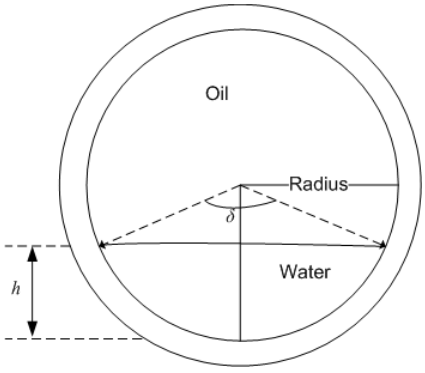

Figure A 10 Description of water height (h) and wetted angle (δ).

Appendix 13 Model comparison

Table A 7 Re-classification of Elseth's (2001) flow regimes.

	Old	**New (50% inversion water cut)**
	Velocity equal to 2 m/s	
10	Do-I	w/o
20	Do-I	Do/w & o
25	SM	Do/w & o
30	SM	ST & MI
40	SM	ST & MI
50	SM	ST & MI
50	SM	ST & MI
60	SM	ST & MI
70	Dw-DP	Dw/o & w
75	Dw-I	Dw/o & w
80	Dw-I	Dw/o & w
85	Dw-I	o/w
90	Dw-I	o/w
	Velocity equal to 3 m/s	
35	Do-I	Dw/o & Do/w
40	Dw-I	Dw/o & Do/w
45	Dw-I	Dw/o & Do/w
50	Dw-I	Dw/o & Do/w
60	Dw-I	Dw/o & Do/w
70	Dw-I	o/w
80	Dw-H	o/w